DEM Modelling of Multi-Component Segregation in the Blast Furnace Charging System

Ahmed Hadi

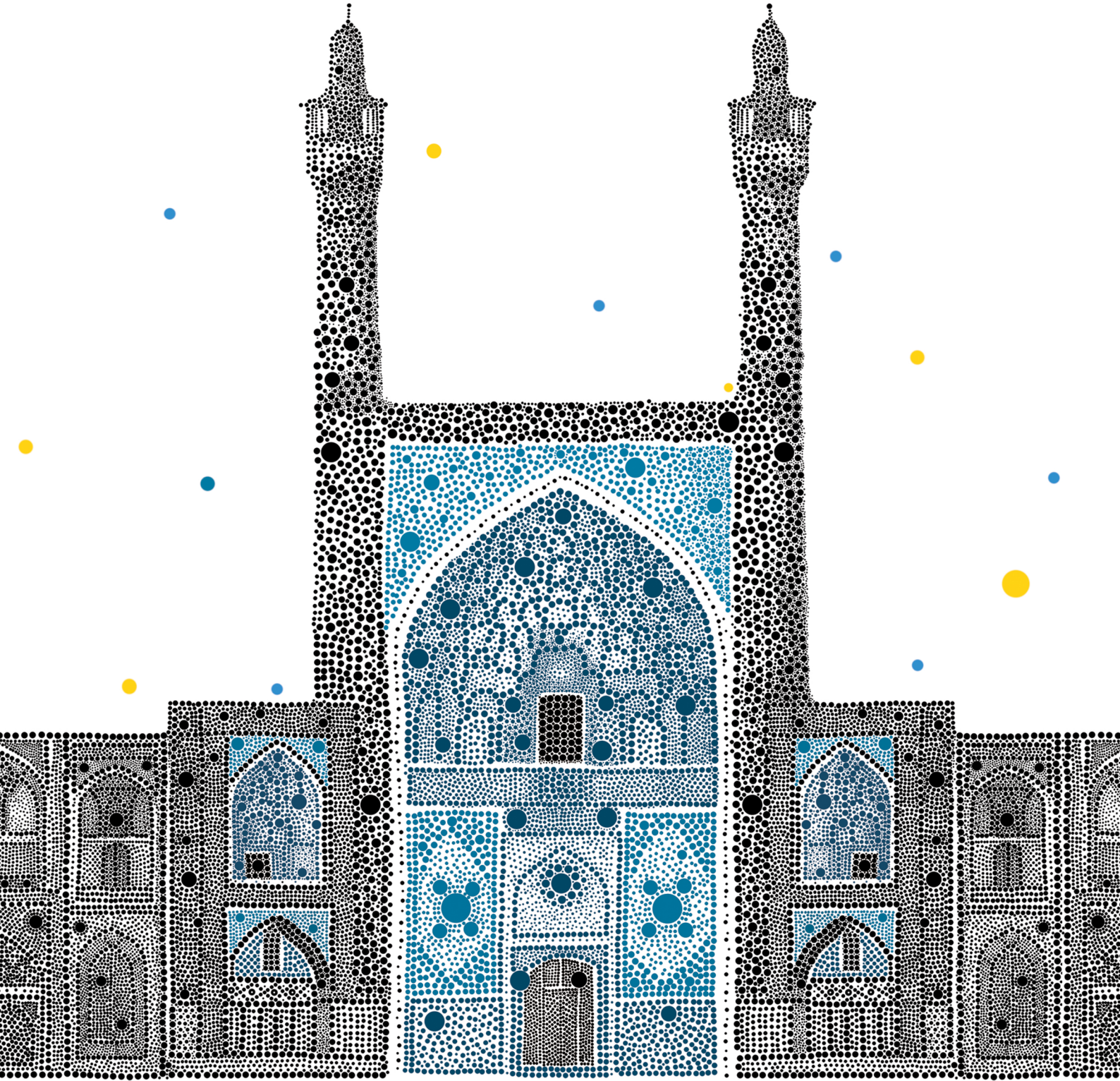

DEM Modelling of Multi-Component Segregation in the Blast Furnace Charging System

Ahmed Hadi

DEM Modelling of Multi-Component Segregation in the Blast Furnace Charging System

Dissertation

for the purpose of obtaining the degree of doctor
at Delft University of Technology
by the authority of the Rector Magnificus, Prof. dr. ir. H. Bijl
chair of the Board for Doctorates
to be defended publicly on
Tuesday February 3rd, 2026 at 12:30

by

Ahmed Hussein HADI
Master of Science in Civil Engineering - Geotechnics
University of Tehran
born in Isfahan, Iran

This dissertation has been approved by the promotors.

Composition of the doctoral committee:

Rector Magnificus	Chairperson
Prof. dr. ir. D. L. Schott	Delft University of Technology, promotor
Dr. ir. Y. Pang	Delft University of Technology, copromotor

Independent members:

Prof. dr. ir. J. R. van Ommen,	Delft University of Technology
Prof. dr. H. Saxén,	Åbo Akademi University
Prof. dr. V. Magnamino	University of Twente
Prof. dr. G. D. Weymouth	Delft University of Technology
Dr. Y. Yang	Delft University of Technology

This research was carried out under project number T18019 in the framework of the Research Program of the Materials innovation institute (M2i) (www.m2i.nl) supported by the Dutch government.

TRAIL Thesis Series no. T2026/5, The Netherlands Research School TRAIL

TRAIL
P.O. BOX 5017
2600 GA Delft
The Netherlands
E-mail: info@rsTRAIL.nl

Keywords: discrete element method, granular materials, mixing and segregation, blast furnace, DEM calibration, surrogate modelling, machine learning

Cover by: Mohammad Soleymanshah

ISBN: 978-90-5584-380-0

Printed in the Netherlands

To Parvin

Contents

Chapter 1

Introduction

Granular materials are widespread and are the second most handled materials in industry after water [1]. They appear in a variety of natural and industrial settings, including pharmaceuticals, agriculture, food processing, construction, and mining and metallurgy, as illustrated in Figure 1.1. Given their wide use, it is crucial to study and understand the behaviour of granular materials to optimise relevant industrial processes.

Figure 1.1 The wide range of applications of granular materials in industry.

One significant challenge encountered during the handling and processing of granular materials is segregation (or de-mixing). Segregation refers to the phenomenon in which particles with similar characteristicssuch as size, density, or shapecollect in specific spatial regions of the mixture, which disrupts the uniformity [2]. Generally, segregation is considered undesirable, as it may lead to numerous problems during handling, processing, manufacturing, or unit operations [3]. These include inconsistent product quality, poor flowability, process inefficiencies, increased material waste, and even safety problems. Such issues translate directly into

increased operational costs as well as reduced efficiency and productivity. Therefore, a comprehensive understanding of segregation and effective control strategies for minimising it should be explored for optimising material handling and processing.

Many industrial applications involve processing mixtures of multiple materials (referred to in this thesis as "multi-component mixtures") in which the constituent materials differ in size, density, and/or shape. Two types of segregation can occur within multi-component mixtures: 1) Intra-component segregation, occurring within each single material type, typically driven by particle size differences, and 2) Inter-component segregation, involving separation between different materials (components). Due to the differences in particle properties both within and between components, achieving and maintaining a homogeneous mixture is often challenging, as segregation tends to occur during handling.

1.1 Segregation mechanisms

Segregation may occur when materials are in motion and can result from several mechanisms that depend on particle properties, equipment and material flow conditions. While particle shape may also cause segregation [4], the most commonly identified mechanisms are based on particle size and density. Four main segregation mechanisms are identified, as shown in Figure 1.2 (a)-(d) [2, 4, 5]:

- Percolation segregation: Smaller particles tend to move downward through voids between larger particles.
- Trajectory segregation: Larger particles travel further in the air due to differences in momentum.
- Brazil-nut effect: Larger or less dense particles rise to the surface of the mixture under vibration.
- Buoyancy-driven segregation: Differences in density cause heavier particles to sink within the mixture.

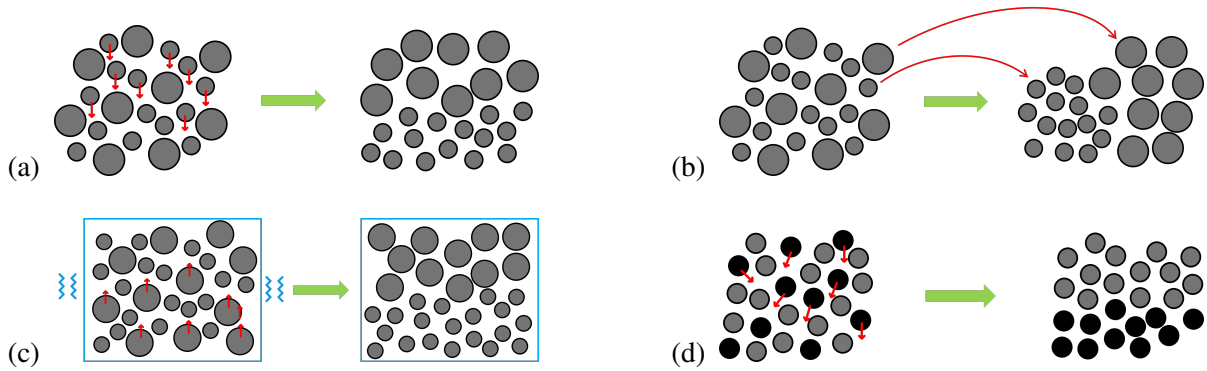

Figure 1.2 Four main segregation mechanisms based on particle size and density: (a) percolation, (b) trajectory, (c) Brazil-nut effect, and (d) buoyancy segregation.

The simultaneous occurrence of multiple segregation mechanisms makes the prediction of segregation behaviour highly challenging, especially in multi-component mixtures. Consequently, despite the insights that can be gained from understanding individual segregation mechanisms, each scenario of handling mixtures of granular materials must be studied individually to determine the dominant segregation mechanism(s) under specific conditions.

One industrial sector significantly influenced by segregation is the steel industry, particularly in blast furnace (BF) operations. In the BF process, a ferrous mixture consisting of multiple components such as pellets, sinter, and lump ore is charged into the furnace. This research specifically focuses on segregation occurring before the BF, using a typical BF operated by Tata Steel IJmuiden as a case study to investigate and model segregation throughout the charging process.

1.2 Segregation in the blast furnace charging system

The BF is a counter-current reactor widely used in steelmaking. Figure 1.3 schematically illustrates the BF charging system, where raw materials are handled, transported, and delivered to the furnace throat. The materials within the furnace (collectively referred to as the burden), consist of alternating layers of two main constituents: coke and the ferrous mixture. This study focuses on the ferrous mixture, which is a multi-component mixture of pellets, sinter, and lump ore (Figure 1.4). In some operations, other materials such as nut coke (small-sized coke) and other additives may also be added to the ferrous mixture.

The main components of the charging system and their functions are as follows:

- Storage bunkers: Raw materials are stored separately in individual bunkers.
- Conveyor belts: The materials from storage bunkers are transferred via conveyor belts to sieves. Sinter and pellets are discharged on separate belts, while lump ore and additives are charged together on one belt.
- Sieves: Sieves remove dust and smaller particles (typically below 5 mm) from materials, ensuring suitable particle size distributions.
- Weighing bunkers: After sieving, materials are precisely measured and collected in weighing bunkers. Pellets and sinter each have their own weighing bunkers, while a mixture of lump ore and additives charges into a single weighing bunker.
- Skip car: All materials from the weighing bunkers are combined into the skip car, forming the final ferrous mixture. Approximately 34 tons of ferrous materials are loaded into the skip car. It then moves up on the rail to the top of the furnace and discharges the ferrous mixture into the Paul-Wurth (P-W) bell-less charging system.
- Paul-Wurth (P-W) bell-less charging system: This system consists of a receiving funnel, two top hoppers, and a rotating chute, charging the materials to the furnace throat. In each charging cycle, two skip car loads are discharged into one of the top hoppers (alternating between the left and right), resulting in approximately 68 tons of ferrous mixture. This corresponds to roughly 3040 million particles.

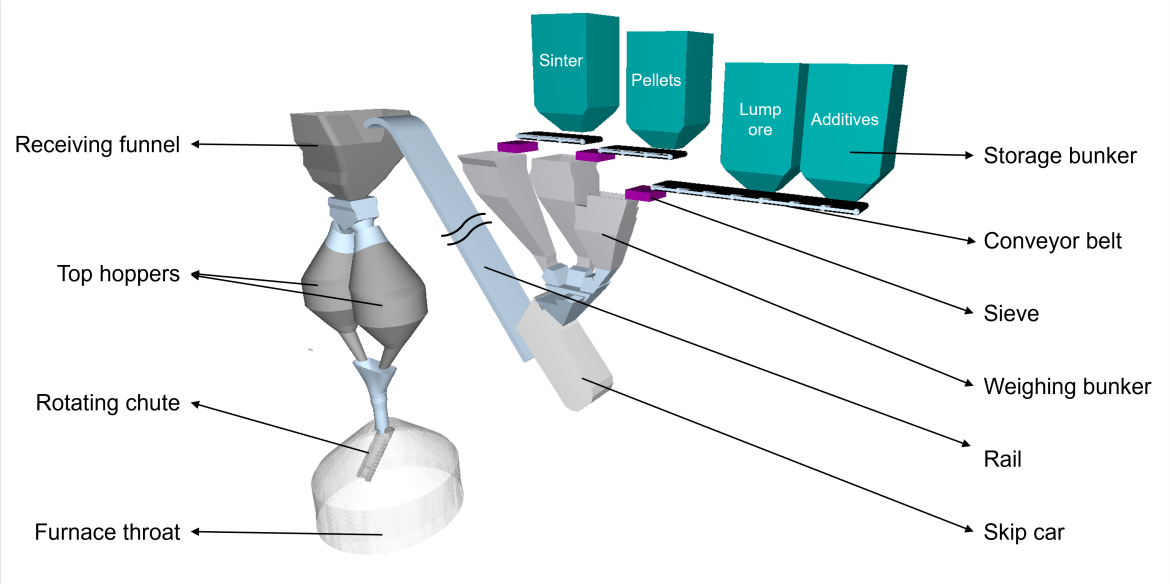

Figure 1.3 Schematic view of the blast furnace charging system (not to scale).

Figure 1.4 The main components of the ferrous mixture: sinter (left), pellets (middle), and lump ore (right) [6].

Typically, the burden is charged into the furnace in alternating layers of ferrous materials and coke, as shown in Figure 1.5. The hot gas generated near the bottom of the furnace, following the injection of preheated air (blast) and auxiliary hydrocarbons, performs crucial functions such as heat transfer and iron melting [6]. Because these functions directly influence process efficiency, fuel consumption, and overall productivity [6, 7], ensuring optimal interaction between the gas and burden is crucial. The optimal gas-burden interaction strongly depends on the permeability of the burden layers, which refers to the ability of gas to flow through the interconnected voids between particles [8]. However, segregation of the ferrous mixture leads to uneven burden layers at the furnace throat, which significantly reduces permeability [9, 10].

Zooming out to the whole blast furnace charging system (Figure 1.3), every upstream handling step may contribute to the final burden segregation at the BF throat. Therefore, it is important to evaluate segregation throughout the whole charging system. Since the ferrous mixture (as a multi-component mixture) is formed when materials are discharged from the weighing bunkers into the skip car, the scope of this research spans from the weighing bunkers to the top hopper of the blast furnace. The downstream material flow from the top hopper to the furnace throat is beyond this scope, as they are addressed comprehensively in another research project executed in parallel to this research [11].

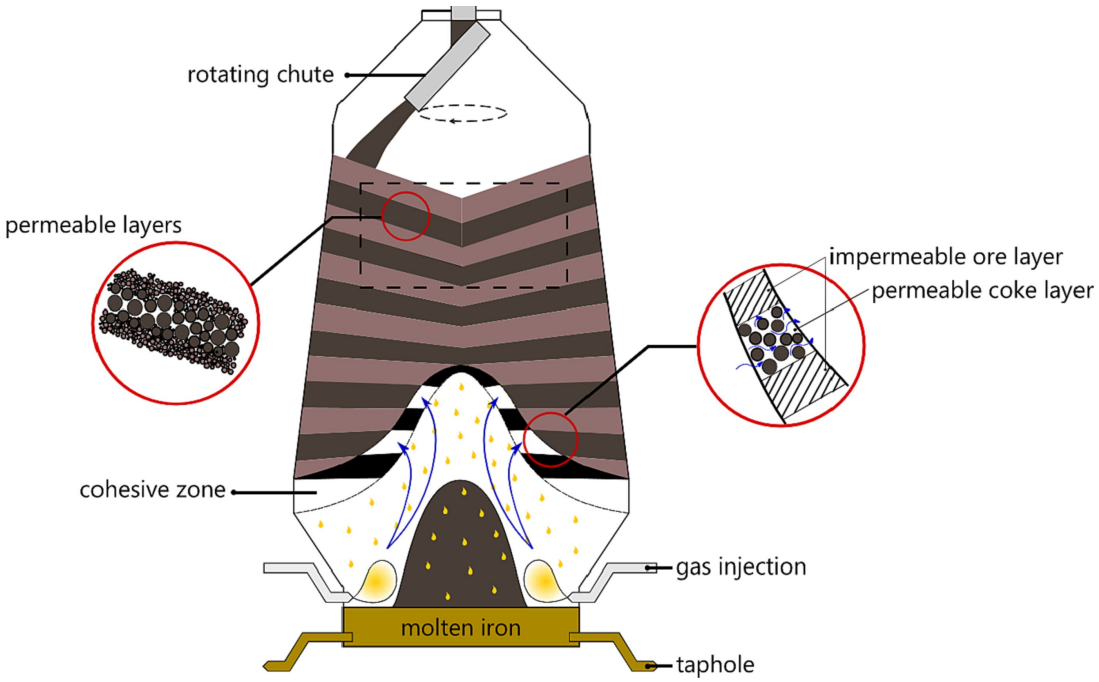

Figure 1.5 Schematic illustration of the blast furnace [12].

1.3 Problem statement

The extremely high temperatures within the blast furnace (ranging from approximately 2000 řC in the raceways to around 100 řC at the throat [6]) make physical inspections and real-time segregation measurements nearly impossible. Consequently, computational modelling has become an essential tool for investigating burden distribution and segregation behaviour within the furnace. Traditional continuum models, especially those based on kinetic theory, often fail to predict segregation accurately in dense granular flows [13]. A particularly powerful alternative is the Discrete Element Method (DEM), first introduced by Cundall and Strack [14], which resolves individual particle motions and contacts, thereby capturing the detailed segregation patterns that continuum models miss.

To accurately predict multi-component segregation within the blast furnace charging system, a reliable and computationally efficient DEM-based modelling approach is required. This approach should realistically represent the complexity of the multi-component mixture and include careful calibration, whereby model parameters are tuned to reproduce the observed bulk behaviour from real-world experiments. However, current DEM studies [9, 15–18], commonly rely on simplified mixture representations (such as single- or binary-sized mixtures), which do not adequately capture the complex interactions found in ferrous mixtures composed of multiple components. Moreover, most existing research neglects modelling the stockhouse, where burden materials are stored, handled, and prepared before charging. Given that segregation may already begin at (or even before) the stockhouse (see Figure 1.3), including it in the model is required to ensure accurate segregation predictions downstream, at the furnace throat.

Addressing these limitations requires advancing the DEM modelling of the blast furnace by considering the multi-component mixtures and extending the simulation scope to cover the whole charging process, from the stockhouse to the furnace throat (shown in Figure 1.3). Fur-

thermore, DEM is computationally expensive, and simulating millions of particles, even using high-performance GPU clusters, can take from hours to days. Considering the large industrial scale of BF and the large number of particles (in the order of 30-40 million) involved, improving computational efficiency is essential. A promising strategy to enhance computational efficiency is the use of machine learning (ML)based surrogate models [19], which approximate complex DEM simulations and thereby substantially reduce computational costs. Although this approach has demonstrated considerable potential, its application to DEM modelling of granular flows remains relatively limited. Further research is therefore required to integrate surrogate modelling more systematically within the DEM framework. Such integration would allow the DEM community to benefit from rapid developments in ML and AI, enabling more efficient optimisation and facilitating comprehensive parametric studies across a wide range of design and operational scenarios.

1.4 Research objectives and research questions

The primary aim of this thesis is to develop a systematic, accurate, and computationally efficient approach for modelling the segregation of multi-component granular mixtures throughout the entire blast furnace charging systemfrom the stockhouse (i.e., weighing bunkers) to the top hopper. This is achieved by establishing a robust DEM simulation framework that integrates surrogate modelling to effectively and efficiently reproduce realistic material behaviour and segregation patterns. The main question being addressed in this study is:

How can the segregation behaviour of multi-component granular mixtures in the blast furnace charging system be accurately and efficiently modelled using DEM, in order to identify strategies for segregation reduction?

This main question is answered through the following sub-questions:

1. What is the state-of-the-art in modelling and assessing segregation of single- and multi-component mixtures using DEM?
2. What are the dominant factors influencing multi-component segregation at different components of the blast furnace charging system?
3. How can one accurately predict segregation for various initial configurations of the mixture using adaptable ML-based surrogate models?
4. How can one efficiently and accurately calibrate, verify and validate a DEM model for multi-component segregation against experimentally obtained data using ML-based surrogate models?
5. What is the root cause of segregation, and what practical strategies can contribute to reducing segregation in the blast furnace charging process, based on insights from the DEM modelling?

By addressing these research questions, this study bridges fundamental insights and practical industrial needs, with the aim of improving operational efficiency in blast furnace steelmaking.

1.5 Methodology

This research employs a combination of computational modelling, experimental measurements, and surrogate modelling techniques to study and mitigate segregation in the blast furnace charging system. The main methods adopted in this research are as follows:

- Literature review: A comprehensive literature review was first conducted to examine the latest developments in DEM modelling of segregation of single- and multi-component mixtures. This review helped identify existing research gaps and provided insights into potential strategies for mitigating segregation in granular systems.
- Discrete Element Method (DEM) modelling: Accurate DEM models were developed and employed to simulate the granular segregation behaviour within the blast furnace charging system. DEM allowed detailed investigation of segregation patterns at various handling stages.
- Experimental investigation: Laboratory experiments were carried out using a controlled setup to characterise multi-component mixtures (i.e. ferrous materials) at both bulk scale (e.g., angle of repose) and local scale (e.g., segregation). These experimental data were mainly used to calibrate and validate the DEM model to ensure reliable and realistic DEM simulations.
- Sensitivity analysis: Sensitivity analyses, using the definitive screening design (DSD), were carried out to identify the critical DEM parameters influencing segregation and other bulk measurements. This step significantly reduced the complexity and computational cost of DEM calibration by highlighting the parameters essential for accurate modelling.
- Surrogate modelling and optimisation techniques: To address the high computational costs of DEM simulations, surrogate models were developed using ML techniques. Surrogate models efficiently predict segregation outcomes, enabling rapid analysis of various mixture configurations and facilitating extensive parametric studies. Moreover, they were used to accelerate the calibration process by substituting the full DEM simulation during the optimisation. To systematically calibrate the DEM simulations, genetic algorithms (GA) were integrated with these surrogate models. This integration ensures that the calibration process is both computationally efficient and accurate.
- Application to an industrial-scale case study: Finally, the calibrated DEM model was applied to an industrial-scale case study of the blast furnace charging system at Tata Steel IJmuiden. The simulations were used to quantify segregation under actual operating conditions, to investigate alternative scenarios through systematically designed case studies, and to assess the influence of key material and process parameters. The outcomes provide a detailed understanding of the mechanisms governing segregation in industrial practice and point towards practical strategies to enhance mixing efficiency and reduce segregation in the blast furnace charging process.

1.6 Thesis structure

The structure of this thesis is illustrated in Figure 1.6 and a brief description of each chapter is as follows:

- Chapter 2 presents a comprehensive literature review, examining the state-of-the-art in DEM modelling of segregation. It discusses existing DEM approaches and identifies critical limitations and knowledge gaps in modelling multi-component mixtures.
- Chapter 3 investigates the dominant factors influencing multi-component segregation at various stages of blast furnace charging. Through DEM simulations and sensitivity analysis, critical DEM parameters and the initial configuration of the mixture affecting segregation are explored.
- Chapter 4 introduces the machine learning-based surrogate model as an efficient tool for predicting segregation. The chapter describes the surrogate model development and validation processes and highlights the benefits of employing transfer learning for adapting an existing model to new mixture configurations.
- Chapter 5 describes the integration of surrogate models with optimisation techniques for efficient and accurate calibration of DEM simulations for multi-component mixtures. This chapter details the methodology, including sensitivity analysis and genetic algorithm-based optimisation.
- Chapter 6 presents an industrial case study conducted at Tata Steel IJmuiden. The calibrated DEM is applied to the real-scale blast furnace to assess segregation occuring at different parts of the charging system in the current industrial practice. Moreover, various practical adjustments are explored to improve burden distribution and reduce segregation.
- Chapter 7 concludes the research and provides recommendations for future work.

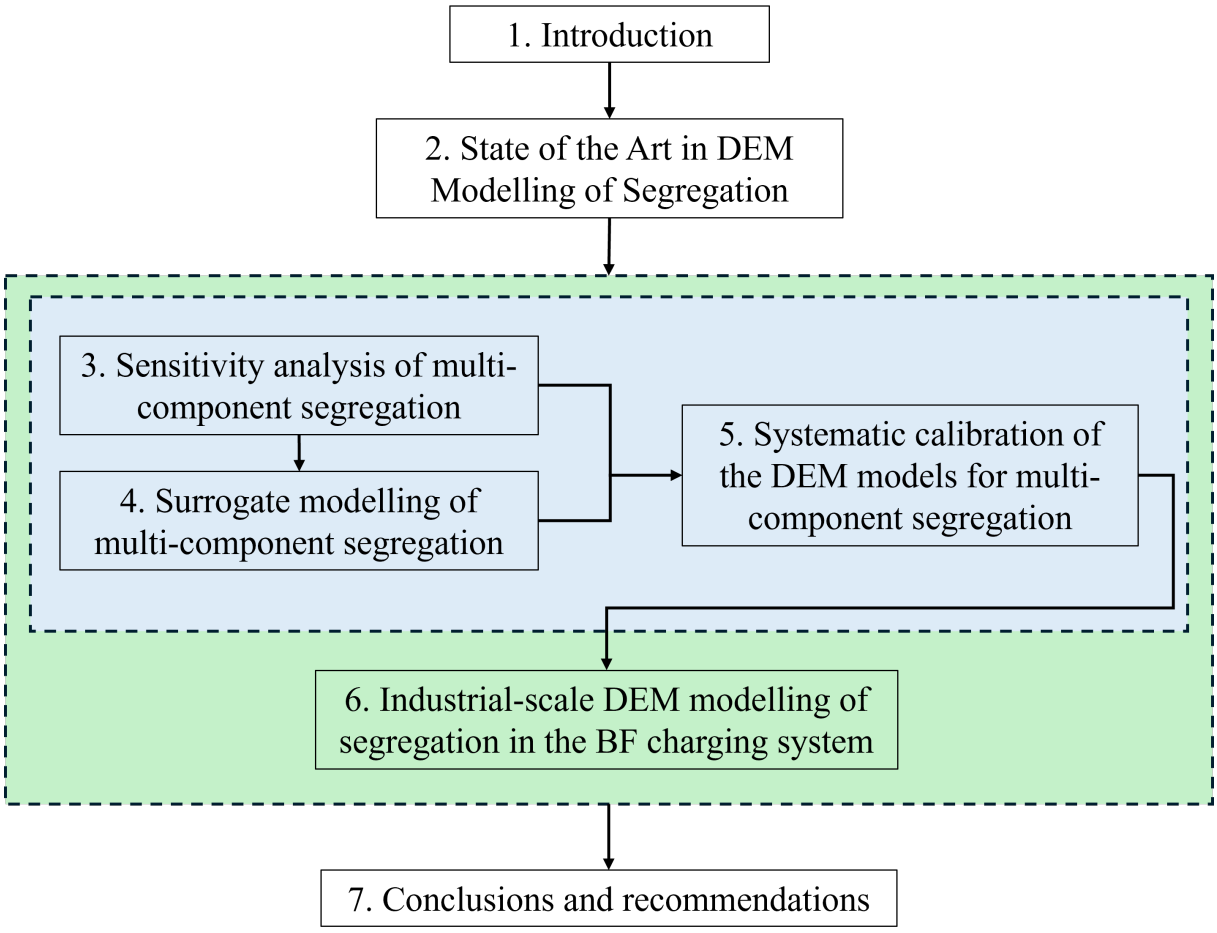

Figure 1.6 Visual outline of this thesis.

Chapter 2

State of the Art in DEM Modelling of Segregation*

As mentioned in Chapter 1, segregation (or de-mixing) is a significant challenge encountered during the handling and processing of granular materials, and DEM can offer valuable insights into this phenomenon. A key challenge in developing DEM models is balancing particle-level accuracy with computational efficiency. This is particularly relevant for industrial applications, where multi-component mixtures involving particles with various irregular shapes and wide size distributions are encountered in large quantities.

In this chapter, the state of the art in DEM modelling of segregation in industrial applications involving the gravity-driven flow of dry, cohesionless granular materials is reviewed. Following a brief introduction, a novel scientific notation is introduced to distinguish between different types of mixtures. Then, the methods used in the current literature to determine parameters for mixture models are reviewed, along with how material, geometric, and operational parameters affect segregation based on these models. Finally, existing segregation indices and their applicability to multi-component segregation are examined.

2.1 Introduction

Except for a few specific applications in mining and agricultural engineering [20], segregation is generally considered an undesirable occurrence negatively affecting product homogeneity. Therefore, the underlying mechanisms driving segregation, as well as how these mechanisms are influenced by material and system parameters, need to be fully explored.

According to de Silva et al. [21], there are thirteen segregation mechanisms in general. However, some of these mechanisms are either rare or special cases of others. As mentioned in Section 1.1, the four main segregation mechanisms are percolation, trajectory, Brazil-nut effect, and buoyancy segregation [2, 4, 5]. Often, multiple mechanisms might take place simultane-

*This chapter is based on: A. Hadi, R. Roeplal, Y. Pang, D.L. Schott, *DEM Modelling of Segregation in Granular Materials: A Review*, *KONA Powder and Particle Journal* (2023). https://doi.org/10.14356/kona.2024017

ously, making the prediction of the segregation pattern extremely challenging. Furthermore, since segregation only occurs for particles that are in motiondue to either shearing, by means of moving walls (such as in a shear cell or bladed mixer) or as a result of gravitational force (as is the case in hoppers) or vibrationit can be deduced that the formation of segregation patterns depends not only on the properties of the components relative to each other, but also on the system configuration and the degree and type of agitation imposed on the material. Although having knowledge of the mentioned mechanisms can shed light on the segregation behaviour of particulate mixtures, it is necessary to investigate each case independently to determine the dominant segregation mechanism(s).

Researchers have attempted to experimentally observe segregation phenomena in common applications since the early 1970s in order to first understand why and how granular mixture components tend to separate spatially during different types of agitation [22] and subsequently developed models capable of capturing the observed phenomena. Given the complexity of the segregation problem, the general approach was to scrutinize the effects of different material properties separately by considering material mixtures differing only in either size [23] or density [24] and, ultimately, the combined effect of size and density [25]. This allowed researchers to systematically observe and incorporate the effect of each material property in mathematical models. However, there are several limitations associated with the experimental investigation of segregation. First, despite the recent advances in measurement techniques [26, 27], extracting data on the composition of a granular mixture is still not a trivial task. Second, it is nearly impossible to obtain all the information on a particle scale which can shed light on the macro-scale granular behaviour. Finally, it is expensive and time-consuming to systematically study the effect of various factors on segregation in experiments.

As computational models gained popularity, DEM, initially introduced by Cundall and Strack [14], became a widely used tool for simulating granular phenomena. The main advantage of DEM is that any mixture of materialswhether they have different sizes, densities, shapes, or combinations thereofcan be modelled to provide detailed, particle-level insight on segregation patterns, which is both difficult and expensive to achieve experimentally and is not yet possible with mathematical models for segregation. This is highly relevant since most materials encountered in industry are of this complex nature. Hence, DEM has expedited researchers ability to predict segregation in multi-component mixtures, irrespective of the application, and can therefore be considered a practical tool for modelling and optimising industrial processes. However, until now, it is unclear to what extent the existing DEM models of segregation are representative of the complex multi-component mixtures often encountered in real-world applications. Moreover, a DEM model can accurately represent granular material behaviour only if its parameters are reliably chosen, i.e., the model is calibrated and validated.

The objective of this chapter is to provide an overview of the state of the art in modelling the segregation behaviour of complex multi-component mixtures using DEM. Specifically, this review assesses to what extent the existing DEM studies of segregation in cohesionless materials represent actual mixtures encountered in industry. Furthermore, the reliability of these existing studies in terms of their approach to calibration and validation is evaluated. This literature review focuses on DEM-based studies of gravity-driven segregation in dry, cohesionless granular materials, which closely reflect those found in blast furnace charging systems. Studies on fluidised segregation are excluded since investigating such a phenomenon is conducted using the coupled CFD-DEM approach, which does not fit in this review. Also, applications such as

rotating drums and various types of mixers in which gravity is not the only source of energy causing segregation are beyond the scope of this review.

2.2 Terminology

For consistency and to make a clear distinction between various terminologies used in this chapter regarding mixtures, Figure 2.1 is presented. In this figure, a component is defined as a material with constant particle density. In case a mixture is composed of more than one component, it is generically referred to as a multi-component or more specifically, as two-component, three-component, etc. by mentioning the exact number of components. Moreover, the particles constituting each component can be mono- to poly-sized and/or mono- to multi-shaped. In this regard, referring to complex mixtures composed of several components is not yet straightforward. To overcome this issue, Eq. 2.1 is presented as a novel way to define multi-component mixtures

$$nC\left[\sum_{k=1}^{n}(i_kS/j_kSh)\right] \tag{2.1}$$

where n is the number of components and the composition of each component is specified in the corresponding parenthesis. That is, i_k is the number of sizes in kth component, which could be 1, 2, 3, M or P, representing a mono-, binary-, ternary-, multi- or poly-sized component. Similarly, representing the shape, j_k might take the value of 1, 2, 3 or M, denoting a mono-, binary-, ternary- or multi-shaped component. For instance, $2C[(2S/1Sh+(MS/1Sh)]$ represents a two-component ($2C$) mixture composed of a binary- sized ($2S$) mono-shaped ($1Sh$) component mixed with a multi-sized (MS) mono-shaped ($1Sh$) one. This formula will be consistently used in this review to refer to different types of mixtures in a concise way.

2.3 Discrete element method for segregation

2.3.1 Overview of DEM

A DEM model calculates the forces and moments of inertia acting on all particles and subsequently uses Newtons second law to compute their positions at each time step through numerical integration. The interaction forces between particles and their surroundings are determined using contact models such as the Linear spring-dashpot [28] and Hertz-Mindlin model [29], which are the most widely used for cohesionless granular materials. The model inputs can generally be divided into three categories: (i) morphological parameters such as particle size and shape distributions; (ii) material parameters such as particle density (ρ), shear modulus (G) and Poisson ratio (ν); and (iii) interaction parameters such as sliding and rolling friction coefficients (μ_s and μ_r, respectively) and the restitution coefficient (C_r).

The first step in developing a DEM model is generally measuring morphological parameters, and determining how they will be included in the model. In industrial applications, millions of particles with many irregular shapes and wide size distributions are typically handled. From a

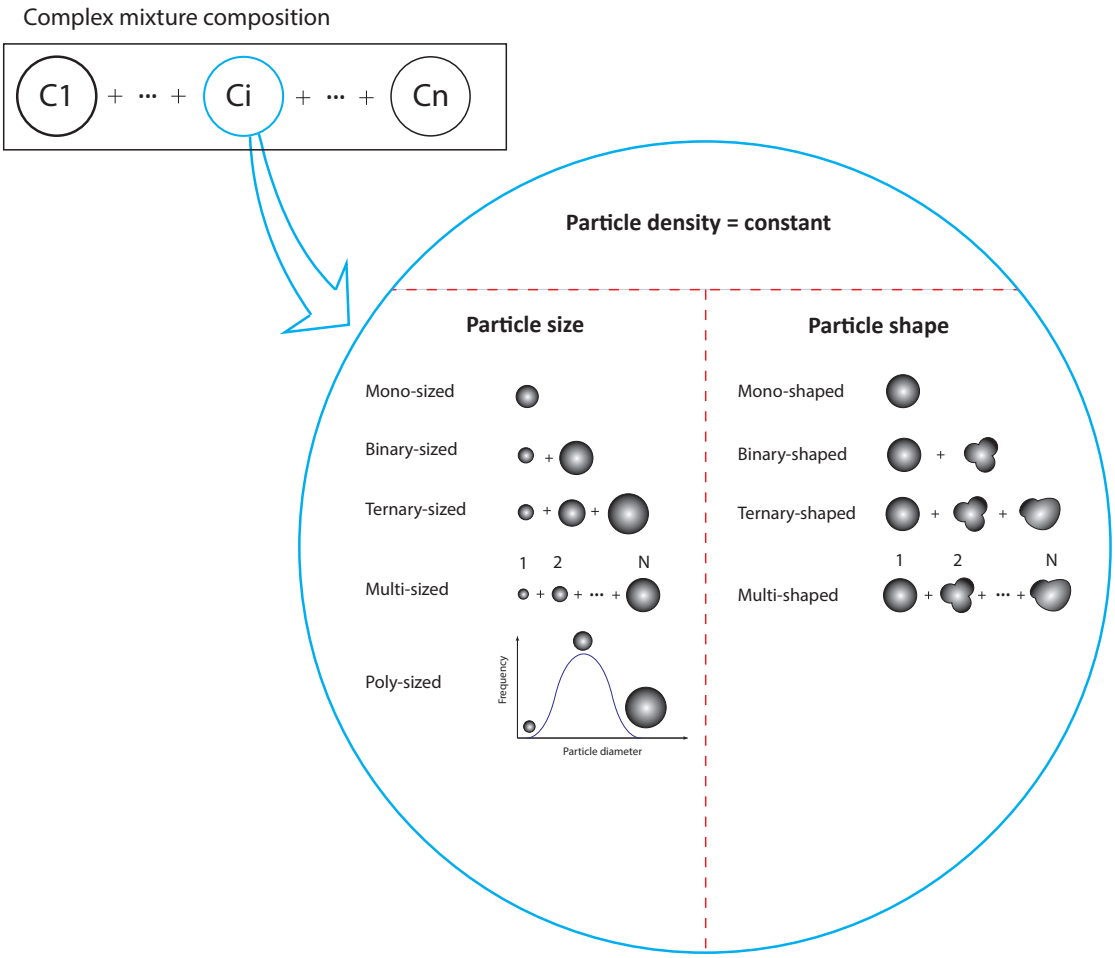

Figure 2.1 Terminology to describe various types of mixtures.

computational standpoint, modelling the true size and shape distributions for such applications can be very challenging for several reasons [30–32]. First of all, tracking a large number of particles and their mutual interactions demands huge amounts of computational power, even for simulating a few seconds of a simple process. Secondly, modelling the actual size distribution can prolong simulation times significantly since the numerical time step is determined by the smallest particle in the flow. Finally, realistic (non-spherical) particle shapes can be modelled using multi-spheres or superquadrics, which require computationally expensive algorithms [33]. Several solutions have been proposed to reduce computational effort such as downscaling the full three-dimensional system to a 2D representation or simulating a portion using periodic boundaries [34, 35] using larger, so-called "coarse-grained" or "upscaled" particles [31, 36, 37], ignoring small sizes of the full particle size distribution (PSDalso referred to as "scalping" or "cut-off" [38]and reducing the shear modulus (G), although the latter should be carried out with caution as it might cause serious errors [39]. Besides all these techniques, DEM code development in conjunction with parallel computing techniques using high-performance clusters (HPC) look promising to overcome the high computational time in due course [30].

The next step is determining the remaining model parameters such that the simulated flow behaviour matches the real behaviour to an acceptable degree [30]. When it comes to modelling

segregation, the parameters should be determined in a way that not only the global behaviour (e.g., angle of repose, mass flow rate, etc.) but also the local behaviour, i.e., spatial concentration of components, are captured. The reliability of DEM predictions depends on the proper selection of a contact model for a specific application and the values assigned to the model parameters, given the simplifications which have been made for computational reasons. Model validation is therefore an important final step for both verifying and demonstrating the models credibility.

A total of 63 papers on the segregation of the gravity-driven flow of cohesionless granular materials were encountered in the literature. These studies are mostly focused on segregation during hopper filling and discharge, chute flow and heap formation and are summarised in Table 2.1. These studies have been categorised into four groups based on their approach to obtaining DEM parameters. In the remainder of this section, the studies from Table 2.1 will be reviewed with respect to the methods used to quantify segregation (Section 2.3.2) and model development practices (Sections 2.3.3 and 2.3.4).

Table 2.1 Overview of DEM studies for segregation (LSD = Linear spring dashpot, HM = Hertz-Mindlin, n.s. = not specified, N/A = not applicable, *for the definition and notation of the mixture type see Eq. 2.1 in Section 2.2).

Group	Source	Software	Contact model	Mixture type*	Material (in experiments)	Particle shape
I. Parametric sensitivity studies	Tripathi and Khakhar [40, 41]	n.s.	LSD	$1C[(2S/1Sh)]$ $2C[(1S/1Sh)+(1S/1Sh)]$		Sphere
	Ketterhagen et al. [42]	n.s.	LSD	$1C[(2S/1Sh)]$ $2C[(1S/1Sh)+(1S/1Sh)]$		Sphere
	Pereira and Cleary [43]	n.s.	LSD	$2C[(1S/1Sh)+(1S/1Sh)]$	N/A	Sphere
	Panda and Tan [44]	LIGGGHTS	HM	$1C[(2S/1Sh)]$		Sphere
	Huang et al. [45]	n.s.	n.s.	$1C[(2S/1Sh)]$		Sphere
	Yu and Saxén [15]	EDEM	HM	$1C[(3S/1Sh)]$		Sphere
	Xu et al. [46]	n.s.	HM	$3C[(MS/1Sh)+(MS/1Sh)+(MS/1Sh)]$		Sphere
	Li et al. [18]	n.s.	HM	$2C[(2S/1Sh)+(2S/1Sh)]$	N/A	Sphere
	Vuilloz et al. [47]	LMGC90	n.s.	$1C[(2S/1Sh)]$		Sphere
	Zhao et al. [48]	PFC3D	LSD	$1C[(3S/1Sh)]$		Sphere
II. Parameter assumption	Tao et al. [49]	n.s.	n.s.	$1C[(2S/2Sh)]$	Soybean	Ellipsoidal, corn-shaped, cylinder, spherical
	Shirsath et al. [50]	n.s.	LSD	$2C[(1S/1Sh)+(1S/1Sh)]$	Glass beads	Sphere
	Xu et al. [51]	n.s.	n.s.	$1C[(2S/1Sh)]$	Alumina spheres	Sphere
	Zhang et al. [52]	n.s.	HM	$1C[(2S/1Sh)]$	Plastic pellets, rape seeds	Sphere
	Mantravadi and Tan [53]	LIGGGHTS	HM	$1C[(2S/1Sh)]$	Glass beads	Sphere
	Mio et al. [16]	n.s.	Voigt	$1C[(MS/1Sh)]$	Sintered ore, coke	Sphere
	Zhang et al. [54]	n.s.	HM	$1C[(MS/1Sh)]$	Coke, iron ore	Sphere
	Zhao et al. [55]	LIGGGHTS	HM	$1C[(PS/1Sh)]$	Glass beads	Sphere
	Zhao and Chew [56]	LIGGGHTS	HM	$1C[(PS/1Sh)]$	Glass particles	Sphere, ellipsoid, cylinder, cuboid
	Kumar et al. [57]	LIGGGHTS	HM	$1C[(PS/1Sh)]$	Glass beads	Sphere
	Ketterhagen et al. [58]	n.s.	LSD	$1C[(2S/1Sh)]$ $2C[(1S/1Sh)+(1S/1Sh)]$	Glass beads, cast steel shot	Sphere
	Ketterhagen and Hancock [59]	n.s.	LSD	$1C[(2S/1Sh)]$	Glass beads	Sphere

Table 2.1 – continued from previous page

Group	Source	Software	Contact model	Mixture type*	Material (in experiments)	Particle shape
III. Parameters from literature	Kou et al. [60, 61]	n.s.	HM	$4C[(1S/1Sh)+(1S/1Sh)+(1S/1Sh)+(1S/1Sh)]$	Pellet, ore, coke, flux	Sphere
	Cliff et al. [62]	MFiX	LSD	$1C[(2S/1Sh)]$	Mustard seed	Sphere
	Yu and Saxén [63]	EDEM	HM	$1C[(2S/1Sh)]$	Pellet	Sphere
	Liao et al. [64]	n.s.	n.s.	$2C[(1S/1Sh)+(1S/1Sh)]$	Lump ore, pellet	Sphere, clumped spheres
	Asachi et al. [65]	EDEM	HM	$3C[(1S/1Sh)+(1S/1Sh)+(1S/1Sh)]$	TAED, BP, EPG (detergent)	Sphere, clumped spheres
	Tian et al. [66]	n.s.	HM	$1C[(3S/1Sh)]$	Coke	Sphere, clumped spheres
	Yu et al. [67]	EDEM	HM	$1C[(2S/1Sh)]$	Pellet	Sphere
	Xu et al. [68]	n.s.	HM	$1C[(2S/1Sh)]$	Mung bean	Sphere
	Mandal and Khakhar [69]	n.s.	LSD	$1C[(2S/1Sh)]$	N/A	Spheres, dumbbells
	Zhao and Chew [70]	LIGGGHTS	HM	$1C[(1S/2Sh)]$	N/A	Ellipsoids, cylinders, cuboids
	Zhang et al. [71]	n.s.	HM	$1C[(2S/1Sh)]$	Coke	Sphere
	Yu and Saxén [9]	EDEM	HM	$1C[(3S/1Sh)]$	Pellets	Sphere
	Yu and Saxén [72]	EDEM	HM	$1C[(3S/1Sh)]$	Pellets, coke, steel ball	Sphere, clumped spheres
	Kou et al. [73]	n.s.	Voigt	$1C[(3S/1Sh)]$	Coke	Sphere
	Wu et al. [74]	n.s.	HM	$1C[(3S/1Sh)]$	Sinter	Sphere
	You et al. [75]	n.s.	HM	$1C[(3S/1Sh)]$	Coal	Sphere
	Xu et al. [76]	n.s.	n.s.	$1C[(MS/1Sh)]$	Coke	Sphere
	Kou et al. [77]	n.s.	HM	$3C[(1S/1Sh)+(1S/1Sh)+(1S/1Sh)]$	Sinter, pellet, lump ore	Sphere
	Chibwe et al. [78]	LIGGGHTS	HM	$2C[(MS/1Sh)+(1S/1Sh)]$	Sinter, pellet	Sphere
	Hong et al. [79]	n.s.	HM	$3C[(1S/1Sh)+(1S/1Sh)+(1S/1Sh)]$	Sinter, pellet, ore	Sphere
IV. Parameter calibration/measurement	Z. Zhang et al. [80]	EDEM	HM	$1C[(2S/1Sh)]$	Acrylic spheres	Sphere
	Izard et al. [81]	EDEM	HM	$1C[(2S/1Sh)]$	Sinter	Clumped spheres
	Alizadeh et al. [82]	EDEM	HM	$2C[(1S/1Sh)+(1S/1Sh)]$	TAED, BP (detergent)	Clumped spheres
	Kim et al. [83]	EDEM	HM	$2C[(3S/1Sh)+(3S/1Sh)]$	Sinter, Briquette	Sphere, clumped sphere
	Qiu and Pabst [84]	PFC3D	LSD	$1C[(MS/1Sh)]$	Waste rock	Sphere
	Wang et al. [85]	LIGGGHTS	HM	$2C[(1S/1Sh)+(1S/1Sh)]$	Steel and aluminium spheres	Sphere
	Barik et al. [86]	LIGGGHTS	HM	$1C[(3S/1Sh)]$	Microcrystalline cellulose	Sphere
	Mio et al. [87–90]	n.s.	Voigt	$1C[(3S/1Sh)]$	Sintered ore	Sphere
	Nakano et al. [91]	n.s.	Voigt	$1C[(3S/1Sh)]$	Sinter	Sphere
	Bhattacharya and McCarthy [10]	n.s.	HM	$1C[(3S/1Sh)]$	Polystyrene spheres	Sphere
	Li et al. [92]	n.s.	HM	$1C[(MS/1Sh)]$	Iron ore	Sphere
	Li et al. [93]	LIGGGHTS	HM	$1C[(MS/1Sh)]$	Iron ore	Sphere
	Shimosaka et al. [94]	n.s.	LSD	$1C[(MS/1Sh)]$	Glass bead, Sand, alumina	Sphere
	Combarros et al. [95]	LIGGGHTS	HM	$1C[(2S/1Sh)]$ $2C[(1S/1Sh)+(1S/1Sh)]$	Aluminium oxide	Sphere, Cylinders
	Combarros et al. [96]	LIGGGHTS	HM	$1C[(2S/1Sh)]$	Sand	Sphere
	Terui et al. [97]	n.s.	Voigt	$2C[(1S/1Sh)+(1S/1Sh)]$	Coke, sinter	Sphere

2.3.2 Methods for assessing segregation

Since DEM allows tracking the position of each individual particle, it becomes relatively simple to assess the degree of segregation within a system. This can be done in different ways. One approach is to divide the system into subdomains and subsequently determine how different mixture components are distributed in the subdomains by means of plots. Gradient plots are useful for visualising the distribution of a single mixture component in a system. For example, a gradient plot as in Figure 2.2 has been used to visualise how small particles within a binary mixture were distributed after filling a hopper [51]. Since they were dealing with a binary mixture, showing the distribution of one component was sufficient to demonstrate how well the material was mixed in the hopper. When dealing with multi-component mixtures, however, monitoring only one component is no longer sufficient, and alternative visualisation approaches are required. In such cases, line plots representing the radial distribution of multiple particle size classes have been used to analyse burden distribution in blast furnaces [54]. The plot method is beneficial as it provides two important insights: (1) whether or not different mixture components are evenly distributed, and (2) where the different components are concentrated in the case of uneven distribution.

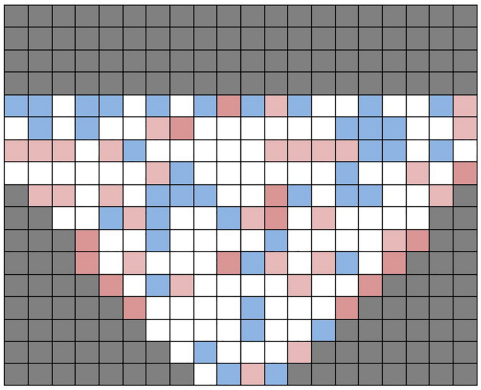

Figure 2.2 Gradient plot for demonstrating how a single component is spatially distributed inside a system, where white colour represents a well-mixed status and red and blue colours denote segregated areas. Reproduced with permission from Ref. [51]. Copyright 2017, Elsevier.

Another method is to use an index which reflects the degree of segregation based on its value. There are generally two types of segregation indices: grid-dependent and grid-independent [98]. In the first type, the system is divided into subdomains, similar to the method of plots. The distribution of one mixture component (referred to as the tracer) is evaluated, and the segregation index is then determined through statistical analysis of the tracer distribution. If the tracer is distributed evenly, then the material is considered to be well-mixed, and this is reflected by the value of the segregation index. In the second type, the value of the segregation index is determined by considering how the tracer particle is distributed within the system as a whole, rather than in subdomains. The tracers distribution is generally evaluated on a distance or contact basis, as described by Bhalode and Ierapetritou [98]. The index value reflects how spread out the tracer particles are in the whole system.

The benefit of using an index is that it allows for a quantitative comparison of segregation for different scenarios by means of a single value. This might be more difficult to do with the method of plots, which provides a more qualitative comparison. However, it is generally

known that grid-dependent indices depend on the chosen size of the subdomains [99–101], which makes it difficult to judge the degree of segregation based on the index value. For this reason, researchers often investigate how sensitive their segregation predictions are to the grid size. While the grid-independent indices do not have this shortcoming, they are often computationally intensive, especially for industrial applications where millions of particles are involved.

The majority of literature from Table 2.1 used the plot method to quantify segregation, with only a few using segregation indices. These indices are presented in Table 2.2 and are grouped by the calculation method (grid dependent/ independent). The equations for calculating the indices are given along with the range of values that can be assigned to each index. Additionally, the type of segregation index based on the classification according to Bhalode and Ierapetritou [98] is indicated. It is important to note that, similar to the method of plots, the single-tracer approach is only useful when considering a binary mixture. Therefore, it has also been indicated whether the segregation indices are based on the distribution of a single tracer. The common symbols used in the index no. 18 from Table 2.2 are defined in Table A.1 in Appendix A, and for index no. 910, the reader is referred to the respective references.

It is concluded that all grid-dependent indices in Table 2.2 are based on a statistical analysis of a single tracer, which is not surprising given that they were applied in studies of binary mixtures. In studies of three or more particle types, the plot method was used to visualize the degree of segregation [98]. For indices that can be applied to multi-component segregation, the reader is referred to the work of Cho et al. [99], who studied segregation in a mixer.

2.3.3 Determination of DEM parameters for segregation

The literature mentioned in Table 2.1 has been categorised based on the way in which the authors dealt with model parameters. The following four categories were identified:

I. **Parametric sensitivity studies.** This group of studies carried out parametric sensitivity studies to identify the critical factors (i.e., model, material, geometric and operational parameters) affecting the segregation behaviour of mixtures in different systems. Hence, parameter values in these studies are systematically varied. Since they are not aimed at modelling a specific material, calibration and validation are not performed in these studies.

II. **Parameter assumption.** The second group contains studies in which the authors assumed parameters without any justification or referring to related resources (for instance chosen by experience). Although these studies attempted to justify the parameter values by comparing the DEM results with physical tests, this is insufficient because more than one parameter set can yield the same bulk behaviour [102]. Furthermore, major errors were reported in some cases [49], which could be the consequence of not calibrating the parameters.

III. **Parameters from literature.** Many DEM studies on segregation have taken either all or merely a selection of the parameters from the literature [9, 58–79, 103]. This approach has the same limitation as the previous group, as the parameters are derived from sources where no calibration was performed. Furthermore, it is unclear if the material under study is similar or exactly the same as in the literature [71].

Table 2.2 Common segregation indices used in DEM studies of Table 2.1. Legend: refer to Table A.1 in Appendix A for symbol definitions. Subscripts: "t" refers to "tracer" when a single tracer is used; t_i refers to the i-th tracer when multiple tracers are used(*).

No.	Source	Segregation index	Values (mixed–segregated)	Classification
1	Panda and Tan [44]	$SI = \sqrt{\frac{\sum_{j=1}^{m}\left(c_t^j - c_t\right)^2}{m}}$	0-(**)	Variance-based / single tracer
2	Li et al. [18]	$SI = \frac{\sum_{j=1}^{m}\left[\frac{N^j}{N}\left(y_t^j - y_t\right)^2\right]}{y_t(1-y_t)}$	0–1	Variance-based / single tracer
3	Mantravadi and Tan [53]	$SI = \sqrt{\frac{\sum_{j=1}^{m}\left[\frac{x_L^j}{x_t} - \left(\frac{x_L^j}{x_t}\right)_{\text{avg.}}\right]^2}{m-1}}$	0-(**)	Variance-based / single tracer
4	Mantravadi and Tan [53]	$SI = \frac{\sigma_0^2 - \sigma^2}{\sigma_0^2 - \sigma_r^2}$	0-(***)	Variance-based / single tracer
5	Zhang et al. [54], Ketterhagen and Hancock [59]	$SI = \sqrt{\frac{\sum_{j=1}^{m}\left[\frac{x_L^j}{x_t} - \left(\frac{x_L^j}{x_t}\right)_{\text{avg.}}\right]^2}{m}}$	0-(**)	Variance-based / single tracer
6	Zhao et al. [55]	$SI = \frac{\frac{\sum_{j=1}^{m}\left[x_{t_1}^j \cdot h_j\right]}{\sum_{j=1}^{m}\left[x_{t_2}^j \cdot h_j\right]} - 1}{\frac{2x_{t_2}+x_{t_1}}{x_{t_1}} - 1}$	0–1	Distance-based / two tracers
7	Combarros et al.[95]	$SI = \sqrt{\frac{\log\sigma_0^2 - \log\sigma^2}{\log\sigma_0^2 - \log\sigma_r^2}}$	1–0	Variance-based / single tracer
8	Zhang et al. [52]	$SI = \frac{\sigma_0^2 - \sigma^2}{\sigma_0^2 - \sigma_r^2}$ *	1–0	Contact-based
9	Mandal and Khakhar [69]	$SI = \frac{COM_{\text{final}} - COM_{\text{initial}}}{\delta}$	0–0.5	Variance-based / single tracer
10	Chibwe et al. [78]	$SI = \frac{\bar{l} - l_{\min}}{l_{\text{ud}} - l_{\min}}$	1–0	Variance-based / single tracer

(*) The readers are referred to Table A.1 in Appendix A for detailed equations on calculating component concentrations of indices 18.

(**) For these indices, the maximum value of SI depends on the mixture composition, as the equations contain the variables c_t, y_t and x_t which represent the concentration of the tracer in the entire mixture.

(***) In these equations, σ^2, σ_0^2 and σ_r^2 are calculated by

$$\sigma^2 = \sum_{i=1}^{n}\frac{(y_t^i - y_t)^2}{n-1}, \quad \sigma_0^2 = y_t(1-y_t), \quad \sigma_r^2 = \frac{y_t(1-y_t)}{N^i}$$

IV. **Parameter calibration/measurement.** Several past studies have established DEM parameters through either direct measurements or bulk calibration [10, 80–91, 93–97]. Each of these approaches comes with a set of advantages and disadvantages as summarised in Table 2.3. The calibration approaches of the studies in this group are summarised in Table 2.4. All calibration tests presented in this table capture only the global behaviour of granular materials (e.g., angle of repose), and none of them have calibrated the DEM model for local behaviour using a segregation test.

Table 2.3 Pros and cons of two main approaches to determining DEM parameters [30, 104, 105].

	Advantage	**Disadvantage**
Direct measurement	+ Independent of the contact model + Independent of the DEM code + Maintaining physical meaning	– Mostly limited to mm-sized particles – Not practical for irregular particles – Not practical for all parameters – Not considering the stochastic nature of the parameters
Bulk Calibration	+ Compensating for the inaccuracy of the parameters + Obtaining values for all parameters	– Probability of losing physical meaning on particle level – DEM code dependency – Probability of not resulting in a unique parameter set – Challenging in the case of a high number of parameters

Table 2.4 Detailed calibration approach of studies in group IV of Table 2.1.

Source	**Direct measurement**	**Bulk calibration test**
Z. Zhang et al. [80]	$\mu_{s,pp}, \mu_{s,pg}, C_r$	—
Izzard et al. [81]	$\mu_{s,pg}, \rho_s$	$\mu_{s,pp}$ (angle of repose)
Alizadeh et al. [82]	C_r, $\mu_{s,pp}$, particle shape	Number of spheres in clumped approach, μ_r (angle of repose), $\mu_{s,pp}$ (sliding process)
Kim et al. [83]	PSD, ρ_s, C_r, μ_s, E	μ_r (angle of repose)
Qiu and Pabst [84]	PSD	μ_t, μ_t (angle of repose, both at lab and field scales)
Wang et al. [85]	ρ_s, C_r	—
Barik et al. [86]	—	μ_s (silo discharging)
Mio et al. [87–90]	PSD, ρ_s	μ_s (shear test), μ_r (particle rolling test)
Nakano et al. [91]	—	μ_r (angle of movement)
Bhattacharya and McCarthy [10]	PSD, ρ_s	Tuning the contact model
Li et al. [92]	PSD, ρ_s, G	μ_s, μ_r (angle of repose)
Li et al. [93]	PSD, ρ_s, G, μ_s, μ_r	—
Shimosaka et al. [94]	—	μ_r (inclined plate test)
Combarros et al. [95]	PSD, ρ_s	μ_s, μ_r (sensitivity analysis + dynamic and static angle of repose)
Combarros Garcia et al. [96]	ρ_s, D_{50}	μ_s, C_r(sensitivity analysis + shear test, angle of repose and drop fall test)
Terui et al. [97]	—	μ_s (stationary bed angle), μ_r (angle of repose)

Calibration of DEM models against experimental data ensures that the model captures the material behaviour and therefore provides credibility [104]. However, calibration can be very time-consuming. This is especially true for multi-component mixtures since the number of model parameters increases with the number of components in the mixture. Sensitivity studies enable us to explore the importance of the model parameters for inclusion in the calibration step. Table 2.5 presents a summary of the results of the existing DEM sensitivity studies on segregation. As can be seen, the significance of DEM parameters depends on the system and

Table 2.5 A summary of the results of DEM sensitivity studies on the significance of model parameters for segregation.

DEM parameter	Range (source)	System	Significance
Particle-particle sliding friction ($\mu_{s,pp}$)	(0.0–0.5) (Ketterhagen et al. [42])	Hopper discharge	High
	(0.01–0.9) (Yu and Saxén [9])		Low
	(0.15–0.95) (Z. Zhang et al. [80])		High
	(0.1–1.0) (Zhang et al. [52])	Hopper filling	High
	(0.3–0.9) (Li et al. [18])	Blast furnace throat	Low
Particle-geometry sliding friction ($\mu_{s,pg}$)	(0.0–0.5) (Ketterhagen et al. [42])	Hopper discharge	High
	(0.01–0.9) (Yu and Saxén [9])		High
	(0.05–0.85) (Z. Zhang et al. [80])		High
Particle-particle rolling friction ($\mu_{r,pp}$)	(0.0–0.045d) (Ketterhagen et al. [42])	Hopper discharge	Low
	(0.05–0.9) (Yu and Saxén [9])		Low
	(0.001d–0.2d) (Zhang et al. [52])	Hopper filling	High
Particle-geometry rolling friction ($\mu_{r,pg}$)	(0.0–0.045d) (Ketterhagen et al. [42])	Hopper discharge	Low
	(0.01–0.9) (Yu and Saxén [9])		High
Particle-particle coefficient of restitution ($C_{r,pp}$)	(0.2–0.94) (Ketterhagen et al. [42])	Hopper filling	High
Particle-geometry coefficient of restitution ($C_{r,pg}$)	(0.2–0.9) (Ketterhagen et al. [42])		High
Local damp	(0.2–0.8) (Qiu and Pabst [84])	Pile formation	Low

the granular flow regime being studied.

Figure 2.3 visually presents deeper insight into studies listed in Table 2.1 to highlight the percentage of studies with respect to the approach for determining DEM parameters, reproducibility, and the types of mixture being studied.

According to Table 2.1, not all past DEM studies have determined the parameters in a proper way. To highlight this with respect to segregation, Figure 2.3(a) shows the percentage of studies in groups II to IV, where only studies in group IV include calibration. It should be noted that group I is excluded since calibration is not necessary for parametric sensitivity analysis. As can be seen, 66% of the existing studies have omitted the calibration of the DEM model. This is relevant since calibrated DEM models are required in case it is intended to be used as a predictive tool that yields reliable results [104]. Even though the studies in group IV have applied calibration to some extent, not all of them have carried it out in a systematic way (cf. Table 2.4). In several studies, only a portion of the parameters has been calibrated [91, 94]. Also, in several cases, a single experiment is used to determine the values of more than one parameter [81, 92]. As shown by Wensrich and Katterfeld [106], this approach leads to ambiguity since an infinitive combination of parameter values might lead to the same bulk behaviour.

There are good examples of systematic calibration of DEM models with respect to bulk material behaviour for various operational conditions in the literature [30, 102, 107–110]. When it comes to the calibration of models for segregation, several authors have shown that bulk calibration also ensures that the local material behaviour is accurately captured. For example, Li

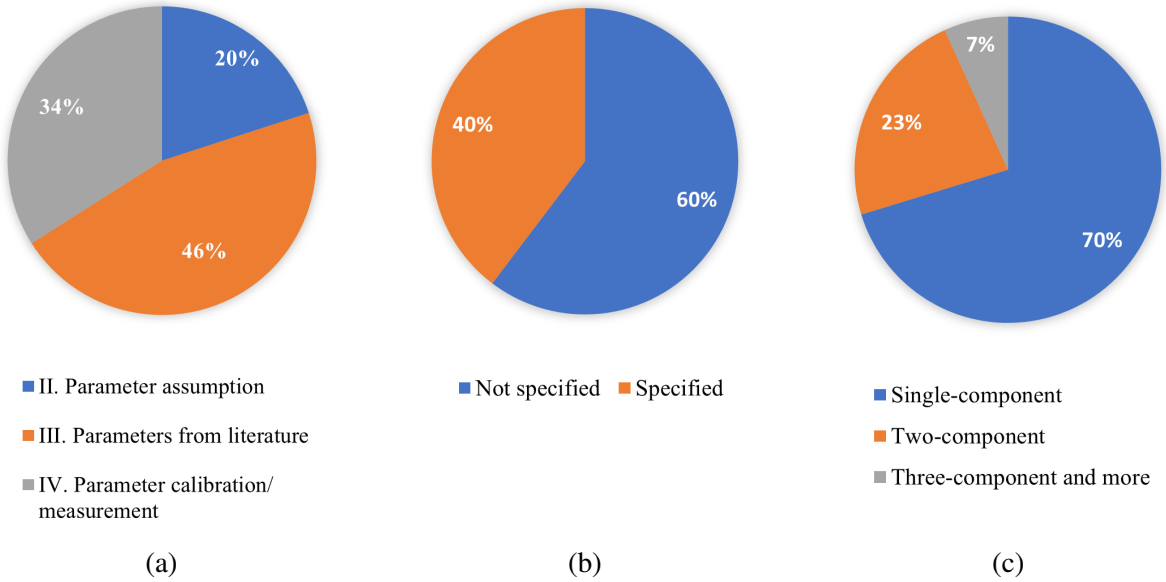

Figure 2.3 Distribution of past DEM-based studies of segregation by (a) approach of calibration, (b) DEM software, and (c) types of mixtures.

et al. [92] calibrated the friction coefficients of iron ore pellets using a repose angle test and verified that the calibrated model could reproduce the experimentally observed size segregation in simulations. Similarly, Izard et al. [81] modelled the size segregation of sinter particles after determining the model parameters through bulk calibration. However, it is not yet addressed to what extent the DEM parameters obtained through bulk calibration (e.g. dynamic and static angle of repose) can be employed to accurately replicate the segregation of the granular materials, which is essentially a local occurrence. Furthermore, the systematic calibration of mixture models has received little attention. One of the few studies where mixture calibration was performed is the work of Alizadeh et al. [82]. The authors modelled the segregation of a detergent mixture during heap formation and found that the segregation behaviour was not accurately captured by their model, which was calibrated using a combination of direct measurement and bulk calibration. They attributed the models inaccuracy to the fact that spheres were used to model the particle shape. When using clumped spheres to approximate the actual particle shape, the predicted segregation behaviour was in good agreement with the experiments. Other researchers have also modelled the segregation of mixtures, but the interaction parameters between mixture components were not mentioned [95, 97].

Figure 2.3(b) illustrates the various DEM software that have been used by past researchers to investigate segregation. It is notable that 60% of the studies have not specified the DEM software they have employed. This is highly important because not only might the same DEM parameters be defined in different ways in various software, but also models may be differently implemented, making the parameters code-dependent [104, 111]. It means that the calibrated parameters of these studies cannot be reliably and directly used by others to reproduce the work or to model the same material. Therefore, it is essential to specify the used DEM code or software in detail in future studies.

The different types of mixtures that have been modelled and studied segregation are shown in Figure 2.3(c). A vast majority of past studies (i.e. 70%) have been dedicated to single-

component mixtures, i.e., with the general form of $1C[(iS/jSh)]$ (see Section 2.2), most of which have modelled simple binary- or ternary-sized mixtures with spherical particles (i.e., $1C[(2S/1Sh)]$ or $1C[(3S/1Sh)]$). In addition, few studies considered two or three components [18, 43, 44, 50, 77–79, 95, 97, 103, 112], but they also simplified the mixtures by modelling mono-sized and mono-shaped components. In conclusion, although past DEM studies have attempted to shed light on segregation in granular materials, they have failed to represent the real-world complex mixtures, which are mostly multi-component with each component having a size distribution and different particle shapes [113].

As can be seen in Table 2.1 (columns *mixture type* and *particle shape*), the particle shape and size distribution have often been simplified, mainly to prevent high computational time. The effect of particle shape on segregation is not crystal clear yet, as can be illustrated by seemingly contradictory results in the literature. For instance, Yu and Saxén [15] asserted that particle shape has an insignificant effect on the size segregation during charging and discharging from a hopper since spherical particles yielded the best agreement with the experimental results of [114]. It is notable that they used the same DEM parameters for both spherical and non-spherical particles which can lead to misinterpretation. In another study, Alizadeh et al. [82] concluded that modelling non-spherical particles as spherical with rolling friction underestimates the segregation extent during heap formation. Despite this conflict, Lu et al. [115] and Combarros Garcia et al. [96] concluded that particle shape has to be modelled as accurately as possible to ensure that the DEM model is accurate and predictive. Similarly, particle size distribution has usually been approximated either by using a limited number of sizes or scalping (cf. Section 2.3.1). However, since particle size is the most crucial parameter affecting segregation [116], size distribution should be modelled as concisely as possible. As stated by Coetzee [104], particle shape along with the particle size distribution should be explicitly included in the calibration process, and they have to be determined prior to other parameters.

2.3.4 Validation of DEM models for segregation

The parameters obtained through calibration must be independent of the application [107]. Therefore, once the model is calibrated, it should be capable of accurately reproducing other experiments. In order to prove this, the results of the DEM simulation have to be compared with either experimental tests, analytical, or "well-established" numerical results related to segregation, which are available in the literature. In case a "good agreement" is observed, the model is validated. Regardless of the above-mentioned approaches being adopted for determining the DEM parameters, the studies in groups II, III, and IV of Table 2.1 (except for parametric studies in group I) attempted to validate their DEM model for segregation. The validation techniques found in the literature overview of Table 2.1 can be classified into two main categories as illustrated in Table 2.6: (1) using other research results as the benchmark and (2) using first-hand experimental results.

Table 2.6 Validation approaches of past DEM studies on segregation (cf. Table 2.1 for the type of mixture in each study).

Approach for validation		**Source**
(1) Other work's results	Experimental	[52, 55, 56, 64, 74, 117]
	DEM	[53, 57, 69]
	Mathematical	[42, 59, 63, 70]
(2) First-hand experimental results	**Flow-related (bulk behaviour)**	
	The mass fraction of the whole particles discharged from the hopper	[49]
	The velocity profile of particles using particle tracking velocimetry (PTV)	[50]
	Angle of repose measured in practice	[61, 66]
	The discharge time of the particles from the hopper	[51, 68]
	Burden profile	[63, 73]
	Mass distribution of "all" particles in the radial direction in furnace throat	[73]
	Laser grid measurement [118] of burden falling trajectories	[54]
	Bed height	[93]
	Segregation (local behaviour)	
	Invasive	
	Sampling spaces composed of 24 cuboid-shaped cells inside the hopper	[96]
	The discontinuous start-stop sampling method [119] has been mostly adopted	[9, 80, 103]
	Including a number of sampling boxes at the bottom to capture the trajectory segregation of materials	[10, 72, 87–90]
	Heaps are divided into a number of sub-regions in the horizontal and/or vertical direction	[16, 75, 84, 92, 97]
	Using rotating sampling table with pie slicing configuration	[62]
	Measuring mass flow rate of fine particles using Copley flowability tester BEP2 model	[86]
	Sampling in the horizontal and vertical direction of the sinter cooler	[81]
	Sampling box in QPM segregation tester	[95]
	Non-invasive	
	Taking pictures and counting the number of different components	[67]
	Colouring equal-sized components and using image analysis to analyse segregation	[95]
	Taking pictures and using image processing to measure the fraction of components	[82, 120]

(1) Validation using other works results. In this approach, existing experimental, mathematical, or numerical (i.e., DEM) results on segregation are used to validate the DEM model. Although adopting this approach facilitates the process of developing a DEM model, it suffers from several drawbacks. Firstly, some of these references have not particularly investigated

the local behaviour (i.e., segregation) of granular materials, and as a result, even in the case of an acceptable agreement, one cannot make sure the DEM model is valid for segregation. Secondly, in some cases, the size distribution of the DEM model differs from the source study against which the model has been validated. For example, Zhao et al. [55] compared the results of the model for mono-sized particles and used the same model for modelling the segregation behaviour of granular materials with log-normal size distribution. However, according to Coetzee [104], if particle size in the model changes, the model parameters must be re-calibrated, i.e., the previous parameters values are not valid anymore. Thirdly, some studies employed a different setup in DEM than the experiment in the benchmark, which might significantly affect the simulation results. For instance, Wu et al. [74] simulated a virtual factory instead of a conveyor belt in the original study [121]. While simplifying real-life scenarios is a common practice among researchers, it's crucial to ensure that the velocity field is accurately mimicked, as it has a significant impact on segregation.

All in all, the approach of using other works results to validate the DEM model can have serious shortcomings. In other words, the model can be validated in this way only if all the details are accurately documented. This is often challenging since some data may have been omitted due to confidentiality. In addition, this approach is limited to specific materials (e.g., glass beads, iron ores), because there is a shortage of experimental data on the segregation of various kinds of granular materials in the literature.

(2) Validation by conducting experiments. Unlike the above-mentioned category, which relied on existing data in the literature, other studies have conducted experiments themselves and used first-hand experimental data to validate the DEM model. Two types of experiments have been carried out (cf. Table 2.6): the flow-related measurements of the granular materials, i.e., global/ bulk behaviour, or segregation-related measurements, i.e., local behaviour.

Examples of the first type of experiment in which physical measurements related to global behaviour have been carried out are listed in Table 2.6. With respect to segregation, this approach fails to provide detailed spatial and temporal or "local" information about segregation such as the fraction of different components. Although this approach can be adequately adopted to validate DEM models for "flow behaviour" on the bulk level, it cannot necessarily prove the validity of the model for segregation. In other words, to validate the models for segregation, component fractions are required to obtain local information and assess segregation.

The second group of studies has relied on segregation-related measurements. As can be seen in Table 2.6, there are two main ways of measuring segregation, namely invasive and non-invasive methods [122]. Invasive methods for evaluating segregation simply involve taking a number of samples, separating the components in each sample, and weighting each component to obtain its mass fraction. Several sampling methods have been adopted by researchers for different systems, as listed in Table 2.6. Although all the mentioned invasive methods are relatively simple and can provide valuable information about the local composition of granular mixtures, they have a number of disadvantages. First and foremost, invasive methods disturb the original structure of the mixture, which affects the accuracy of the measurement. Moreover, particles from locations other than the target points might be collected during sampling [123]. And, as mentioned above, components in each sample must be separated to further calculate their fractions. This can be straightforward for components differing in size; however, for multi-component mixtures with overlapping particle sizes, this can be challenging and time-consuming. Terui et al. [97] successfully employed the gravity separation method

to separate sinter and coke particles based on the density difference. However, besides being time-consuming, this method is not applicable to all types of materials.

The mentioned drawbacks of invasive methods have pushed for seeking non-invasive techniques as an alternative. Because they are not disturbing the granular structure, these techniques have been increasingly employed in recent years, especially in the powder blending industry [124]. There are several comprehensive review papers in the literature explaining the pros and cons as well as the applications and limitations of these methods in detail [26, 27, 122, 124]. Because of the inherent limitations of those techniques, not all of them are applicable to the segregation analysis of any granular mixtures. For instance, the electrical conductivity method, electrical capacitance tomography (ECT), positron emission particle tracking (PEPT), and magnetic resonance imaging tomography (MRI) cannot be readily utilised to analyse the mixing and segregation of all multi-component mixtures [26]. This is because the electrical conductivity method and ECT work based on the noticeable difference in electrical conductivity and permittivity, respectively, which is not the case in all multi-component mixtures [26, 125]. Also, a limited number of tracers are tracked in PEPT, which is not suitable to measure segregation, and in MRI, the component should be coated with oil to be detectable, which might significantly affect its flow behaviour [126]. Other techniques, such as Raman spectroscopy, near-infrared spectroscopy (NIR), and acoustic emissions, which are feasible for multi-components, are conducted on very small samples [27], which deems them unsuitable for coarser particles.

Image analysis is another existing non-invasive method that has been widely used due to its simplicity and low cost. The main advantage of image analysis over other techniques is that it is applicable to multi-component mixtures. However, this method is limited to surface analysis; it requires a transparent vessel, and the components must differ in colour [127]. This method has been successfully employed by a number of studies to provide experimental results for the calibration and validation of DEM models of segregation. Yu et al. [67] took photos of the heap, divided the heap into sub-regions radially, and counted the number of small and coarse particles in each region to analyse segregation. Adopting a more robust approach, Wang et al. [120] and Alizadeh et al. [82] employed image processing techniques to measure local concentrations of mixture components at the surface of the heap. To be fully consistent, they used the same approach in DEM by taking snapshots of the granular system and applying image processing, as shown in Figure 2.4.

In conclusion, all the methods being adopted to validate DEM models come with a set of advantages and disadvantages. Although using existing results in the literature facilitates the validation, it is often difficult to precisely replicate the experimental setup, and sometimes the other study has not been validated itself. Additionally, utilising existing results is confined to

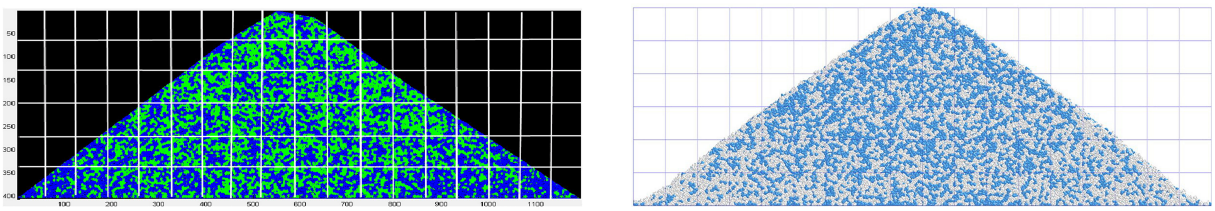

(a) (b)

Figure 2.4 An example of using image analysis to measure segregation in a) experiments and b) DEM. Reproduced with permission from Ref. [82]. Copyright 2017, Elsevier.

a few materials that have already been investigated. To overcome these obstacles, carrying out experiments and using first-hand results would be beneficial. However, it should be noted that the experimental measurements should provide detailed spatial information for segregation on the local level, supplemented by global level or bulk behaviour such as mass flow rate. The segregation-related measurements can be performed using either invasive or non-invasive methods. Image analysis as a non-invasive method is considered superior to invasive techniques since it not only maintains the structure of the granular materials but also is applicable to multi-component mixtures, provided that the components differ in colour.

2.4 Results of DEM-based studies on segregation

The work presented in Table 2.1 in the previous section will be elaborated in detail here. The findings of those studies on how segregation is affected by adjusting material properties, system configurations, and operational parameters are gathered and analysed.

2.4.1 Material properties

Generally, any difference between the particles of a particulate system can cause segregation. For free-flowing granular materials, it has been proven that particle size, density and shape affect segregation more than other factors such as surface roughness and elasticity [3]. The studies listed in Table 2.1 are analysed, and the effects of these factors are presented in the following paragraphs. To systematically discuss the results in the literature, Figure 2.5 is presented to illustrate the possible combinations of different particle properties, and Table 2.7 is used to indicate the relevant subsection addressing the corresponding type of mixture.

(A) Particle size. Particle size is unequivocally the most influential property contributing to segregation among the other particle properties [116]. This is why numerous research studies

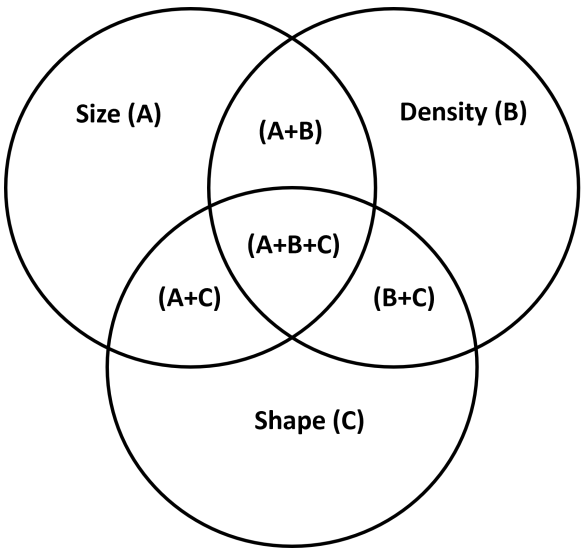

Figure 2.5 Different possible combinations of particle properties.

Table 2.7 Corresponding sub-section for different types of mixture.

Section	**Type of mixture**		
	Symbol	**Notation**	
Particle size	A	1C[(iS/1Sh)]	$i = 2,3,\ldots,M,P$
Particle density	B	nC[(1S/1Sh) + $\cdots$ + (1S/1Sh)]	$n = 2,3,$etc.
Particle shape	C	1C[(1S/jSh)]	$j = 2,3,$etc.
Combinations of particle size, density and shape	(A+B)	nC[(i_1S/1Sh) + $\cdots$ + (i_nS/1Sh)]	$n = 2,3,$etc. & $i = 2,3,\ldots,M,P$
	(A+C)	1C[(iS/jSh)]	$i = 2,3,\ldots,M,P$ & $j = 2,3,$etc.
	(B+C)	nC[(1S/j_1Sh) + $\cdots$ + (1S/j_nSh)]	$n = 2,3,$etc. & $j = 2,3,$etc.
	(A+B+C)	nC[(i_1S/j_1Sh) + $\cdots$ + (i_nS/j_nSh)]	$n = 2,3,$etc. & $j = 2,3,$etc.

have been dedicated to gaining a full understanding of the effect of particle size and especially particle size distribution (PSD) on segregation.

In the case of binary-sized mixtures, i.e. mixtures in form of $1C[(2S/1Sh)]$, the effect of size distribution can be investigated by varying either the size ratio or the mass fraction of the components. It is generally accepted that a larger size ratio leads to more pronounced segregation [128]. Figure 2.6 shows the investigated ranges of size ratio in the DEM-based studies of binary-sized free-flowing mixtures in various systems. For hoppers and in one of the earliest attempts to study segregation using DEM, Ketterhagen et al. [103] concluded that the extent of segregation significantly increases for size ratios greater than 1.9. Using the velocity difference between small and large particles as an indicator of percolation, T.F. Zhang et al. [117] investigated the segregation during conical hopper discharging and found that in their case percolation was not dominant for size ratios smaller than 6.0 (i.e., corresponding to the velocity difference of 0.07 mm/s). Z. Zhang et al. [80] observed that the percolation, which occurred during discharging of a wedge-shaped hopper near the wall and the bottom of the hopper, was eliminated for a size ratio lower than 1.2. Varying size ratio from 1.3 to 4.0, Yu and Saxén [9] observed significant segregation even for the minimum ratio of 1.3. Unlike these studies, Ketterhagen et al. [42] found that in the case of the hopper bottom wall angle of 15ř (as opposed to 90ř), no considerable segregation was observed for all size ratios tested.

In addition to hoppers, several studies have examined the effect of size ratio on segregation in other systems such as inclined planes, chutes, the throat of the blast furnace and V-blender. Tripathi and Khakhar [41] in their work on the segregation of binary mixtures down an inclined plane found that varying size ratio does not affect the extent of segregation. In the case of a chute, Panda and Tan [44] observed that although the stream-wise, cross-stream and vertical velocities all increase with increasing size ratio, the degree of segregation did not increase significantly in the stream-wise direction. Li et al. [18] studied the particle segregation in the throat of the blast furnace. For this, they charged a layer of binary-sized coke followed by a layer of binary-sized ore particles. Varying the size ratio equally for coke and ore particles, they observed that larger size ratios result in a more segregated state, which was more evident for the coke mixture. In their study on de-mixing of binary-sized mixtures during discharging from a V-blender, Pereira and Cleary [43] observed that the segregation extent becomes significant for large size ratios, i.e., 3 and 4.

Apart from the particle size ratio, the mass fraction of fine particles has been proven to have a significant impact on segregation [3]. Artega and Tüzün [129] proposed a model for binary-

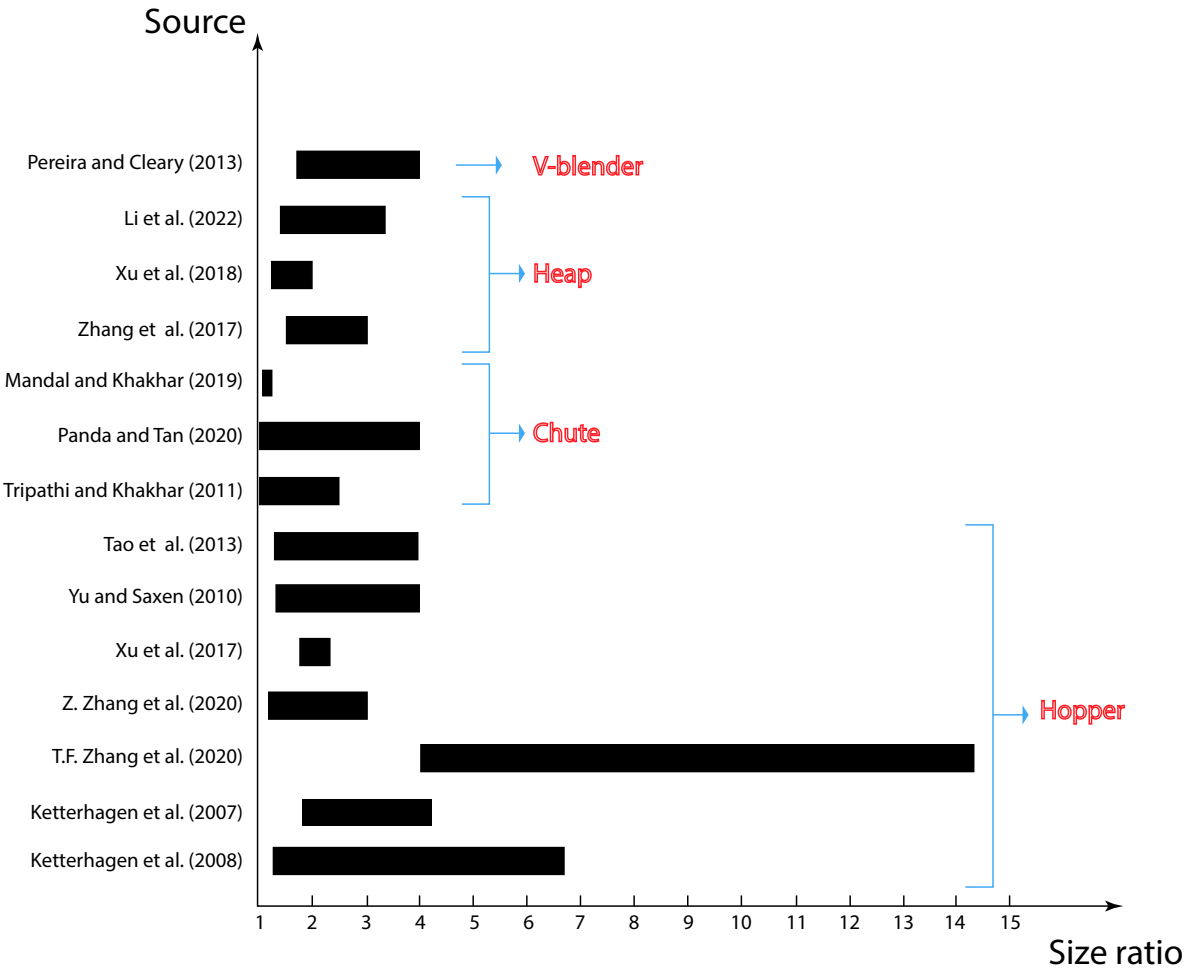

Figure 2.6 Range of size ratios between large and small particles used in previous DEM studies on segregation.

sized mixtures to determine the fine mass fraction (x_f) for which segregation via percolation becomes feasible during hopper discharge. They claimed that percolation no longer occurs when the surface area of the large spheres is completely covered by small spheres, implying that percolation only occurs if the mass fraction of finer particles is lower than the limiting value defined as $x_{L,\text{crit}} = [4/(4+\Phi_R)]$, where Φ_R is the size ratio. This model is applicable to free-flowing materials with approximately spherical shape and is independent of the hopper geometry. While the findings of Ketterhagen et al. [42] and Z. Zhang et al. [80] are in accordance with Artega and Tüzüns model, Xu et al. [51] observed segregation for mass fractions higher than the above-mentioned $x_{L,\text{crit}}$. Nevertheless, all of these studies agree that increasing the fine mass fraction decreases segregation [42, 51, 52, 66, 80, 86].

While in most of the DEM studies a limited number of particle sizes has been used, Zhao et al. [55] and Kumar et al. [57] used a continuous distribution of particle size, i.e. poly-sized mixtures with the general form of $1C[(PS/1Sh)]$. Zhao et al. [55] studied the discharge of mixtures with a log-normal size distribution from a conical hopper. As shown in Figure 2.7, they examined the effect of the width of size distribution, defined as the ratio of standard deviation to mean diameter (σ/μ), on segregation and concluded that the higher the width, the greater the size segregation will be. This agrees with observations on the impact of size ratio on the

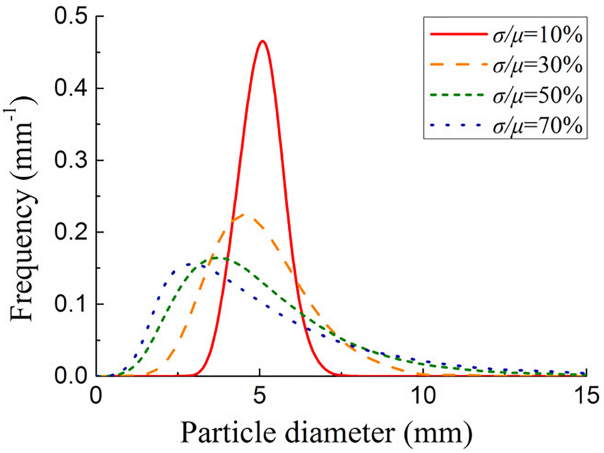

Figure 2.7 Different log-normal size distributions. Reproduced with permission from Ref. [55]. Copyright 2017, John Wiley and Sons.

segregation of binary-sized mixtures, as the size ratio in binary-sized mixtures is essentially the same as the width of the size distribution in poly-sized mixtures.

In another study, Kumar et al. [57] studied the discharge from a hopper of mixtures with the Rosin-Rammler size distribution

$$R = 1 - \exp\left[-\left(\frac{x}{x'}\right)^{n}\right] \tag{2.2}$$

with size distributions width (n) and location parameters (x'). It was found that the width has more impact on the segregation than the location parameters. Moreover, they conducted a comparative analysis between the log-normal and Rosin-Rammler particle size distribution (PSD) with the same width and observed that the latter showed a higher segregation extent. They also reported that the extent of segregation is increased with more fine particles which contradicts the observations in past studies on the segregation of binary-sized mixtures [42, 51, 52, 80]. This conflict may lie in the fact that comparing a continuous size distribution with a binary-sized mixture requires selecting the right cut-off size between fine and coarse particles, which is not always a trivial task.

To date, a large number of segregation-related studies have focused on the effect of particle size and mass fraction in binary-sized mixtures. Generally, it has been found that reducing the size ratio as well as increasing the mass fraction of fine particles alleviate segregation. With respect to the size ratio, however, there is no unanimous agreement either on the critical size ratio which promotes segregation or on the effect of increasing the size ratio on segregation in general. Overall, there is no single limiting size ratio above which segregation happens. Also, there is no unanimous agreement on the effect of increasing the size ratio on segregation. The reason behind these is twofold. Firstly, aside from size ratio, other factors such as material properties (e.g. mass fraction), geometric, and operational parameters also play a crucial role in segregation phenomena. Secondly, percolation rate measurements in shear cells have shown that segregation can occur for all size ratios, and larger size ratios only serve to accelerate its occurrence [128, 130, 131]. As with size ratio, the effect of fine-particle mass fraction on segregation is inconsistent, indicating that results from a single study cannot be generalised because geometry and operating conditions also play a decisive role.

(B) Particle density. The difference in particle density is another known factor to cause segregation. As mentioned in Section 2.2, the density of particles in a single material is assumed to be constant. Therefore, the difference in particle density is equivalent to having different materials. For instance, what is referred to as a "binary-density" mixture is basically a two-component mixture with the notation of $2C[(1S/1Sh)+(1S/1Sh)]$.

While a number of earliest experimental studies on the mixing and segregation of granular materials argued that particle density does not affect segregation considerably [116, 132], some others suggested that the difference in density should be taken into account in segregation analysis [130, 133, 134]. There has been, however, little systematic analysis of density-driven segregation in free-flowing granular materials using DEM. Seil et al. [135] investigated the segregation of mixtures discharging from two hoppers. They observed that the heavier particles tend to gather in the center areas and that the extent of segregation is linear to the density ratio. In another study on an inclined plane, Tripathi and Khakhar [40] observed heavy particles sink to near the base, and light particles form a layer close to the free surface with a mixed region in between, which was confirmed in other studies [44, 85, 120]. Furthermore, they showed that higher density ratios result in stronger segregation.

In conclusion, particle density has been shown to affect segregation to some extent. However, the significance of its effect compared to other factors such as the difference in particle size, is unclear yet. More effort on density-induced segregation in various systems is required to pave the way for developing DEM models for multi-component segregation.

(C) Particle shape. Only a few of the found studies focused on modelling the effect of particle shape on the extent of segregation. These studies can be classified into two groups. The first group include studies in which the mixtures are composed of two particle shapes to investigate shape-induced segregation. Using the multi-sphere approach, Mandal and Khakhar [69] studied the flow of mixtures of spherical and non-spherical particles having the same volume down a rough inclined plane (cf. Figure 2.8). They found that the geometric mean diameter (i.e. $d_g = \lambda^{1/3} d$, where λ is the aspect ratio and d is the diameter of the constituent spheres) is a good representative of the effective size for irregularly-shaped particles, and the extent of segregation of two species depends on the ratio of the geometric mean diameter of particles. Moreover, it was observed that at the steady state, the particles with a larger geometric mean diameter accumulate near the free surface.

Zhao and Chew [70] studied the flow behaviour of binary-shaped mixtures during discharg-

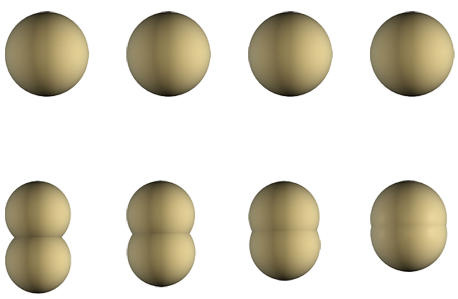

Figure 2.8 Different combinations of spherical and non-spherical particles. Reproduced with permission from Ref. [69]. Copyright 2019, AIP Publishing.

ing from a hopper. They modelled seven different particle shapes (a sphere, two ellipsoids, two cylinders, and two cuboids, as shown in Figure 2.9, all with an aspect ratio between 0 and 2 and the same volume. Considering various combinations of these particle shapes, they observed that mixtures of cylinders and cuboids exhibited the least segregation, and the ellipsoids mixed with cylinders were the most segregated mixtures.

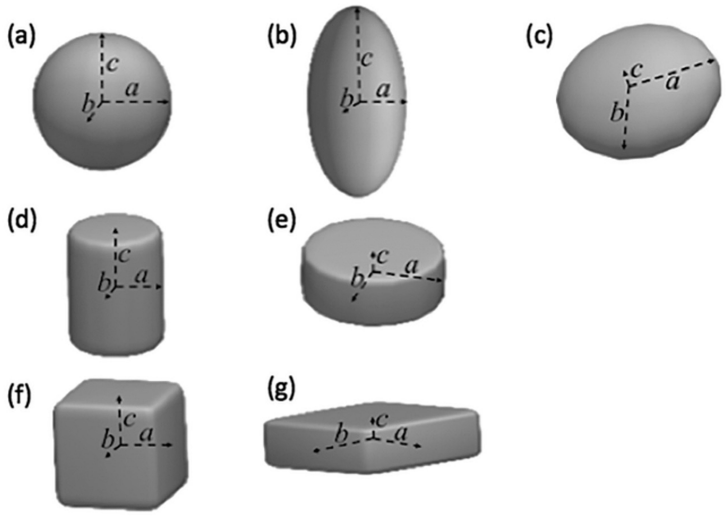

Figure 2.9 Different particle shapes modelled. Reproduced with permission from Ref. [70]. Copyright 2020, John Wiley and Sons.

Second, studies in which the segregation behaviour of different mixtures, each component composed of a particular shape, is analysed. Zhao and Chew [56] compared the discharging behaviour of mixtures with log-normal PSD, composed of ellipsoids, cylinders, or cuboids, and observed that ellipsoids show very similar segregation behaviour as spheres. The cuboids and ellipsoids exhibit the lowest and the highest segregation extent, respectively.

In conclusion, very little attention has been paid to shape-induced segregation in DEM-based studies. Past studies have demonstrated that the difference in particle shape itself can induce segregation [69, 70]. However, it is unclear how particle shape induces segregation and specifically, which shape characteristics are more significant for segregation. Therefore, further work needs to be done to shed light on shape-induced segregation. Challenging herein are the computational expense of simulating the motion of irregularly shaped particles and the fact that particle shape is not independent of particle size. This is very important since, in case the segregation induced only by particle shape is of interest, "effective" particle size should be the same to avoid misinterpretation [136]. Therefore, it is recommended that efforts be made to establish criteria for determining the "effective" size of non-spherical particles for segregation [137].

Combinations of particle size, density, and shape: While the preceding subsections have focused on studies examining variations in a single particle property (such as size, density, or shape), a limited number of research works have investigated mixtures with multiple properties that vary simultaneously. To systematically discuss them, these studies are grouped below using the symbol in Figure 2.5 and Table 2.7:

(A+B). Most of the studies varied the particle size and density at the same time. Two different scenarios can be distinguished: 1. a mixture of (small/heavy) and (large/light) particles, in which the percolation and buoyancy mechanisms work together, or, 2. a mixture composed of small/light and large/heavy particles where percolation and buoyancy mechanisms oppose each other. Figure 2.10 illustrates these two scenarios. As can be seen in Figure 2.10(a), in the first scenario, both percolation and buoyancy mechanisms act together, and (small/heavy) particles sink into the mixture. However, in the second scenario, as in Figure 2.10(b), the dominant segregation mechanism is not known a priori and should be studied case by case. Past studies indicated that in the first scenario, reducing the size ratio and/or density ratio leads to less segregation and could be used as a way to suppress segregation [51, 68, 97]. For the second scenario, Ketterhagen et al. [42] varied the density ratio from 0.33 to 3.0 for a size ratio of 4.3, and no significant segregation was detected during discharging from a wedge-shaped hopper. Similarly, Tao et al. [49] increased the density ratio from 0.5 to 2.0 for a mixture with a size ratio of 4.0 and observed that segregation was negligible.

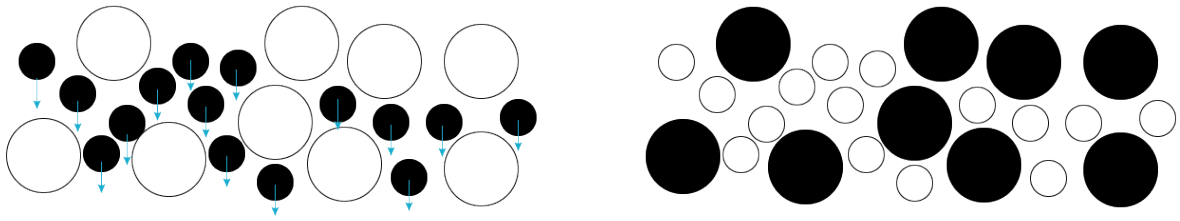

(a) (b)

Figure 2.10 Two scenarios for particles differing in both size and density (solid black colour indicates heavier particles), a) first scenario; a mixture of (small/heavy) and (large/light) particles, and b) second scenario; a mixture of (small/light) and (large/heavy) particles.

(A+C). In attempts to explore the simultaneous effect of particle size and shape on segregation, several studies varied the particle shape of binary-sized mixtures, i.e. mixtures in the form of $1C[(2S/2Sh)]$. Mandal and Khakhar [69] studied the flow of mixtures of non-spherical particles where the two particle types differ in both volume (i.e., size) and shape and observed that segregation extent increases for larger geometric mean diameter ratios. Tao et al. [49] simulated binary-sized mixtures with different particle shapes, including spherical, corn-shaped, cylindrical, and ellipsoidal particles. It was observed that particle shape has a significant effect on segregation extent, with the most segregated system for ellipsoidal particles and the least for spherical ones.

(A+B+C). Few studies examined the segregation in mixtures differing in particle size, density, and shape. Liao et al. [64] investigated the segregation behaviour of lump ore and pellets that differed in size and density. To examine the impact of particle shape on segregation, they simulated three different shapes of lump ore particles, namely spheres, cylinders, and schistous particles, and concluded that particle shape has a significant effect on segregation, with spheres showing the least amount of segregation. In mixtures of sinter and briquettes, Kim et al. [83] varied both the briquette shape and its mass fraction, defined as the mass of briquettes divided by the total mass of briquettes and sinter. They observed that while particle shape had little effect on segregation, a briquette mass fraction exceeding 20% led to significant segregation.

Despite previous efforts to investigate the influence of various material properties on segregation, there remains a significant knowledge gap. While the majority of natural and industrial mixtures are multi-component, i.e. (A+B+C) in Table 2.7, most studies have concentrated on binary or ternary-sized mixtures consisting of spheres. Therefore, a more comprehensive and rigorous approach towards material properties that takes various combinations of size, density, and shape into account is required to accurately predict segregation patterns and occurrences.

2.4.2 System configurations

In addition to the material properties, system parameters play a key role in segregation phenomena occurring in particulate systems, because they influence the motion of the particles. In gravity-driven handling processes, two main pieces of equipment can be distinguished: hopper/silo and chute/inclined surfaces. A review of these systems in the context of segregation is presented in the following paragraphs.

I. Hopper. Segregation during hopper discharge has been studied since the early 80s, when most studies were experimental. Ketterhagen et al. [103] were one of the first to model segregation during cylindrical hopper discharge using DEM in 2007. Since then, a number of DEM studies have investigated the influence of geometric properties on the extent of segregation, by varying the outlet width, the slope of the bottom wall, and the smoothness of the walls.

Two main flow regimes are distinguished during hopper discharge: mass flow, where the entire body of mass inside the hopper is in motion during discharge and funnel flow [138–140]; funnel flow, which is less desirable as it imposes asymmetric pressure distribution and causes significant segregation which can be harmful to both hopper structural stability and particulate homogeneity [139]. The flow mode is mainly dependent on the bottom wall angle, θ_c (measured with respect to the vertical), and wall friction angle, φ_x. Smoother and steeper walls (i.e., lower θ_c) most likely induce mass flow regime and are less likely to induce segregation. This was also confirmed in several DEM studies [9, 42, 58, 139].

Several studies used DEM to gain deeper insight into segregation during hopper discharging. T.F. Zhang et al. [117] varied the angle of the hopper wall from 15ř to 90ř and observed that larger angles (i.e., flatter walls) lead to faster percolation of small particles, increasing their tendency to gather at sidewalls (cf. Figure 2.11(a)). Similarly, Z. Zhang et al. [80] showed that the increase in the hopper angle promotes segregation in bottom regions (red regions in Figure 2.11(b)). However, they found that with larger angles, the percolation near the wall region decreases. This disagreement might be because of the different size ratio, wall condition (i.e. boundary walls in [117]), or a different method of assessing segregation (cf. Section 2.3.2). Also, it is remarkable that in [117], the hopper outlet size of $3d_l$ (where d_l is the diameter of the large particles) is used, which does not adhere to the fundamental hopper design principles [140] and can affect the segregation results.

Stating that the bottom angle of the hopper is a decisive factor in the flow mode, Huang et al. [45] proposed an optimised design which increases the mass flow zone and as a result, achieves less size segregation (cf. Figure 2.12).

In addition to the hopper wall angle, the outlet size can also affect the segregation during hopper discharging. Ketterhagen et al. [42] found that the increase in outlet width reduces the

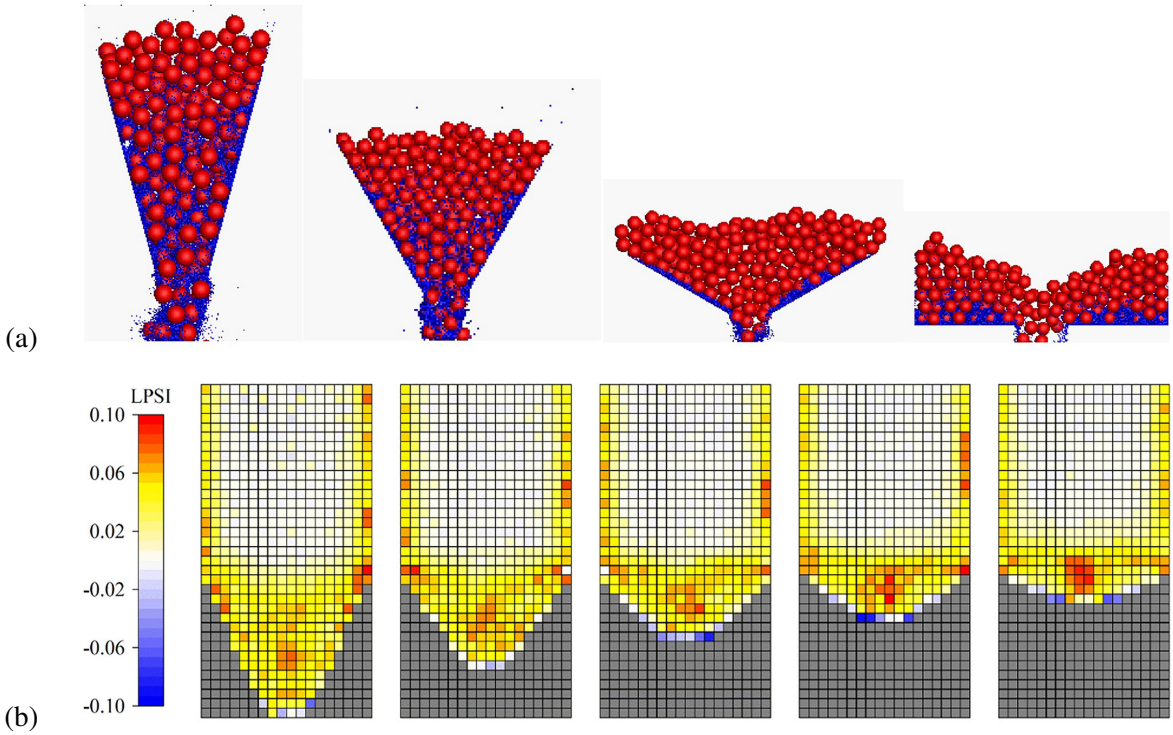

Figure 2.11 The effect of hopper wall angle on size segregation in two studies: (a) Reproduced with permission from Ref. [117]. Copyright 2020, Elsevier; and (b) Reproduced from Ref. [80], used under Creative Commons CC-BY-NC-ND License.

segregation of mixtures discharging from wedge-shaped hoppers. Although Z. Zhang et al. [80] confirmed that the percolation in the bottom part of the hopper reduces in the case of a bigger outlet, a higher segregation degree near hopper walls was observed, which can be related to wall effects. Taking the effect of both the hopper outlet and wall angle into account, Ketterhagen et al. [42] claimed that segregation conditions remain the same for hoppers with the same aspect ratio of hopper height to hopper width. To investigate the effect of flow-correcting inserts, Cliff et al. [62] compared the segregation behaviour of a binary-sized mixture during discharging from a hopper between a hopper with (cf. Figure 2.13(a)) and without an insert. They stated that in the case of a hopper with an insert, lower velocity gradients at the free surface lead to less segregation (cf. Figure 2.13(b)).

While most of the works mentioned above, studied concentric hoppers, Ketterhagen and Hancock [59] compared the segregation of binary-sized mixtures between eccentric and concentric hoppers (cf. Figure 2.14(a)). They found that while the eccentric hopper had slightly less segregation, the segregation profiles around the outlet were completely different (cf. Figure 2.14(b)). Additionally, they modified the design of the eccentric hopper, resulting in improved segregation.

In conclusion, designing for mass flow is beneficial to avoid size segregation during hopper discharge. This can be achieved by steeper and smoother walls. However, several studies observed insignificant effects of these factors on segregation. The reason for the conflict between these studies is that, besides geometric parameters, material properties and operational parameters can influence particle velocities and segregation. This makes it challenging to compare the findings of different studies and arrive at a definitive conclusion. Therefore, a more

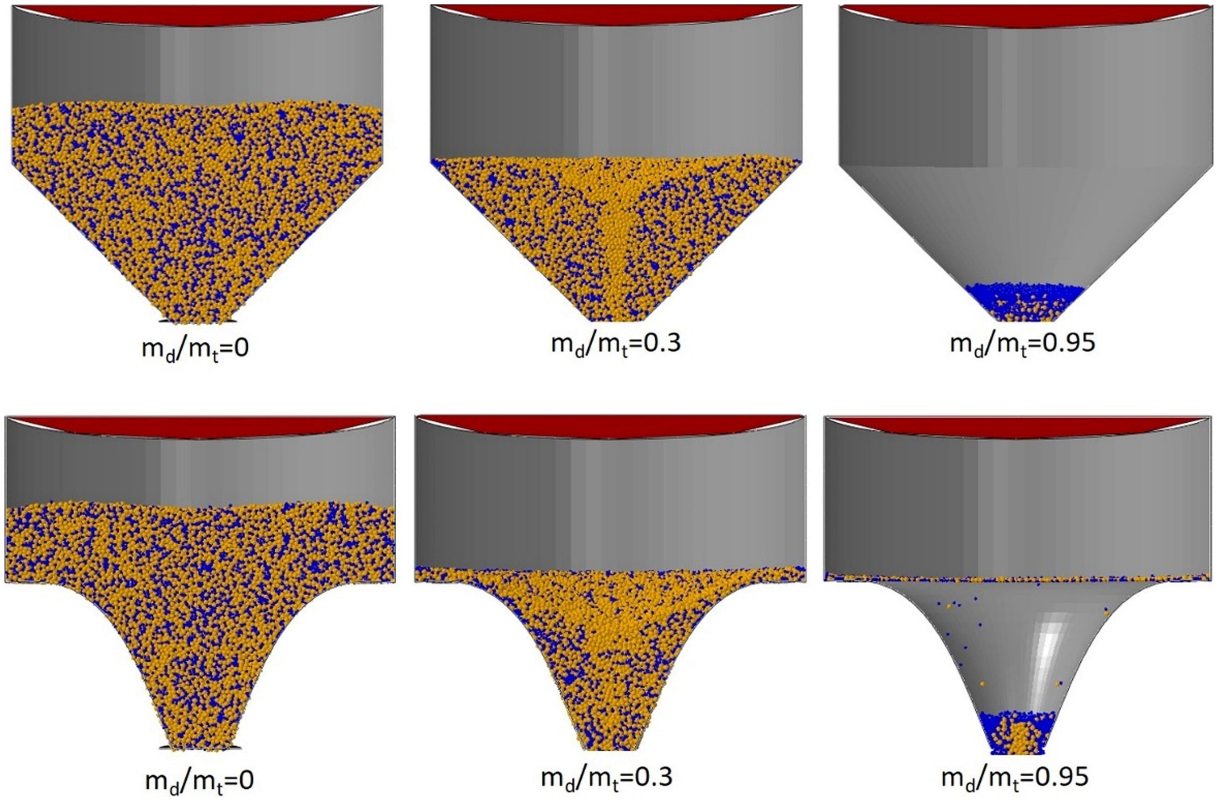

Figure 2.12 The effect of different hopper designs on segregation during discharging the hopper at different discharging fractions ($m_d m_t$). Reproduced with permission from Ref. [45]. Copyright 2022, Elsevier.

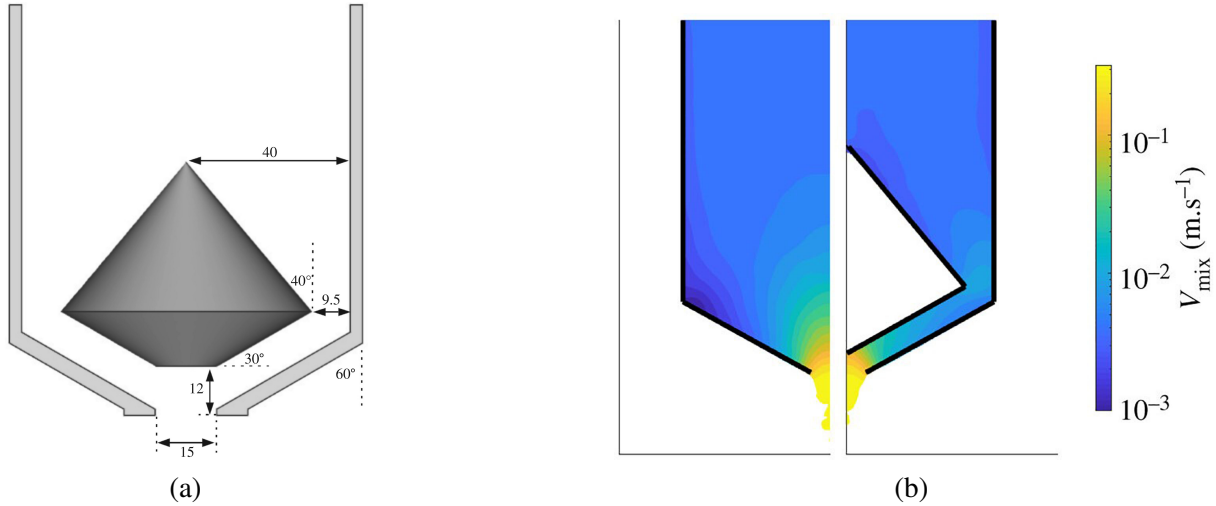

Figure 2.13 The cross-sectional view of the hopper with insert, b) difference in the velocity gradient between the hopper with (right) and without (left) insert. Reproduced with permission from Ref. [62]. Copyright 2021, The Royal Society.

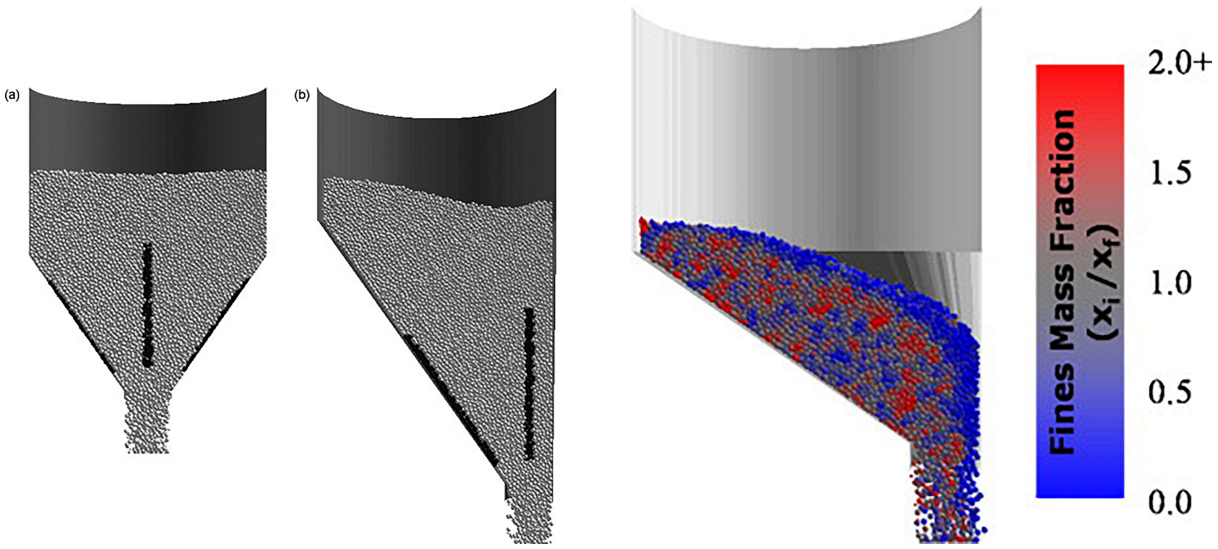

(a) (b)

Figure 2.14 a) Concentric and eccentric hopper, and b) segregation profile in the eccentric hopper. Reproduced with permission from Ref. [59]. Copyright 2010, Elsevier.

robust approach is needed to investigate the simultaneous effect of different geometric factors on segregation and its dependence on material properties. Moreover, the found work evaluated only single-component mixtures, and the effect of geometric design parameters in the case of multi-component segregation is missing.

II. Chutes. Chutes are often used to transfer materials from one piece of equipment to another. They can have different cross-sectional shapes (e.g., semi-circular, rectangular), lengths, curvatures, and wall roughness. While chute angle may be regarded as a system configuration parameter in certain cases, e.g., transfer chutes, it is considered an operational parameter in dynamic systems such as blast furnaces. Therefore, the chute angle will be discussed later in Section 2.4.3 of this chapter.

Segregation can occur simultaneously in three directions: in the direction of the flow (longitudinal/ stream-wise segregation), from the chute to the free surface (vertical/ normal segregation), and from one side wall to the other (horizontal/cross-stream-wise segregation). During chute flow, segregation can happen in two stages. Firstly, when the material is inside the chute, gravitational forces, centrifugal and Coriolis forces, inter-particle friction, and particle-geometry friction forces act on the particles [54]. Mio et al. [87] found that particles segregate inside the chute, with smaller particles at the bottom wall of the chute and larger ones on top. In the second stage, the material leaves the chute, and trajectory segregation causes larger particles to travel further [87]. The effect of chute-related geometric parameters on segregation was researched by employing either a simple inclined plane [48] (to minimise the effect of side walls) or a real 3D chute [44].

With respect to the effect of the cross-section shape of the chute, Kou et al. [77] investigated three different shapes, namely semicircle, trapezoid, and rectangle, on the segregation of ferrous burden (i.e., pellet, sinter, and lump ore) forming a heap in the blast furnace throat. They found that chute cross-section shape significantly affects the radial size distribution of materials, and the effect is intensified with larger chute angles and higher rotating speeds. Moreover,

unlike trapezoid and rectangular chutes, the semicircle chute was reported to maintain a uniform radial size distribution regardless of the chute angle and rotating speed. Panda and Tan [44] focused on the segregation inside the chute and compared the segregation between rectangular and semi-circular chutes. It was observed that the rectangular channel resulted in slightly higher segregation in the stream-wise direction, while there were barely any differences in cross-stream and vertical directions.

In terms of the impact of chute length, the observations revealed that since segregation occurs within the chute, an increase in the chute length leads to a greater extent of segregation [10, 54, 72, 73]. Bhattacharya and McCarthy [10] determined the critical chute length for trajectory segregation of ternary-sized mixtures discharging from a hopper onto the chute, using both theoretical equations and simulations, which yielded 4.0 and 5.4 m, respectively. They claimed that with other parameters fixed, there is significant segregation in the sampling boxes located under the chute for the chute longer than the critical length. For the radial segregation of multi-component mixture of sinter, pellet, and ore, Hong et al. [79] observed that the effect of chute length is negligible.

Mantravadi and Tan [53] examined the effect of bend angle (i.e., curvature) in periodic flow inversions (see Figure 2.15), an idea initially introduced by Shi et al. [141], on reducing the size segregation of binary-sized mixtures and observed that a bend angle between 120 and 150 degrees leads to the minimum extent of segregation.

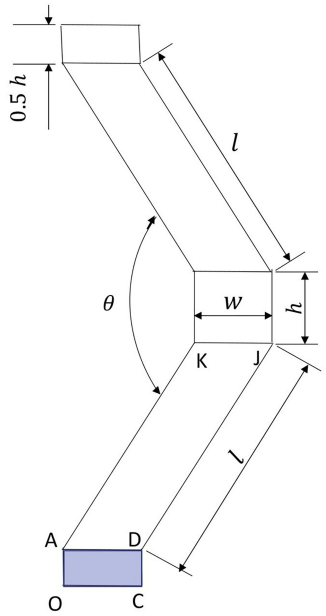

Figure 2.15 The periodic flow inversion with a bend angle of θ. Reproduced with permission from Ref. [53]. Copyright 2020, Elsevier.

Zhou et al. [142] varied the wall roughness by using the wall friction coefficient and found that higher base roughness significantly accelerates the segregation. However, in the case that base friction was larger than inter-particle friction, no effect on the flow regime and segregation was observed. Shirsath et al. [50] studied the effect of chute wall roughness on the segregation of binary density mixtures, i.e. $2C[(1S/1Sh)+(1S/1Sh)]$. They implemented the roughness artificially by modelling a number of particles at chute walls, attributing the ratio of the diameter between surface particles and flowing particles (ranging from 0.5 to 2.0) to the degree of

roughness. They reported that wall roughness has a considerable effect on the segregation as it is negligible for the smooth (but frictional) chute wall. While it was observed that the degree of the segregation increases with the wall roughness, this increase plateaus when the diameter of the wall particles exceeds the flowing particle size. However, it is unclear to what extent the way of modelling wall roughness in this work is representative of roughness at micro scale.

Concluding, the geometric aspects of chutes, including cross-section shape, length, curvature, and wall roughness, can significantly influence segregation. Generally, it has been found that longer chutes with rougher walls promote segregation.

2.4.3 Operational parameters

Besides material properties and system configurations discussed above, operational parameters are also among the influencing factors on segregation. In order to gain a deeper insight, related studies are reviewed in the following sub-sections under different categories based on the system type, namely hopper, chute, and other systems.

I. Hopper filling operations. Various hopper-related operational parameters, including filling method, filling angle, and filling position, have been studied in past studies. Several studies investigated the influence of various hopper filling methods, i.e., different components/sizes being charged in separate layers or in a pre-mixed state, on segregation after discharging the hopper [9, 42, 78, 89, 103]. Although Ketterhagen et al. [42], Yu and Saxén [9], and Chibwe et al. [78] used slightly different setups and filling patterns, their conclusion was that the initial filling method significantly affects the segregation.

Apart from the filling method, the filling position is found to significantly influence segregation. Wu et al. [74] investigated the effect of burden apex (i.e., the highest point on the hill formed when materials are charged into the hopper) on the segregation during the charging and discharging of a hopper. It was found that the burden apex mostly influences the particle size distribution during charging and it has little effect during discharging. In the case of a Paul-Wurth hopper, Zhang et al. [71] also observed that the filling position has a significant effect on the segregation, and there was strong segregation in the case of the right and left filling positions (cf. Figure 2.16(a)). Moreover, they observed that the filling angle closer to the vertical position (cf. Figure 2.16(b)) and a larger charging outlet (cf. Figure 2.16(c)) reduced the extent of segregation.

Cliff et al. [62] showed that a continuous filling operation, as opposed to batch processing, significantly reduces the amount of segregation because segregation mostly occurs in the last 25% of hopper discharge.

In conclusion, the filling method, filling position, and filling angle are significantly affecting segregation downstream (i.e., during discharging the hopper). This means that all the handling steps should be accurately modelled if a reliable assessment of segregation is to be achieved.

II. Chute operations. With respect to chute-related operational parameters, several studies have investigated the effect of chute angle (θ) [41, 54, 60, 68, 73, 75, 77, 88, 91, 143], tilting direction [97], rotating speed (ω) [73, 75, 77], fill level [44, 81], the number of chute rotations

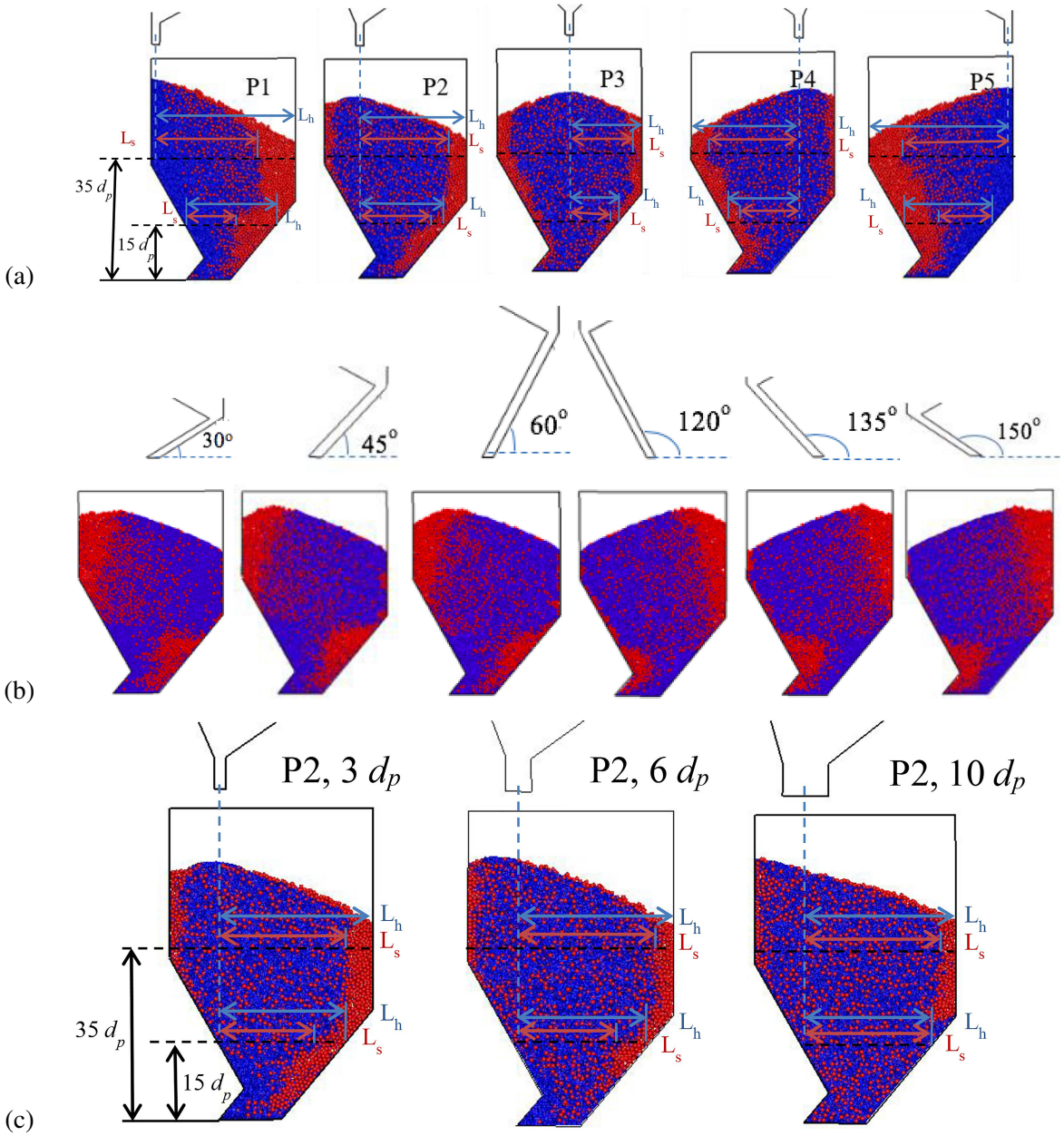

Figure 2.16 The effect of a) filling position, b) filling angle, and c) hopper outlet on segregation during charging a hopper. Reproduced with permission from Ref. [71]. Copyright 2021, Elsevier.

[90] and installing a damper [87]. Some of the parameters are schematically illustrated in Figure 2.17.

It should be noted that in a rotating chute, particles are subjected not only to gravitational forces but also to Coriolis and centrifugal forces [50]. The relative impact of inertial and Coriolis forces is quantified by the Rossby number

$$Ro = \frac{v_a}{2\omega L \cos\theta} \tag{2.3}$$

where v_a, ω, L, θ denote the flow velocity, chute rotation rate, chute length, and chute angle, respectively. In the case of $Ro \gg 1$, the effect of the rotation rate can be neglected. For instance, Shirsath et al. [50] varied the chute rotation rate from 4 to 16 rpm and observed Ro larger than

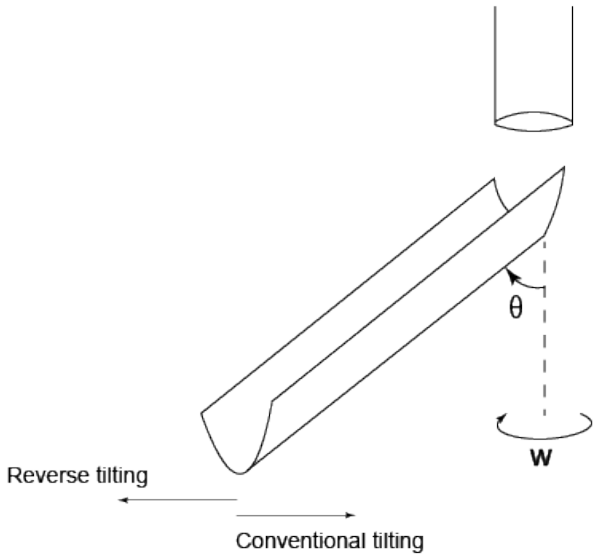

Figure 2.17 Schematic view of a rotating chute and related operational parameters. chute angle (θ), rotating speed (ω).

1, concluding that the flow was gravity driven. Also, the Froude number (Eq. 2.4) can be used to quantify the relative significance of the centrifugal force compared to the gravitational force [50]:

$$Fr = \frac{\omega^2 L \cos\theta}{g} \tag{2.4}$$

In the case of $Fr \ll 1$, the gravitational force is dominant, preventing the particles from escaping the chute.

The chute angle is an important flow control parameter, as it is used to increase or decrease the flow velocity (cf. Figure 2.17). Past DEM studies have investigated the effect of chute angle on the segregation occurring either inside the chute or when particles flow out and form a heap. Regarding the segregation happening inside the chute, Tripathi and Khakhar [41] observed that the shear rate and extent of segregation in a vertical direction increased with a lower angle. Similarly, Jing et al. [143] found that segregation occurs faster as the angle decreases, which was expected since the rate of acceleration increases as the chute is steeper. However, the final (converged) segregation degree was similar for different chute angles, and, surprisingly, the converged state was reached at approximately the same time for different angles.

For segregation occurring after discharging from chutes, several studies have found that reducing the chute angle intensifies the segregation in different systems, namely blast furnace throat [54, 68, 77, 88], feed bed of sintering machine [91], COREX melter gasifier [61, 73, 75]. However, Zhang et al. [54] varied the chute angle from 21ř to 37ř and observed that the radial segregation index (RSI) would not necessarily decrease (cf. Figure 2.18). Also, Kou et al. [73] observed that increasing the chute angle from 10ř to 30ř first leads to a decrease of the segregation of large particles and then to an increase.

In modern blast furnaces equipped with the Paul-Wurth bell-less top charging system, as well as in the COREX process, a rotating chute is used to distribute materials in the circumfer-

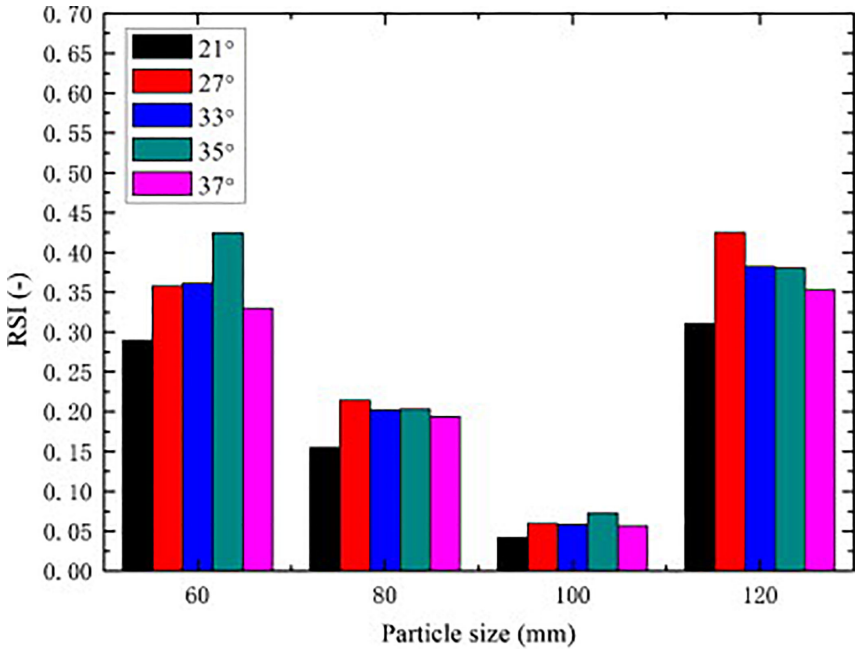

Figure 2.18 Change in radial segregation index (RSI) with different chute angles. Reproduced with permission from Ref. [54]. Copyright 2014, Elsevier.

ential directions of the furnace throat [7, 73]. In addition to the chute angle discussed above, rotating speed, tilting direction (i.e., changing the angle from low to high or vice versa as shown in Figure 2.17), and the number of rotations are other operational parameters that have been studied with respect to segregation. Terui et al. [97] modelled a mixture of coke and sinter, and two types of tilting directions, namely conventional tilting (i.e., from wall to center direction) and reverse tilting (i.e., from center to the wall direction). They found that with reverse tilting, coke particle are less segregated as shown in Figure 2.19. The rotating speed of the chute was found to have a negligible effect on segregation compared to the chute angle [73, 75, 77]. Mio et al. [90] observed that the increase in the number of chute rotations intensifies segregation, leading to a larger mean particle size near the center of the blast furnace.

The volume (or mass) flow rate through a chute is another operational parameter that is generally varied on an on-demand basis. For a given chute design, increasing/decreasing the flow rate results in a higher/lower fill level of the chute. Panda and Tan [44] found that the increase in the fill level causes the small and large particles to move together, i.e. decreases the velocity difference, resulting in lower segregation in the cross-stream and vertical directions of the chute. Although it was observed that the fill level does not affect velocities in a streamwise direction, segregation was decreased because of less available space for percolation due to denser packing. In a study on sinter cooler charging systems, Izard et al. [81] investigate the effect of the fill level of the chute (i.e., 20%, 50% and 90%) on the segregation pattern in the trolleys and found that while the filling ratio smaller than 50% impose an increasing size heterogeneity in the trolley, no change in the segregation pattern was observed for filling ratio larger than 50%.

In conclusion, the operational parameters for operating moving chutes, including chute angle, tilting direction, rotating speed, and fill level, affect the segregation to some extent. Based on the studies reviewed here, it appears that chute angle and fill level may be more significant than the other parameters. However, further research is needed to confirm this hypothesis and

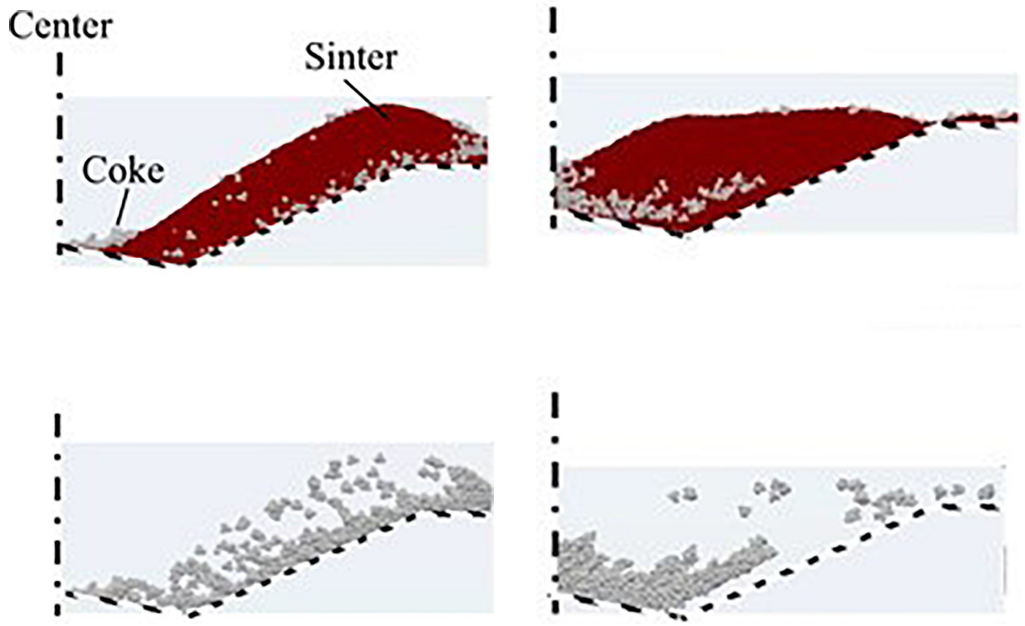

Figure 2.19 Cross-sectional view of radial distribution of coke-sinter mixture for a) reverse tilting and b) conventional tilting. Reproduced with permission from Ref. [97]. Copyright 2017, J-STAGE.

to better understand the complex nature of segregation in granular mixtures discharging from moving chutes. Nevertheless, all the parameters have the potential to be adjusted with the purpose of reducing or controlling segregation, although in practice, these adjustments might be constrained by space, time, cost, and technical limitations.

III. Other systems. In addition to hoppers and chutes, other operation-related factors have been investigated in the context of gravity-driven segregation of cohesionless materials. This includes the falling height in the stockpile [73, 144], the method of "discharge" from a v-blender (which is essentially a gravity-driven flow) [43], the burden surface shape of the COREX furnace (cf. Figure 2.20) [60], and feed rate as well as rill plate angle in an iron ore sinter strand [93]. Hence, in every industrial system, there are several operational parameters that can affect segregation. Detecting these parameters and studying their effect utilising DEM, can pave the way to optimise the industrial processes with respect to segregation. This is highly advantageous because, in industrial applications, it is not always possible to control segregation by modifying material properties and system configurations.

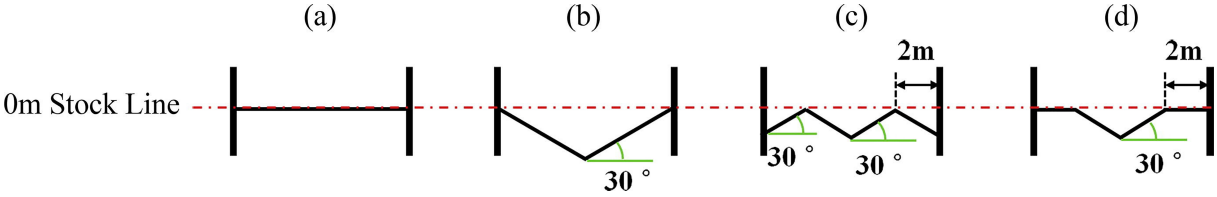

Figure 2.20 Different burden surface shape of the COREX furnace. Reproduced with permission from Ref. [60]. Copyright 2018, Elsevier.

2.5 Conclusion

This chapter presented an overview of the state-of-the-art in DEM modelling of segregation behaviour of complex multi-component mixtures in applications involving the gravity-driven flow of dry, cohesionless granular materials. The main findings of this review can be summarised as follows:

- Although most of the mixtures existing in nature and industrial settings are considered multicomponent (i.e., they contain particles differing simultaneously in size, density, and shape), very few studies have investigated the segregation behaviour of such mixtures.
- Despite the fact that calibration is an essential part of developing a reliable DEM model, most of the past studies have omitted it. This is especially true when it comes to models of multi-component mixtures. For instance, the effect of interaction parameters between components has not yet been studied in detail. Furthermore, it is not clear whether calibrated parameter values obtained for a certain mixture composition are applicable to other compositions as well.
- The effect of size distribution and particle shape on segregation has not yet been well understood. Considering the fact that including small particles and irregular particle shapes increases the computational time considerably, the effect of approximating real-world mixtures with a finite number of particle sizes and spherical particles should be comprehensively studied.
- When quantifying segregation experimentally, non-invasive techniques such as image analysis are generally more suitable than the conventional invasive methods (i.e., sampling and weighting) since they do not disturb the mixture structure and they are applicable to mixtures differing in both size and density. However, these techniques are inherently limited in their ability to characterise the internal state of granular beds.
- Results of the past DEM studies on segregation show that the effect of different parameters influencing segregation, i.e., materials properties, system configurations, and operational parameters, should be considered together since they are highly intertwined.
- Compared to material properties and system configurations, operational parameters are easier to modify. Hence, to reduce and control segregation in industrial applications, operational parameters are preferred.

The findings of this literature review emphasise the critical need for systematic calibration of DEM models, especially when modelling segregation in complex multi-component mixtures. As highlighted, interaction parameters between different particle types have rarely been examined comprehensively, leading to significant gaps in the understanding of multi-component segregation phenomena. To address these gaps, Chapter 3 investigates the relative importance of various DEM parameters through a systematic sensitivity analysis. Specifically, it identifies dominant parameters influencing segregation during hopper discharge, chute flow, and heap formation using a representative industrial mixture composed of iron ore pellets and sinter typically encountered in blast furnace operations.

Chapter 3

Sensitivity Analysis of DEM Parameters for Multi-Component Segregation*

In Chapter 2, the literature review highlighted significant gaps in the systematic calibration of DEM parameters, especially on the modelling of segregation in multi-component granular mixtures. In particular, the interaction parameters between different particle types have not been adequately studied, and conflicting findings have been reported regarding the significance of various particleparticle and particlegeometry interaction parameters. To address these shortcomings, this chapter provides a detailed sensitivity analysis aimed at identifying the dominant DEM parameters that influence segregation behaviour. A representative multi-component mixture of iron ore pellets and sinter, which is used in the blast furnace operations, is used to systematically evaluate the significance of DEM parameters across commonly used equipment in bulk handling. The sensitivity analysis covers hopper discharge, chute flow, and heap formation, all of which are relevant to the blast furnace charging system.

*This chapter is based on: A. Hadi, H. Shi, Y. Pang, D.L. Schott, *Identification of dominant DEM parameters for multi-component segregation during heap formation, hopper discharge and chute flow*, *Powder Technology* (2024). https://doi.org/10.1016/j.powtec.2024.119985

3.1 Introduction

As mentioned in previous chapters, with the development of computational power in the last decades, DEM [14] has become a widely used approach to simulate granular materials. DEM involves iteration over several time steps, within each, Newtons second law of motion is used to update particle trajectories, while contact models are used to compute forces due to inter-particle and particle-geometry interactions. DEM offers significant advantages over experiments for investigating the segregation, as it not only allows the modelling of mixtures of particles with any combination of size, density and shape but also provides detailed particle-level information that is hardly acquirable in experiments.

Although DEM is extensively used, there are still various challenges to be solved, mainly related to computational efficiency (i.e. feasibility) and model accuracy (i.e. reliability) [12]. Achieving a balance between computational efficiency and model accuracy requires making trade-offs between conflicting interests, i.e. feasibility and reliability. Several solutions, such as reducing particle stiffness [39] and employing upscaled particles [36, 37], have been proposed to enhance the computational efficiency of DEM. However, the reliability of the developed model heavily depends on the proper determination (calibration) of the input parameters of the modified particles. This process can be time-consuming, particularly in complex multi-component mixtures with a high number of parameters. To tackle this issue, the calibration can be focused on only the "significant" parameters. Several previous researchers have attempted to identify the most significant parameters for segregation [9, 42, 52, 80]. However, these studies have several shortcomings. Firstly, they primarily investigated size segregation, and the dominating parameters for component segregation are missing. Secondly, none of these studies has included all DEM interaction parameters, i.e., both particle-particle and particle-geometry interactions, thus the true/relative significance of these parameters remains unknown. Thirdly, segregation is only studied in a single geometry, while its behaviour can vary during different stages/geometries in a full process. Lastly, conflicting findings regarding the significance of certain DEM parameters have been reported in some cases [9, 42]. To address these gaps, a comprehensive sensitivity analysis is performed in this study to gain deeper insights into the significant DEM parameters influencing multi-component segregation in various geometries, including hopper discharge, chute flow, and heap formationrepresenting typical burden charging processes in the blast furnace. This is demonstrated for a mixture of iron ore pellets and sinter, which are charged into the blast furnace as ferrous burden, with a focus on interaction parameters such as sliding and rolling friction. A sensitivity study is also conducted for various initial configurations of pellets and sinter to identify the dominant parameters across different hopper filling configurations. Furthermore, the study is extended to investigate the effects of several factorsnamely, the shape of sinter particles and the mass ratio of pellets to sinteron the segregation observed at different locations, including after the hopper, after the chute, and in the heap.

This chapter is structured as follows. In Section 3.2, an in-depth explanation of the DEM model employed is provided, detailing the simulated materials and their fixed DEM parameters, as well as the setups used for investigating segregation. Section 3.3 describes the design of experiments (DoE) employed in this study. The varied DEM parameters in the DoE, aimed at identifying the dominant ones, are discussed, along with the key performance indicators (KPIs) that are quantified and employed as responses in the DoE. In Section 3.4, the findings regarding the dominant DEM parameters for segregation, as well as the effect of certain factors (i.e.,

the shape of sinter particles and the mass ratio of pellets to sinter) on segregation occurring at different locations, are presented. Finally, in Section 3.5, the main findings and further work are concluded.

3.2 Materials and methods

3.2.1 Discrete Element Method

The DEM model employs the Hertz-Mindlin (no-slip) [29] contact model with an elastic-plastic spring-dashpot rolling friction model (type C according to Ai et al. [145]) that has been successfully applied in previous studies modelling iron ore pellets and sinter [146, 147]. Figure 3.1 provides a schematic representation of the interaction forces between two particles in DEM. For detailed equations and further information on the contact model, readers are referred to the relevant literature [29, 106, 145, 146]. The commercial software EDEM version 2022.3 was used to develop the DEM model, and all simulations were conducted on the DelftBlue high-performance cluster [148]

3.2.2 Simulation configuration

I. Materials and fixed DEM parameters. A mixture of iron ore pellets and sinter is simulated (cf. Figure 3.2), which serves as a good example of a real-world multi-component mixture charged into the blast furnace. For modelling pellets and sinter in DEM, fixed parameter values for intrinsic material properties (Table 3.1) as well as for morphological parameters, including particle shape and particle size distribution, were used. Particle densities for pellets and sinter

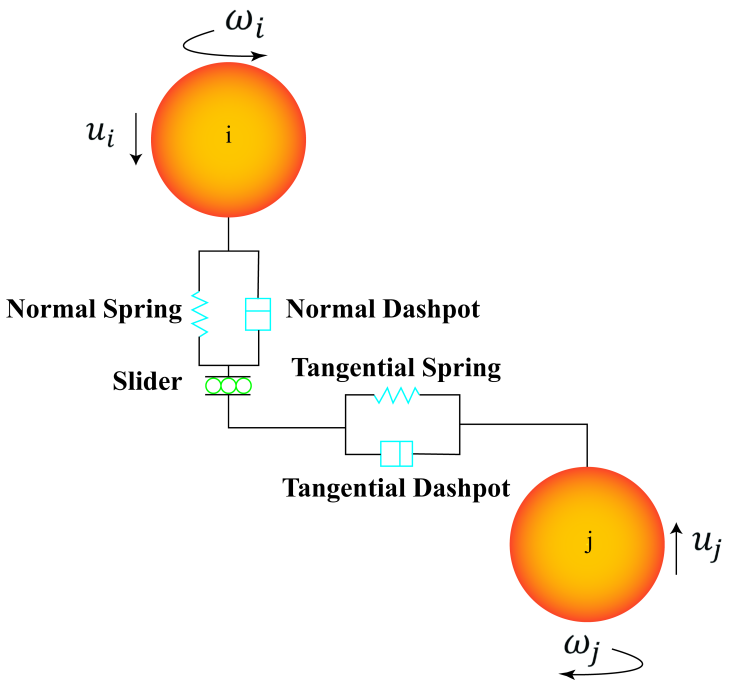

Figure 3.1 A schematic definition of interaction forces between two particles in DEM.

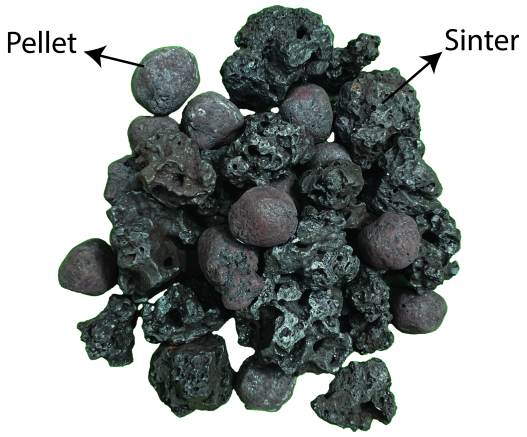

Figure 3.2 A mixture of pellets and sinter.

Table 3.1 Intrinsic material properties used in DEM simulations.

DEM Parameter	Pellet	Sinter	Geometry
Shear modulus (G)	1×10^8 Pa [147]	1×10^8 Pa [147]	2×10^{11} Pa [150]
Poissons ratio (ν)	0.25 [147]	0.25 [147]	0.3 [150]
Solid density (ρ_s)	1951 (kg/m^3)	1731 (kg/m^3)	7800 (kg/m^3) [150]

were calibrated against their bulk densities in previous work [149]. Moreover, particle size distribution was measured using sieves in the same work, as illustrated in Figure 3.3.

For particle shape, spheres are well-suited for pellets since they are nearly spherical. However, sinter particles are highly irregular in shape (cf. Figure 3.2), requiring a non-spherical representation for segregation modelling [96]. Here, a clumped sphere approach is adopted to represent the irregular shape of sinter particles. As increasing the number of spheres in the clumped sphere significantly increases the computational time, a three-sphere clumped particle is chosen as shown in Figure 3.4, which has yielded good results in previous sinter studies [81, 147]. A detailed overview of all DEM input parameters can be found in Table B.1 in Appendix B.

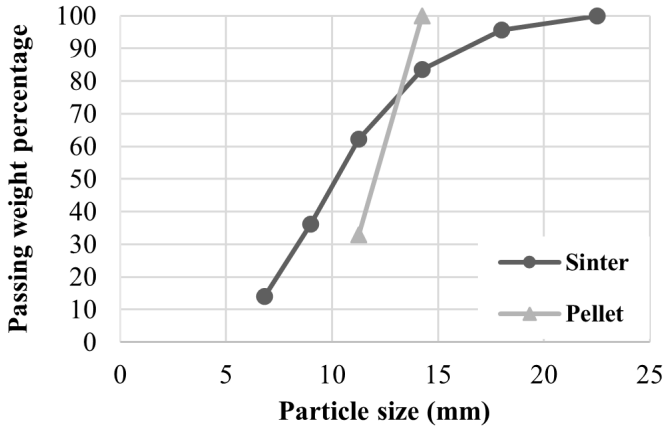

Figure 3.3 Particle size distribution (PSD) for pellets and sinter [149].

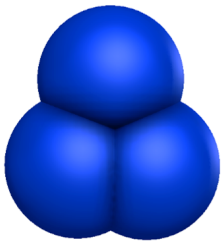

Figure 3.4 The clumped spheres model used to simulate sinter particles.

II. System and geometry. A set of geometries is employed, which consists of a hopper, a chute, and a receiving bin to investigate and quantify the segregation at various stages (i.e., after hopper discharge, after chute flow, and during heap formation) within a single system. Figure 3.5(a) schematically illustrates the geometries and their dimensions. Additionally, three cylindrical sampling locations (SLs) were created right after the hopper and chute, as well as around the heap to measure segregation, as shown in Figure 3.5(b).

The initial mixture of pellets and sinter is generated within the hopper with an equal mass ratio of 50%-50%. To examine the effect of different initial configurations of pellets and sinter, various initialisations within the hopper were used, as shown in Figure 3.6(a)-(c). Notably, the difference between L1 (cf. Figure 3.6(a)) and L2 (cf. Figure 3.6(b)) lies in the order of

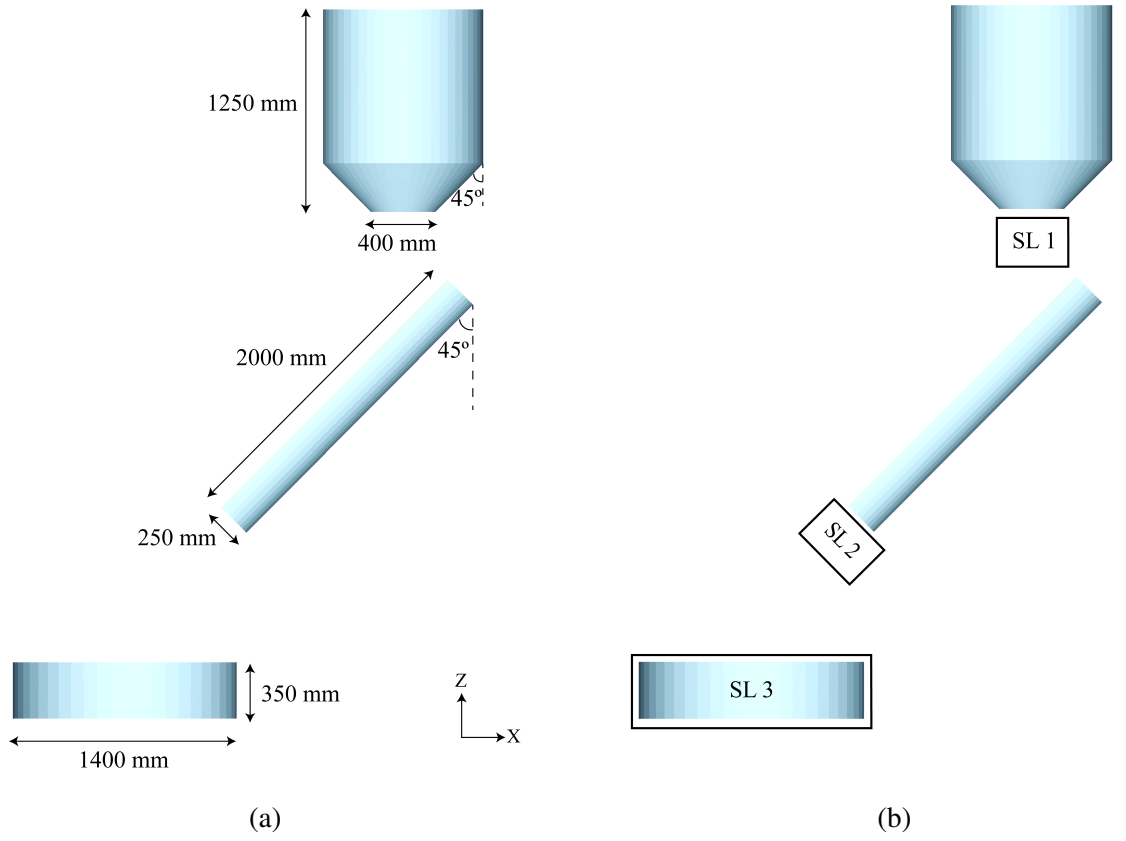

Figure 3.5 a) The geometries used in the simulations and their dimensions, and b) cylindrical sampling locations (SLs) used to quantify segregation.

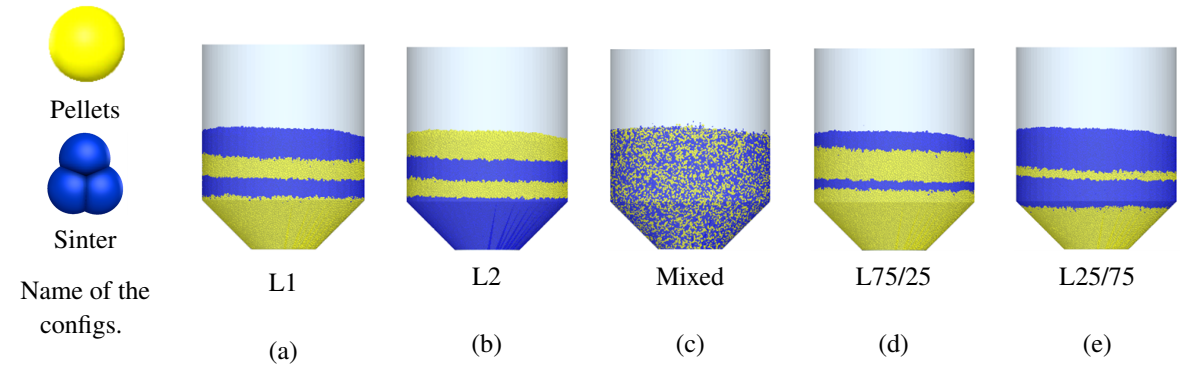

Figure 3.6 Various hopper filling configurations used in the simulations (yellow and blue particles represent pellets and sinter, respectively).

pellets and sinter layers. Moreover, to study the impact of the mass ratio, two additional cases were defined with the pellets-to-sinter mass ratios of 75%-25% and 25%-75%, as illustrated in Figure 3.6(d) and Figure 3.6(e), respectively.

Following the generation of the mixture within the hopper, the hopper outlet was opened, allowing the materials to discharge under the influence of gravity, as shown in Figure 3.7(a). It is important to note that the hopper's geometry was designed in a way to ensure a consistent core flow under all circumstances, to have a mixed flow. Subsequently, these materials were charged into the receiving bin via a chute featuring a semi-circular intersection to form a heap. Figure 3.7(b) provides a side view example of the heap formed in the receiving bin.

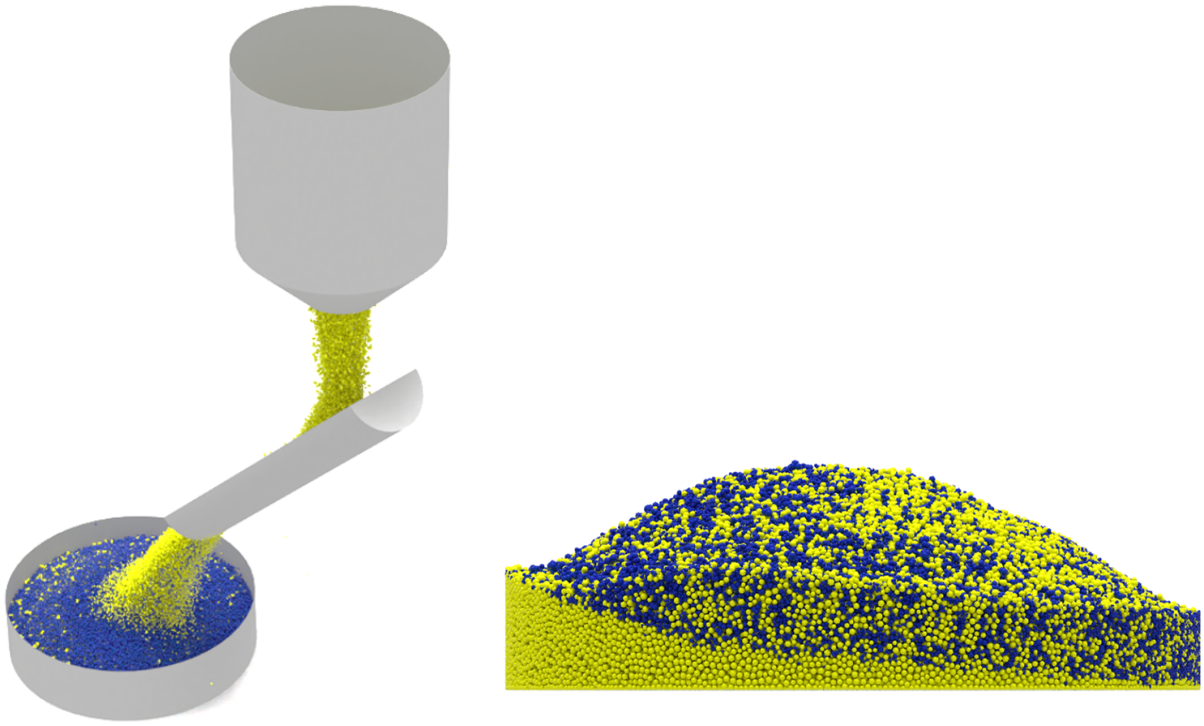

Figure 3.7 a) Materials flowing from the hopper to the receiving bin through the chute, b) an example of the heap formed in the receiving bin.

3.3 Design of experiment (DoE)

DoE is employed to efficiently explore the relationship between certain input variables and one or more outputs (or responses). Screening designs, a subset of DoE are helpful in identifying the most significant variables for a given response. Three main types of screening designs are frequently used: fractional factorial [151, 152], Plackett-Burman (PB) [153, 154], and definitive screening design (DSD) [98, 155, 156]. In this study, the definitive screening design was chosen due to its requirement for a relatively small number of runs. The DSD was designed using JMPő 17 Pro software (SAS Institute, USA).

3.3.1 Definitive screening design

The DSD, a novel three-level design introduced by Jones and Nachtsheim [157], was employed in this study. DSD can detect not only the main effects but also two-factor and quadratic terms. DSD offers an advantage over the PB design in that main effects are not confounded with two-factor interactions, two-factor interactions are not fully confounded with each other, and quadratic effects are not confounded with other two-factor interactions [98]. The number of runs required for k variables is $2k+1$ for even k and $2k+3$ for odd k. Moreover, Jones and Nachtsheim [158] recommended adding four extra runs to enhance the power of the design. Upon conducting the DSD, the p-values of the variables are determined through fitting a model. These p-values reflect the validity of the null hypothesis, which assumes no effect of the variables on the response. In other words, a lower p-value indicates a greater likelihood that the corresponding variable has a significant effect on the response. Therefore, variables with p-values less than a pre-defined threshold can be considered statistically significant.

3.3.2 Investigated parameters and levels

The parameters investigated in this study include all the interaction parameters for particle-particle and particle-geometry contacts. Table 3.2 provides a list of these parameters (15 in total) along with their corresponding low and high levels. The low and high levels were selected based on a thorough review of the relevant literature, and the middle level (0) was defined as the average between the low and high values. In the absence of literature on pellet-sinter interaction, the low and high levels for pellet-sinter interactions were established using the minimum and maximum values obtained from pellet and sinter interactions, which are underlined in Table 3.2. In this study, where 15 parameters are investigated, 37 runs are required by the DSD, as outlined in Table B.2 in Appendix B. Three repetitions of the simulations were conducted to account for the variability arising from the stochastic nature of DEM.

3.3.3 Quantifying segregation

I. Segregation after hopper discharge (KPI 1) and chute flow (KPI 2). The segregation of pellets and sinter after the hopper discharge (KPI 1) and after chute flow (KPI 2) are a function of time. To resemble the stop-start sampling method used by Standish and Kilic [119], two cylindrical sampling spaces located right after the hopper (SL1) and chute (SL2) were used (cf.

Table 3.2 Investigated DEM parameters using the definitive screening design with their low, middle and high values. (μ_s = coefficient of sliding friction, μ_r = coefficient of rolling friction, C_r = coefficient of restitution. The underlined values for pellet-pellet and sinter-sinter parameters are used for pellet-sinter interactions.)

Factor		Low level (-1)	Middle level (0)	High level (+1)
Pellet–pellet	$\mu_{s,pp}$	0.21 [63]	0.455	0.7 [159]
	$\mu_{r,pp}$	0.05 [72]	0.145	0.24 [150]
	$C_{r,pp}$	0.3 [160]	0.5	0.7 [9]
Sinter–sinter	$\mu_{s,ss}$	0.43 [87]	0.595	0.76 [150]
	$\mu_{r,ss}$	0.08 [147]	0.23	0.38 [150]
	$C_{r,ss}$	0.01 [161]	0.18	0.35 [150]
Pellet–sinter	$\mu_{s,ps}$	0.21	0.485	0.76
	$\mu_{r,ps}$	0.05	0.215	0.38
	$C_{r,ps}$	0.01	0.355	0.7
Pellet–geometry	$\mu_{s,pg}$	0.31 [160]	0.405	0.5 [162]
	$\mu_{r,pg}$	0.05 [160]	0.2	0.35 [159]
	$C_{r,pg}$	0.2 [9]	0.41	0.62 [150]
Sinter–geometry	$\mu_{s,sg}$	0.38 [146]	0.64	0.9 [81]
	$\mu_{r,sg}$	0.08 [147]	0.14	0.2 [146]
	$C_{r,sg}$	0.05 [81]	0.275	0.5 [161]

Figure 3.5(b)). The mass of the pellets (W_p) and sinter (W_s) within the sample space was then measured every 0.2 seconds. The segregation index (SI) was then defined as

$$SI = \frac{|\chi_p - \chi_0|}{|\chi_{\max} - \chi_0|} \tag{3.1}$$

where $\chi_p = W_p/(W_p + W_s)$ is the instantaneous mass ratio of pellets within the sample, χ_0 is the initial mass ratio of pellets in the hopper, and $\chi_{\max}$ is the maximum mass ratio possible which is always equal to 1. Figure 3.8 presents a typical example of SI over time. To minimise the error, the mass ratio measurements were restricted to instances when the total mass within the sampling space exceeded 2% of the full state, i.e., to determine t_{min} and t_{max}. Then the time values were normalised using

$$\hat{t}_i = \frac{t_i - t_{\min}}{t_{\max} - t_{\min}} \tag{3.2}$$

where t_i and $\hat{t}_i$ are the instantaneous time and its corresponding normalised time, respectively. Finally, the mean value of the SIs across the normalised time was calculated as

$$\overline{SI} = \frac{\sum_{i=1}^{n} SI_i}{n} \tag{3.3}$$

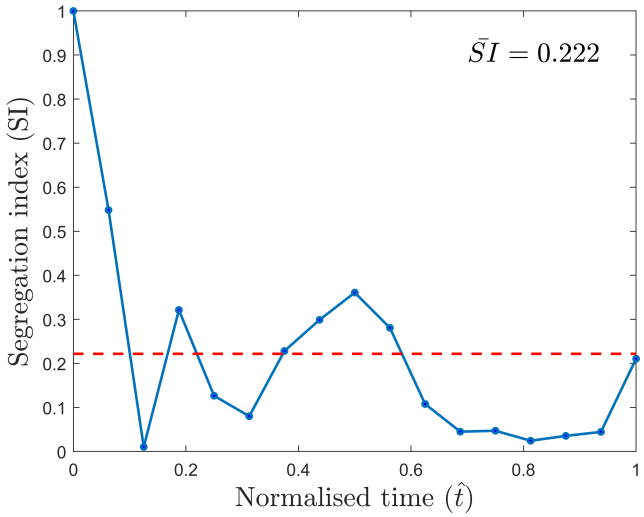

Figure 3.8 An example of the segregation index as a function of the normalised time (run 36 with L1 initial configuration). The red dashed line indicates "SI bar".

where n is the number of data points in Figure 3.8 , SI_i is segregation index at ith normalised time (i.e. at $\hat{t}_i = (i-1) \times ((t_{\max} - t_{\min})/n)$). $\overline{SI}$, which is denoted as the red dashed line in Figure 3.8, was used to quantify KPI 1 and KPI 2.

II. Segregation in the heap (KPI 3). Unlike KPI 1 and KPI 2, which involved segregation over a period of time, KPI 3 is measured in a static heap (SL3) at the end of the simulations using the relative standard deviation (RSD). This grid-dependent index is determined by initially defining a grid system to partition the heap into a specified number of bins, denoted as m. Within each bin, the mass ratio of one component, such as pellets (C_{p_m}) is measured. Afterwards, the standard deviation (σ) and mean (μ) of C_{p_m}s are computed, and finally, RSD is calculated using

$$RSD = \frac{\sigma}{\mu} \tag{3.4}$$

Segregation in the heap can occur in different directions, i.e., radial, vertical, circumferential, as well as throughout the whole volume. Therefore, KPI 3 was assessed by employing four distinct grid systems: radial, vertical, circumferential, and cubic grids, as illustrated in Figure 3.9(a)-(d), respectively.

3.4 Results and discussion

The results are presented and discussed in two sub-sections. In Section 3.4.1, the findings regarding the dominant DEM parameters for each KPI are highlighted. In Section 3.4.2, the focus is shifted to the effect of several factors, including sinter particle shape, layering mode, and pellets-sinter mass ratio, on the KPIs. Finally, a summary of the findings of this study is presented in Section 3.4.3.

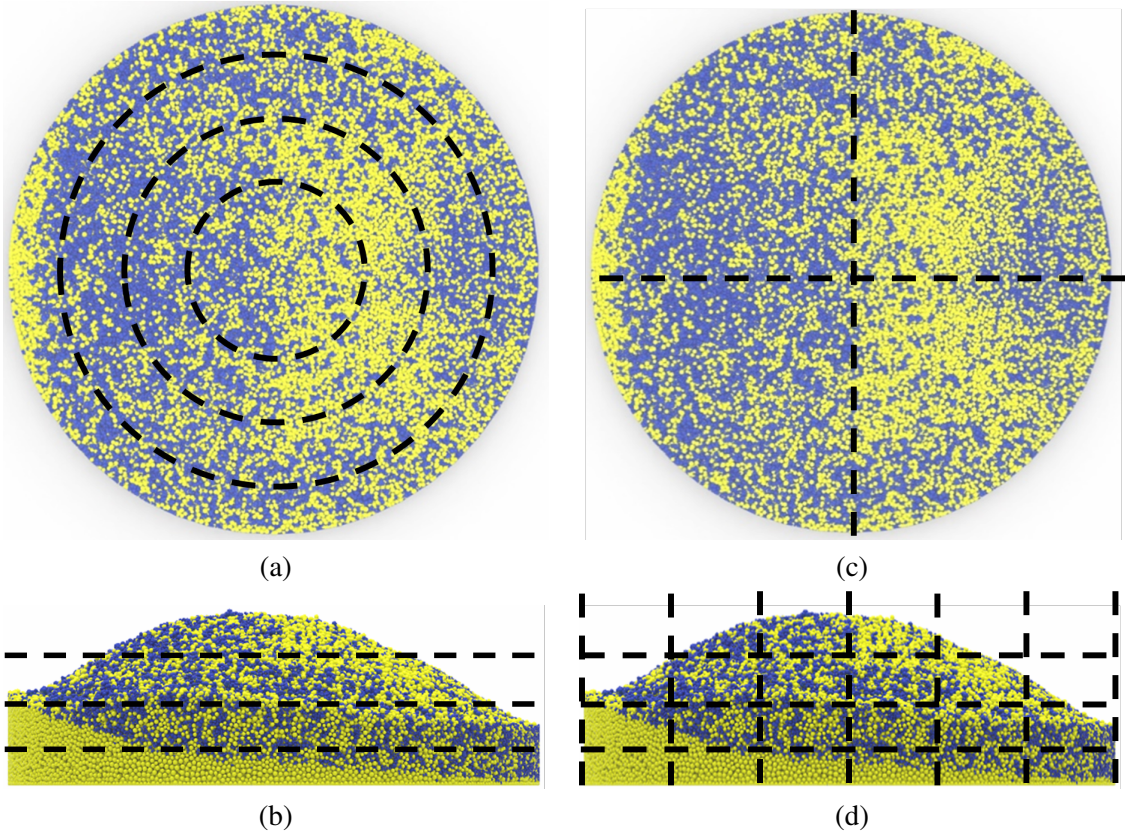

Figure 3.9 Different grid systems to measure the segregation within the heap, a) radial, b) vertical, c) circumferential, and d) cubic.

3.4.1 Identification of dominant DEM parameters

Several steps were followed to identify the dominant parameters for each KPI (refer to Section 3.3.3). Firstly, all the necessary simulations with the specified parameters, as outlined in Table B.2 in Appendix B, were conducted. Secondly, the data were processed and the values for each KPI were computed. Thirdly, the "fit definitive screening" platform in JMPő Pro was utilised to perform the design of experiments (DoE). In the JMP Pro software, the stepwise regression method with a p-value threshold of 0.01 was employed. Finally, an analysis of variance (ANOVA) was conducted to determine the p-values of the significant parameters, and the variables with p-values lower than 0.01 were considered statistically significant. The findings for each KPI are presented in the following paragraphs.

I. Segregation after hopper discharge (KPI 1). Table 3.3 displays the p-values derived from ANOVA analysis of the DSD for KPI 1. Two key observations arise from Table 3.3. Firstly, there are no significant DEM interaction parameters for the mixed initial configuration. Secondly, for all other initial configurations, pellet-geometry and/or sinter-geometry interaction parameters are dominant.

The first observation is elaborated on as follows. As mentioned in Section 3.3.2, 37 simulations were conducted (cf. Table B.2 in Appendix B) with three repetitions to account for the stochastic nature of DEM. The stochastic nature of DEMresulting from variations in the generated particles positions and orientationscan lead to different degrees of mixing within the

Table 3.3 p-values for the effect of DEM interaction parameters on KPI 1 for various hopper filling configurations, with the effect of each significant parameter on KPI 1 in parentheses (e.g., "(+)" denotes that with an increase in the parameter value, KPI 1 increases). "x" means insignificant effect.

Factor	Mixed	L1	L2	L75/25	L25/75
Pellet-pellet (P–P)					
$\mu_{s,pp}$	x	x	x	x	x
$\mu_{r,pp}$	x	x	x	x	x
$C_{r,pp}$	x	x	x	x	x
Sinter-sinter (S–S)					
$\mu_{s,ss}$	x	x	x	x	x
$\mu_{r,ss}$	x	x	<0.0001 (+)	x	x
$C_{r,ss}$	x	x	x	x	x
Pellet-sinter (P–S)					
$\mu_{s,ps}$	x	x	x	x	x
$\mu_{r,ps}$	x	x	x	x	x
$C_{r,ps}$	x	x	x	x	x
Pellet-geometry (P–G)					
$\mu_{s,pg}$	x	<0.0001 (+)	x	<0.0001 (+)	0.0003 (–)
$\mu_{r,pg}$	x	<0.0001 (+)	x	<0.0001 (+)	<0.0001 (–)
$C_{r,pg}$	x	x	x	x	x
Sinter-geometry (S–G)					
$\mu_{s,sg}$	x	x	<0.0001 (+)	x	0.005 (–)
$\mu_{r,sg}$	x	x	x	x	x
$C_{r,sg}$	x	x	x	x	x

hopper, which may significantly influence the subsequent segregation [42, 78]. Therefore, the variation in ($\bar{SI}$) across the runs may primarily be attributed to random degrees of mixing within the hopper rather than to variations in DEM parameters. To quantitatively assess this, a comparison was made between the standard deviation resulting from the three repetitions and the standard deviation of the mean ($\bar{SI}$) values for the 37 runs. This comparison was carried out using

$$\alpha = \frac{\sigma(\mu(\overline{SI}))}{\overline{\sigma}_{\text{reps}}} \tag{3.5}$$

where $\sigma(\mu(\overline{SI}))$ is the standard deviation of the mean $\overline{SI}$s (i.e., mean segregation index calculated using Eq. 3.3) across 37 runs, and $\overline{\sigma}_{\text{reps}}$ represents the average of standard deviation resulting from the three repetitions for each run. If the value of α approaches 1.0, it indicates that alterations in $\overline{SI}$ across the runs primarily stem from the random degree of mixing within the hopper and not from varying the DEM parameters. Figure 3.10 illustrates the coefficient α corresponding to various initial configurations for KPI 1. As expected, the value of α for the mixed configuration is close to 1.0 and is significantly lower than the value for other initial con-

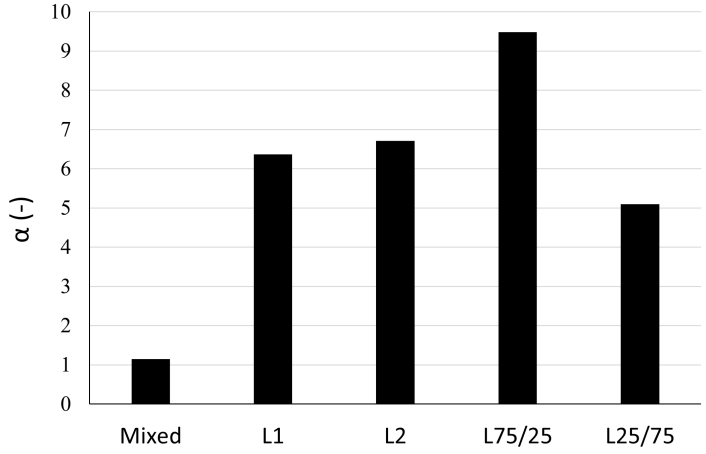

Figure 3.10 The value of α (cf. Eq. 3.5) for the initial configurations presented in Figure 3.6.

figurations. Additionally, the sheer amount of segregation occurring for the mixed configuration is negligible (i.e. $\overline{SI} \leq 0.014$).

The second observation is that, based on the p-values, KPI 1 is predominantly influenced by particle-geometry interaction parameters. However, as mentioned earlier, the p-value only addresses the validity of the null hypothesis (i.e., the assumption of no effect of the variables) rather than directly showing the parameters' significance [163]. To validate these findings, the statistical analysis was complemented with physics-based interpretations through a supplementary contact data analysis. This involved extracting the average contact force for each contact type (e.g., the pellet-geometry contact) by dividing the aggregate contact force by the total number of contacts of that specific type at each time step within the hopper. Average contact force was chosen as the metric because the segregation of the two components arises from differences in their velocities, which, in turn, result from varying forces acting on them in the DEM simulation. This systematic approach facilitates the identification of the relative contributions of individual contact types to the dynamics of the flow, allowing us to assign significance based on their respective contributions.

Figure 3.11 presents the average contact force for two significant contact types based on Table 3.3, i.e., pellet-geometry and sinter-geometry interactions, across various initial configurations (cf. Figure 3.6). It is noted that using clumped spheres for sinter particles allows for multiple simultaneous contacts with the geometry, leading to lower absolute normalised force values for sinter-geometry compared to pellet-geometry contacts, as reflected in Figure 3.11. The mixed configuration was also included for the sake of comparison.

Figure 3.11(a) shows that the average pellet-geometry (P-G) contact force for L2 initial configurations is lower compared to other configurations. This confirms the ANOVA analysis findings in Table 3.3, highlighting the dominance of pellet-geometry (P-G) interaction parameters across all initial configurations except for L2. This exception can be attributed to the different layering composition of L2, where the bottom layer, which has extensive contact with the bottom part of the hopper, primarily consists of sinter particles. Similarly, regarding sinter-geometry interaction, Figure 3.11(b) shows that the average S-G contact force for the configurations L2 is higher than the rest, consistent with the p-values in Table 3.3. However, for L25/75, the average contact force is lower than the mixed configuration, indicating a reduced

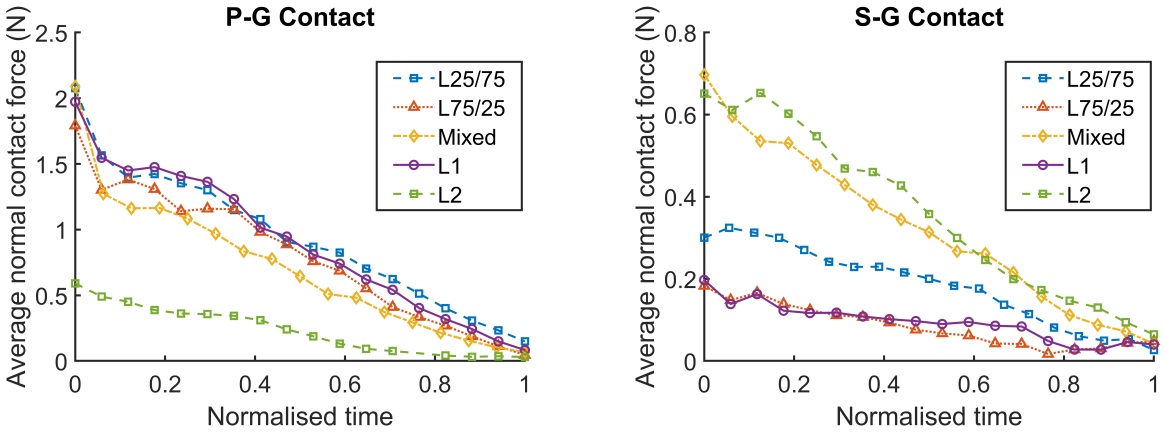

Figure 3.11 Average contact force within the hopper for different types of contact in various initial configurations (P-G: pellet-geometry/ S-G: sinter-geometry).

significance of sinter-geometry interaction parameters. This observation is also reflected in Table 3.3, where S-G interaction parameters exhibit the highest p-value. Overall, this supporting observation confirms that the results of the ANOVA analysis are also valid from physics-based observations.

By comparing the p-values in Table 3.3 between various cases, further conclusions are drawn regarding the impact of layering mode and mass ratio on the dominant parameters. With respect to the layering mode, it is deduced that the interaction parameters between the particles at the bottommost layer and the hopper play the key role. In other words, in L2, where the bottom particles consist of sinter, sinter-geometry interactions dominate, whereas in the L1 case, pellet-geometry interactions are significant. These conclusions are also reflected in Figure 3.11(a), where the average pellet-geometry contact force in L1 is higher than in L2, while the opposite trend is observed for the sinter-geometry contact force in Figure 3.11(b).

When comparing the L1, L75/25, and L25/75, it is noted that the effect of the pellet-sinter mass ratio is twofold. Firstly, it influences the dominant parameters, e.g., by increasing the sinter mass ratio to 0.75 (i.e., L25/75), the sinter-geometry coefficient of static friction becomes significant. This is because, in this case, as shown in Figure 3.11(b), the average sinter-geometry contact force, in L25/75 is significantly higher compared to both L1 and L75/25 configurations. Secondly, while in L25/75, an increase in the pellet-geometry coefficients of rolling and static friction ($\mu_{r,pg}$ and $\mu_{s,pg}$) leads to a reduction in segregation after hopper discharge, this is reversed in all other initial configurations.

II. Segregation after chute flow (KPI 2). Before continuing with KPI 2, a comparison was first made between the segregation occurring after the hopper discharge (KPI 1) and following the chute flow (KPI 2) to assess whether significant segregation takes place in between, i.e., on the chute itself. To quantitatively evaluate the similarity between KPI 1 and KPI 2, the coefficient of correlation (R) of the segregation indices (SIs) for each run between KPI 1 and KPI 2 was calculated using

$$R = \frac{1}{N-1} \sum_{i=1}^{N} \left(\frac{SI_i^1 - \overline{SI^1}}{\sigma_{SI^1}} \right) \left(\frac{SI_i^2 - \overline{SI^2}}{\sigma_{SI^2}} \right) \tag{3.6}$$

where SI_i^1 and SI_i^2 denote the segregation indices (SIs) at ith normalised time (i.e., at $\hat{t}_i = (i-1) \times ((t_{\max} - t_{\min})/n)$) in the plots of KPI 1 and KPI 2 (cf. Figure 3.8), respectively. Figure 3.12(a) presents the correlation coefficients for all initial configurations across all runs. Here, the mixed initial configuration was excluded for the same reasons mentioned before. It shows that for most runs, the correlation coefficient is higher than 0.7, indicating a strong correlation between KPI 1 and KPI 2 [164]. To further confirm this strong correlation, KPI 2 was plotted against KPI 1, as shown in Figure 3.12(b). Notably, most of the runs align closely with the line of equality, indicating a robust linear correlation between KPI 2 and KPI 1.

To examine differences between KPI 1 and KPI 2 for the runs with low correlation coefficients as well as the runs falling below the line of equality in Figure 3.12(b) (e.g. a group of blue triangles), the plots for run 19 are compared with the L2 initial configuration, which has the lowest correlation coefficient (~ 0.4) in Figure 3.12(a). The segregation plots for KPI 1 and KPI 2 are displayed in Figure 3.13. It demonstrates that, despite a low correlation coefficient, the plots are qualitatively and quantitatively similar. The main discrepancy is observed only at the first normalised time, when pellets and sinter are mixed on the chute, leading to a lower SI for KPI 2 at time zero. Hence, it is concluded that, for the setup and materials being studied in the present work, no significant segregation happens on the chute itself. It should be noted that this conclusion is valid within the scope of this study. For instance, significant segregation might occur on the chute if it is sufficiently long, as demonstrated in previous studies [10, 54, 72]. As a result, within the scope of this study, the substantiated assumption is adopted that the dominant DEM parameters influencing KPI 1 also have a significant influence on KPI 2.

III. Segregation in the heap (KPI 3). In this section, the dominant factors influencing heap segregation are explored. As outlined in Section 3.3.3, segregation within the heap is assessed across various directions, namely radial, vertical, and circumferential ones. To identify the most pronounced direction of segregation, a comparative analysis of RSD across all 37 runs was conducted. Figure 3.14 presents this comparison for both mixed and L1 configurations in the hopper, revealing a considerably higher degree of segregation in the radial direction compared to the vertical and circumferential directions for both configurations. Therefore, primary emphasis is placed on explaining the key parameters influencing segregation in the radial direction. Throughout the remainder of the chapter, the radial segregation is referred to as KPI 3.

Table 3.4 presents the p-values resulting from ANOVA analysis of DSD for radial segregation for all initial configurations within the hopper, together with their effect on KPI 3. To better understand these results, it is essential to consider that heap segregation measured at the end of the simulation arises from three main occurrences: 1) segregation present before materials are loaded into the bin (SL3), 2) segregation occurring at the start of material charging into the bin due to particle-geometry interactions, and 3) segregation during heap formation, primarily influenced by particle-particle interactions. Given that the first two occurrences are mainly influenced by particle-geometry interactions, it is anticipated that particle-geometry parameters are dominant for KPI 3. This is reflected in Table 3.4, where particle-geometry interactions

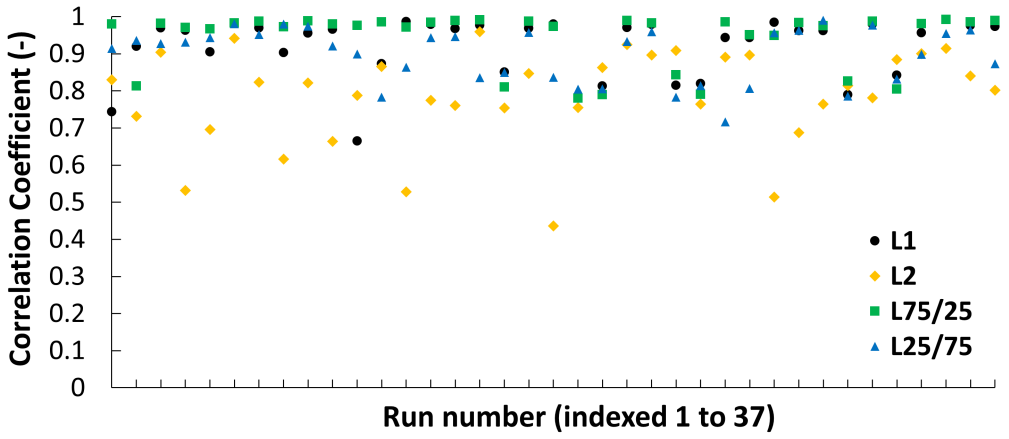

(a)

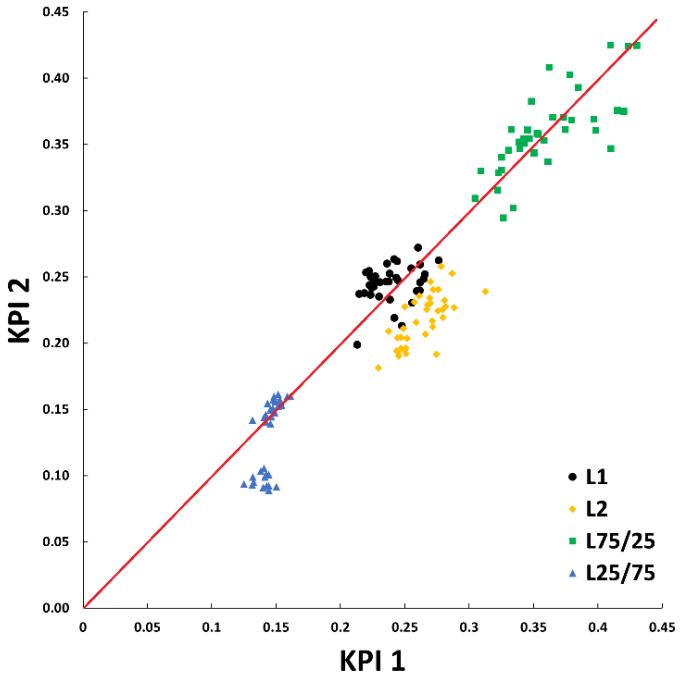

(b)

Figure 3.12 a) Correlation coefficients between KPI 1 and KPI 2 (i.e. segregation after the hopper and after chute flow, respectively) for all initial configurations across all runs (Run numbers are indexed 137; x-axis values are omitted for clarity.), and b) The relationship between KPI 2 and KPI 1 (red line represents the line of equality).

were found to be significant for all configurations. Additionally, particle-particle interaction parameters are also expected to be influential due to the third occurrence, where most interactions happen between particles, which is also reflected in Table 3.4.

Similar to KPI 1, an attempt is made to support the statistical findings regarding the significance of the parameters. To achieve this, the average normal contact force within the heap for significant interaction parameters (based on Table 3.4) during the formation of the pile for all initial configurations is illustrated in Figure 3.15. To facilitate a comparison, pellet-pellet interactions are considered as an example. As indicated in Table 3.4, pellet-pellet interaction parameters were found to be significant for all cases except for L25/75. This observation is also reflected in Figure 3.15(a), where L25/75 exhibits the lowest average normal contact force for P-

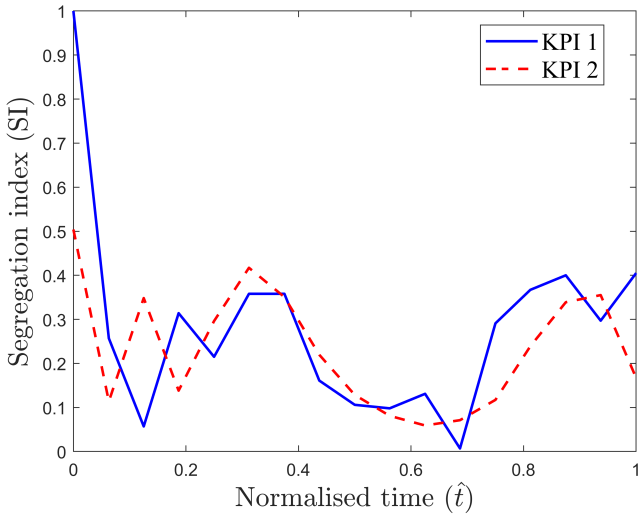

Figure 3.13 Comparison of segregation plots of KPI 1 and KPI 2 (i.e. segregation after the hopper and after chute flow, respectively) for the run with the lowest found correlation 0.40 (run 19 with L2 hopper filling configuration).

P interactions. A similar trend is observed for sinter-sinter interaction, where in Figure 3.15(b), L2 displays the lowest average normal contact force, which aligns with the higher p-value in Table 3.4 compared to other cases. Hence, this supports the results of the conducted statistical analysis.

In addition to the dominant parameters, extra insights into the influence of various factors on the dominance of segregation parameters can be derived through a detailed analysis of Table 3.4. These factors include pellet-sinter interaction parameters, pellet-sinter mass ratio, coefficient of restitution, and sinters rolling friction. These findings will be discussed in the following paragraphs.

Effect of pellet-sinter interaction parameters

Based on Table 3.4, the impact of the pellet-sinter interaction on radial segregation is statistically insignificant. While previous research has shown the negligible influence of pellet-sinter interaction parameters on the angle of repose [147], there exists a scarcity of studies examining their effects on segregation. To validate this observation, additional simulations were conducted, focusing on the comparison of pellet-sinter interactions with influential parameters (cf. Table 3.4) such as the sinter-sinter (S-S) coefficient of static friction and the pellet-pellet (P-P) coefficient of rolling friction. Run 9 with the L1 configuration was chosen since all mentioned parameters are at their low levels (cf. Table B.2 in Appendix B). Subsequently, the value of each parameter was systematically increased to the high level (cf. Table 3.2) individually to observe its impact on radial segregation. The findings, presented in Figure 3.16, are inline with Table 3.4 and confirm that pellet-sinter interaction parameters are insignificant for radial segregation here.

Effect of pellet-sinter mass ratio

To examine the effect of the pellet-sinter mass ratio on the parameters significance, the dominant parameters between the L1 configuration (i.e., with a mass ratio of 50/50), L75/25, and L25/75 in Table 3.4 were compared. The findings suggest that the mass ratio has some influence on the dominant parameters for segregation. Although the significance of sinter interaction parameters

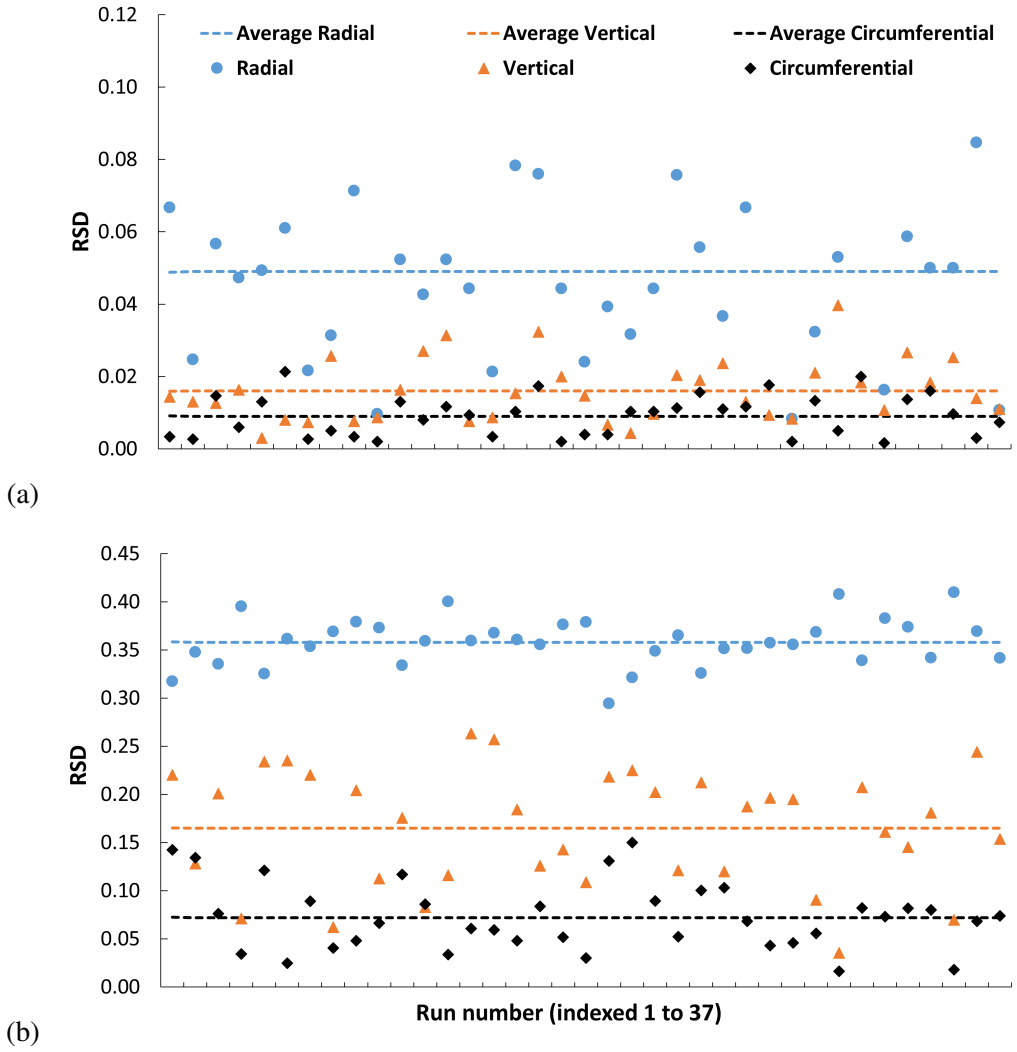

Figure 3.14 Comparison of RSDs in the radial, vertical and circumferential directions of the heap across all runs for a) mixed and b) L1 configurations within the hopper (the dashed lines represent the average RSD across the runs).

remains unchanged, the significance of both pellet-pellet and pellet-geometry interactions are affected by changes in pellet mass ratio. Specifically, when the pellet mass ratio is reduced to 25%, both pellet-pellet and pellet-geometry interactions lose their statistical significance.

Effect of the coefficient of restitution (C_r)

Table 3.4 shows that the coefficient of restitution (C_r) is not statistically significant for radial segregation across all observed cases. To validate this observation, a series of targeted comparisons were performed by varying C_r in isolation and comparing its effect with that of another statistically significant parameter. Specifically, the sintersinter coefficient of restitution ($C_{r,ss}$) and the coefficient of static friction ($\mu_{s,ss}$) were selected. Starting from run 5 of Table B.2, where both parameters are at their low levels and the L1 initial configuration is used, two additional simulations were conducted: one in which $C_{r,ss}$ was increased, and another in which $\mu_{s,ss}$ was increased. The resulting changes in radial segregation were then compared.

Table 3.4 P-values for all DEM parameters for KPI 3 (i.e., radial segregation in the heap) across various initial configurations, with the effect of each significant parameter on KPI 3 in parentheses (e.g., "(+)" denotes that with an increase in the parameter value, KPI 3 increases; "x" means no significant effect).

Factor	Mixed	L1	L2	L75/25	L25/75
Pellet–pellet (P–P)					
$\mu_{s,pp}$	0.0038 (+)	x	x	x	x
$\mu_{r,pp}$	x	0.0004 (–)	0.009 (+)	0.0012 (–)	x
$C_{r,pp}$	x	x	x	x	x
Sinter–sinter (S–S)					
$\mu_{s,ss}$	<0.0001 (–)	<0.0001 (–)	0.0007 (+)	<0.0001 (–)	<0.0001 (–)
$\mu_{r,ss}$	x	x	x	x	x
$C_{r,ss}$	x	x	x	x	x
Pellet–sinter (P–S)					
$\mu_{s,ps}$	x	x	x	x	x
$\mu_{r,ps}$	x	x	x	x	x
$C_{r,ps}$	x	x	x	x	x
Pellet–geometry (P–G)					
$\mu_{s,pg}$	x	<0.0001 (–)	x	<0.0001 (–)	<0.0001 (–)
$\mu_{r,pg}$	x	<0.0001 (–)	x	<0.0001 (–)	x
$C_{r,pg}$	x	x	x	x	x
Sinter–geometry (S–G)					
$\mu_{s,sg}$	<0.0001 (+)	<0.0001 (–)	<0.0001 (–)	x	<0.0001 (–)
$\mu_{r,sg}$	x	x	x	x	x
$C_{r,sg}$	x	x	x	x	x

A similar procedure was applied to sintergeometry interactions, using run 10 (L1 configuration), where both the sintergeometry coefficient of restitution ($C_{r,sg}$) and static friction ($\mu_{s,sg}$) are at low levels. Again, two simulations were conducted to independently increase each parameter and assess their impact.

Figure 3.17 presents the results, showing the variations in the relative standard deviation (RSD) of radial segregation. The findings confirm that increasing C_r, whether for sintersinter or sintergeometry interactions, has minimal effect on radial segregation compared to increasing the corresponding static friction coefficient. These results support the conclusion that C_r is not a significant factor for radial segregation in the heap.

This weak sensitivity to C_r is also physically anticipated in the hopperchutebin system, where the flow is typically dense and frictional. In such regimes, stresses and particle rearrangements are mainly transmitted through enduring contacts involving sliding and rolling, rather than brief collisions. Since C_r mainly governs the energy restitution from collisions, it has limited influence on shear-driven segregation in the heap [165, 166].

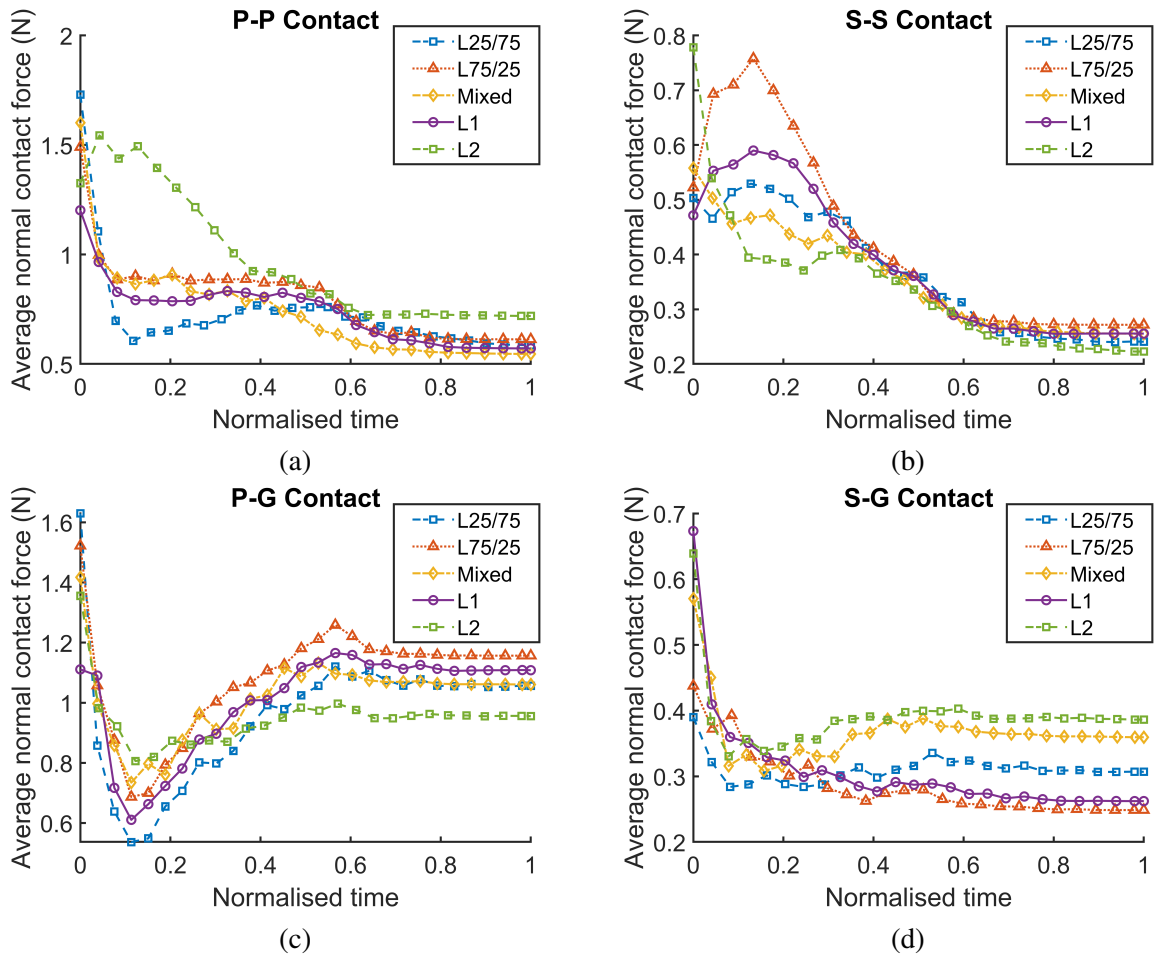

Figure 3.15 Average contact force within the heap for different types of contact in various initial configurations. (Abbreviation: P-P = pellet-pellet, S-S = sinter-sinter, P-G = pellet-geometry, and S-G = sinter-geometry.)

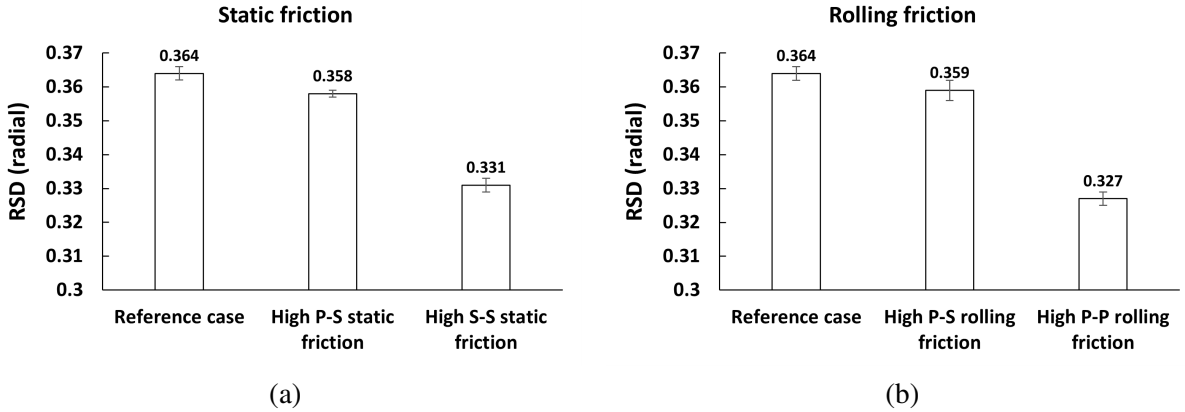

Figure 3.16 Comparison between the effect of changing a) pellet-sinter (P-S) and sinter-sinter (S-S) coefficient of static friction, and b) pellet-sinter (P-S) and pellet-pellet (P-P) coefficient of rolling friction on radial segregation in the heap. The value above each bar denotes the mean RSD and the error bar represents the standard deviation from three repetitions.

Effect of the sinters rolling friction

Although rolling friction of pellet-pellet and pellet-geometry interactions were found to be sig-

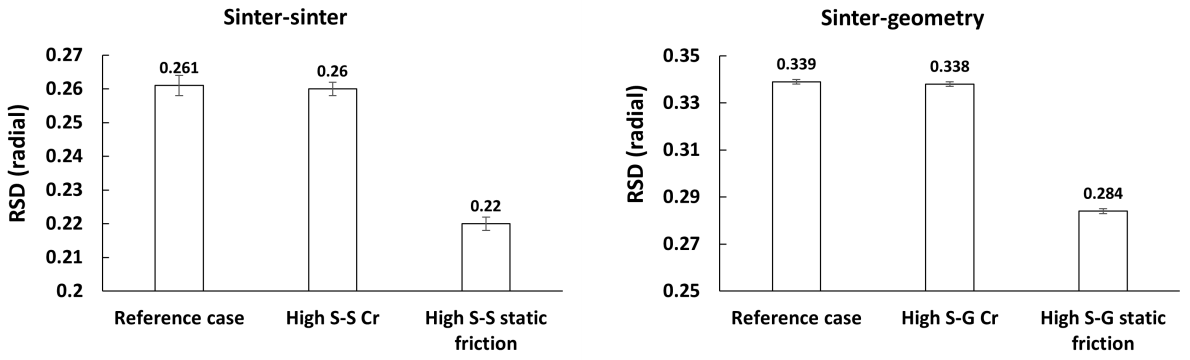

(a) (b)

Figure 3.17 Comparison between the effect of changing the coefficient of restitution and static friction on radial segregation for a) sinter-sinter, and b) sinter-geometry interactions. The value above each bar denotes the mean RSD and the error bar represents the standard deviation from three repetitions.

nificant (cf. Table 3.4), sinter-sinter and sinter-geometry interactions are insignificant. This implies that the chosen particle shape (cf. Figure 3.4) based on the literature on segregation [81], can adequately replicate the rolling behaviour of sinter particles in capturing segregation, regardless of the rolling frictions value.

3.4.2 Effect of sinters particle shape, layering mode, and mass ratio on segregation

In this section, it is examined how the shape of sinter particles, layering mode, and the mass ratio of pellets to sinter influence segregation. This adds to the previous section (i.e., Section 3.4.1), which mainly looked at which DEM parameters dominate segregation.

I. Effect of particle shape on segregation. As noted in Section 3.2.2, a non-spherical particle shape was employed to represent sinter particles (cf. Figure 3.4). However, the use of non-spherical particles in the DEM model substantially increases computational time. It would be beneficial to investigate whether using spherical sinter particles can still accurately capture their segregation behaviour. To investigate this, an additional set of simulations (with L1 initial configuration) was conducted using volume-equivalent spheres to model sinter, specifically to examine the effects of particle shape on segregation.

Figure 3.18 illustrates the results regarding the segregation after the hopper discharge (KPI 1) and the radial segregation in the heap (KPI 3) for spherical and non-spherical sinter particle cases across all runs. Notably, particle shape seems to have a more significant effect on KPI 3 compared to KPI 1. To quantitatively assess the effect of sinters particle shape on both KPIs, Cohens d [62] was used. This is a statistical metric for evaluating the effect size, or the magnitude of difference, between two sets of data. Cohens d is computed as

$$d = \frac{\bar{x}_1 - \bar{x}_2}{s} \tag{3.7}$$

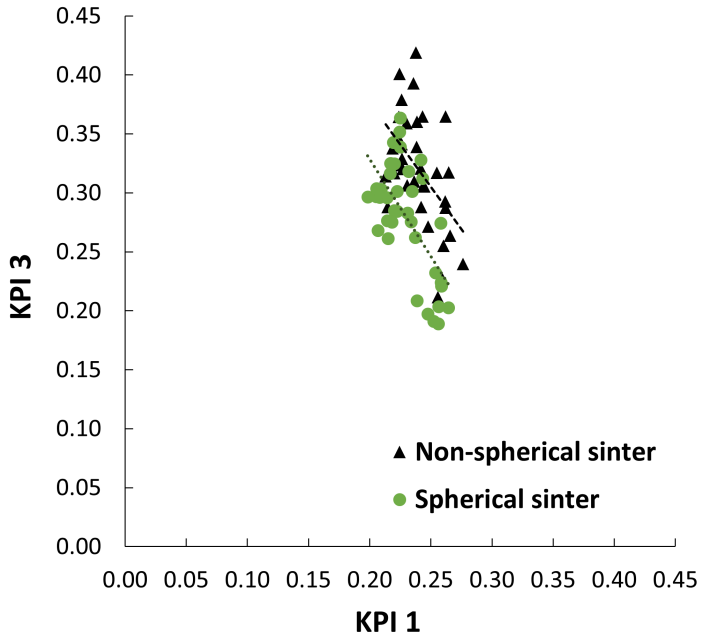

Figure 3.18 The effect of the sinters particle shape on KPI 1 and KPI 3, i.e. segregation after hopper and radial segregation in the heap, respectively (the dashed lines denote linear regression fits.)

where $\bar{x}_1$ and $\bar{x}_2$ denote the mean values of samples 1 and 2, corresponding respectively to the runs with non-spherical sinter particles (L1 initial configuration) and spherical sinter particles in this study. The term s represents the pooled standard deviation

$$s = \sqrt{\frac{\sigma_1^2 + \sigma_2^2}{2}} \tag{3.8}$$

where σ_1 and σ_2 are the standard deviations of samples 1 and 2, respectively. Cohens d was calculated as 0.48 and 0.87 for the effect of sinters particle shape on KPI 1 and KPI 3, respectively. According to [167, 168], these two Cohens d values indicate small and large effect sizes, respectively. Hence, it is concluded that while changing the sinters particle shape significantly influences radial segregation in the heap, it has an insignificant impact on the segregation after hopper discharge.

As discussed in Section 3.4.1, the segregation in the heap results from various stages: before materials enter the bin (during hopper discharge and on the chute), during the initial charging into the bin where interactions with the geometry are dominant, and when materials interact with each other on the heap surface. Since the segregation before materials enter the bin is not significantly impacted by particle shape (cf. Figure 3.18), the two subsequent causes are focused on to understand the role of particle shape.

Radial segregation stems from differences in the X and Y coordinates between pellets and sinter (cf. Figure 3.19(a)). To further explore this, the average Y coordinates of pellets and sinter within half of the heap were extracted, given its symmetry in the Y direction (see Figure 3.19(a)). Run 12 is taken as an example, which exhibits the highest difference in RSD. Figure 3.19(b) illustrates the average Y for pellets and sinter inside the heap for L1 (i.e., with non-spherical sinter particles) and spherical sinter particles. The graph reveals a greater devi-

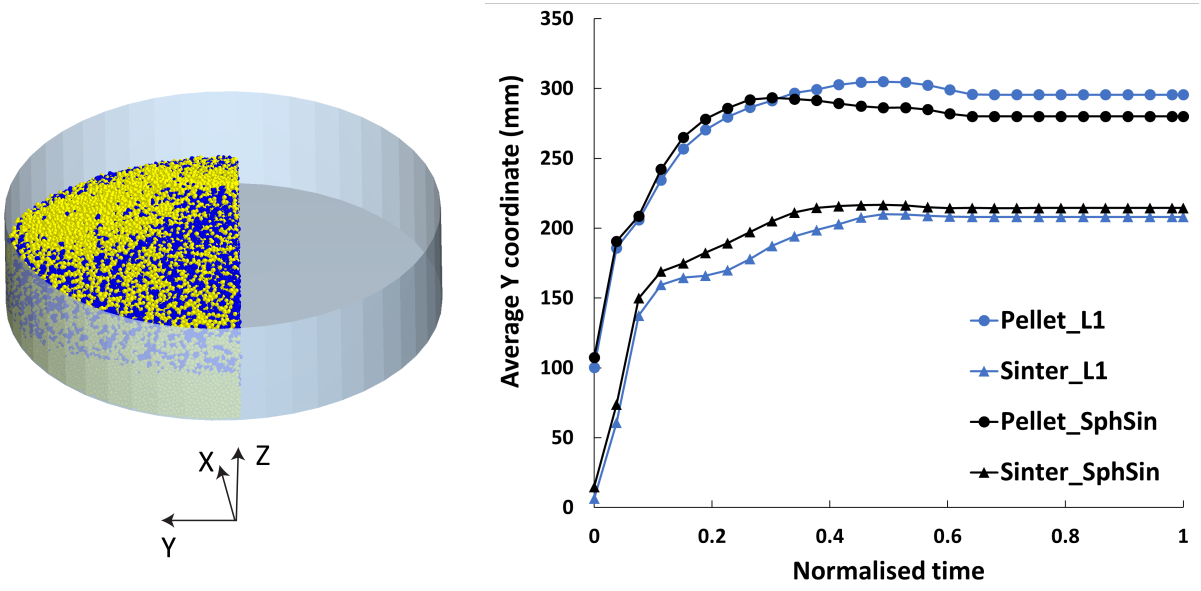

(a) (b)

Figure 3.19 a) Half of the heap in the Y direction, b) average Y coordinates of pellets and sinter in the half heap for L1 (non-spherical) and spherical sinter particles.

ation in the Y coordinates of pellets and sinter in the case of L1, indicating higher radial segregation. This could be attributed to two factors: first, spherical sinter particles exhibit higher rollability than non-spherical ones, causing them to roll more towards the sides of the heap and resulting in a higher Y. Second, in the case of L1, where the rollability of non-spherical sinter particles is less than that of (spherical) pellets, the non-spherical sinter particles tend to remain close to the centre of the heap, allowing pellets to roll over them towards the sides, leading to higher Y coordinates for pellets compared to the case of spherical sinter particles.

II. Effect of layering mode on segregation. Similar to the effect of particle shape, the influence of layering mode on segregation is examined by comparing cases L1 and L2 (cf. Figure 3.6). Figure 3.20 shows how the layering mode affects segregation after hopper discharge (KPI 1) as well as radial segregation in the heap (KPI 3). Similar to the influence of sinter particle shape, the layering mode has a more significant effect on KPI 3 compared to KPI 1. Cohens d (cf. Eq. 3.7) was used to quantitatively assess these effects, resulting in 1.45 and 2.34 for the effect of layering mode on KPI 1 and KPI3, respectively. According to [167, 168], these values indicate a huge effect size. Hence, it is concluded that the layering mode significantly influences both KPI 1 and KPI 3.

To understand the reason behind the impact of the layering mode on KPI 1, the segregation occurring after the hopper was compared between L1 and L2 cases for Run 36, which has the highest effect of the layering mode. The comparison, presented in Figure 3.21, highlights that the main difference between L1 and L2 occurs at the end of hopper discharge, i.e., after the normalised time of 0.6 (equivalent to the simulation time of 2.4 seconds).

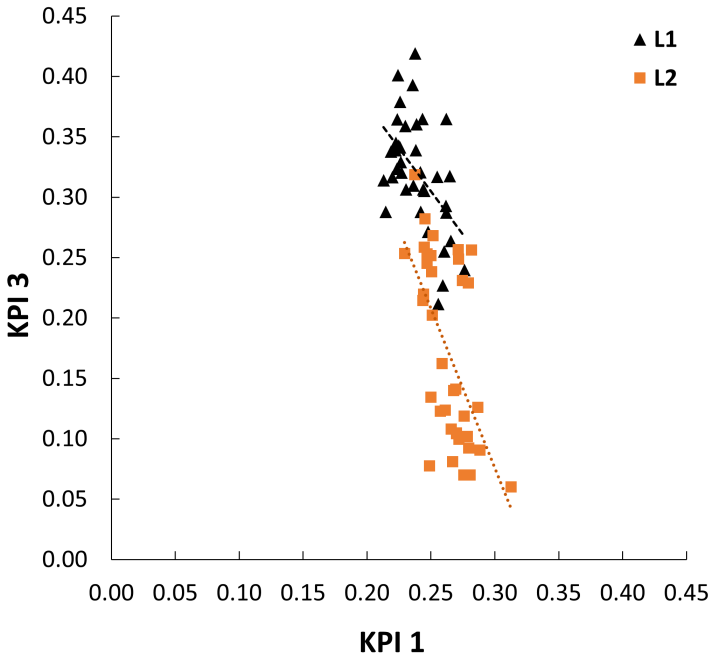

Figure 3.20 The effect of layering mode on KPI 1 and KPI 3, i.e. segregation after hopper and radial segregation in the heap, respectively (the dashed lines denote linear regression fits.)

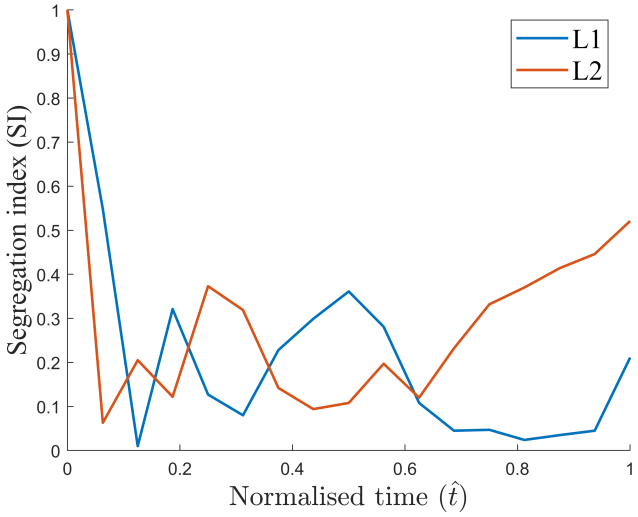

Figure 3.21 Comparison of KPI 1 between L1 and L2 cases for run 36.

To explore this further, the velocity profiles of pellets and sinter within the half-cut hopper for both L1 and L2 configurations were examined, focusing on Run 36, as shown in Figure 3.22. A comparison of Figure 3.22(a) and Figure 3.22(b) on the left reveals that in L1, two distinct layers of pellets are being discharged alongside sinter particles, preventing segregation. However, in L2, the high rolling resistance between the bottommost layer of sinter and the geometry prevents the discharge of sinter particles, while the majority of pellets have already been discharged. Consequently, at the end of the hopper discharging, the mixture is predominantly composed of sinter particles, resulting in a high segregation index (SI), as shown in Figure 3.21. Therefore, it is concluded that the main reason behind the layering effect is the difference in the

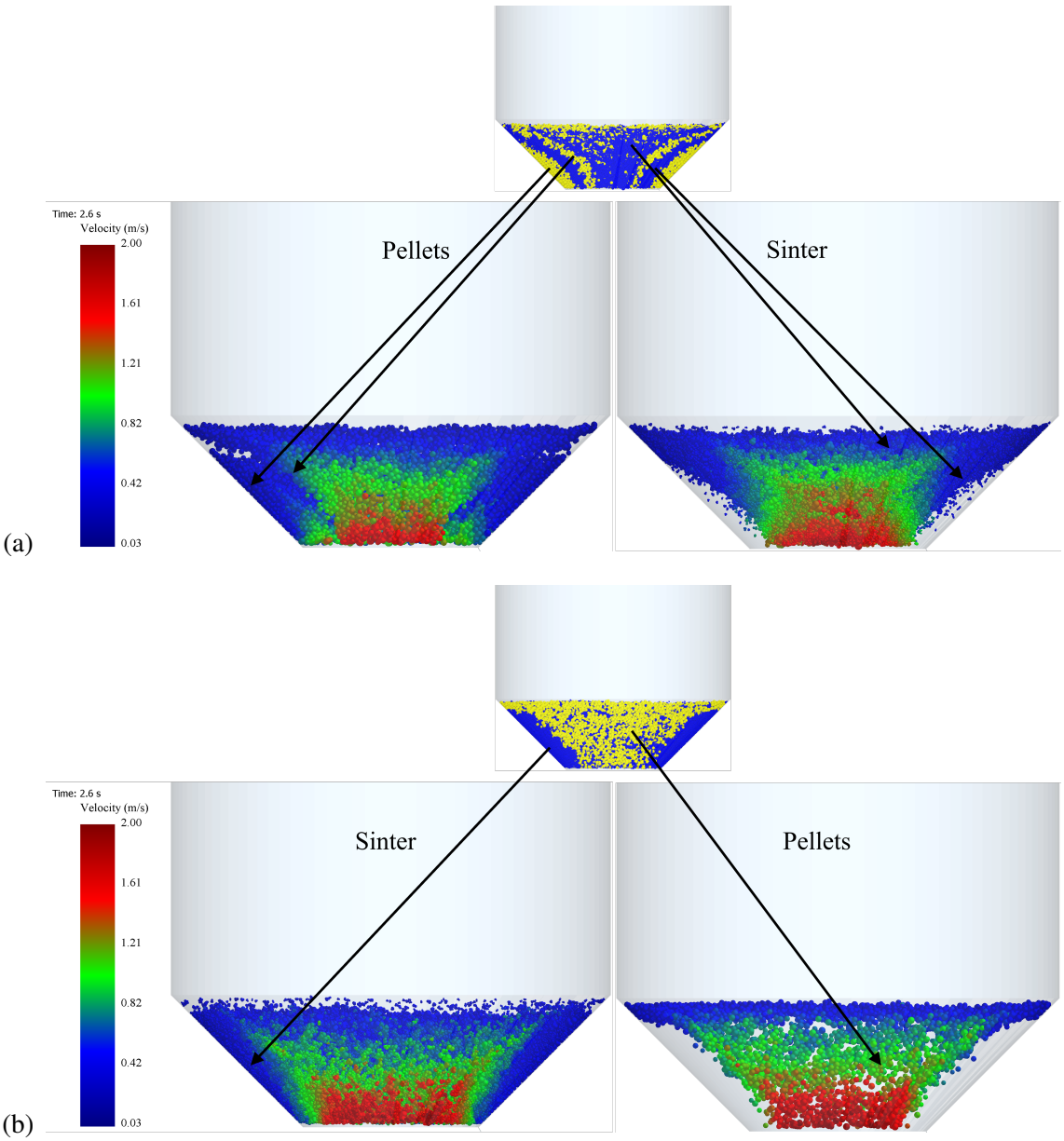

Figure 3.22 Velocity profiles within the half-cut hopper for a) L1, and b) L2 initial configurations at t = 2.6 sec.

rolling behaviour of pellets and sinter particles. This elucidates why in certain runs such as 8, 17 and 35, where pellets have high rolling friction, the effect of layering mode on KPI 1 is minimal.

Regarding the effect of the layering mode on KPI 3, Figure 3.20 illustrates that in most runs, L2 leads to less segregation. Two main reasons contribute to this observation. First, in the case of L2, sinter particles exit the hopper first and fall onto the chute. Due to the lower flowability of sinter particles on the chute, the flow velocity of particles decreases, causing a semi-blockage of the flow. Figure 3.23 presents snapshots of the flow on the chute for both L1 and L2, accompanied by the average velocity measured at the velocity sensor located at the beginning of the chute. The comparison in Figure 3.23(c) reveals a significant difference in the flow velocity between L1 and L2, with L2 exhibiting lower velocities. This reduced velocity in

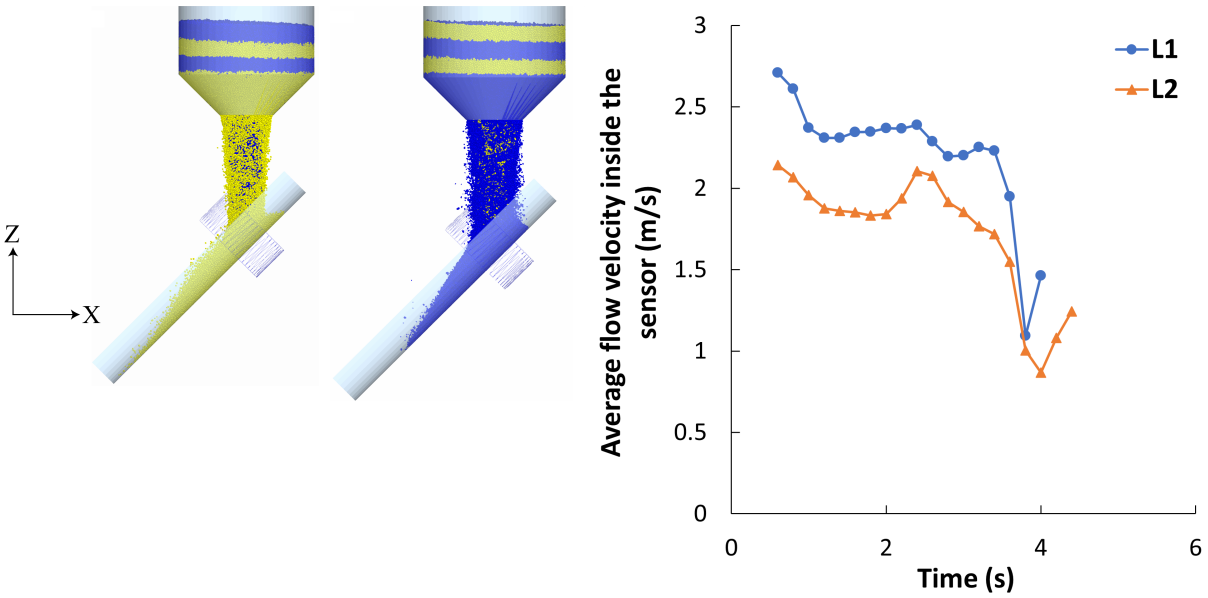

(a) (b) (c)

Figure 3.23 Simulation results showing the flow behaviour on the chute at t = 0.6s for: (a) L1 case, (b) L2 case, and (c) a comparison of the average flow velocity between L1 and L2 cases.

L2, not only results in better mixing of pellets and sinter on the chute but also generally reduces the segregation afterwards.

Second, during the process of materials charging into the bin to form the heap, any velocity difference between pellets and sinter could contribute to radial segregation. Since the heap is symmetric in the Y direction, as illustrated in Figure 3.19(a), the velocity of pellets and sinter in the Y direction for half of the heap was extracted, as shown in Figure 3.24. The observed difference in velocity in the Y direction is higher for L1 between the normalized times of 0.2 and 0.6 (cf. Figure 3.24(a)), primarily due to the higher velocity of pellets.

In the case of L1, the bottom layer of the heap, which is in direct contact with the geometry, contains pellets. Because of their spherical shape, pellets have a high tendency to roll and be pushed towards the edge of the bin as more materials are charged into the bin, resulting in higher velocity in the Y direction for pellets in L1. However, in L2, the bottom layer mostly consists of sinter particles surrounding the pellets, preventing easy sliding and rolling of pellets toward the edge. Once the pellets reach the edge of the bin in L1 (around the normalized time of 0.56), the velocity of pellets starts to decline.

Therefore, it is concluded that the difference in sliding and rolling friction between pellets and sinter is the main reason for the effect of layering mode on radial segregation. This clarifies why in Runs 2, 7, and 29 (cf. Table B.2), where pellets and sinter have similar rolling and sliding characteristics (i.e., low S-G and high P-G sliding and rolling friction), have minimal radial segregations.

III. Effect of mass ratio on segregation. Here, an investigation was conducted into the effect of the pellet-sinter mass ratio on radial segregation in the heap. Due to the division of the standard deviation by the mean in Eq. 3.4, using the Relative Standard Deviation (RSD) to assess the effect of mass ratio on segregation may lead to misleading interpretations. Therefore,

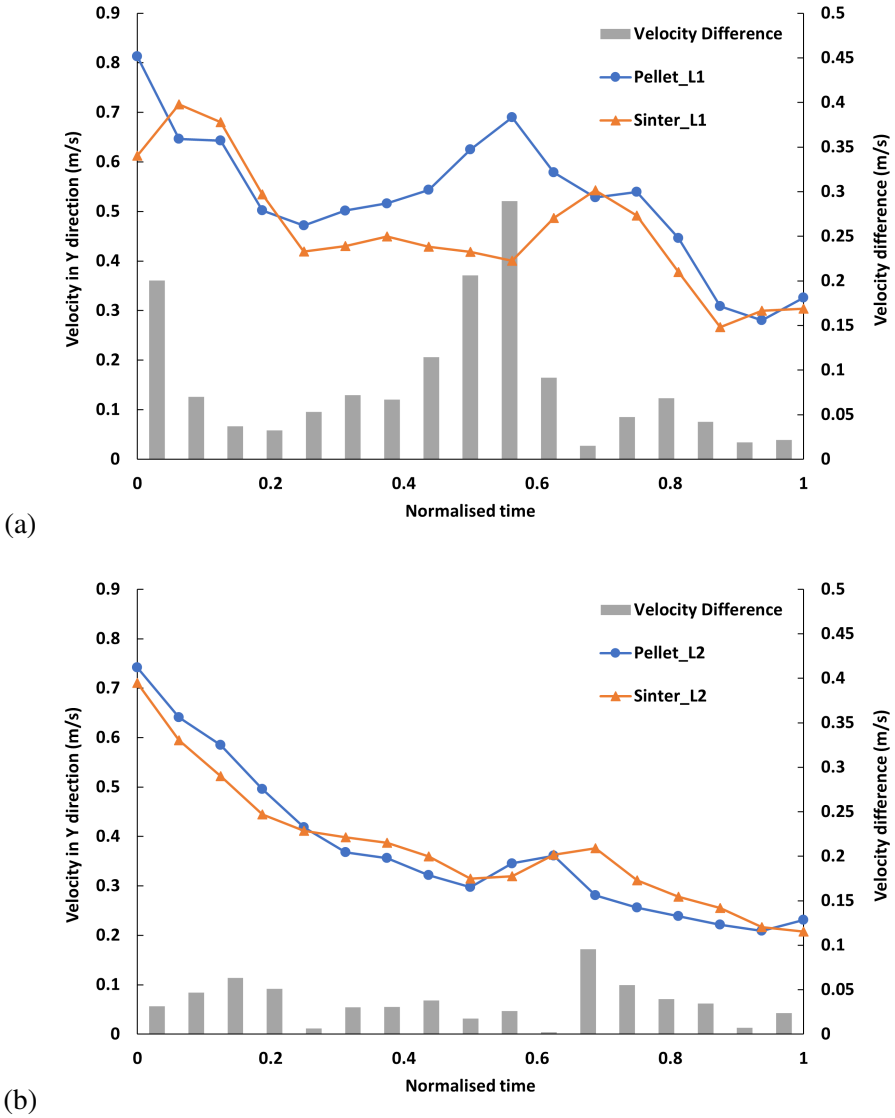

Figure 3.24 The velocity of the pellets and sinter in the Y direction during the heap formation for a) L1 and b) L2 cases.

the standard deviation (denoted as σ in Eq. 3.4) was used for comparison purposes. Figure 3.25 illustrates the standard deviation (σ) for three cases: L1 (with an initial mass ratio of 50-50), L75/25, and L25/75, across all 37 runs.

Once again, Cohens d (cf. Eq. 3.7) was used to quantitatively evaluate the effect size of the pellet-sinter mass ratio on σ. Cohens d was calculated for three possible pairs, as reported in Table 3.5. The results indicate that changing the mass ratio of pellets from 50% (i.e. L1) to either 75% or 25% significantly influences the radial segregation (σ). However, changing pellets mass ratio from 25% to 75% has an insignificant effect on σ. Additionally, Figure 3.25 shows that while L1 consistently demonstrates the highest segregation across all runs, the trend between L75/25 and L25/75 is not consistent.

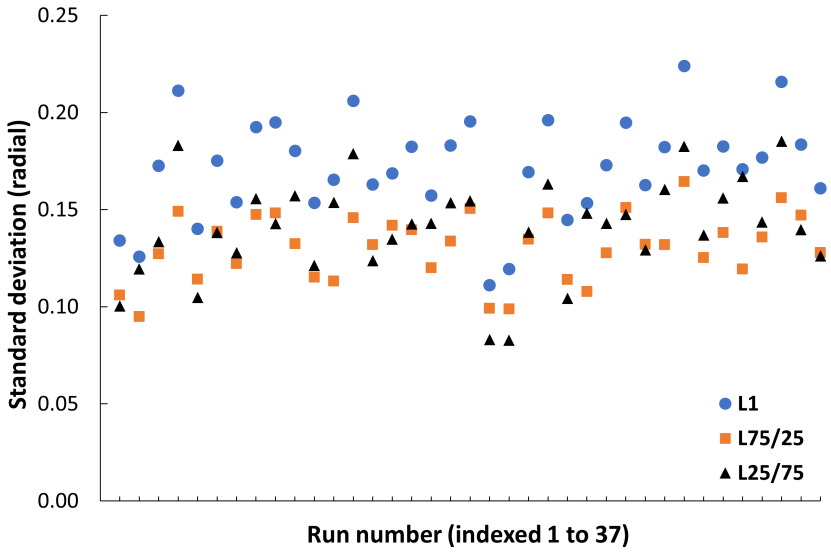

Figure 3.25 The standard deviation (SD) for L1 (50/50), L75/25 and L25/75 across all runs.

Table 3.5 Results of Cohens *d* effect size regarding the effect of mass ratio on radial segregation in the heap.

Configuration tested for Cohens *d* test	**Cohens *d***	**Interpretation**
L1 & L75/25	1.87	Very large effect size
L1 & L25/75	1.2	Very large effect size
L75/25 & L25/75	0.47	Small effect size

3.4.3 Summary of the results

In this section, a summary of the findings from this study regarding both the dominant DEM interaction parameters for the KPIs and the effect of specific factors on segregation is provided in Table 3.6 and Table 3.7, respectively. It is important to note that the results provided in Table 3.6 offer a broad overview. That is, the significance of the parameters and their correlation with KPIs vary depending on the hopper filling configurations (cf. Figure 3.6).

Table 3.6 Summary of the significance of various DEM interaction parameters for different KPIs across all hopper filling configurations. The arrow () indicates the significant parameter. "(+)" and "()" show a positive and negative correlation with KPI, respectively. "(ś)" indicates that the parameter correlation can vary depending on the hopper filling configuration. "x" denotes no significant effect on the KPI. Abbreviation: PP = pelletpellet, SS = sintersinter, PS = pelletsinter, PG = pelletgeometry and SG = sintergeometry.

KPI	**PP**	**SS**	**PS**	**PG**	**SG**
KPI 1 (segregation after the hopper discharge) and KPI 2 (segregation after chute flow)*	x	(+)	x	(ś)	(ś)
KPI 3 (segregation in the radial direction of the heap)**	(+)	(ś)	x	()	()

* cf. Figure 3.5(b)
** cf. Figure 3.9(a)

Table 3.7 Summary of the effect of sinters particle shape, layering mode and pelletsinter mass ratio on KPIs. "x" denotes no significant effect on the KPI. The arrow () indicates a significant effect.

KPI	Sinters particle shape	Layering mode	Pelletsinter mass ratio
KPI 1 (segregation after the hopper discharge) and KPI 2 (segregation after chute flow)*	x	L2 configuration (cf. Figure 3.6) leads to more segregation than L1.**	NA
KPI 3 (segregation in the radial direction of the heap)***	(Using spherical particles for sinter leads to less segregation.)	(L2 configuration (cf. Figure 3.6) leads to less segregation than L1.)	(A 50%50% mass ratio of pellets and sinter results in the highest segregation compared to 75%25% and 25%75% mass ratios.)

* cf. Figure 3.5(b)
** See Figure 3.6 for L1 and L2
*** cf. Figure 3.9(a)

Additionally, Figure 3.26 provides a comprehensive overview of the results of this study. It illustrates the relationship between KPI 1 and KPI 3 across all hopper filling configurations. The plot reveals possible correlations between these two KPIs, suggesting the possibility of predicting KPI 3 based on KPI 1. Essentially, it shows that the segregation occurring downstream is influenced by both the degree of segregation present upstream and the filling configurations of the discharge hopper.

3.5 Conclusion

In this chapter, the dominant DEM parameters influencing multi-component segregation under various flow conditions and initial configurations of the mixture were identified. This was done for a mixture of pellets and sinter and quantified segregation at distinct stages, using blast furnace processes as a studied case: after hopper discharge (KPI 1), after chute flow (KPI 2), and in the static heap (KPI 3). Additionally, the investigation was expanded to assess the effect of certain factors, such as the shape of sinter particles, initial layering mode, and pellet-sinter mass ratio on KPIs. The conclusions of this chapter are as follows:

- Particle-geometry interaction parameters predominantly influence the segregation after hopper discharge (KPI 1). Particle-particle interaction parameters appear to be insignificant for KPI 1. Furthermore, within the scope of this study, no significant segregation occurs on the chute itself.
- In the heap, the segregation occurring in the radial direction is significantly higher than in the vertical and circumferential directions. For radial segregation (i.e. KPI 3), both particle-geometry and particle-particle interaction can be significant depending on the initial configuration.

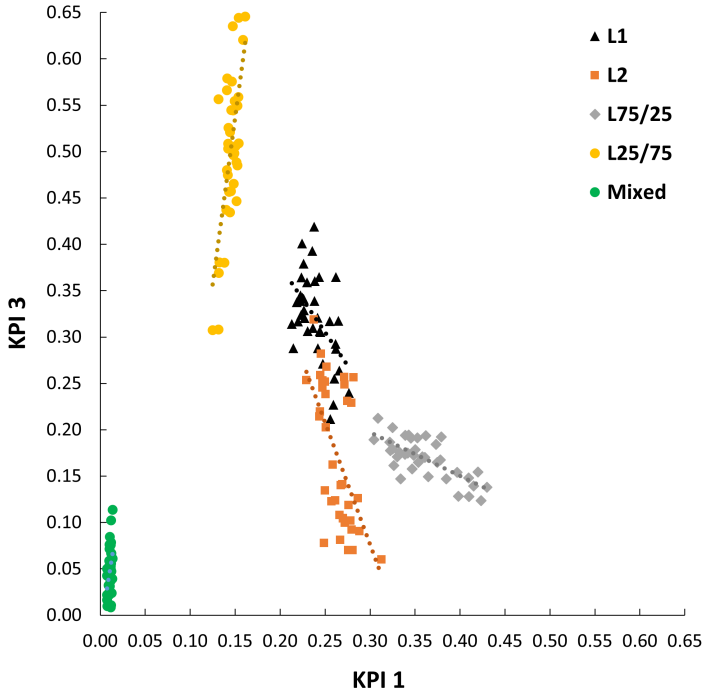

Figure 3.26 The relationship between KPI 3 and KPI 1 based on the results obtained in this study for all hopper filling configurations.

- The hopper filling configuration significantly affects both dominant DEM parameters and the extent of segregation. Shifting from L1 to L2 (i.e., changing the bottommost particle from pellets to sinter) not only makes sinter-geometry parameters significant but also reduces radial segregation in the heap. Additionally, varying the mass ratio affects parameter dominance; for example, reducing the pellet mass ratio from 50% to 25% diminishes pellet-pellet interaction significance. Moreover, the 50%-50% mixture shows the highest segregation level.

- Pelletsinter interaction parameters, along with the coefficient of restitution (C_r) for all interaction types (including pelletpellet, sintersinter, pelletgeometry, and sintergeometry), were found to be insignificant for all KPIs. The insensitivity to C_r is expected for flow behaviour in hopperchutebin systems, where the flow is mainly dense and friction-dominated. In such regimes, stress transmission and particle movement occur mainly through enduring sliding and rolling contacts, while the effect of C_r, which governs energy damping during collisions, becomes negligible in driving segregation [165, 166].

These conclusions are valid within the specific scope investigated in this chapter. Nonetheless, it is emphasised that the overall upstream flow condition is crucial in the segregation downstream. Although the insights obtained here significantly advance the understanding of granular segregation dynamics, further investigations are required to improve generalisability, particularly by exploring a broader range of filling configurations, system geometries, and material properties (e.g., varying size distributions).

The findings of this chapter facilitate more efficient DEM calibration by highlighting which parameters significantly affect segregation and under which conditions. However, performing a

large number of full-scale DEM simulations for calibration remains computationally expensive, particularly when dealing with complex, multi-component mixtures. To address this challenge, the next chapter explores the use of machine learning-based surrogate models as a means to accelerate the DEM calibration process.

Chapter 4

Surrogate Modelling of Multi-Component Segregation*

In Chapter 3, a detailed sensitivity analysis was conducted to identify the dominant DEM parameters influencing multi-component segregation under various flow conditions and mixture configurations. These insights form a solid foundation for guiding the DEM calibration process by prioritising the dominant parameters. However, the high computational cost associated with DEM simulations is the major challenge that remains. Calibrating a DEM model for multi-component segregation still requires a large number of expensive simulations. Furthermore, when a similar system needs to be modelled, the entire calibration process must typically be repeated from scratch.

To address these challenges, this chapter explores the use of surrogate models (SMs) to reduce the computational burden of DEM calibration. Several machine learning (ML) algorithms are systematically evaluated for their ability to develop high-accuracy SMs. Additionally, a transfer learning (TL)-based approach is introduced that enables the reuse of knowledge from previously trained SMs to adapt to new but similar configurations using only a small number of additional DEM simulations. This approach significantly reduces the data preparation effort while maintaining high predictive accuracy, paving the way for more efficient and scalable DEM calibration strategies.

*This chapter is based on: A. Hadi, M. Moradi, Y. Pang, D.L. Schott, *Adaptive AI-based surrogate modelling via transfer learning for DEM simulation of multi-component segregation*, *Scientific Reports* (2024). https://doi.org/10.1038/s41598-024-78455-7

4.1 Introduction

DEM has been widely used as an alternative to physical experiments for simulating granular materials. Specifically for segregation, DEM offers significant advantages, as it enables the modelling of mixtures with arbitrary combinations of size, density, and shape, while providing detailed particle-level insights that are often difficult or impossible to obtain through experiments [169]. While DEM is widely used, achieving a balance between model accuracy and computational efficiency remains a challenge [12]. The accuracy of the DEM model heavily depends on the proper determination of its parameters through a process called calibration. However, the calibration process can be time-consuming, particularly for multi-component mixtures, where the number of DEM parameters significantly increases.

Trial and error is still extensively employed for calibrating DEM models [102, 170–173]. However, it is not only inefficient but also depends on the users expertise and barely results in an optimal parameter set [174]. To systematically calibrate the DEM model, several approaches have been proposed. Typically, these approaches use optimisation techniques to update the parameters and determine the calibrated parameter set. Examples include using advanced design of experiments (DoE) in combination with simple optimisation algorithms [175], particle swarm optimisation [176], and genetic algorithms [108, 110]. However, these methods are still not computationally efficient due to the high number of simulations required [174].

Richter et al. [174] conducted a thorough literature review on various optimisation techniques, concluding that surrogate-based optimisation is the most suitable approach for DEM calibration. A surrogate model (SM) is an approximation of a more complex and computationally expensive model (such as DEM) aimed at mapping the relationship between the models input(s) and output(s) [177]. They can be built using advanced mathematics or machine learning (ML). Surrogate-based optimisation is effective at finding a global optimum, is computationally efficient, and can handle parameter limitations and multi-objective problems [174]. Additionally, ML-based surrogates can take advantage of the rapid progress in the field of machine learning in other fields [173, 178]. Several studies have used surrogate-based optimisation for DEM calibration. This includes using Gaussian process regression (GPR) and Kriging [174, 179–182], multi-objective reinforcement learning [183], Bayesian filtering [184, 185], multi-variate regression analysis [186], neural networks [187–189], and random forest (RF) [173].

Despite the advancement of surrogate-based DEM calibration, several challenges remain to be addressed. Firstly, the vast array of available algorithms can make it challenging to choose the most suitable approach, often leading to subjective decision-making. Secondly, while using the SM reduces the computational cost of the DEM calibration, training the SMs themselves, especially when employing sampling techniques such as Latin Hypercube Sampling (LHS), requires a substantial number of simulations. Thirdly, most existing studies consider only a limited number of DEM parameters to construct the SM, potentially overlooking significant DEM parameters. Lastly, most studies aim at single granular materials, and no study has yet explored surrogate modelling for multi-component granular mixtures. This study attempts to address these challenges by developing SMs that effectively link particle-particle and particle-geometry DEM interaction parameters to segregation. This is demonstrated on the basis of a case study for the reliable estimation of radial segregation of multi-component mixtures in a heap.

The objective of this chapter is twofold:

1. Several ML models are evaluated to develop surrogate models for DEM simulations involving a two-component mixture (i.e., pellet-sinter) that flows from a hopper through a chute into a receiving bin. The goal is to develop SMs that capture the relationship between all particle-particle and particle-geometry DEM interaction parameters to radial segregation in the heap. To investigate the effect of the initial configuration (IC) of the mixture within the hopper on heap segregation, the mixing degree, pellet-to-sinter mass ratio, and layering order are varied within the hopper. For each IC, the definitive screening design (DSD), a cost-effective three-level DoE technique, is used to efficiently create the dataset. To construct effective SMs, ICs are encoded, which consist of a combination of categorical and numerical variables, to prepare them as input features for the SMs.

2. Following the identification of the most effective SMs, a transfer learning (TL) approach is innovatively implemented to transform the surrogate into an adaptive SM tailored for new, unseen ICs, referred to as the transfer learning-based surrogate model (TL-SM), thereby addressing the second objective. To achieve this, one IC is systematically excluded from the training-validation dataset and designated as the unseen IC, which serves as the target domain for TL. Subsequently, the SM, coupled with Bayesian optimisation (BO), is trained and cross-validated using the remaining dataset as the source domain for TL. Using the TL methodology, the pre-trained ML model is deployed as the surrogate for the unseen target IC. The SM is then updated and retrained by integrating new data points from the unseen IC, while performance enhancements are monitored. The effectiveness of the proposed data-driven SM is assessed through nested cross-validation (NCV), in which each IC is iteratively excluded. Additionally, the stability of the TL-SM is evaluated using distinct random seed numbers for weight and bias initialisation.

Achieving these two objectives will pave the way for efficiently building generalised SMs for various scenarios. These SMs, in turn, will facilitate and speed up the DEM calibration process, contributing to the development of more robust and reliable DEM models in a significantly shorter time.

4.2 Simulation method and established dataset

4.2.1 Discrete Element Method

The DEM simulation data from Chapter 3 were used for building the surrogate model in this chapter. The details of the DEM model, simulation setup, and system geometry are provided in Section 3.2.1.

4.2.2 Established dataset

The dataset used for training the surrogate models was established based on the DEM simulations conducted in Chapter 3. For each initial configuration (IC) of the mixture within the hopper (cf. Figure 3.6), 37 simulation runs with five repetitions were performed according the

definitive screening design (DSD) matrix, as listed in Table B.2. Table B.2 shows that, in each run, 15 DEM parameters were varied, including particle-particle interaction parameters (pellet-pellet, sintersinter, and pelletsinter) and particlegeometry interaction parameters (pelletgeometry and sintergeometry). The output variable of interest in this chapter is radial segregation in the heap, which corresponds to KPI 3 described in Chapter 3, Section 3.3.3(II). At this stage, the dataset consists of 15 inputs (DEM parameters) and one output (radial segregation).

To effectively distinguish between these ICs, it was essential to perform feature engineering to create additional features (i.e., inputs) that describe these configurations. This feature engineering could potentially enhance the performance of ML models [190]. Three features were specifically selected: segregation index (of the mixture within the hopper), pellets mass ratio, and layering mode, which can distinguish between the five ICs used. Since the layering mode is a categorical variable, the label encoding technique, which is known for its computational simplicity, was employed to convert it into a numerical format [191]. Table 4.1 presents these three features along with their values for all ICs.

Table 4.1 Three features used to describe the initial configurations (see Figure 3.6) along with their values.

Initial configuration	Segregation index	Pellets mass ratio	Layering mode
IC1	1	0.5	1
IC2	1	0.5	2
IC3	0	0.5	3
IC4	1	0.75	1
IC5	1	0.25	1

4.3 Data-driven surrogate models

The overall proposed framework for designing data-driven SMs is illustrated in Figure 4.1. The dataset underwent nested cross-validation (NCV), one of the most rigorous validation approaches, which involves two other cross-validation (CV) steps. Several ML models were used and trained in this study, including linear regression, support vector machine (SVM), regression tree, ensemble learning, Gaussian process regression (GPR), and artificial neural network (ANN). In this section, ensemble learning and Gaussian process regression (GPR) are briefly described. For detailed mathematical formulations of other models, the reader is referred to the published article on which this chapter is based [192]. Next sections elaborate on NCV and hyperparameter optimisation for the mentioned ML models.

4.3.1 Ensemble learning

While regression trees are easy to interpret and fast for fitting and prediction, like other weak learners, they are susceptible to overfitting and have sensitivity to training data. Integrating several weak learners makes the model more resilient and less prone to overfitting, as each learner depends on a different set of data points. Ensemble learning in ML is the process of combining several weak learners. Given regression trees, one way to overcome this issue is to

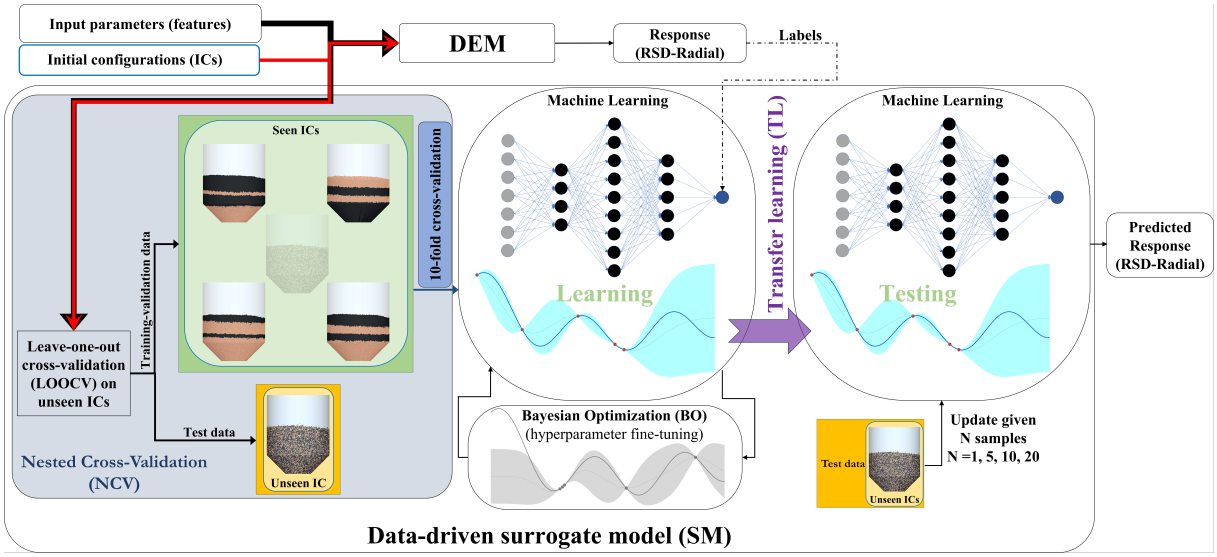

Figure 4.1 The overall proposed framework to design data-driven SM leveraged by TL.

construct a weighted collection of multiple regression trees to build models called ensembles of trees. Combining many regression trees generally improves the prediction capability and accuracy. Several ensemble learning methods exist, including bagging and boosting.

Bagging (bootstrap aggregation) involves training many weak (base) learners simultaneously (in parallel) and integrating them using averaging techniques [193]. Considering the original data set as $D = \{(x_1, y_1), (x_2, y_2), \ldots, (x_n, y_n)\}$, first, a number of bootstrap samples (D_i, $i = 1, 2, \ldots, B$) is created by randomly choosing n samples from D with replacement. Then, a base learner f_i is trained based on D_i to minimise the error between y and $f_i(x)$. Finally, the aggregated prediction model $f(x)$ is obtained by averaging the predictions:

$$f(x) = \frac{1}{B} \sum_{i=1}^{B} f_i(x) \tag{4.1}$$

By training each learner with the output of the preceding learner, the boosting approach progressively boosts the model's overall performance. One boosting technique used for building regression ensembles is least-squares boosting (LSBoost) [194]. This technique successively fits a set of weak learners (e.g., decision trees), with each new learner trained to reduce residual errors from the ensemble's total predictions. The approach iteratively improves the ensemble's predictions by including fresh weak learners. First, the ensemble prediction is initialised as the mean of the target values ($y_i, i = 1, 2, \ldots, n$):

$$f_0(x) = \frac{1}{n} \sum_{i=1}^{n} y_i \tag{4.2}$$

Then, for iteration m ($m = 1, 2, \ldots, M$), the residuals between the target values and the accumulated prediction ($f_{m-1}(x_i)$) for each observation is calculated as:

$$r_i^m = y_i - f_{m-1}(x_i) \qquad 1 \leq i \leq n \tag{4.3}$$

Next, a new weak learner (h_m) is trained by fitting it to the residuals:

$$h_m = \arg\min_h \left(\frac{1}{2n} \sum_{i=1}^{n} [r_i^m - h(x_i)]^2 \right) \tag{4.4}$$

Finally, the ensemble model is updated:

$$f_m(x) = f_{m-1}(x) + \eta_m h_m \tag{4.5}$$

where η is the learning rate (the shrinkage parameter), which controls the contribution of each weak learner and ranges from 0 to 1.

4.3.2 Gaussian process regression (GPR)

Gaussian process regression (GPR) is a probabilistic and non-parametric kernel-based machine learning regression model [195] rooted in Bayesian principles. Due to its simplicity of use and flexibility in obtaining hyperparameters, GPR is well-suited to handle small-sized datasets and nonlinear problems [196]. A Gaussian process (GP) is a collection of random variables having a Gaussian distribution and is fully defined by its mean function $\mu(x)$ and covariance kernel function $k(x,x')$.

Considering x_i and y_i as the input and corresponding output vectors, respectively, the GPR model with Gaussian noise is formulated as:

$$y_i = f(x_i) + \varepsilon_i \tag{4.6}$$

where ε_i denotes a constant additive noise term assumed to follow a Gaussian distribution with a mean of 0 and a standard deviation of σ (i.e., $\varepsilon_i \sim \mathcal{N}(0,\sigma^2)$). The objective of GPR is to infer the function f in a non-parametric and Bayesian approach, utilising the provided training dataset $\{(x_i,y_i); i = 1,2,\ldots,n\}$. A prior distribution on f needs to be established in order to learn this function. Typically, this prior is utilised to encapsulate qualitative attributes of the function such as continuity, differentiability, or periodicity. In GPR, the prior distribution for f as the regression function is represented by:

$$f(x) \sim \mathcal{GP}(\mu(x), k(x,x')) \tag{4.7}$$

In this formulation, while the mean function $\mu(x)$ is often set constant, the covariance kernel $k(x,x')$ varies. When the values of the function $f(x_i)$ have a joint Gaussian distribution defined by $\mu(x)$ and $k(x,x')$ for every finite set of inputs x_i, then the function $f(x)$ is a GP, implying:

$$\begin{bmatrix} f(x_1) \\ \vdots \\ f(x_n) \end{bmatrix} \sim \mathcal{N} \left(\begin{bmatrix} \mu(x_1) \\ \vdots \\ \mu(x_n) \end{bmatrix}, \begin{bmatrix} k(x_1,x_1) & \cdots & k(x_1,x_n) \\ \vdots & \ddots & \vdots \\ k(x_n,x_1) & \cdots & k(x_n,x_n) \end{bmatrix} \right) \tag{4.8}$$

which using the notation below:

$$\mu \triangleq \begin{bmatrix} \mu(x_1) \\ \vdots \\ \mu(x_n) \end{bmatrix}, \quad \mathcal{K} \triangleq \begin{bmatrix} k(x_1,x_1) & \cdots & k(x_1,x_n) \\ \vdots & \ddots & \vdots \\ k(x_n,x_1) & \cdots & k(x_n,x_n) \end{bmatrix}, \quad \hat{k}(x_*) \triangleq \begin{bmatrix} k(x_1,x_*) \\ \vdots \\ k(x_n,x_*) \end{bmatrix} \tag{4.9}$$

the equation can be simplified. In the process of learning functions through GPR, the implications of expanding equation (17) by including a new data point x_*, separate from the training data, are being considered. The objective is to predict the value of the function at this particular location, i.e., $f(x_*)$. To do so, given the already observed values $\mathbf{y} = [y_1 \dots y_n]^T$, the relationship can be expressed by incorporating Eqs. 4.6–4.9

$$\begin{bmatrix} \mathbf{y} \\ f(x_*) \end{bmatrix} \sim \mathcal{N}\left(\begin{bmatrix} \mu \\ \mu(x_*) \end{bmatrix}, \begin{bmatrix} \mathcal{K}+\sigma^2 I_n & \hat{k}(x_*) \\ \hat{k}(x_*)^T & k(x_*,x_*) \end{bmatrix} \right) \tag{4.10}$$

where I_n is the $N \times N$ identity matrix. Conditioning on the new data based on observations, the posterior probability distribution for $f(x_*)$ can be estimated as

$$f(x_*)|\mathbf{y} \sim \mathcal{N}(\mu_*, \sigma_*^2) \tag{4.11}$$

where

$$\mu_* = \mu(x_*) + \hat{k}(x_*)^T (\mathcal{K}+\sigma^2 I_n)^{-1} (\mathbf{y}-\mu) \tag{4.12}$$

$$\sigma_*^2 = k(x_*,x_*) - \hat{k}(x_*)^T (\mathcal{K}+\sigma^2 I_n)^{-1} \hat{k}(x_*) \tag{4.13}$$

The posterior probability distribution is Gaussian once more, allowing for Bayesian reasoning on the function f. One noteworthy aspect of these formulations is that the function's posterior expected value, $\mathbb{E}(f(x_*)|\mathbf{y})$, could be stated using a weighted sum of kernel functions

$$\mathbb{E}(f(x_*)|\mathbf{y}) = \hat{k}(x_*)^T (\mathcal{K}+\sigma^2 I_n)^{-1} (\mathbf{y}-\mu) = \sum_{i=1}^{n} k(x_*,x_n)\alpha_i \tag{4.14}$$

where

$$\begin{bmatrix} \alpha_1 \\ \vdots \\ \alpha_n \end{bmatrix} \triangleq (\mathcal{K}+\sigma^2 I_n)^{-1} (\mathbf{y}-\mu) \tag{4.15}$$

The weighted sum formulation presented in Eq. 4.15 offers a key advantage, as it allows for efficient computation of predictions that would otherwise be challenging.

The details on the kernel functions used in this study are presented in Table C.1 in Appendix C. It is possible to use either isotropic or non-isotropic kernel functions with GPR. In contrast to isotropic kernels, non-isotropic ones give each predictor variable a distinct correlation length scale. This results in an improved accuracy at the cost of slowing down the fitting process.

4.4 Hyperparameters optimisation and model validation

Overfitting is a common challenge in ML models, requiring the use of cross-validation (CV) methods to validate the effectiveness of the model. As illustrated in Figure 4.2, nested cross-validation (NCV) was employed, which consists of two CV steps:

I. An external loop conducts CV on the dataset based on the number of ICs, excluding one IC at each iteration to create a distinct test set of "unseen ICs".

II. An internal loop performs CV on the remaining dataset after the execution of the external loop to tune hyperparameters and mitigate overfitting.

This NCV technique properly estimates model performance by combining 5-fold outer loops based on the number of ICs with 10-fold inner loops. In the outer loop, the dataset was split into a trainingvalidation set (four ICs) and an independent test set (one IC), corresponding to a leave-one-out cross-validation (LOOCV) scheme at the IC level [197]. Within each outer iteration, the trainingvalidation set was further partitioned using 10-fold cross-validation to estimate generalisation error and tune hyperparameters. Hyperparameter optimisation was performed using Bayesian optimisation (BO) [198], which iteratively updates a probabilistic model of the objective function and selects promising parameter sets via an acquisition function. Compared with grid or random search, BO explores the hyperparameter space more efficiently and typically requires fewer evaluations.

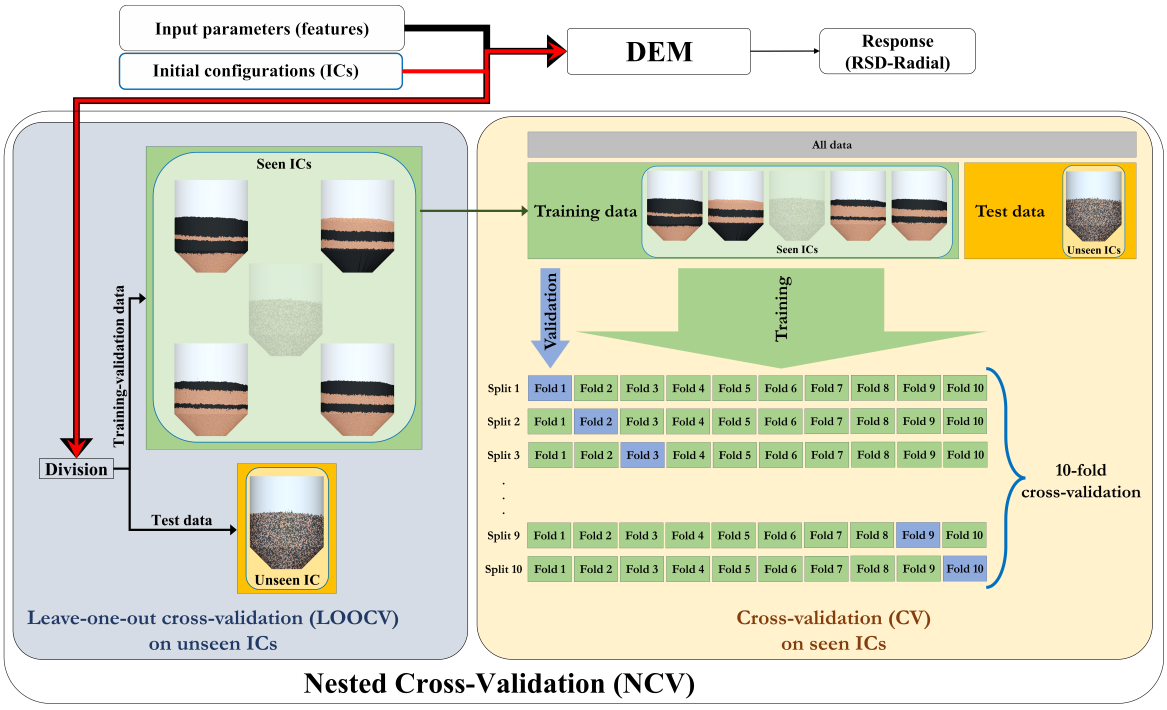

Figure 4.2 The process of nested cross-validation (NCV), given LOOCV in the outer loop and 10 folds in the inner loop.

4.5 Transfer learning (TL) for unseen ICs

In this section, the application of transfer learning (TL) is explored to enhance the performance of the SM when a new, previously unseen IC is encountered. TL is a powerful technique that leverages knowledge gained from related tasks or domains to improve performance on a target task [199–201]. TL is specifically advantageous when providing a sufficient number of training samples is costly. In the context of granular material segregation, the IC is crucial as it can significantly influence segregation outcomes [169]. Consequently, if the IC changes, the DEM model must be recalibrated, which is very time-consuming. To address this challenge, prior knowledge gained from previously encountered ICs can be leveraged as the source domain to pre-train the SMs. Subsequently, the pre-trained SMs can be transferred as base learners for new, unseen ICs, which are treated as the target domain in TL. In the next stage, the pre-trained SMs are updated by incorporating a small number of samples from the target domain through model retraining while retaining the prior information from the source domain. This approach allows TL to expedite the learning process, as the SMs require fewer samples from the unseen ICs to achieve effective learning. Additionally, it eliminates the need for full retraining and cross-validation, coupled with BO, using data from both the source and target domains, thereby reducing computational demands.

Considering x_i and y_i representing the input and output vectors, TL involves extracting knowledge from the source domain ($\mathcal{D}_s = \{(x_j^s, y_j^s)\}_{j=1}^{N_s}$), and use it to pretrain the model for the target domain ($\mathcal{D}_t = \{(x_i^t, y_i^t)\}_{i=1}^{N_t}$). Here, the effectiveness of TL in updating the model is investigated by varying the number of samples from the newly unseen IC. This includes the following steps:

- **Initial model training:** Initially, the SM model is trained using cross-validation on data from four out of the five ICs, yielding a baseline model f_s. This baseline model provides a starting point for the TL approach.

  For example, the training of the source model for GPR can be expressed as

  $$\{f_s(x, \mathbf{w}_s, \theta_0) \sim \mathcal{GP}(\mu(x), k(x,x') \mid (\mathbf{w}_0, \theta_0)) : x \in \mathcal{D}_s\} \tag{4.16}$$

  where the initial learnable parameters are denoted as $\mathbf{w}_0$ and the trained learnable parameters as $\mathbf{w}_s$. If initial hyperparameters of $f(x)$ is denoted with θ_0, the BO algorithm (given $x \in \mathcal{D}_s$) is applied to tune hyperparameters of $f_s(x)$, after which they are denoted by θ_s.

- **Testing the unseen IC:** Subsequently, the performance of the pretrained baseline model is evaluated on the data from the new unseen IC.

  $$\{f_s(x, \mathbf{w}_s, \theta_s) : x \in \mathcal{D}_t\} \tag{4.17}$$

  However, the results indicated suboptimal performance, highlighting the need for further model refinement.

- **TL with limited samples:** To address the limitations in performance, the transferred model is updated using limited samples from the target domain $\mathcal{D}_t = \{(x_i^t, y_i^t)\}_{i=1}^{N_t}$ alongside the source domain data $\mathcal{D}_s$. For example, the updating of the source model for GPR can be expressed as:

  $$\{f_t(x, \mathbf{w}_t, \theta_s) \sim \mathcal{GP}(\mu(x), k(x,x') \mid (\mathbf{w}_s, \theta_s)) : x \in (\mathcal{D}_s \cup \mathcal{D}_t)\} \tag{4.18}$$

Specifically, N_t values of 1, 5, 10, and 20 samples from the new unseen IC were experimented with to investigate the impact of varying sample sizes of the target domain on model improvement.

4.6 Evaluation metrics

Several metrics were used to compare the performance of the trained ML models. These metrics can be categorised into two groups: metrics that evaluate the accuracy of the models and those that assess the speed of the training and prediction processes. Regarding the first group, root-mean-square error (RMSE), coefficient of determination (R-squared or R^2), and mean-absolute-error (MAE) were used, with the following equations

$$RMSE = \sqrt{\frac{\sum_{i=1}^{n}(y_i - \hat{y}_i)^2}{n}} \tag{4.19}$$

$$R^2 = 1 - \frac{\sum_{i=1}^{n}(y_i - \hat{y}_i)^2}{\sum_{i=1}^{n}(y_i - \bar{y})^2} \tag{4.20}$$

$$MAE = \frac{\sum_{i=1}^{n}|y_i - \hat{y}_i|}{n} \tag{4.21}$$

where n is the number of data points, y is the actual value vector, $\hat{y}$ is the predicted value vector, and $\bar{y}$ is the mean of actual values.

In addition to the metrics used to assess accuracy, two additional metrics were also employed: training time and prediction speed. The former indicates the time required for the model to be trained (in seconds), while the latter represents the number of predictions the model can make per second. Therefore, models with low training times and high prediction speeds are preferred.

4.7 Results and discussion

In this section, the performance of various ML models (mentioned in Section 4.3), considered as the SM, is first compared in the subsection "surrogate model selection". The influence of including or excluding initial configurations (ICs) as complementary input features through label encoding is investigated to select the best models and determine the optimal approach for shaping the feature input. This step is crucial for further evaluations and subsequent steps toward nested cross-validation (NCV) on unseen ICs and updating the SM using TL, as will be discussed in the subsection "Transfer Learning (TL) for Unseen ICs". MATLAB 2022a was used on a laptop with an Intel Core i7-8665U CPU and 16 GB of RAM to train and evaluate ML models.

4.7.1 Surrogate model selection

Various ML models were trained to compare and select those showing the best performance for the next steps. The models were trained under two distinct scenarios with respect to ML inputs: 1. using only DEM interaction parameters, and 2. considering extra inputs to characterise the ICs of the mixture within the hopper (see Figure 3.6). Figure 4.3 illustrates an example of the regression tree models performance for both scenarios. Obviously, the models performance is significantly enhanced in the case of the extra inputs related to ICs. This improvement is anticipated as the segregation (or degree of mixing) of multiple materials heavily depends on their ICs6. The results for the first scenario (i.e., excluding ICs as ML inputs) are given in Table C.2 of Appendix C, where it is evident that the model's performance is unsatisfactory even with optimised hyperparameters. As a result, the models are trained using the second scenario.

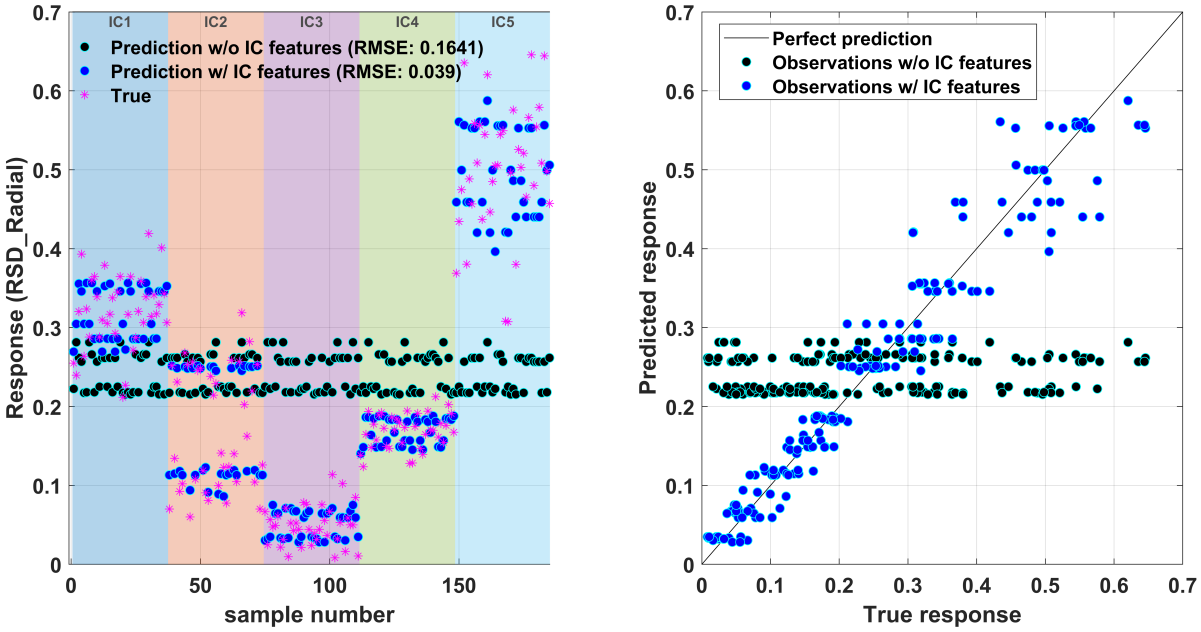

Figure 4.3 Comparison of the impact of input features with (w/) and without (w/o) initial configurations (ICs) on fine-tuned regression tree outcomes using Bayesian optimisation (BO), assessed via 5-fold cross-validation.

The training results of various ML models are presented in Table 4.2, where ICs were included as complementary features. The training was performed with 5-fold cross-validation on 185 samples and 18 features. Optimisable models were fine-tuned using the Bayesian optimisation (BO) algorithm with 50 iterations. Notably, the performance of the models significantly improved when the hyperparameters were optimised using BO, underscoring the importance of fine-tuning hyperparameters in the ML training process. It is also worth mentioning that despite increasing the number of hidden layers and neurons, the performance of ANN did not improve, possibly due to overfitting or vanishing gradient problems [202].

Based on the evaluation metrics employed in this study, the optimal model is characterised by minimal error (i.e., RMSE and MAE), maximal R^2, low training time, and high prediction speed. According to Table 4.2, two models are identified that fulfil the majority of these criteria

Table 4.2 Performance comparison of regression models, including 3 features representing initial configurations (ICs). Optimisable models hyperparameters were fine-tuned using the BO algorithm.

Model	**Adjustments**	**RMSE**	**R^2**	**MAE**	Training time (s)	Prediction speed* (obs/s)
Linear Regression	–	0.0506	0.91	0.0406	9.98	1600
	Interactions	0.0244	0.98	0.0200	33.32	620
	Robust	0.0509	0.91	0.0404	31.00	910
	Stepwise	0.0237	0.98	0.0188	539.56	3000
Regression Tree	Fine	0.0423	0.93	0.0301	28.25	3400
	Medium	0.0420	0.94	0.0293	27.12	3700
	Coarse	0.1288	0.39	0.1048	25.35	3000
	Optimisable (BO)	0.0390	0.94	0.0277	34.97	5600
SVM	Kernel: linear	0.0505	0.91	0.0388	19.18	3500
	Kernel: quadratic	0.0310	0.96	0.0245	17.22	2800
	Kernel: cubic	0.0384	0.95	0.0300	14.18	3400
	Kernel: Fine Gaussian	0.1616	0.04	0.1325	43.12	4700
	Kernel: Medium Gaussian	0.0642	0.85	0.0478	42.76	4500
	Kernel: Coarse Gaussian	0.0755	0.79	0.0585	41.94	3000
	Optimisable (BO)	0.0251	0.98	0.0201	461.24	5900
Ensemble of Trees	Boosted	0.0362	0.95	0.0265	41.19	790
	Bagged	0.0703	0.82	0.0590	40.11	650
	Optimisable (BO)	**0.0231**	**0.98**	**0.0173**	**472.77**	**260**
GPR	Kernel = Exponential	0.0485	0.91	0.0370	36.89	2100
	Kernel = Squared Exponential	0.0239	0.98	0.0184	38.62	1100
	Kernel = Rational Quadratic	0.0239	0.98	0.0184	36.13	2200
	Kernel = Matern 5/2	0.0255	0.98	0.0197	37.68	3400
	Optimisable (BO)	**0.0162**	**0.99**	**0.0119**	**348.61**	**4600**
ANN	One layer [10] neurons	0.0378	0.95	0.0282	34.86	1000
	One layer [25] neurons	0.0452	0.93	0.0349	34.10	2300
	One layer [100] neurons	0.0703	0.82	0.0560	33.43	1200
	Two layers [10,10] neurons	0.0719	0.81	0.0541	32.68	3300
	Three layers [10,10,10] neurons	0.0921	0.69	0.0637	31.86	2800
	Optimisable (BO)	0.0245	0.98	0.0201	602.92	9400

* For reference, each DEM simulation takes approximately 3 hours (10,800 seconds), highlighting the significant speed advantage of the surrogate models.

simultaneously: Gaussian process regression (GPR) and Ensemble of trees, with GPR being superior across all metrics.

4.7.2 Transfer Learning (TL) for Unseen ICs

In this section, the outcomes of the TL method and the updating process utilised in this study, as explained in Section 4.5, are presented. Results for TL-based ensemble learning (TL-Ensemble) and GPR (TL-GPR) are given in Table 4.3 and Table 4.4, respectively. To ensure stability and repeatability, five different random seed numbers were used to initialise the ML models parameters during training. This strategy ensures a reliable assessment of the model's performance. The results in Table 4.3 and Table 4.4 are reported as (mean ś standard deviation) resulting from these five repetitions. All training procedures were performed with 10-fold cross-validation and

Table 4.3 Performance of TLEnsemble averaged over 5 different random seed numbers for initialisation.

Unseen ICs	Num. of samples to update	RMSE		R^2		MAE	
		Validation	Unseen IC	Validation	Unseen IC	Validation	Unseen IC
All ICs were seen		0.0217 ± 0.0012	NA	0.98 ± 0.00	NA	0.0162 ± 0.0010	NA
1	0	0.0286 ± 0.0019	0.1426 ± 0.0116	0.97 ± 0.00	0.00 ± 0.00	0.0211 ± 0.0021	0.1390 ± 0.0123
	1	0.0310 ± 0.0017	0.0987 ± 0.0269	0.97 ± 0.00	0.00 ± 0.00	0.0218 ± 0.0017	0.0927 ± 0.0276
	5	0.0298 ± 0.0026	0.0524 ± 0.0140	0.97 ± 0.01	0.04 ± 0.08	0.0213 ± 0.0018	0.0441 ± 0.0092
	10	0.0296 ± 0.0013	0.0350 ± 0.0061	0.97 ± 0.01	0.04 ± 0.21	0.0216 ± 0.0019	0.0273 ± 0.0047
	20	0.0270 ± 0.0011	0.0259 ± 0.0035	0.98 ± 0.00	0.63 ± 0.08	0.0200 ± 0.0007	0.0220 ± 0.0031
2	0	0.0216 ± 0.0022	0.1023 ± 0.0231	0.98 ± 0.00	0.03 ± 0.01	0.0158 ± 0.0016	0.0845 ± 0.0177
	1	0.0234 ± 0.0042	0.1016 ± 0.0162	0.98 ± 0.01	0.00 ± 0.01	0.0164 ± 0.0021	0.0853 ± 0.0127
	5	0.0287 ± 0.0040	0.0892 ± 0.0154	0.97 ± 0.01	0.01 ± 0.02	0.0196 ± 0.0033	0.0741 ± 0.0121
	10	0.0313 ± 0.0027	0.0569 ± 0.0147	0.97 ± 0.01	0.41 ± 0.28	0.0214 ± 0.0026	0.0467 ± 0.0135
	20	0.0263 ± 0.0031	0.0363 ± 0.0117	0.98 ± 0.00	0.73 ± 0.16	0.0193 ± 0.0023	0.0301 ± 0.0105
3	0	0.0302 ± 0.0041	0.1516 ± 0.0083	0.96 ± 0.01	0.02 ± 0.01	0.0220 ± 0.0023	0.1243 ± 0.0077
	1	0.0330 ± 0.0057	0.1262 ± 0.0324	0.95 ± 0.02	0.00 ± 0.00	0.0229 ± 0.0031	0.1008 ± 0.0243
	5	0.0348 ± 0.0048	0.0789 ± 0.0131	0.95 ± 0.01	0.00 ± 0.01	0.0242 ± 0.0026	0.0655 ± 0.0233
	10	0.0323 ± 0.0043	0.0405 ± 0.0188	0.96 ± 0.01	0.00 ± 0.02	0.0228 ± 0.0025	0.0332 ± 0.0167
	20	0.0301 ± 0.0040	0.0246 ± 0.0061	0.96 ± 0.01	0.15 ± 0.12	0.0210 ± 0.0024	0.0187 ± 0.0050
4	0	0.0262 ± 0.0032	0.1539 ± 0.0220	0.98 ± 0.00	0.00 ± 0.01	0.0195 ± 0.0012	0.1516 ± 0.0016
	1	0.0290 ± 0.0026	0.1099 ± 0.0493	0.97 ± 0.01	0.00 ± 0.03	0.0206 ± 0.0016	0.0958 ± 0.0525
	5	0.0269 ± 0.0025	0.0210 ± 0.0078	0.98 ± 0.00	0.26 ± 0.30	0.0171 ± 0.0016	0.0617 ± 0.0021
	10	0.0257 ± 0.0019	0.0167 ± 0.0025	0.98 ± 0.01	0.37 ± 0.18	0.0196 ± 0.0013	0.0139 ± 0.0024
	20	0.0250 ± 0.0027	0.0126 ± 0.0027	0.98 ± 0.01	0.54 ± 0.21	0.0188 ± 0.0018	0.0101 ± 0.0039
5	0	0.0194 ± 0.0012	0.1858 ± 0.0077	0.97 ± 0.00	0.00 ± 0.00	0.0150 ± 0.0012	0.1799 ± 0.0038
	1	0.0287 ± 0.0053	0.1378 ± 0.0574	0.93 ± 0.03	0.13 ± 0.06	0.0183 ± 0.0023	0.1229 ± 0.0600
	5	0.0350 ± 0.0107	0.1134 ± 0.0596	0.91 ± 0.20	0.25 ± 0.25	0.0228 ± 0.0058	0.1044 ± 0.0616
	10	0.0408 ± 0.0053	0.1068 ± 0.0564	0.88 ± 0.10	0.07 ± 0.08	0.0253 ± 0.0030	0.0967 ± 0.0590
	20	0.0284 ± 0.0031	0.0480 ± 0.0081	0.96 ± 0.01	0.62 ± 0.14	0.0203 ± 0.0020	0.0370 ± 0.0083
Mean	0	0.0252 ± 0.0023	0.1472 ± 0.0073	0.97 ± 0.01	0.00 ± 0.01	0.0187 ± 0.0017	0.1359 ± 0.0062
	1	0.0290 ± 0.0040	0.1130 ± 0.0364	0.96 ± 0.01	0.03 ± 0.10	0.0200 ± 0.0027	0.0612 ± 0.0350
	5	0.0310 ± 0.0051	0.0710 ± 0.0248	0.95 ± 0.02	0.11 ± 0.14	0.0216 ± 0.0030	0.0612 ± 0.0224
	10	0.0320 ± 0.0064	0.0512 ± 0.0197	0.95 ± 0.03	0.30 ± 0.20	0.0226 ± 0.0041	0.0473 ± 0.0193
	20	0.0274 ± 0.0028	0.0295 ± 0.0064	0.97 ± 0.01	0.53 ± 0.14	0.0199 ± 0.0018	0.0235 ± 0.0058

18 features. Additionally, hyperparameters were fine-tuned using the BO algorithm. The hyperparameters of these models together with their search space are provided in Table C.3 and Table C.4 in Appendix C.

Initially, the models (i.e., Ensemble learning and GPR) were cross-validated using all 185 available samples, given ten folds to establish a benchmark for comparison. The results are displayed in the first row of Table 4.3 and Table 4.4, labelled as "All ICs were seen". Then, the transfer learning approach was iteratively applied across all ICs. For each iteration, one IC was excluded, and the model was pre-trained on the remaining four ICs (i.e., on 4Œ37 = 148 samples) via a 10-fold cross-validation coupled with BO fine-tuning of hyperparameters. The results of the validation phase are presented under "Validation", excluding the training phases results. Next, the model's performance was tested on the "unseen IC" as the target domain of TL that was previously excluded. Tests were run where the pre-trained model was retrained with 0, 1, 5, 10, and 20 samples from the unseen IC, monitoring its performance each time. These test results are shown under "Unseen IC". For an overall assessment of the model's performance across all unseen ICs, the average of the TL-based outcomes was calculated across all unseen ICs for retraining with different available samples of 0, 1, 5, 10, and 20 from the target domain. These averages are displayed at the bottom of Table 4.3 and Table 4.4, indicated as "Mean".

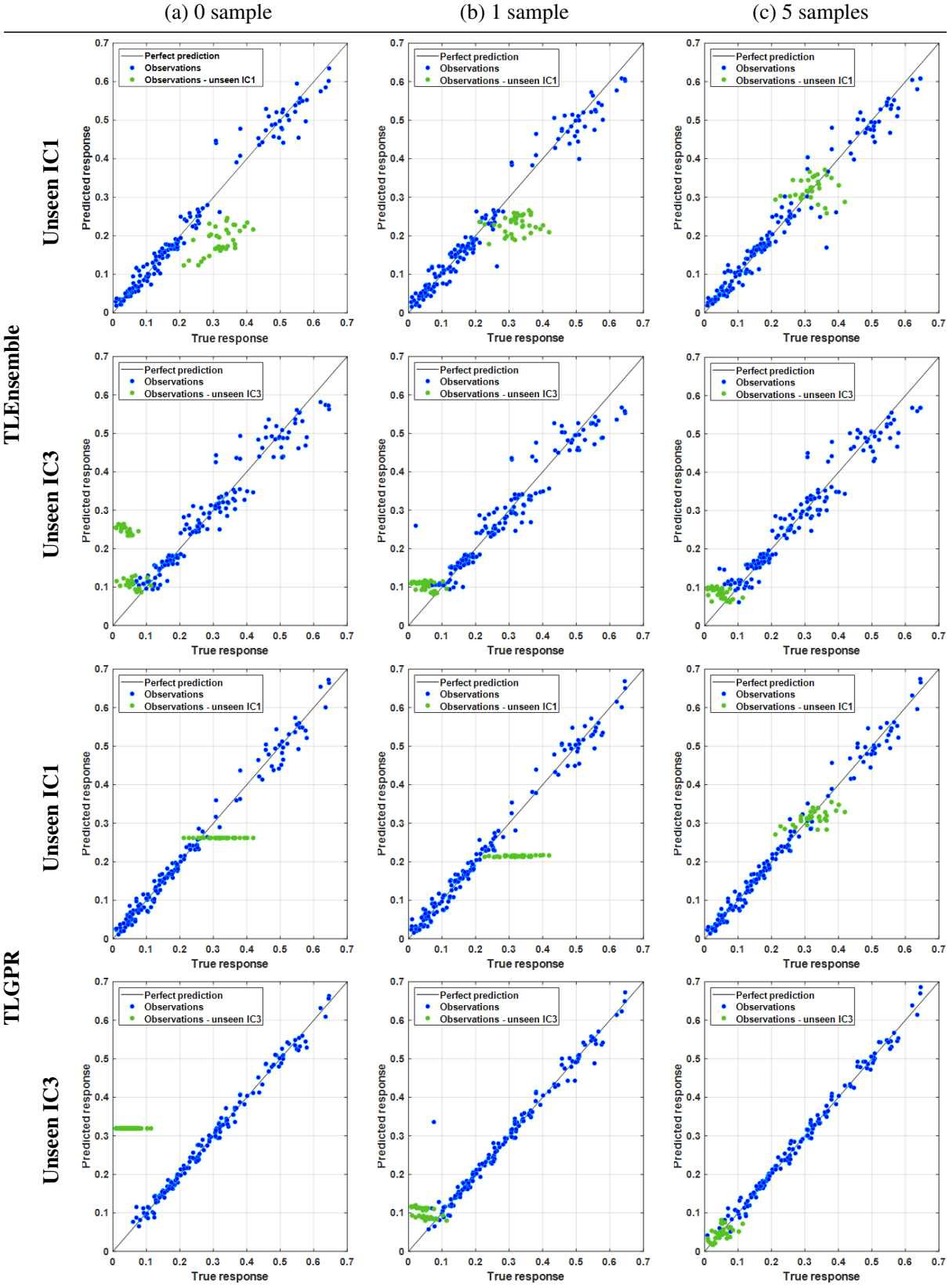

Figure 4.4 Predicted and true responses for unseen initial configurations IC1 and IC3 with TL-Ensemble and TL-GPR, updated with varying numbers of samples: (a) 0 (no update), (b) 1, and (c) 5 from the unseen IC.

Table 4.4 Performance of TLGPR averaged over 5 different random seed numbers for initialisation.

Unseen ICs	Num. of samples to update	RMSE		R^2		MAE	
		Validation	Unseen IC	Validation	Unseen IC	Validation	Unseen IC
All ICs were seen		0.0150 ± 0.0011	NA	0.99 ± 0.00	NA	0.0112 ± 0.0006	NA
1	0	0.0194 ± 0.0009	0.1024 ± 0.0553	0.99 ± 0.00	0.05 ± 0.10	0.0144 ± 0.0006	0.0914 ± 0.0483
	1	0.0234 ± 0.0007	0.0515 ± 0.0351	0.98 ± 0.01	0.38 ± 0.33	0.0152 ± 0.0012	0.0452 ± 0.0335
	5	0.0197 ± 0.0011	0.0205 ± 0.0097	0.99 ± 0.00	0.77 ± 0.23	0.0145 ± 0.0008	0.0166 ± 0.0075
	10	0.0188 ± 0.0019	0.0210 ± 0.0139	0.99 ± 0.00	0.74 ± 0.22	0.0141 ± 0.0015	0.0176 ± 0.0108
	20	0.0177 ± 0.0012	0.0147 ± 0.0055	0.99 ± 0.00	0.90 ± 0.06	0.0130 ± 0.0010	0.0117 ± 0.0033
2	0	0.0140 ± 0.0011	0.1719 ± 0.0070	0.99 ± 0.00	0.20 ± 0.02	0.0114 ± 0.0007	0.1526 ± 0.0074
	1	0.0186 ± 0.0034	0.1015 ± 0.0082	0.99 ± 0.00	0.00 ± 0.00	0.0117 ± 0.0007	0.0839 ± 0.0063
	5	0.0176 ± 0.0032	0.0571 ± 0.0214	0.99 ± 0.00	0.40 ± 0.36	0.0116 ± 0.0010	0.0480 ± 0.0189
	10	0.0155 ± 0.0008	0.0320 ± 0.0034	0.99 ± 0.00	0.82 ± 0.03	0.0112 ± 0.0005	0.0266 ± 0.0032
	20	0.0159 ± 0.0011	0.0224 ± 0.0048	0.99 ± 0.00	0.90 ± 0.04	0.0111 ± 0.0011	0.0271 ± 0.0038
3	0	0.0158 ± 0.0011	0.1803 ± 0.1031	0.99 ± 0.00	0.00 ± 0.00	0.0118 ± 0.0007	0.1758 ± 0.1044
	1	0.0220 ± 0.0056	0.0575 ± 0.0269	0.98 ± 0.01	0.02 ± 0.06	0.0126 ± 0.0014	0.0502 ± 0.0254
	5	0.0166 ± 0.0038	0.0278 ± 0.0068	0.99 ± 0.01	0.10 ± 0.11	0.0123 ± 0.0022	0.0227 ± 0.0060
	10	0.0156 ± 0.0013	0.0247 ± 0.0069	0.99 ± 0.00	0.21 ± 0.18	0.0121 ± 0.0005	0.0227 ± 0.0067
	20	0.0168 ± 0.0011	0.0191 ± 0.0023	0.99 ± 0.00	0.43 ± 0.10	0.0123 ± 0.0009	0.0156 ± 0.0023
4	0	0.0174 ± 0.0021	0.0209 ± 0.0073	0.99 ± 0.00	0.23 ± 0.28	0.0136 ± 0.0010	0.0186 ± 0.0059
	1	0.0184 ± 0.0019	0.0158 ± 0.0044	0.99 ± 0.00	0.46 ± 0.27	0.0142 ± 0.0014	0.0134 ± 0.0039
	5	0.0177 ± 0.0016	0.0100 ± 0.0030	0.99 ± 0.01	0.74 ± 0.08	0.0133 ± 0.0007	0.0091 ± 0.0020
	10	0.0171 ± 0.0010	0.0110 ± 0.0030	0.99 ± 0.01	0.71 ± 0.15	0.0133 ± 0.0007	0.0091 ± 0.0024
	20	0.0161 ± 0.0007	0.0070 ± 0.0018	0.99 ± 0.00	0.90 ± 0.04	0.0120 ± 0.0008	0.0055 ± 0.0025
5	0	0.0163 ± 0.0007	0.0957 ± 0.0256	0.98 ± 0.00	0.13 ± 0.26	0.0124 ± 0.0005	0.0846 ± 0.0253
	1	0.0295 ± 0.0139	0.0641 ± 0.0244	0.91 ± 0.20	0.40 ± 0.35	0.0140 ± 0.0016	0.0503 ± 0.0190
	5	0.0181 ± 0.0022	0.0415 ± 0.0147	0.98 ± 0.01	0.72 ± 0.21	0.0132 ± 0.0012	0.0328 ± 0.0108
	10	0.0180 ± 0.0019	0.0263 ± 0.0044	0.98 ± 0.00	0.90 ± 0.02	0.0133 ± 0.0012	0.0214 ± 0.0022
	20	0.0168 ± 0.0012	0.0235 ± 0.0064	0.99 ± 0.00	0.81 ± 0.05	0.0125 ± 0.0008	0.0142 ± 0.0027
Mean	0	0.0166 ± 0.0010	0.1142 ± 0.0393	0.99 ± 0.00	0.08 ± 0.13	0.0125 ± 0.0007	0.1050 ± 0.0383
	1	0.0224 ± 0.0063	0.0581 ± 0.0198	0.97 ± 0.02	0.25 ± 0.20	0.0150 ± 0.0013	0.0486 ± 0.0177
	5	0.0180 ± 0.0021	0.0314 ± 0.0113	0.99 ± 0.00	0.55 ± 0.23	0.0131 ± 0.0012	0.0256 ± 0.0093
	10	0.0170 ± 0.0041	0.0230 ± 0.0099	0.99 ± 0.00	0.67 ± 0.14	0.0127 ± 0.0010	0.0189 ± 0.0051
	20	0.0167 ± 0.0011	0.0174 ± 0.0036	0.99 ± 0.00	0.81 ± 0.05	0.0123 ± 0.0008	0.0142 ± 0.0027

To visually illustrate the impact of the updating process on the pre-trained TL-SMs, Figure 4.4 shows predicted versus true responses for two different unseen initial configurations, IC1 and IC3, where they were updated with 0 (no update), 1, and 5 samples from the target domain. The models' predictions were initialised using the first random seed number in this figure. As illustrated, providing even a few samples from the unseen IC (i.e., the target domain) for updating leads to a significant improvement.

Figure 4.5 illustrates a comparison between the "mean" performance of TL-Ensemble and TL-GPR across different numbers of available samples from the unseen IC. As shown, TL-GPR consistently outperforms Ensemble-TL across all available sample sizes, highlighting the superiority of TL-GPR over TL-Ensemble. Consequently, attention is focused on TL-GPR for further analysis of the results.

Figure 4.6 illustrates the reduction in RMSE in percentage for different sample sizes used to update the TL-GPR model. The reduction was calculated as $(|RMSE_{ICi} - RMSE_{IC0}|/RMSE_{IC0})100$, where (i=1,5,10,20) corresponds to different numbers of samples to re-train SM, and IC0 denotes the case where no update happens to the pre-trained model. The bar graph demonstrates that updating the TL-GPR model with just one sample from the unseen IC results in a significant reduction ($\approx$50%) in the RMSE. Figure 4.5(a) also shows that by updating the model with

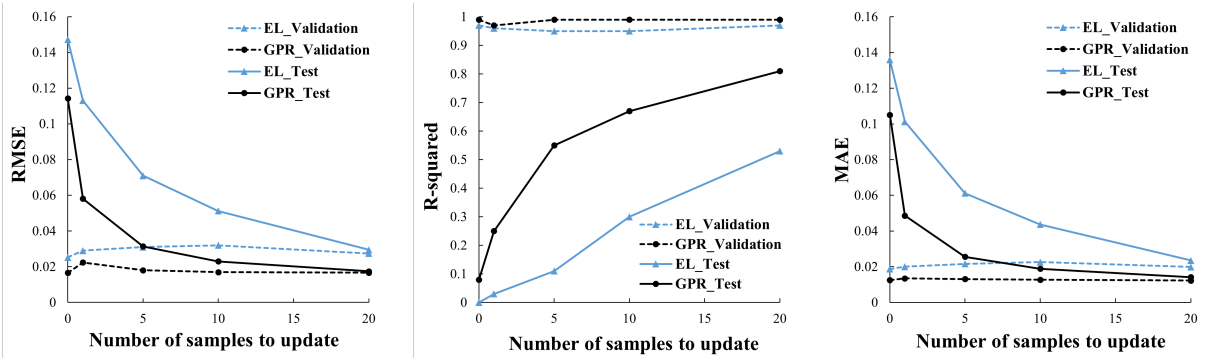

(a) (b) (c)

Figure 4.5 Comparison between the mean performances of TL-Ensemble and TL-GPR during validation and test phases for different numbers of available samples from unseen IC to update in terms of (a) RMSE, (b) R^2, and (c) MAE.

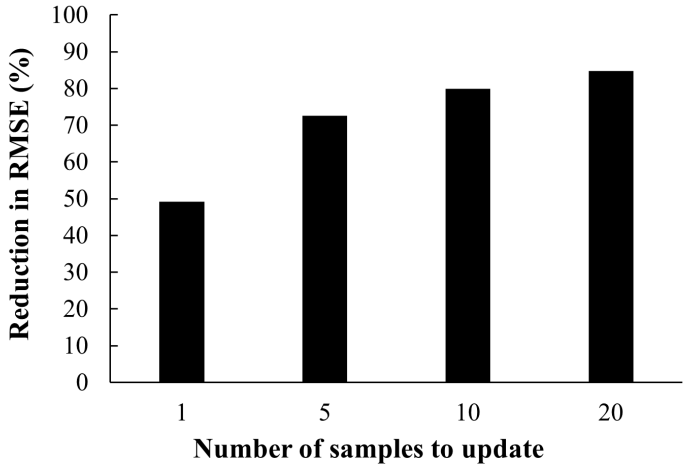

Figure 4.6 Reduction in RMSE of TL-GPR model following updating with different numbers of samples from unseen ICs.

only a few new samples (e.g., 5 samples) from the unseen IC, its accuracy for the new IC can approach that of the validation set. This finding underscores the efficiency of updating the SM with a minimal number of new DEM simulations to achieve improved accuracy of the SM for unseen IC.

It is important to note that the results and analyses discussed above are based on the average performance of the TL-based model across all ICs. However, according to Table 4.4, the models performance varies depending on which IC is considered as unseen. To facilitate a clearer comparison, Figure 4.7 presents the RMSE and R^2 of TL-GPR across all ICs and for different numbers of samples used to update the pre-trained model. It reveals that, when the model is not updated (i.e., 0 sample), the TL-GPR model exhibits the poorest performance for IC3 and IC2, characterised by the highest RMSE and lowest R^2.

The observed performance for IC3, where materials within the hopper are fully mixed (see Figure 3.6), was anticipated. This is because there is no comparable data in the training dataset; the other four initial configurations (IC1, IC2, IC4, and IC5) have fully segregated initial configurations, leading to a far different data distribution for IC3. Similarly, the relatively less

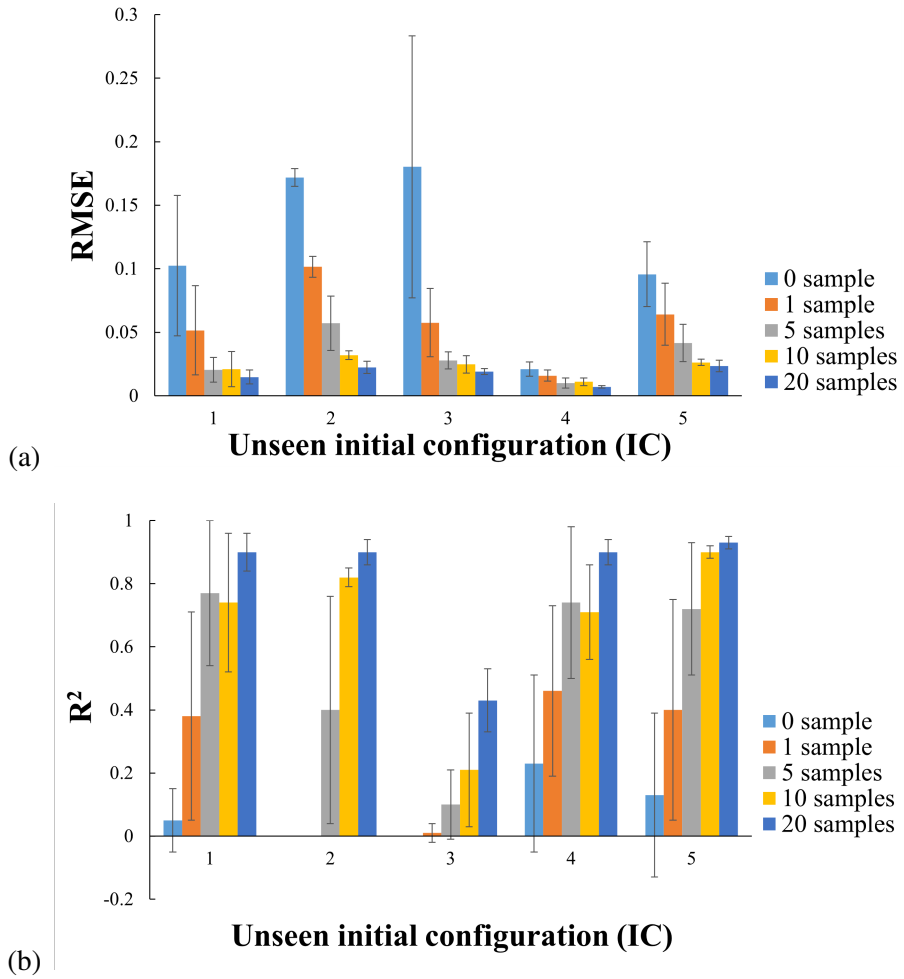

Figure 4.7 Accuracy of TL-GPR across various unseen ICs and for different numbers of samples to update the model in terms of (a) RMSE and (b) R^2.

optimal performance of the model for IC2 can be attributed to its unique feature, i.e., having a reversed layering order, opposite to IC1, IC4, and IC5. Nevertheless, in both IC2 and IC3 cases, after updating the model with only a few data points, a significant improvement in performance is observed. For instance, in IC3, updating the model with only 1 and 5 samples results in a remarkable reduction in RMSE by 68% and 85%, respectively.

4.8 Conclusion

In this chapter, a machine learning (ML)-based framework for building surrogate models (SMs) that link DEM interaction parameters to segregation outcomes in multi-component mixtures was developed and demonstrated. By comparing several ML algorithms, it was shown that Gaussian Process Regression (GPR) and Ensemble Learning provided the most accurate predictions of radial segregation when the initial configuration (IC) of the mixture was properly incorporated through feature engineering. Fine-tuning of hyperparameters via Bayesian optimisation proved essential for achieving optimal SM performance.

To further enhance efficiency, a transfer learning (TL)-based approach was implemented

that reuses knowledge gained from previously seen ICs to predict segregation in unseen configurations. This adaptive TL strategy, particularly using GPR, demonstrated high accuracy with minimal additional simulation data, which significantly reduces the data requirements for new scenarios.

The findings indicate that the performance of TL-SMs varied depending on the specific unseen IC. When testing the pre-trained TL-SMs with new ICs possessing specifications not included in the source dataset, their performance appears to be relatively lower. For instance, IC3 is the only configuration out of five in which the materials are fully-mixed, and the TL-SMs performance for IC3 was inferior compared to other ICs. However, the performance significantly improved after updating the model with a few samples from the "unseen IC". For instance, the RMSE of TL-GPR was reduced by an average of 50% by retraining the model with just one additional sample, highlighting the adaptability and effectiveness of the proposed adaptive TL approach.

While these developments provide a foundation for efficient and adaptive modelling of granular segregation, the current work remains focused on predictive modelling. However, the ultimate goal in this thesis is not only to predict but also to calibrate the DEM parameters systematically against experimental observations.

The next chapter builds directly upon this chapter by applying the developed surrogate modelling framework to the systematic calibration of DEM models for two-component mixtures. Using experimental measurements both at bulk and particle scales as targets, the next chapter demonstrates how surrogate-based optimisation can assist in efficiently and accurately calibrating DEM models.

Chapter 5

Systematic Calibration of DEM Models for Multi-Component Segregation*

In Chapter 4, a surrogate modelling framework was developed to efficiently predict multi-component segregation based on DEM parameters and features describing the initial configuration of the mixture. It was shown that adaptive transfer learning can significantly reduce the computational effort required to predict segregation in previously unseen initial configurations.

This chapter builds on the insights from Chapter 3, in which the most influential DEM parameters were identified, and on the surrogate modelling approach introduced in Chapter 4. These findings are now applied to systematically calibrate DEM models for multi-component mixtures. A two-component pelletsinter mixture, typical of blast furnace operations, is used as the representative case. The proposed calibration framework integrates sensitivity analysis, surrogate modelling with adaptive sampling, and genetic algorithm-based optimisation. This approach is expected to reduce the number of DEM simulations required, which facilitates efficient and accurate DEM model calibration.

*This chapter is based on: A. Hadi, Y. Pang, D.L. Schott, *Systematic DEM calibration of two-component mixtures using AI-accelerated surrogate models*, *Powder Technology* (2025). https://doi.org/10.1016/j.powtec.2025.121190

5.1 Introduction

DEM has become a widely used computational tool for simulating granular materials as it provides particle-level insights into complex granular flows that are virtually impossible to obtain through experiments [153, 203–207]. However, the reliability of DEM outcomes heavily depends on the proper determination of input parameters, which remains a significant challenge.

The use of surrogate models for calibrating DEM models has proven to be an efficient approach [174]. A Surrogate model (SM), also known as a metamodel, is an approximation of a more complex and computationally demanding model, such as DEM [177]. SMs are especially suitable for DEM calibration as they are effective at finding a global optimum, handling parameter constraints, and are computationally efficient [174]. In this approach, an SM is first developed to capture the relationship between DEM parameters and outputs. The outputs typically represent the differences between experimental and DEM measurements of key performance indicators (KPIs), which are minimised during the calibration process. The SM is then used during the optimisation process to identify the optimal (i.e., calibrated) parameter sets. The key advantage of this approach is the significant reduction in computational time, as the fast surrogate model replaces costly DEM simulations during optimisation [174].

With the rapid advancement of AI, machine learning (ML)-based surrogate modelling has gained popularity in recent years. In the context of DEM calibration, several studies have explored the use of various ML models to create surrogate models. These include Gaussian process regression (GPR) and Kriging [174, 179–182], multi-objective reinforcement learning [183], Bayesian filtering [184, 185], multi-variate regression analysis [186], neural networks [187], and random forest (RF) [173].

Despite the advancements in DEM calibration approaches, several challenges remain. First, while SMs can significantly accelerate the optimisation process, the efficient development of accurate SMs is still a big challenge [192]. Second, most studies develop SMs for a limited subset of DEM parameters. A key drawback is that the selection of the parameters to be calibrated is often subjective, which can lead to overlooking other potentially significant parameters. Third, the majority of existing studies focus on the calibration of single-component systems, while DEM calibration for multi-component mixturesdespite being common in industrial applicationsis rare [149, 208, 209]. Multi-component mixtures introduce additional challenges, including a larger set of DEM parameters for individual materials as well as their interactions, the need to account for varying component ratios, and changes in layering order.

This chapter aims to address these challenges by developing a systematic and efficient calibration framework based on ML-based SMs for DEM modelling of multi-component mixtures. As a case study, the framework is applied to the mixture of iron ore pellets and sinter, which is used in blast furnace steelmaking. The proposed framework integrates sensitivity analysis, efficient surrogate modelling, and optimisation techniques to calibrate the DEM parameters effectively and efficiently. Furthermore, the robustness and generalisability of the calibrated parameters are validated across different mass ratios and layering orders of the mixture.

The structure of the chapter is as follows. Section 5.2 describes the experimental setup, procedures, and results. In section 5.3, the DEM model and the proposed systematic calibration framework are outlined. Finally, this chapter concludes with key findings and suggestions for future research endeavours.

5.2 Experiments

This section covers the materials, experimental setup, and procedure, as well as the methodology for measuring the key performance indicators (KPIs) and their corresponding results.

5.2.1 Materials

Figure 5.1 shows iron ore pellets and sinter used in this study. As shown, they have similar colours, making them difficult to distinguish during experiments. To address this issue, the pellets were coated with a thin layer of water-based white/blue paint.[1] In the previous work, a comparative analysis of the angle of repose (AoR) in the ledge test was performed using both painted and unpainted particles [149]. The results showed no significant difference in the AoR, which validates the use of painted particles in the experiments.

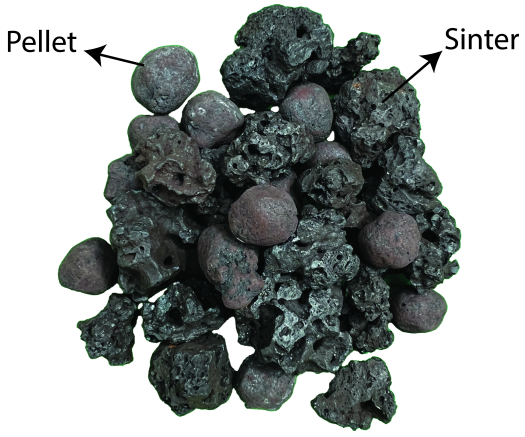

Figure 5.1 A mixture of iron ore pellets and sinter (from [210]).

The size distribution of both pellets and sinter was measured using sieves. The particle density (ρ_s) was also determined by measuring the weight of a number of particles with known volume and dividing their weight by volume. The results of the particle size distribution and particle density measurements are reported in Table 5.1.

5.2.2 Draw down test

The draw down test has been widely used in previous studies to calibrate DEM models [102, 211]. Figure 5.2 schematically illustrates the draw down test setup used in this study. The setup consists of an upper and lower box positioned vertically, with load cells attached to the frame supporting the upper box. The outlet of the upper box is initially sealed with a plate, which can be released using electromagnets.

The procedure for each test is as follows. First, the upper box is filled with 40 kg of materials

[1] Initially, white paint was used, but it was later found that blue provides better contrast, making the use of the "Lab" colour space more effective for image analysis. This colour space separates lightness (L) from chromaticity, where the "a" channel represents the redgreen axis and the "b" channel represents the yellowblue axis.

Table 5.1 The results of the particle size distribution and particle density measurements.

Material properties	**Pellets**	**Sinter**
Particle size distribution	10–12.5 (mm): 48% 12.5–16 (mm): 52%	5.6–8 (mm): 36.4% 8–10 (mm): 23.1% 10–12.5 (mm): 17.6% 12.5–16 (mm): 13.4% 16–20 (mm): 5.1% 20–25 (mm): 4.4%
Solid density (ρ_s)	3602.4 ± 61.7 (kg/m^3)	3449.0 ± 34.0 (kg/m^3)

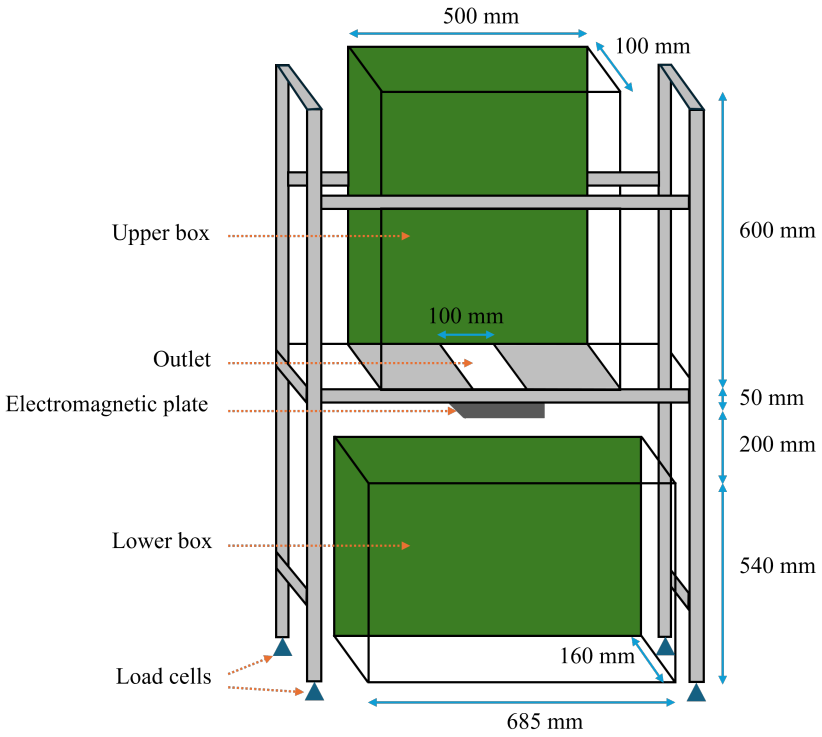

Figure 5.2 Schematic of the draw down test setup used in this study with detailed dimensions.

(Figure 5.3(a)). Next, the magnetic outlet of the upper box is manually removed, allowing the material to discharge into the lower box (Figure 5.3(b)). During discharging, load cells continuously record the remaining weight of the material in the upper box at a frequency of 50 Hz (every 0.02 seconds). This data is used to calculate the mass flow rate and the mass of the materials collected in the lower box. Once the discharge is finished, a photo is captured using a camera to measure the shear angle and the angle of repose (Figure 5.3(c)). Experiments were performed for three different mass ratios of pellet-sinter: 5050, 7525, and 2575. Additionally, for 50-50 ratio, a set of experiments with reverse layering (i.e. sinter-pellets-sinter-pellets from bottom to top) was conducted.

In addition to these measurements, the segregation of pellets and sinter in the lower box was evaluated. As shown in Figure 5.3(a), the upper box was filled with four alternating layers of pellets and sinter. This layering approach was chosen instead of mixing materials to keep con-

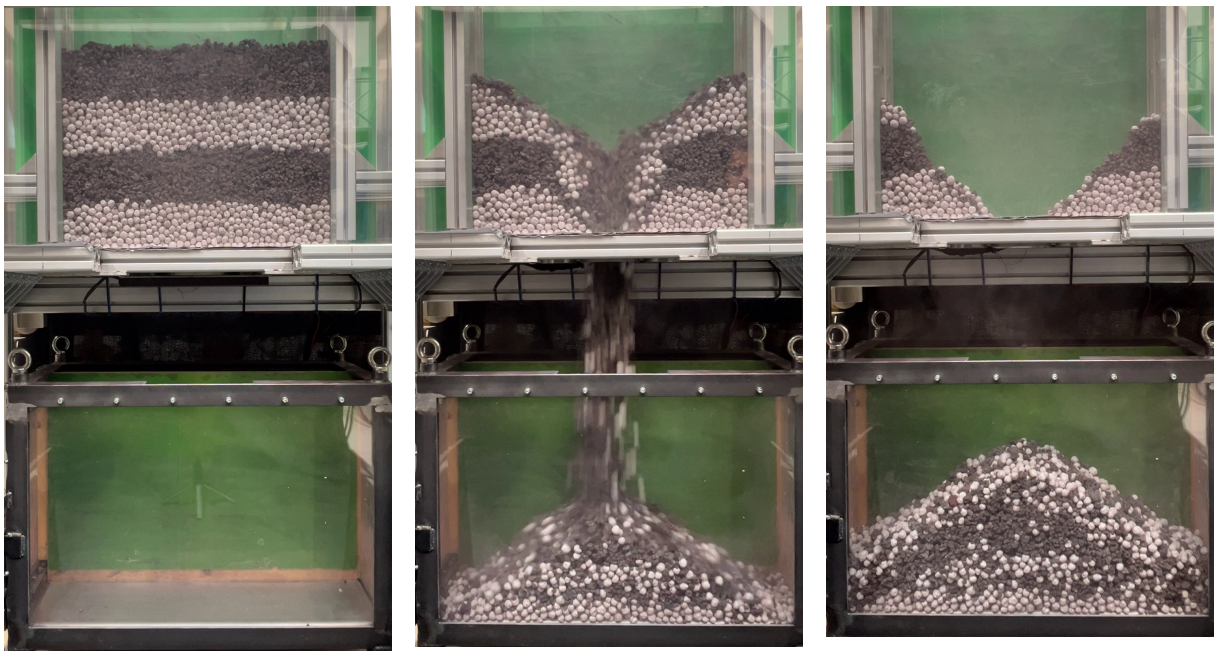

(a) (b) (c)

Figure 5.3 The draw down test procedure. (a) upper box filled with materials where white and dark grey particles represent pellets and sinter, respectively, (b) discharging of materials into the lower box, and (c) the end of a test.

trol over the initial configuration and remove the uncertainty about the segregation produced while filling the upper box [212]. Moreover, previous studies have shown that the initial configuration of materials significantly influences downstream segregation [210, 213]. Therefore, ensuring a consistent initial configuration is crucial, especially when the experiments are used for calibrating or verifying segregation in a DEM model. The same photo used to measure the AoR was analysed to evaluate the segregation in the lower box.

These measurements highlight the versatility of the draw down test in measuring multiple key performance indicators (KPIs) in a single experiment. These KPIs include the shear angle in the upper box, the AoR and segregation in the lower box, the mass flow rate, and the total mass discharged into the lower box.

5.2.3 Measurement of KPIs

I. Shear angle and angle of repose. MATLABs image processing toolbox was used to measure the shear angle and the angle of repose following the same methodology outlined in the previous work [149]. First, the raw image was pre-processed, which involves cropping the image to focus on the region of interest (RoI), removing the background, and inserting an artificial background for improved contrast, as shown in Figure 5.4(a). Next, the pre-processed image was binarized (Figure 5.4(b)), and the edge of the particles was extracted (Figure 5.4(c)). Finally, a linear line was fitted to the detected edge, the slope of which was calculated to determine the shear angle or the angle of repose.

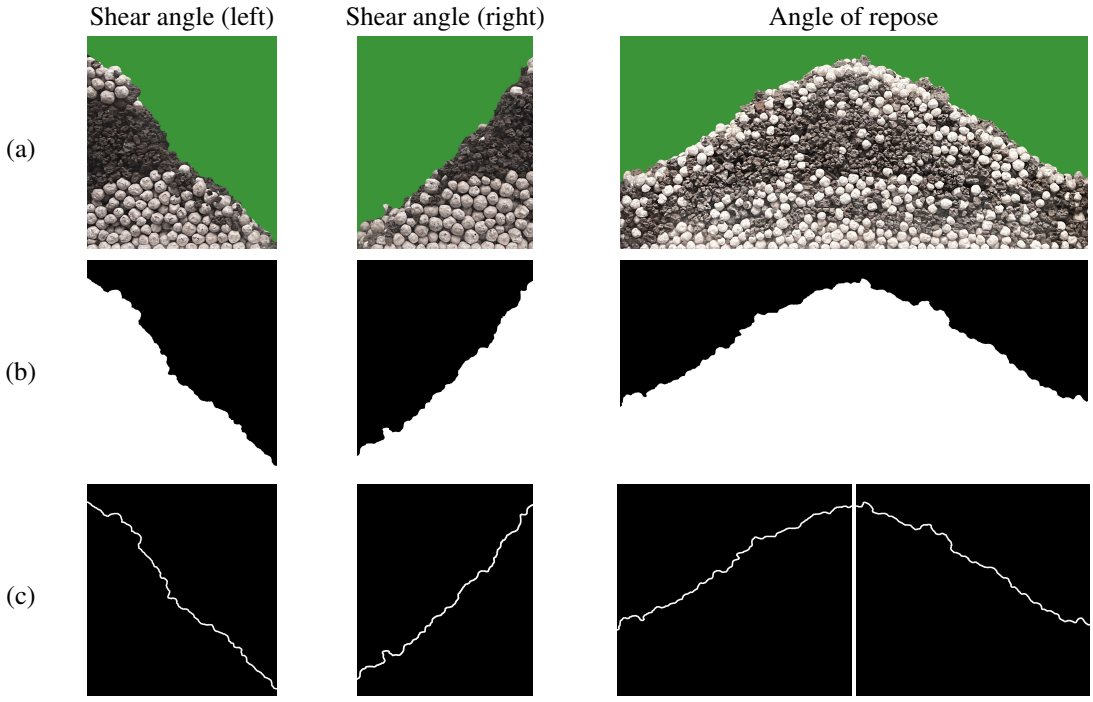

Figure 5.4 The process of measuring the shear angle or the angle of repose in an image: (a) the pre-processed image, (b) the binarized image, and (c) the extracted edge.

The average of two measured angles in the upper box (shear angle (left) and (right) in Figure 5.4 was considered as the shear angle. For the angle of repose in the lower box, the heap was divided at the center (as shown in Figure 5.4(c)), and the angle of repose was determined separately for each half of the heap. The average of these two values was reported as the final angle of repose. While some studies exclude the flattened portion of the heap from the calculation of the angle of repose [211, 214], the entire heap profile was used for consistency. This is because there is no clear rule for determining the extent of the flattened portion to exclude.

II. Segregation in the lower box. Image analysis was employed to evaluate segregation in the lower box. Compared to physical sampling, this method is non-intrusive and avoids the challenge of separating the components for materials overlapping in size [26, 169]. To quantify segregation, the same pre-processed image used for calculating the angle of repose was used (cf. right column in Figure 5.4(a)). The image was then segmented using the colour thresholding capabilities of MATLABs image processing toolbox to create two separate figures: one in which white pixels represent pellets (Figure 5.5(b), right) and the other in which white pixels represent sinter particles (Figure 5.5(b), left). Subsequently, the image was divided into slices, either vertically (Figure 5.5(c)) or horizontally (Figure 5.5(d)), to measure segregation in the respective direction. The effect of the slice size on segregation measurements was evaluated, resulting in 6 and 3 slices for the horizontal and vertical directions, respectively. The pixel fraction of each component (C_{i_k}) in each slice was then measured as

$$C_{i_k} = \frac{N_{i_k}}{\sum_{i=1}^{n} N_{i_k}} \tag{5.1}$$

where N_{i_k} is the number of pixels for component i in the kth slice and n is the total number of components (pellets and sinter). The average (μ_i) and standard deviation (σ_i) of pixel fractions are calculated across all slices for each component. Finally, the Relative Standard Deviation (RSD), used as the segregation index, was calculated as

$$\mathrm{RSD}_i = \frac{\sigma_i}{\mu_i} \tag{5.2}$$

where higher RSD denotes higher segregation.

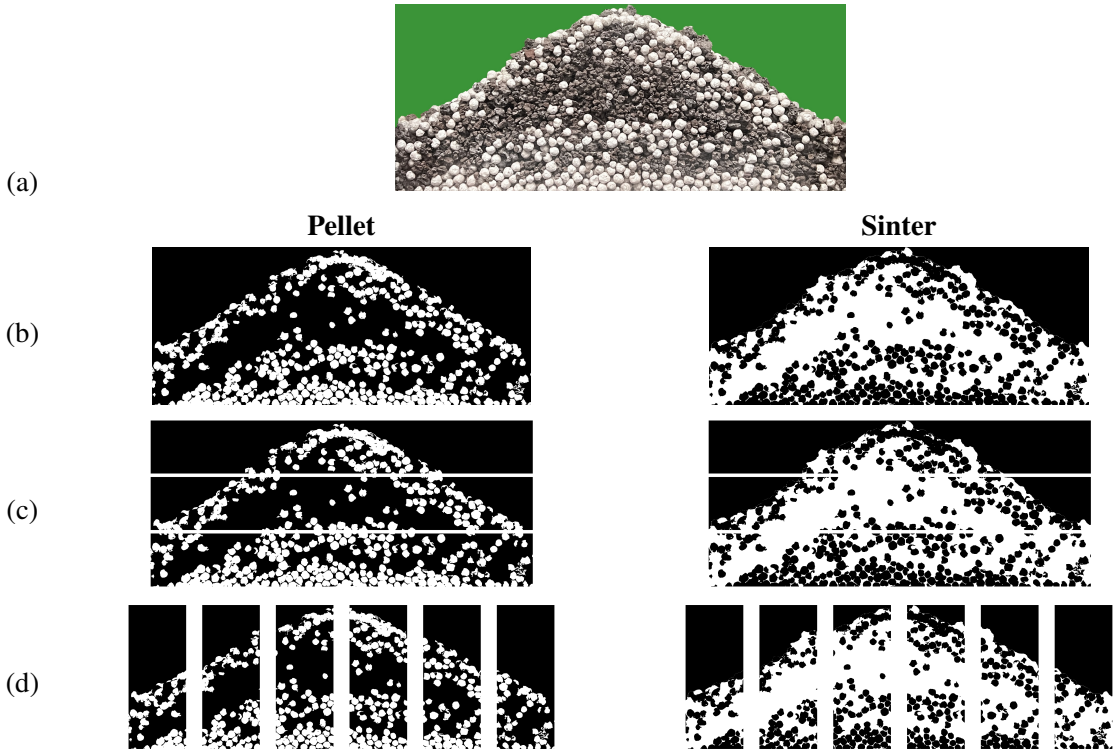

Figure 5.5 The process of image segmentation and slicing for quantifying segregation: (a) the original pre-processed image, (b) the binary images, and the sliced images used for calculating, (c) vertical segregation, and (d) horizontal segregation.

III. Mass flow rate and mass in the lower box. The load cell data recorded during discharge was used to calculate the mass flow rate. As the raw data contained significant noise, a Gaussian filter was applied to smooth the data. Figure 5.6 shows an example of the mass in the upper box plotted against time. The steady mass flow rate was determined from the slope of the nearly linear segment between 0.5 and 2.0 seconds, illustrated by the shaded area in Figure 5.6. Additionally, the discharged mass in the lower box was determined by subtracting the remaining mass in the upper box from the total initial mass of the material.

5.2.4 Results of the experiments

Table 5.2 summarises the results of the measurements mentioned above for all tested pellet-sinter mass ratios as well as the reverse layering case. For the complete experimental data, readers are referred to the published dataset [215].

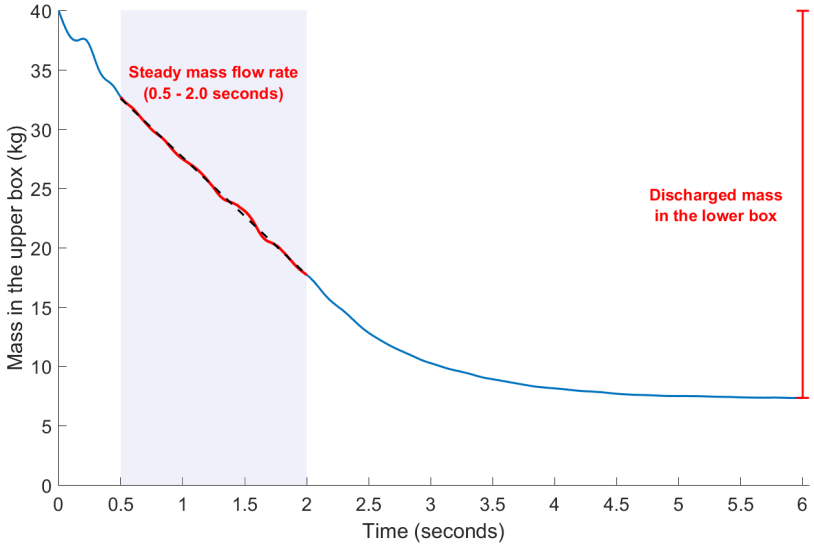

Figure 5.6 An example of the mass in the upper box plotted against time, illustrating the calculation of the mass flow rate and the discharged mass in the lower box.

The results show that increasing the sinter ratio in the mixture leads to a higher angle of repose and shear angle, which aligns with the findings of Chakrabarty et al. [147]. This effect is expected due to the highly irregular shape of sinter particles compared to the near-spherical shape of pellets (see Figure 5.1). Also, this study is one of the first of its kind to investigate the impact of layering order, showing that reversing the order slightly reduces the shear angle compared to the normal 50-50 case, while the angle of repose remains largely unchanged.

The mass flow rate remains relatively constant across different mass ratios and layering orders, indicating that these factors do not significantly influence discharge behaviour under the tested conditions. The mass discharged into the lower box shows a negative correlation with the shear angle, as stated by Wasserfall et al. [211].

For segregation, interpreting the effect of mass ratio using RSD is challenging. Since the RSD formula (Eq. 5.2) normalises the standard deviation by the mean, and the mean is directly linked to the mass ratio, no meaningful conclusions can be drawn about the influence of the mass ratio on segregation [210]. In the reverse layering case, lower horizontal and higher vertical segregation were observed, which is in agreement with the findings of a previous study [210].

Table 5.2 Results of KPIs measured in the experiments. The values are presented with their 95% confidence intervals.

Pellets–sinter mass ratio	**Angle of repose** (°)	**Shear angle** (°)	**Mass flow rate (kg/s)**	**Mass in the lower box (kg)**	**Segregation (RSD)**	
					Vertical	**Horizontal**
50–50	29.5 ± 0.5	42.5 ± 1.6	10.29 ± 0.35	32.32 ± 0.55	0.264 ± 0.07	0.121 ± 0.04
75–25	28.6 ± 0.7	39.0 ± 1.5	10.29 ± 0.10	33.09 ± 0.12	0.151 ± 0.03	0.082 ± 0.02
25–75	29.6 ± 0.8	44.8 ± 1.2	10.24 ± 0.45	32.00 ± 0.48	0.422 ± 0.09	0.116 ± 0.025
Reverse layering	29.7 ± 0.5	41.0 ± 1.6	10.39 ± 0.56	32.97 ± 0.20	0.320 ± 0.03	0.112 ± 0.053

5.3 DEM model

The materials and experimental setup are modelled using DEM. Before presenting the model setup in detail, the calibration approach is first introduced.

5.3.1 Systematic calibration/verification framework

Figure 5.7 illustrates an overview of the systematic calibration framework adopted in this study. The calibration process starts with the reference case, i.e., 50-50 pellet-sinter mass ratio. Next, the calibrated parameters are validated by testing their applicability to the other two mass ratios: 75-25 and 25-75. These steps are further explained in the following subsections.

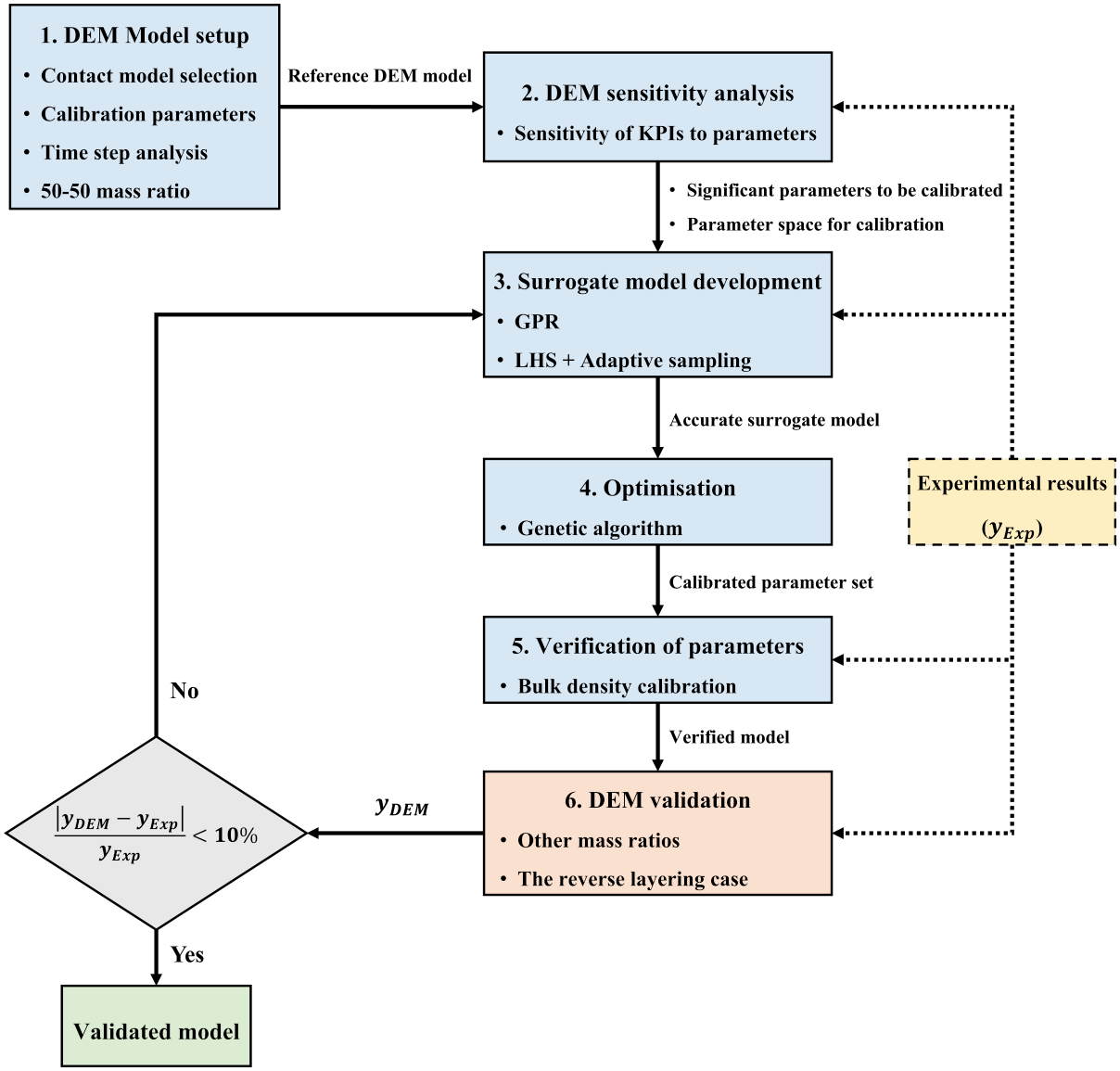

Figure 5.7 An overview of the systematic calibration approach adopted in this study.

5.3.2 Model setup

I. Contact model. The HertzMindlin contact model combined with an elasticplastic spring-dashpot rolling friction model (type C, as classified by Ai et al. [145]) was employed for the DEM simulations. This contact model has already been described in detail in Chapter 3, Section 3.2.1, and has been successfully applied in previous studies on pellets and sinter [146, 147, 149].

II. Fixed DEM parameters. The intrinsic material properties, including the shear modulus and Poissons ratio, were obtained from relevant literature, as listed in Table 5.3 [146, 147]. Pellets were modelled as spheres due to their nearly spherical shape (see Figure 5.1). However, sinter particles, which have highly irregular shapes (see Figure 5.1), were represented using a three-sphere clump shape, as shown in Table 5.3. This shape has been successfully used in previous studies to model sinter particles [81, 147].

For particle size distribution and particle density, the experimentally measured values reported in Table 5.1 were used.

Table 5.3 Intrinsic material properties used in DEM simulations.

DEM Parameter	Pellet	Sinter	Geometry
Shear modulus (G)	1×10^8 Pa	1×10^8 Pa	2×10^{11} Pa
Poissons ratio (ν)	0.25	0.25	0.3
Particle shape			NA

III. DEM parameters to calibrate. All DEM parameters, excluding the fixed parameters listed in Table 5.1 and Table 5.3, were considered for calibration in this study. This included both particle-particle and particle-geometry interaction parameters. However, the pellet-sinter interaction parameters were not directly calibrated. Instead, these parameters were defined as the average of the pellet-pellet and sinter-sinter interaction parameters, following a similar approach used in a previous study on the calibration of pellet-sinter mixtures [147]. To establish a reference case model for time step and sensitivity analyses, particle-particle and particle-geometry interaction parameters were adopted from a similar study on pellet-sinter mixtures [147].

IV. Time step analysis. Selecting the appropriate time step in DEM is a crucial aspect of the calibration process, which ensures numerical stability, computational efficiency, and accurate results [104, 179]. A widely used approach is to consider the time step as a fraction of the Rayleigh time step

$$\Delta t = \frac{\pi r \sqrt{\frac{\rho}{G}}}{0.1631\nu + 0.8766} \tag{5.3}$$

where r, ρ, G, ν are the minimum radius, particle density, shear modulus, and Poissons ratio of particles, respectively. The time step was varied from 5% to 40% to examine its effect on

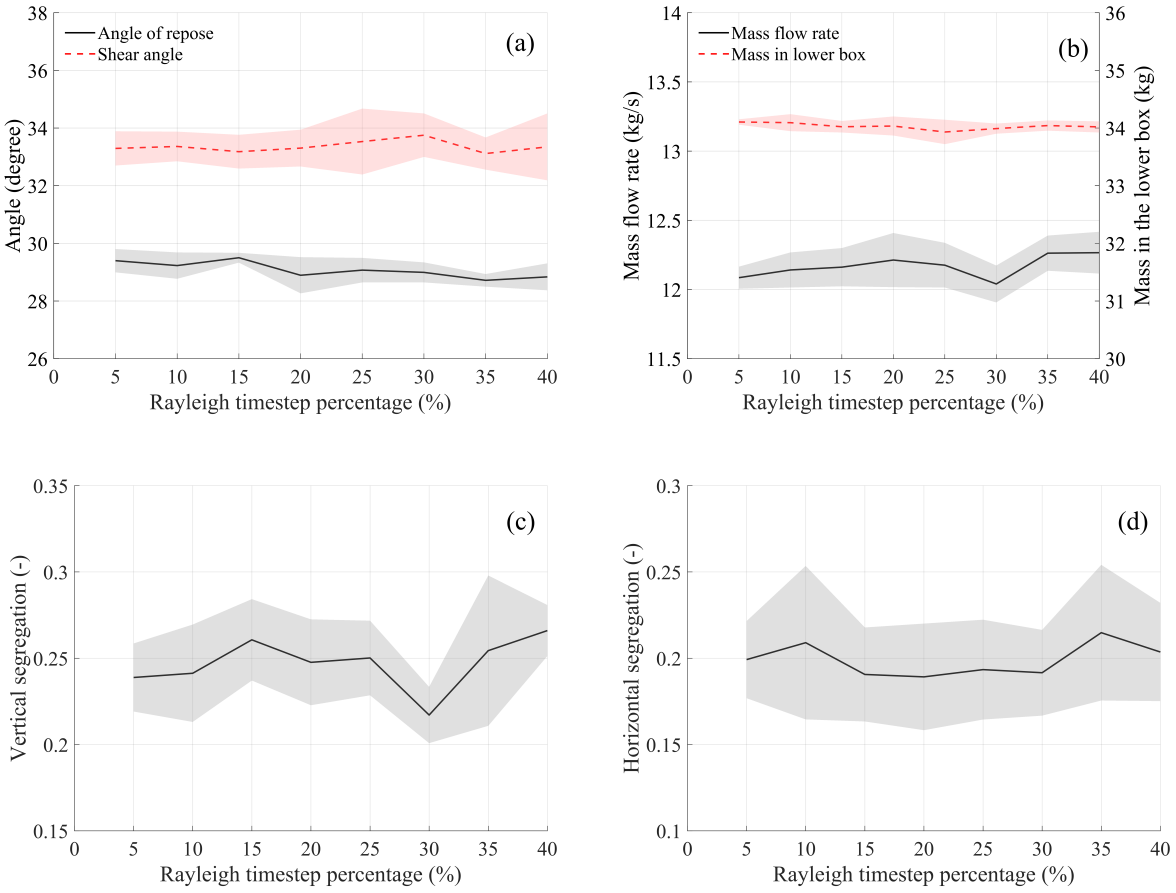

Figure 5.8 The effect of time step on: a) angle of repose and shear angle, b) mass flow rate and mass in the lower box, c) vertical segregation, and d) horizontal segregation. The lines and shaded areas represent the mean and standard deviation, respectively.

all KPIs. The results are presented in Figure 5.8(a)-(d). It is important to note that the same methodology used in experiments was employed to measure KPIs in the DEM simulations. This consistency allowed for a direct and accurate comparison between the DEM results and the experimental measurements.

Two criteria were used to determine the appropriate time step: (1) relatively stable KPI values up to the selected time step and (2) low standard deviation, which indicates high reproducibility. Figure 5.8 shows that most KPIs, including mass flow rate, mass in the lower box, shear angle, and angle of repose, remained stable with low standard deviations up to 15% of the Rayleigh time step (5.91e-6 seconds). Especially, for the angle of repose (Figure 5.8(a)), there is a drop in value and an increase in standard deviation for time steps greater than 15%. Therefore, 15% was selected as it balances computational efficiency, stability, and reproducibility.

5.3.3 Sensitivity analysis

Given the large number of DEM parameters to be calibrated (i.e. 12), a sensitivity analysis was conducted to identify the parameters that significantly influence the KPIs. By focusing the calibration on these significant parameters, the computational expense of the calibration process

is significantly reduced [210]. Moreover, the sensitivity analysis helps define the parameter space for calibration, reveal relationships between KPIs, and determine whether the selected KPIs are suitable for calibrating the DEM model.

The definitive screening design (DSD) [157], a design of experiments (DoE) technique, was employed in this study, building on its successful application in previous work for efficiently identifying significant parameters [210]. With 12 DEM parameters, the DSD required 29 simulation runs, calculated as $2k+5$, where k is the number of parameters [158]. The low and high parameter levels for the DSD, shown in Table 5.4, were set as the reference case values ś25%, with the reference values obtained from [147]. The DSD design is presented in Table D.1 in Appendix D.

Table 5.4 Low, middle, and high levels of DEM parameters used in DSD. (μ_s = coefficient of sliding friction, μ_r = coefficient of rolling friction, C_r = coefficient of restitution)

Parameters	Low level (-1)	Middle level (0) [147]	High level (+1)
Pellet–pellet			
$\mu_{s,pp}$	0.368	0.49	0.613
$\mu_{r,pp}$	0.045	0.06	0.075
$C_{r,pp}$	0.525	0.7	0.875
Sinter–sinter			
$\mu_{s,ss}$	0.525	0.7	0.875
$\mu_{r,ss}$	0.06	0.08	0.1
$C_{r,ss}$	0.263	0.35	0.438
Pellet–geometry			
$\mu_{s,pg}$	0.285	0.38	0.475
$\mu_{r,pg}$	0.045	0.06	0.075
$C_{r,pg}$	0.525	0.7	0.875
Sinter–geometry			
$\mu_{s,sg}$	0.285	0.38	0.475
$\mu_{r,sg}$	0.06	0.08	0.1
$C_{r,sg}$	0.3	0.4	0.5

To account for the stochastic nature of granular systems and DEM, the DSD analysis was repeated five times. Each repetition was analysed independently to identify the significant parameters. The variation in the KPI values can stem from two main sources: (1) the variability introduced by varying the DEM parameters (i.e., DSD design) and (2) the stochastic nature of DEM simulations (i.e., variations across repetitions). To quantify the contribution of each source to the overall variance, the variance decomposition technique [216] was employed. Variance decomposition is based on the law of total variance

$$\mathrm{Var}(Y) = \mathbb{E}[\mathrm{Var}(Y|X)] + \mathrm{Var}(\mathbb{E}[Y|X]) \tag{5.4}$$

where Y represents the KPI of interest and X denotes the set of input parameters. $\mathbb{E}[\mathrm{Var}(Y|X)]$ represents the variance in Y (i.e., KPI) caused by the stochasticity, while $\mathrm{Var}(\mathbb{E}[Y|X])$ quantifies

the variance in Y due to varying the DEM parameters. The variance contribution of each source, i.e., the DEM parameters and stochasticity, is calculated as:

$$P = \frac{\mathrm{Var}(\mathbb{E}[Y|X])}{\mathrm{Var}(Y)} \times 100 \tag{5.5}$$

$$S = \frac{\mathbb{E}[\mathrm{Var}(Y|X)]}{\mathrm{Var}(Y)} \times 100 \tag{5.6}$$

Figure 5.9 presents the variance contribution of DEM parameters and stochasticity for all the KPIs. It reveals that for both horizontal and vertical segregation, the variance caused by DEM stochasticity dominates the variance due to varying the DEM parameters in the DSD design. This indicates that the inherent stochasticity of DEM, related to the initial position and orientation of particles, overshadows the effect of varying parameters on segregation.

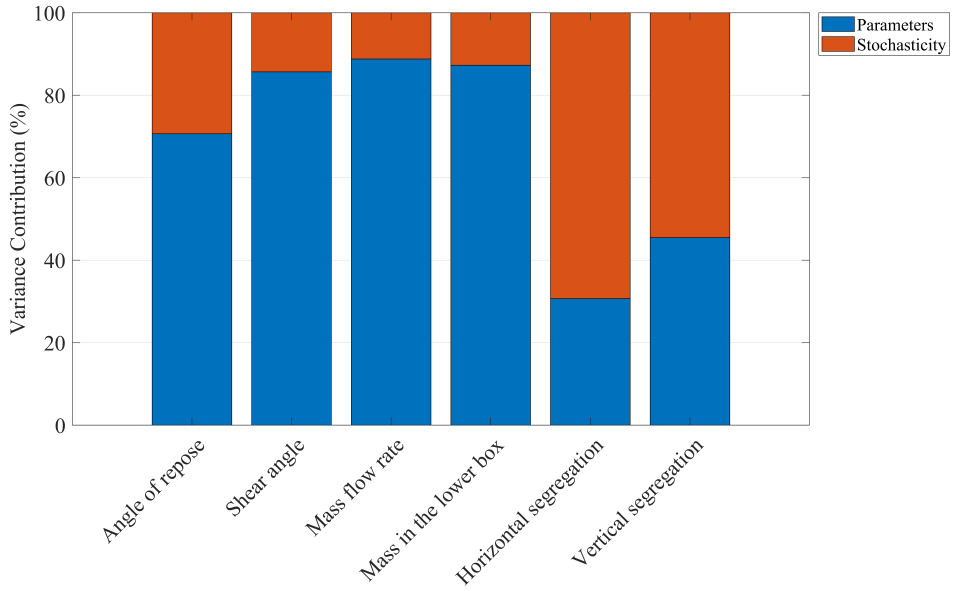

Figure 5.9 Results of variance contribution of DEM parameters and stochasticity for all the KPIs.

Therefore, no meaningful conclusions can be drawn about the sensitivity of segregation to DEM parameters. As a result, segregation measured in the draw down test cannot be used as a KPI to calibrate the DEM model. Consequently, segregation was excluded from both the sensitivity analysis and the DEM calibration process.

For the four remaining KPIs, the "Fit Definitive Screening" platform in JMPő Pro software was used to perform the DoE. Stepwise regression with a p-value threshold of 0.01, combined with analysis of variance (ANOVA), was applied to identify significant parameters, following the previous study [210]. Since the significance of parameters varied slightly across the five sensitivity analysis repetitions, a parameter was considered significant if it appeared as significant in at least 80% of the repetitions (i.e., 4 or 5 times) for at least one of the KPIs. The final results of the sensitivity analysis are presented in Table 5.5, where the significant parameters are shaded to highlight the seven parameters selected for calibration.

Table 5.5 Results of the sensitivity analysis, showing the frequency of each parameter appearing as significant across five repetitions, with the significant parameters shaded. (The +/- signs indicate that with an increase in the parameter value, the corresponding KPI increases/decreases.)

Parameters		Angle of repose	Shear angle	Mass flow rate	Mass in the lower box
Pellet–pellet	$\mu_{s,pp}$	0	5 (+)	1 (-)	5 (-)
	$\mu_{r,pp}$	1 (+)	5 (+)	0	5 (-)
	$C_{r,pp}$	5 (-)	1 (+)	1 (+)	0
Sinter–sinter	$\mu_{s,ss}$	0	0	5 (-)	4 (+)
	$\mu_{r,ss}$	1 (+)	1 (+)	3 (-)	2 (-)
	$C_{r,ss}$	1 (-)	1 (+)	1 (+)	0
Pellet–geometry	$\mu_{s,pg}$	2 (-)	5 (+)	1 (-)	4 (-)
	$\mu_{r,pg}$	1 (-)	4 (+)	1 (+)	5 (-)
	$C_{r,pg}$	1 (-)	0	1 (+)	0
Sinter–geometry	$\mu_{s,sg}$	3 (-)	5 (+)	5 (-)	5 (-)
	$\mu_{r,sg}$	1 (-)	0	2 (+)	0
	$C_{r,sg}$	2 (-)	0	1 (+)	1 (+)

5.3.4 Surrogate model development

In this section, the process of establishing a surrogate model (SM) to map the relationship between the significant parameters (i.e., the seven parameters shaded in Table 5.5) and the KPIs is described.

I. Parameter Space. As mentioned above, one of the advantages of using a screening design is that it helps guide the definition of the parameter space for efficient calibration. To achieve this, the experimental results were compared with the simulation outcomes from the screening runs for each KPI. Figure 5.10 shows the results of the screening design compared to the experimental values for each KPI. This comparison, combined with the correlations in Table 5.5, helped adjust the parameter space of the screening design (Table 5.4). For example, in Figure 5.10(b), the experimental value for the shear angle is higher than all the screening design runs. This indicates that the parameter space for the significant parameters needs to be extended in a way that increases the shear angle. According to Table 5.5, all significant parameters have a positive correlation (+) with the shear angle. This suggests that their parameter space should be extended to higher values, assuming the correlation remains valid beyond the initial range used in the sensitivity analysis. By repeating this process for the other KPIs, the parameter space was finalised and is presented in Table 5.6.

II. Objective function. With four KPIs to calibrate, there are three potential strategies for building SMs: 1) building a separate SM for each KPI, 2) using multivariate models to create a single SM for all KPIs, or 3) combining all KPIs into a single objective and creating a single SM. Each strategy has its advantages and disadvantages. For simplicity and efficiency, the

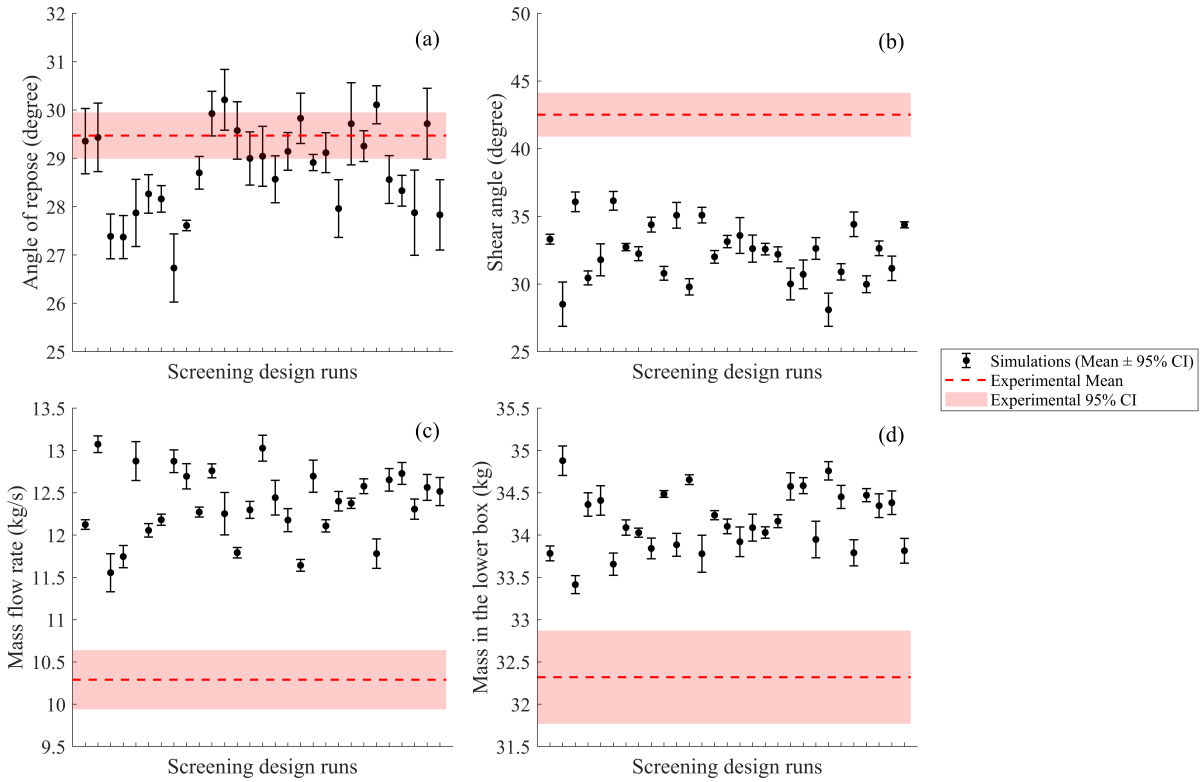

Figure 5.10 Comparison between sensitivity analysis and experimental results for all KPIs. The differences between the two indicate the need to extend the parameter space.

Table 5.6 Extended parameter space used for DEM calibration.

Parameters	Low band	High band
$\mu_{s,pp}$	0.613	1.0
$\mu_{r,pp}$	0.075	0.24
$C_{r,pp}$	0.525	1.0
$\mu_{s,ss}$	0.525	1.0
$\mu_{s,pg}$	0.285	1.0
$\mu_{r,pg}$	0.075	0.24
$\mu_{s,sg}$	0.285	1.0

third strategy was chosen. This approach simplifies the SM development process compared to option 2 since it involves using simpler models. Moreover, option 3 is more efficient than 1, as it requires only a single SM. Following the methodology outlined in [174], the KPIs were combined into a single objective using a weighted sum (WS) of the relative error (RE) between the experimental and DEM measurements of KPIs. The WS is calculated as

$$WS = \sum_{m=1}^{M} (w_m \cdot RE_m), \quad \text{with} \sum_{m=1}^{M} w_m = 1 \tag{5.7}$$

where M is the number of KPIs (four in this study), w_m is the weight for mth KPI, and RE is the absolute relative error

$$RE = \left| \frac{y_{\mathrm{DEM}} - y_{\mathrm{Exp}}}{y_{\mathrm{Exp}}} \right| \tag{5.8}$$

where y_{DEM} and y_{Exp} represent the KPI values obtained from DEM and experiments, respectively. Since all KPIs have equal importance in the calibration process, the same weight (w_m) was assigned to each of them. The weighted sum (WS) is used as the objective function to be minimised in the calibration process.

III. Surrogate model training. Figure 5.11 provides an overview of the approach used to develop the surrogate model (SM) in this study. For the initial sampling, the Latin Hypercube Sampling (LHS) method was used as it randomly and evenly distributes the points in the parameter space (Table 5.6). Following the recommendation by Loeppky et al. [217], 10 points per parameter were sampled, resulting in a total of 70 data points. The DEM simulations were then run with five repetitions for all the points, and the values for all the KPIs were obtained. These KPI values were subsequently converted into a single objective value, as outlined above.

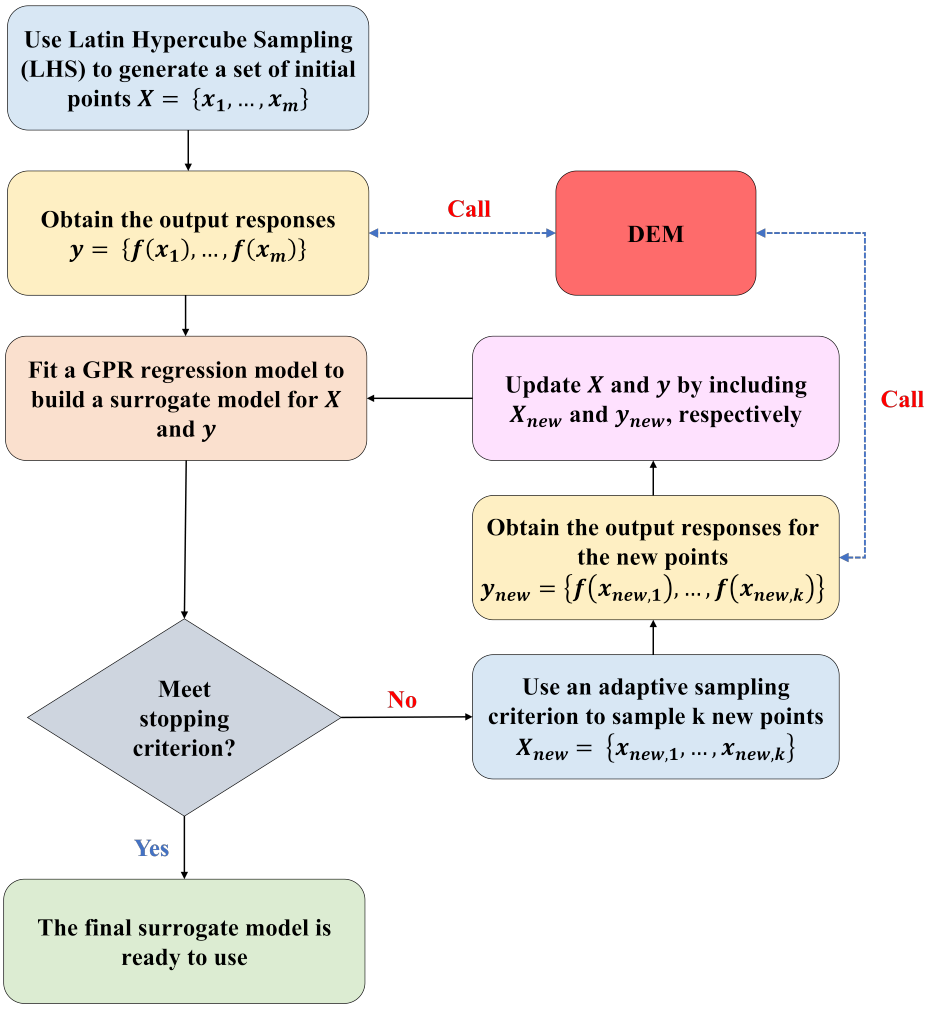

Figure 5.11 Flowchart illustrating the surrogate model development approach used in this study, based on [218].

Gaussian Process Regression (GPR) was selected to develop the surrogate model (SM), as it is well-suited for capturing complex, non-linear relationships. It was specifically selected as the findings of Chapter 4 demonstrated GPR's effectiveness in modelling the relationship between DEM parameters and the corresponding response. The mathematical formulation of GPR and the details of the training procedure are provided in Chapter 4, Section 4.3 and Section 4.4.

Although various metrics can be used to evaluate the performance of the surrogate model (SM), the coefficient of determination (R^2) was selected as the main metric of interest. After rigorously training the GPR model on the initial set of 70 data points, the model achieved an average cross-validation R^2 value of 0.84, which was considered insufficient for calibration. This suggests that the dataset was too small for the model to fully capture the relationship between the seven DEM parameters and the response (i.e., the weighted sum of the relative errors between experimental and DEM results).

There are two general approaches for expanding the dataset to improve the performance of the SMs [218]: 1) traditional space-filling sampling, and 2) adaptive sampling (also known as active learning) approaches. Compared to the space-filling methods, adaptive sampling methods have a higher potential for improving model performance with fewer points by targeting the most informative areas of the design space [218]. Therefore, adaptive sampling was adopted to expand the dataset in this study.

The Expected Improvement (EI) criterion was employed for adaptive sampling, which is well-suited for expensive computational models such as DEM [174, 219]. EI balances exploration (sampling in regions of high uncertainty) and exploitation (sampling in regions with promising predicted performance) [218, 220]. In this approach, let f_min denote the best (i.e., smallest) observed function value (or weighted sum of the relative errors) to date. For any candidate point x, the improvement is defined as:

$$I(x) = \max\{0, f_{\min} - f(x)\} \tag{16}$$

The expected improvement is then given in closed form by

$$EI(x) = (f_{\min} - \mu(x))\,\Phi\left(\frac{f_{\min} - \mu(x)}{\sigma(x)}\right) + \sigma(x)\,\phi\left(\frac{f_{\min} - \mu(x)}{\sigma(x)}\right) \tag{17}$$

where $\Phi(.)$ and $\phi(.)$ are the cumulative distribution function and probability density function of the standard normal distribution, respectively (with the convention that $EI(x) = 0$ when $\sigma(x) = 0$). The next sample point is selected by maximising the expected improvement:

$$x_{\text{new}} = \arg\max EI(x). \tag{18}$$

Adaptive sampling was applied iteratively by adding 10 new data points in each iteration until the stopping criterion was met. An R^2 value of 0.95 was chosen as the stopping criterion to achieve a balance between high model accuracy and computational efficiency.

Figure 5.12 shows the actual responses plotted against the surrogate models predicted values. In the first iteration, adaptive sampling focuses on exploring the parameter space to improve the models global accuracy. From the second iteration onwards, the sampling strategy shifts towards exploiting regions with lower response values, which are of particular interest for model

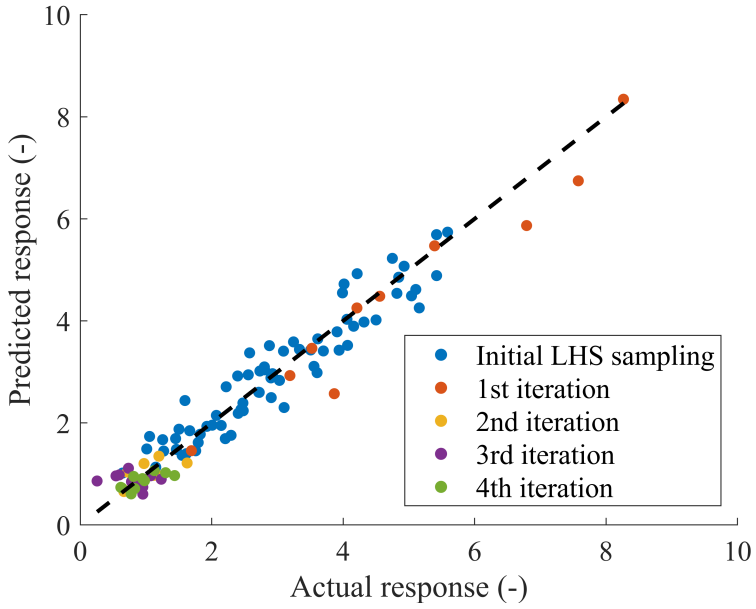

Figure 5.12 Actual vs. predicted responses (i.e., weighted sum of relative errors as defined in Eq. 5.7) during the surrogate model development process using adaptive sampling.

calibration. The performance of the model across different iterations of the adaptive sampling process is presented in Table 5.7.

This integrated approach, which combines GPR with an EI-based adaptive sampling strategy, allows us to efficiently expand the dataset by focusing on the most informative regions. As a result, the accuracy of the SM is improved while minimising computational costs.

Table 5.7 Performance of the SM across adaptive sampling iterations, shown as the [mean ś standard deviation] of R^2 from 5 seed runs.

Iteration	**Number of data points**	**R^2 of the SM**
Initial LHS sampling	70	0.84 ś 0.01
1st iteration	80	0.88 ś 0.03
2nd iteration	90	0.92 ś 0.01
3rd iteration	100	0.93 ś 0.01
4th iteration	110	0.95 ś 0.01

5.3.5 Optimisation algorithm

The Genetic Algorithm (GA) was employed to efficiently optimise the surrogate model. GA is a population-based optimisation technique inspired by the principle of natural selection and genetics [221]. GA was chosen as it is well-suited for solving complex, high-dimensional, and non-linear optimisation problems where traditional gradient-based methods may struggle [174, 222]. However, a common drawback of GA is its slow convergence and the high number of objective function evaluations required [222]. Here, this limitation is mitigated by using a fast

surrogate model instead of computationally expensive DEM simulations during the optimisation process. The parameters of GA are listed in Table D.2 in Appendix D.

The GA was executed to search for a global minimum. Basically, it searches for DEM parameter sets that minimise the objective functionthe weighted sum of the relative errors between experimental and DEM measurements for all KPIs. The optimisation was performed using two approaches:

1. Restricted optimisation: The GA was constrained to search for DEM parameter values below 0.9, as higher values are not reported for sinter and pellets in the literature [210].
2. Unrestricted optimisation: The GA was permitted to search the entire parameter space.

The results of both approaches, including the two best-performing parameter sets from each, are presented in Table 5.8. Since negligible differences are observed in the optimised DEM parameters, the results from the restricted optimisation are used for further analysis.

Table 5.8 The results of the DEM calibration using the restricted and unrestricted genetic algorithms (GA).

Parameters	Restricted GA	Unrestricted GA
$\mu_{s,pp}$	0.73	0.75
$\mu_{r,pp}$	0.12	0.11
$C_{r,pp}$	0.76	0.76
$\mu_{s,ss}$	0.90	0.91
$\mu_{s,pg}$	0.90	1.0
$\mu_{r,pg}$	0.16	0.17
$\mu_{s,sg}$	0.83	0.79

The surrogate model inherently contains some stochasticity, which may lead to slight variations in its predictions. To take this variability into account, the surrogate model was trained 10 times and performed the GA optimisation separately for each trained model. In each run, the parameter set with the minimum fitness value, i.e., the minimum weighted sum of errors, was identified. This process resulted in slightly different calibrated parameter sets, as shown in Table 5.9. However, since the variations between these sets were minimal, only one parameter set with the lowest fitness value (run 4 in Table 5.9) was selected as the final calibrated parameter set.

5.3.6 Verification of the calibrated parameters

To verify the calibration, DEM simulations were performed using the calibrated parameters highlighted in Table 5.9. Figure 5.13 presents the relative errors between the experimental measurements and DEM results, calculated as $((y_{DEM} - y_{Exp}))y_{Exp})$. The consistently low relative errors (all below 2%) confirm the success of the calibration approach.

As shown in Figure 5.7, bulk density in DEM is reassessed after calibration to ensure it matches the experimental bulk density. This is crucial because bulk density can be affected by

Table 5.9 Results of the genetic algorithm optimisation across 10 repetitions of surrogate model training for DEM calibration. The selected parameter set with the lowest fitness value is shaded in green.

Repetition	$\mu_{s,pp}$	$\mu_{r,pp}$	$C_{r,pp}$	$\mu_{s,ss}$	$\mu_{s,pg}$	$\mu_{r,pg}$	$\mu_{s,sg}$	**Fitness value (weighted sum of errors)**
1	0.73	0.12	0.76	0.9	0.9	0.16	0.83	0.5532
2	0.65	0.12	0.75	0.9	0.9	0.17	0.89	0.5975
3	0.62	0.11	0.72	0.9	0.89	0.2	0.92	0.5567
4	0.74	0.12	0.76	0.9	0.9	0.16	0.83	0.5475
5	0.62	0.12	0.72	0.9	0.88	0.19	0.9	0.5676
6	0.69	0.12	0.76	0.9	0.9	0.17	0.85	0.5724
7	0.65	0.12	0.75	0.9	0.9	0.17	0.88	0.5950
8	0.62	0.12	0.72	0.9	0.9	0.18	0.9	0.5856
9	0.74	0.12	0.76	0.9	0.9	0.16	0.93	0.5579
10	0.62	0.12	0.73	0.9	0.88	0.18	0.9	0.5811

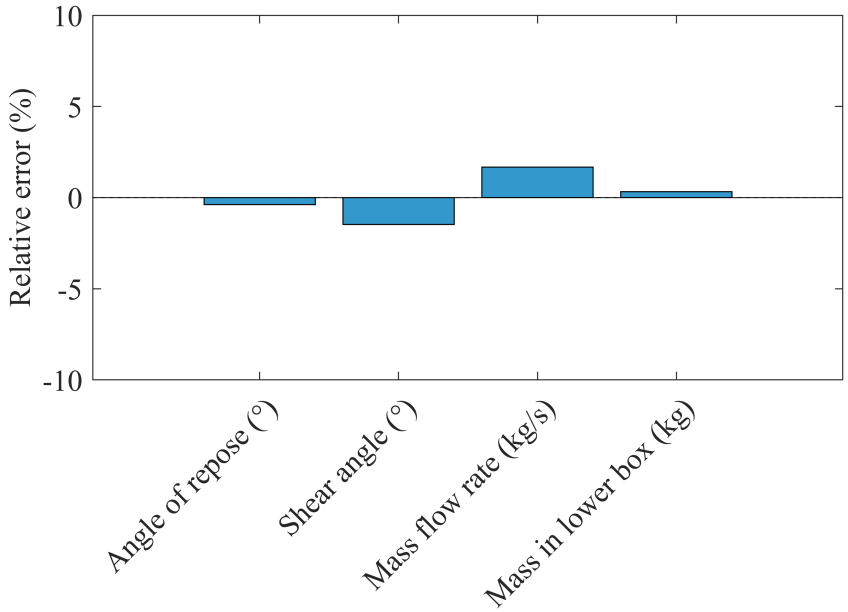

Figure 5.13 DEM calibration results, showing the relative error between experimental measurements and DEM results for each KPI. The exact values of DEM results are provided in Table D.3 in Appendix D

particle-particle friction coefficients [104, 223]. To achieve this, the maximum heap height in the lower box was used as a comparison metric. Figure 5.14 shows that the heap height in DEM (H_{DEM}) is lower than in the experiments (H_{Exp}), indicating a higher bulk density in the DEM model.

To calibrate the bulk density, the particle density in DEM was adjusted by multiplying it by the ratio $H_{DEM}H_{Exp}$. The average of this ratio across all the repetitions was calculated as 0.93. As a result, the calibrated particle densities for pellets and sinter were updated to 3350 (kg/m^3) and 3208 (kg/m^3), respectively.

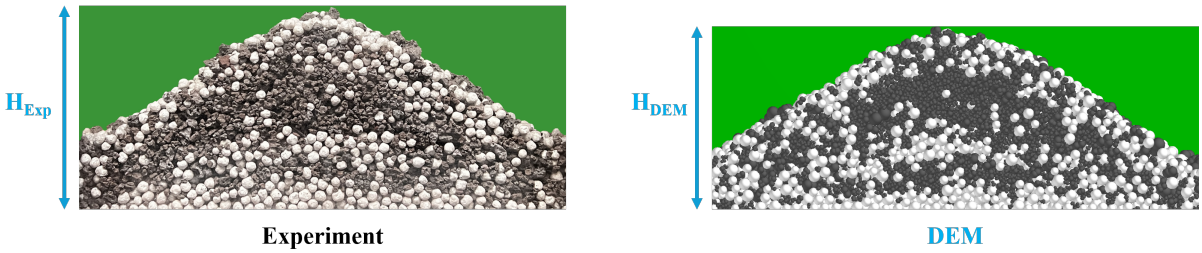

Figure 5.14 Comparison of the height of the heap in the lower box between the experiment and DEM.

A new set of DEM simulations was conducted using the calibrated particle densities. The results, presented in Figure 5.15, show that the errors for most KPIs remain low, confirming the effectiveness of the calibration approach. However, a noticeable increase in the error for the mass flow rate was observed after reducing the particle density. This outcome was anticipated, as the mass flow rate is highly sensitive to changes in particle density [224]. This finding highlights the importance of including particle density as a calibration parameter when an accurate modelling of mass flow rate is of interest. Incorporating particle density in the main calibration process would improve the models ability to capture this behaviour more accurately.

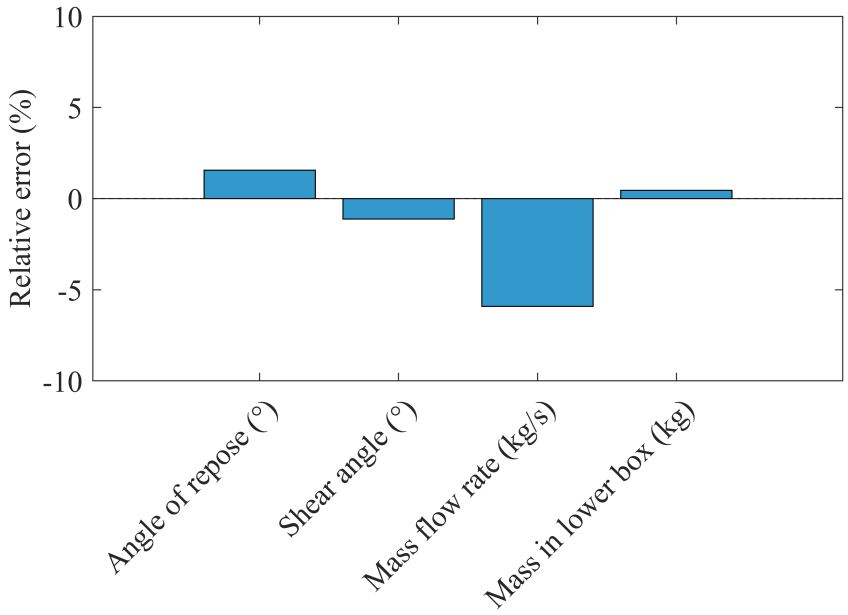

Figure 5.15 DEM calibration results with calibrated particle density, showing the relative error between experimental measurements and DEM results for each KPI. The exact values of DEM results are provided in Table D.4 in Appendix D.

Figure 5.16 provides a visual comparison between the DEM simulations and experiments at different time instances, demonstrating a strong agreement throughout the discharging process. This showcases the model's ability to accurately capture the flow dynamics over time.

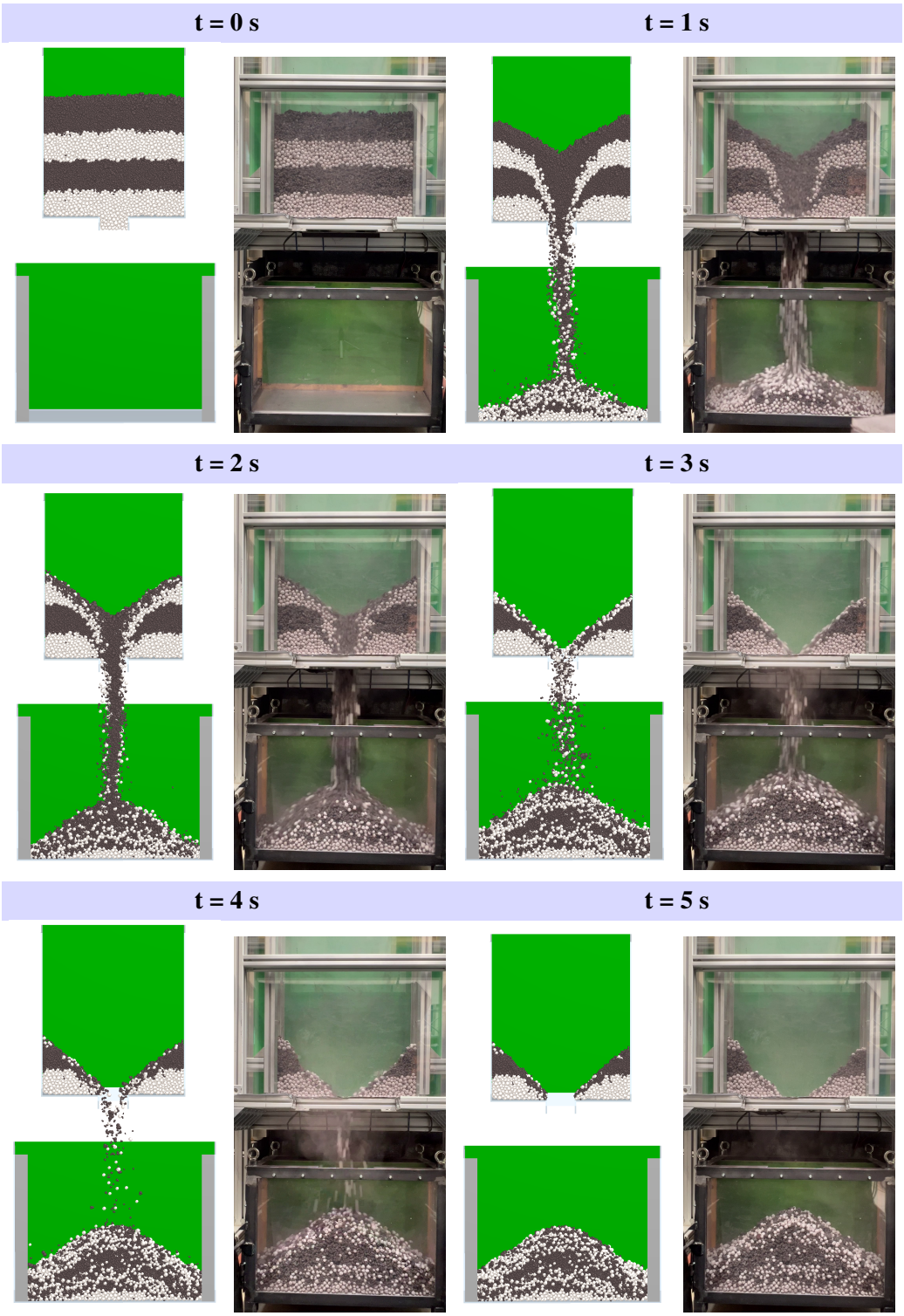

Figure 5.16 Comparison of simulation (left) and experiment (right) at each time step.

5.3.7 Validation of the calibrated parameters

To validate the robustness of the calibrated model developed for the 50-50 pellet-sinter mass ratio, the simulations were extended to three additional cases: 75-25 and 25-75 mass ratios, as well as the reverse layering. In these validation simulations, the pellet-sinter interaction parameters were kept as the average of the pellet-pellet and sinter-sinter interaction parameters, consistent with the parameters used for the 50-50 mixture. The results of these simulations are presented in Figure 5.17, demonstrating good agreement between the DEM results and the experimental measurements for all KPIs. The accuracy of the developed DEM model for different mass ratios and layering orders confirms the generalisability and reliability of the calibrated parameters.

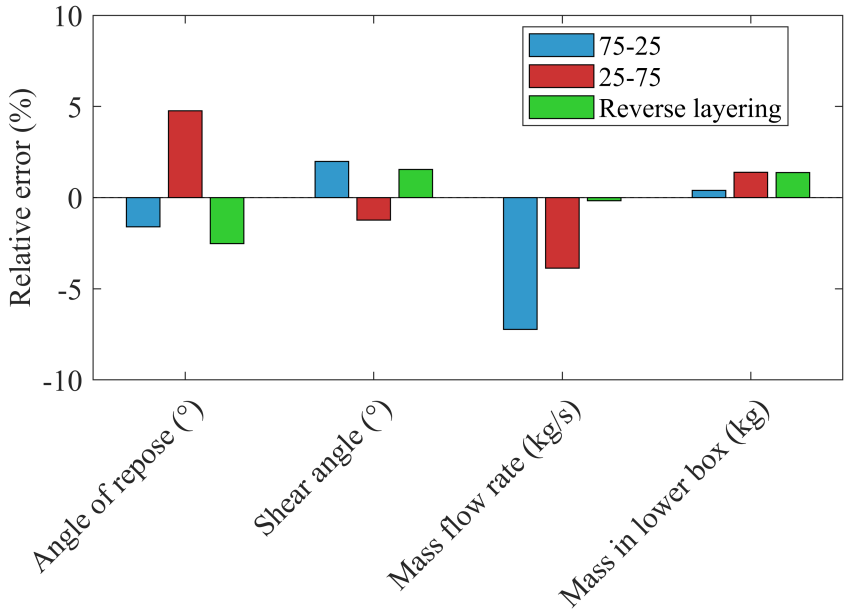

Figure 5.17 Validation of the calibrated DEM parameters, showing the relative error between experimental measurements and DEM results for 75-25 and 25-75 pellet-sinter mass ratio, as well as the reverse layering case. The exact values of DEM results are provided in Table D.5 in Appendix D.

5.4 Conclusion

In this chapter, an efficient and systematic calibration framework for DEM modelling of multi-component mixtures was proposed. The calibration framework was successfully applied to pellet-sinter mixtures, which are used in blast furnace steelmaking. The framework integrates sensitivity analysis based on definitive screening design (DSD), ML-based surrogate modelling using Gaussian process regression (GPR) with adaptive sampling, and optimisation techniques using genetic algorithms (GA) to minimise the number of required DEM simulations. The main findings are as follows:

- The proposed framework achieved a high-accuracy surrogate model (R^2 of 0.95) for 7 DEM parameters using only 110 data points. This represents a 25%-82% reduction in

dataset size compared to previous studies [173, 225], while also achieving higher accuracy. These results highlight the efficiency of the framework in minimising computational costs while maintaining robust performance.

- Calibrated parameters for a 50-50 pellet-sinter mass ratio were valid across the other tested mass ratios and the reverse layering order. This suggests that, within the tested conditions, calibrating DEM parameters for one mass ratio and layering order is sufficient, eliminating the need for re-calibration of DEM parameters for different mixture ratios and layering configurations.

- Recalibrating the particle density at the end of the calibration process introduced errors in predicting the mass flow rate, while the errors for other KPIs remained low. This highlights the importance of actively calibrating particle density when dynamic processes are targeted.

- Interaction parameters for two-component mixtures can be effectively estimated as the average of the coefficients for the individual materials.

- Sensitivity analysis is a crucial step in calibrating a DEM model. It not only reduces the number of parameters to be calibrated but also reveals the sensitivity and relationship of KPIs to the DEM parameters. This insight helps determine whether certain KPIs are suitable for calibrating specific parameters. Moreover, it assists in defining an appropriate parameter space.

- Applying variance decomposition to the sensitivity analysis results revealed that the change in segregation, both in horizontal and vertical directions, is mostly caused by DEM stochasticity; hence, no meaningful conclusion about the sensitivity of segregation to any DEM parameter can be drawn. Therefore, the segregation measured in the draw down test cannot be used for calibration.

The calibration framework developed in this chapter provides an efficient and accurate route for tuning DEM parameters in two-component pelletsinter mixtures. With the DEM model now calibrated and validated, the next step is to test its predictive capabilities under real industrial conditions. Next chapter therefore applies the calibrated DEM model to a full-scale blast-furnace charging system at Tata Steel IJmuiden. In that industrial case study, the model is used to identify where segregation happens along the complete charging path, from weighing bunkers to top hoppers, and to evaluate practical operating strategies for mitigating segregation.

Chapter 6

Industrial-scale DEM Modelling of Segregation in the Blast Furnace Charging System*

In Chapter 5, a DEM model for a mixture of pellets and sinter was calibrated using lab-scale experiments, resulting in parameter sets capable of accurately reproducing observed flow and segregation behaviour. In this chapter, these calibrated parameters are applied to the full-scale charging system at Tata Steel IJmuiden to investigate the segregation of the ferrous mixture, comprising pellets, sinter, lump ore, and nut coke, under industrial operating conditions. The study employs the actual blast furnace charging geometry and introduces quantitative measures of segregation to assess behaviour at different stages of the process. In addition to analysing a reference case that reflects current practice, a series of case studies is performed to evaluate the influence of variations such as bunker configuration, hopper side, and sinter PSD variability. Together, these results provide new insight into the root causes of segregation and the key factors influencing it within the charging system, while also highlighting potential strategies for its mitigation.

*This chapter is based on: A. Hadi, Y. Pang, A. Adema, J. van der Stel, D.L. Schott, *Industrial-scale DEM Modelling of Segregation in the Blast Furnace Charging System*, *Powder Technology* (2026). https://doi.org/10.1016/j.powtec.2026.122116

6.1 Introduction

In blast furnace, segregation can adversely affect the distribution of materials on the burden surface, which in turn has a detrimental effect on bed permeability [9]. This affected permeability leads to inconsistencies in pressure drop, causing inefficient use of reductant gas and resulting in both economic and environmental consequences [10]. Therefore, it is crucial to investigate and understand segregation within the blast furnace processes. Conducting experiments or in-situ measurements of segregation in the blast furnace charging system is costly and/or impractical due to the large-scale equipment and harsh environment. Alternatively, DEM can be employed to gain insight into segregation in blast furnace.

Many DEM studies have investigated segregation in the blast furnace [12, 15, 17, 18, 226–228]. However, the majority of these studies have focused on segregation happening after the top hopper, i.e., on the chute and the blast furnace burden [74, 227, 229]. Additionally, they have mostly studied the size segregation of individual materials such as pellets, sinter, or coke, with only a few addressing the segregation of multiple materials, referred to as multi-component segregation [169]. Furthermore, most of these studies employed down-scaled dimensions of the blast furnace geometry to reduce DEM computational time [17, 18, 228].

In this chapter, these gaps are addressed by modelling the blast furnace charging process at full industrial scale, covering the entire sequence from the weighing bunkers to top hopper discharge. The primary objectives are (i) to identify the root causes of multi-component segregation within the charging system, and (ii) to systematically evaluate the influence of different factors, including material properties, particle characteristics, and operational factors, on segregation behaviour through a series of case studies.

This chapter is structured as follows. Section 6.2 presents the DEM modelling framework, including the model setup, geometries, and the approach used to quantify segregation. Section 6.3 introduces the defined case studies, discusses the results of the reference case in detail, and compares the outcomes of the remaining cases against this baseline. Finally, Section 6.4 summarises the key findings of the chapter.

6.2 Materials and Methods

6.2.1 Discrete element method

DEM simulations were carried out using the Hertz-Mindlin (no-slip) contact model [29], combined with an elastic-plastic spring-dashpot rolling friction model (referred to as type C in Ai et al. [145]), as described in Section 3.2.1. All simulations were performed using the commercial software EDEM v2024.1 and were executed on the DelftBlue supercomputing cluster [148]

6.2.2 Simulation configuration

I. Materials and DEM parameters. The ferrous mixture used in the blast furnace charging system is modelled to reflect industrial practice. As illustrated in Figure 1.4, this mixture mainly consists of pellets, sinter, and lump ore. In certain operations, including at Tata Steel IJmuiden,

a small proportion of nut coke (i.e., fine-sized coke) is also introduced into the ferrous mixture to increase the productivity.

For pellets and sinter, the calibrated DEM parameters obtained in Chapter 5 (see Table 5.9) were employed to ensure an accurate representation of the flow behaviour [230]. For lump ore and nut coke, where direct calibration was not conducted, the DEM parameters were adopted from the study by [227], which investigated similar materials under comparable conditions. For interactions between different material types (e.g., pelletsinter or pelletlump ore), the inter-material contact parameters were estimated as the average of the corresponding values for the two interacting materials, as concluded to be accurate in the previous chapter.

The realistic size distributions of all materials, as used in Tata Steel's operations, were implemented in the simulations, as shown in Figure 6.1. The detailed PSD of all materials is presented Table E.1 in Appendix E.

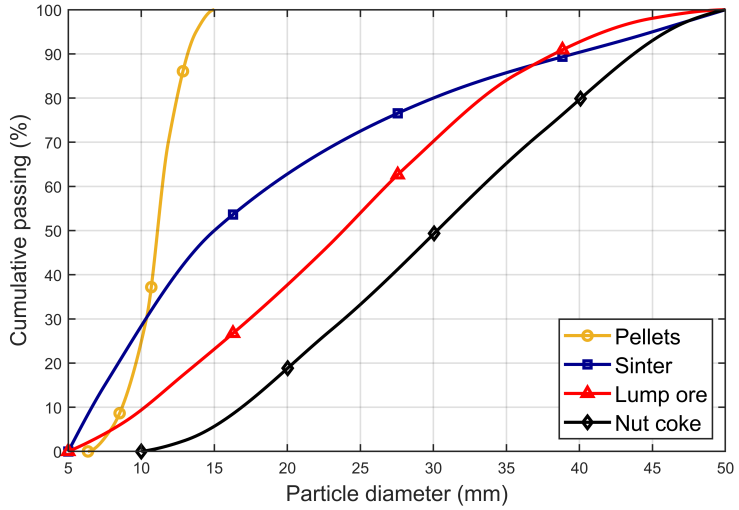

Figure 6.1 Cumulative particle size distribution of the materials used in this study.

To improve computational efficiency, spherical particles were mainly used to represent particle shapes in the simulations. However, in one specific case study, non-spherical particles, illustrated in Figure 3.4, were employed to investigate the effect of explicitly modelling the irregular shape of sinter particles on flow and segregation behaviour. A comprehensive list of all DEM parameters used is listed in Table E.2 in Appendix E.

II. Geometries and the charging process. Figure 6.2 illustrates the simulation geometry used in this study to model the blast furnace charging system at Tata Steel IJmuiden. For a more comprehensive overview of the complete charging system refer to Figure 1.3.

The system contains three weighing bunkers (WBs), designated for storing pellets, sinter, and a mixture of lump ore and nut coke, respectively. During each charging cycle, approximately 20 tonnes of pellets, 12 tonnes of sinter, 2.4 tonnes of lump ore, and 0.75 tonnes of nut coke are loaded into the corresponding bunkers.

The outlets of the pellet and sinter WBs are opened simultaneously in a controlled manner to ensure that both materials are emptied at the same time. In contrast, the outlet of the lump ore/nut coke bunker is opened fully and it is emptied instantly (Figure 6.3(a)).

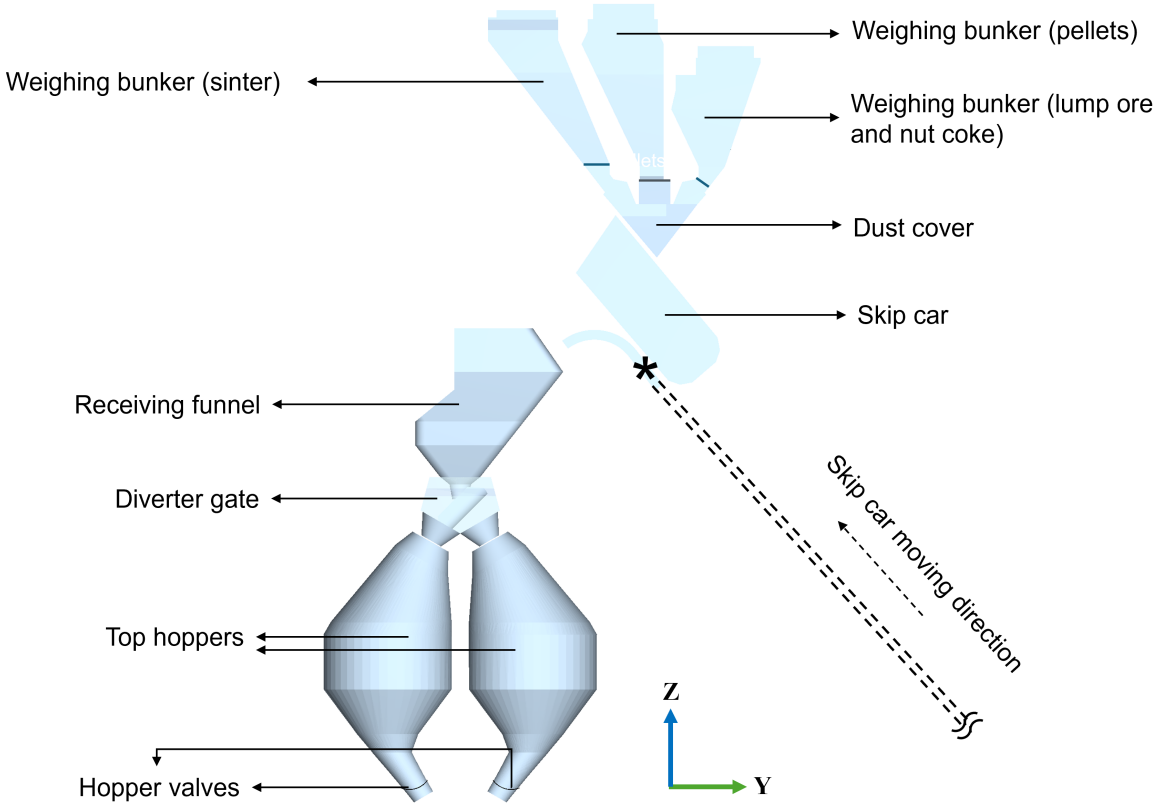

Figure 6.2 The geometry model used in this study. For practical reasons, the WBs and the skip car are placed at the location (*), while in practice, they are located at the bottom, and the skip car moves up in the mentioned direction.

In the actual industrial process, the filled skip car moves up along an inclined rail before discharging the materials. However, since this upward movement is not expected to induce any significant material segregation, it was excluded from the simulation for computational efficiency. Therefore, the skip car was directly positioned at the top discharge point (* in Figure 6.2), where it begins to tilt.

Upon tilting, the ferrous mixture is discharged into the receiving funnel and then flows through a series of components, including a semi-cylindrical chute at the diverter gate, before being deposited into one of the top hoppers (Figure 6.3(b)). This entire charging sequence is then repeated for the second skip car to complete a full batch cycle.

Afterwards, the valve of the top hopper is opened (Figure 6.3(c)), allowing the ferrous material to discharge into the lower funnel, and subsequently flow through a rotating chute, where it is finally deposited at the furnace throat (see Figure 1.3).

6.2.3 Quantifying segregation

Segregation was measured at three key locations: within the skip car, within the top hopper (after both skip cars are loaded), and after the discharge from the top hopper. The approach used to quantify segregation at these locations is described below.

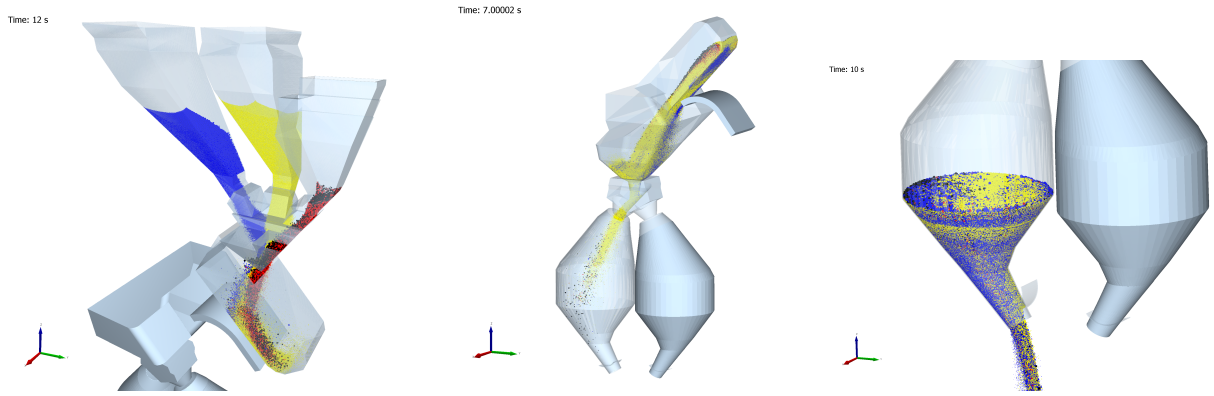

(a) (b) (c)

Figure 6.3 Snapshots of the DEM simulation showing the charging sequence: (a) discharge of weighing bunkers into the skip car, (b) discharge of the skip car into the receiving funnel, and (c) discharge of the top hopper. The particle colours are consistent in all simulations: pellets (yellow), sinter (blue), lump ore (red), and nut coke (black).

I. Segregation in the skip car and top hopper. The relative standard deviation (RSD), a grid-dependent segregation index, was used to quantify segregation in both the skip car and the top hoppers. The procedure for calculating RSD is explained in detail in Section 3.3.3. An RSD value of zero corresponds to a perfectly homogeneous mixture, whereas higher RSD values indicate a greater degree of segregation.

Since segregation can occur in different spatial directions, namely horizontal, vertical, and throughout the full volume, RSD was calculated separately for each of these directions. Furthermore, because the segregation behaviour may vary across different material types, the RSD was also computed individually for each material (i.e., pellets, sinter, lump ore, and nut coke).

To complement the RSD analysis and gain insights into the local distribution of the materials, the normalised mass ratio (NMR), $\tilde{\chi}_i(k)$, was also calculated for material i in the k-th bin

$$\tilde{\chi}_i(k) = \frac{\chi_i(k)}{\chi_i^0} \tag{6.1}$$

where $\chi_i(k)$ is the local mass ratio of material i in bin k, and χ_i^0 is its initial mass ratio in the system (e.g., skip car). A value of $\tilde{\chi}_i(k) = 1$ indicates that the local proportion of material i matches the initial bulk proportion; $\tilde{\chi}_i(k) > 1$ indicates over-representation, and $\tilde{\chi}_i(k) < 1$ indicates under-representation. An example of the NMR representation is shown in Figure 6.4, illustrating the material distribution in both the skip car and the top hopper. For each geometry, the yz view is used to present the NMR in the vertical and horizontal (y) directions, while the xz view is used to present the NMR in the horizontal (x) direction.

It is important to note that the particle size distributions differ across materials, and using a uniform bin size based on a single particle type could bias the RSD calculation. To ensure consistency and comparability across materials, the bin size was set to 10 times a reference particle diameter (through a sensitivity analysis of the bin size effect), d_{ref}, calculated as the mean of the median diameters (D_{50}) of all materials. This approach provides a representative sampling resolution relative to the overall particle size range in the mixture.

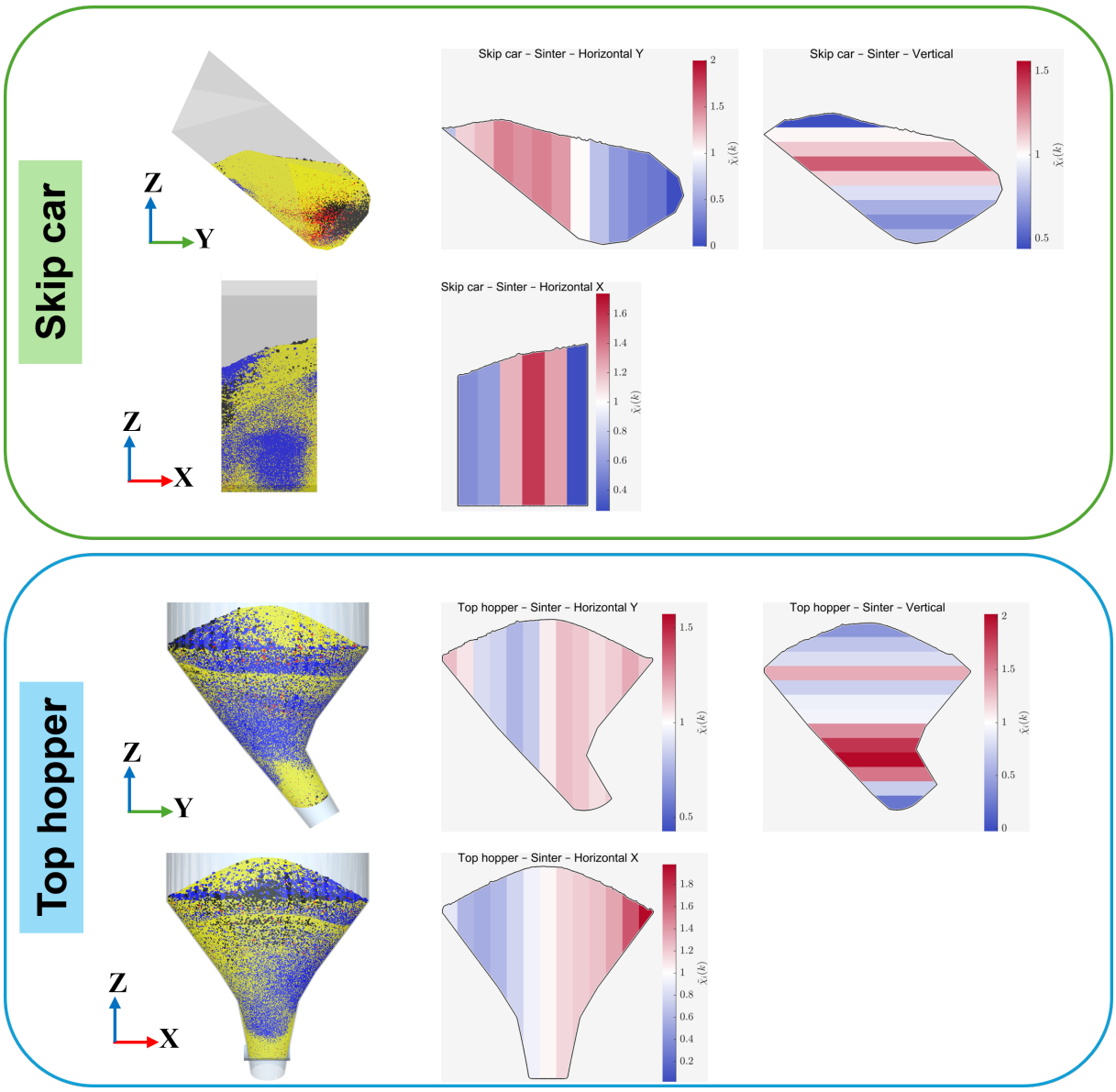

Figure 6.4 An example of illustration of the normalised mass ratio (NMR) for sinter in the skip car (top) and top hopper (bottom), shown in the horizontal (x and y) and vertical (z) directions, alongside the corresponding views of the geometries.

II. Segregation after discharging the top hopper. Unlike the other two regions within the skip car and top hopper, where a static measurement of segregation is possible, segregation after hopper discharge is dynamic and measured over time during the discharge process. To enable the measurement, a cylindrical sampling volume was defined just below the hopper outlet, as shown in Figure 6.5. This region captures the mixture of materials exiting the hopper and allows for time-resolved segregation analysis. During the discharge process, the mass of each material (i.e., pellets, sinter, lump ore, and nut coke) within the sampling volume was recorded at 1-second intervals during a total discharging time of roughly 50 seconds.

At each recorded time step t, the instantaneous mass ratio of material i was computed by dividing its mass by the total mass of all materials within the sampling volume

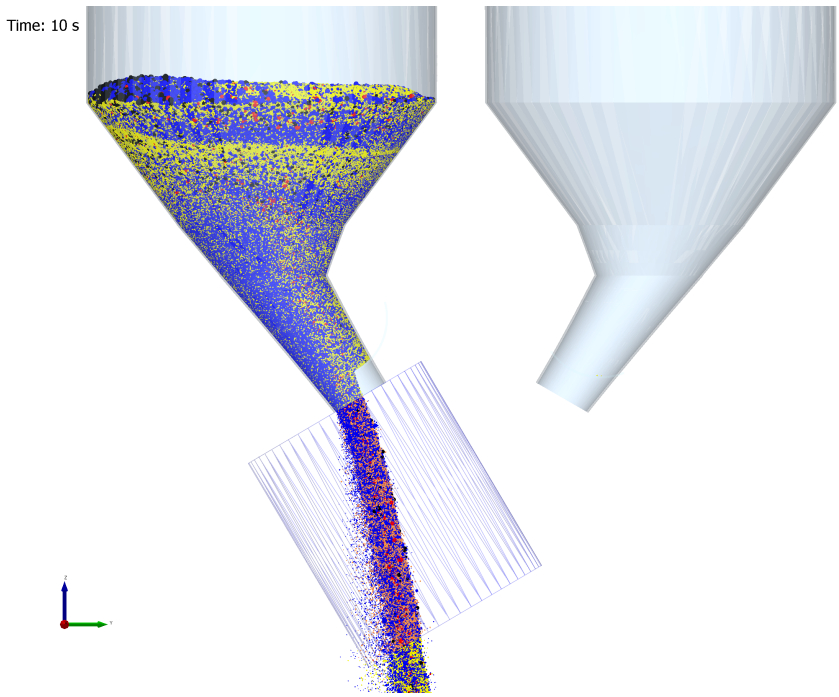

Figure 6.5 The cylindrical sampling volume used to measure the mass ratio of each material at each time step during top hopper discharge.

$$\chi_i(t) = \frac{m_i(t)}{\sum_{j=1}^{n} m_j(t)} \tag{6.2}$$

where $\chi_i(t)$ is the mass ratio of material i at time t, $m_i(t)$ is the mass of material i at time t, and n is the total number of material types (i.e., 4: pellets, sinter, lump ore, and nut coke).

To assess segregation over time, the normalised mass ratio was then calculated by comparing the instantaneous value to the initial mass fraction of that material in the hopper

$$\tilde{\chi}_i(t) = \frac{\chi_i(t)}{\chi_i^0} \tag{6.3}$$

where $\tilde{\chi}_i(t)$ is the normalised mass ratio (NMR) of material i at time t, and χ_i^0 is the initial mass ratio of material i, based on the total mass loaded into the top hopper.

This formulation is similar to Eq. 6.1, with the distinction that here the sampling is performed over time rather than across spatial bins. Similarly, in an ideally mixed system, $\tilde{\chi}_i(t)$ remains constant at 1 throughout the discharge period. Any deviation from this value indicate segregation:

- $\tilde{\chi}_i(t) > 1$: the material is over-represented at time t
- $\tilde{\chi}_i(t) < 1$: the material is under-represented at time t

To visualise these dynamics, time series of $\tilde{\chi}_i(t)$ were plotted for each material, with a reference line at $\tilde{\chi}_i = 1$ indicating perfect mixing, as illustrated in Figure 6.6. To ensure the reliability of the results, a threshold filter was applied: only time steps where the total mass in

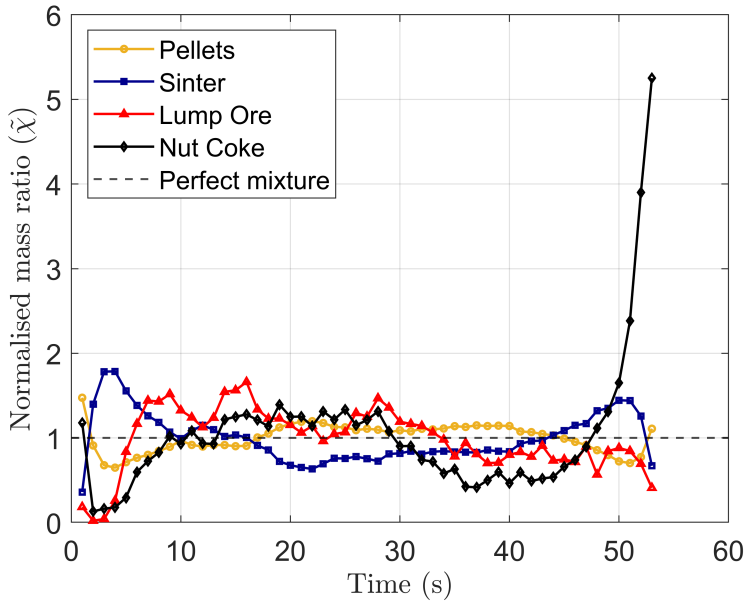

Figure 6.6 Example plot showing the segregation behaviour of different materials during top hopper discharge, based on their normalised mass ratios (NMR) over time. The dashed line represents a perfectly mixed state.

the sampling volume exceeded 50 kg were considered. This step minimised numerical artefacts that can arise during the early stages of discharge when mass flow is low.

6.3 Results and discussion

A preliminary study was first conducted to gain early insights into segregation during blast furnace charging [231]. That work considered only pellets and sinter, employed literature-based DEM parameters, and the scope was limited to hopper filling without subsequent discharge. Two key findings emerged: (i) scaling the particle size by a factor of two substantially reduced computational cost while still yielding accurate segregation predictions, and (ii) when pellets and sinter were perfectly mixed upstream in the weighing bunkers, segregation was virtually eliminated. In contrast, under current practice, the mixture remained largely segregated in the top hopper. Further details of this study can be found in the corresponding conference paper [231].

While the preliminary study provided valuable initial insights into the segregation behaviour of pellets and sinter during blast furnace charging, it was based on a simplified modelling approach with several limitations. First, the study used literature-based parameter values instead of calibrated ones. Second, the material scope was limited to only pellets and sinter, excluding other relevant components such as lump ore and nut coke. Third, the use of simplified particle size distributions (PSDs) and spherical particle shapes limited the models ability to capture realistic charging behaviour. Finally, the simulations were not repeated, so it remains unclear whether DEM stochastic effects would have a significant impact and should be further assessed.

To address these limitations and explore additional factors that may influence segregation, a more comprehensive and realistic study was carried out. This extended study incorporated the calibrated parameters from Chapter 5, added lump ore and nut coke as additional materials, and used realistic PSDs based on data provided by Tata Steel. It further investigated the effects of PSD variability, the influence of non-spherical sinter shapes, and the sensitivity of segregation to key operational and design parameters. In addition, the simulation scope was extended to analyse the material composition during discharge from the top hopper valve. Overall, the objective was to achieve a more realistic representation (by using calibrated parameters and industrial PSDs) and to develop a broader and deeper understanding of ferrous mixture segregation within the BF charging system. Moreover, alternative operational settings were tested to evaluate their potential for reducing segregation.

6.3.1 Definition of case studies

A total of nine case studies were defined to investigate the influence of operational, material, and particle-related factors on segregation during the BF charging process. The cases are summarised in Table 6.1. Two distinct reference cases were used: Case 1, based on the initial PSD data, served as the baseline for operational and material variations (Cases 2, 3, 4, 7, and 8), while Case 1A, defined using updated plant data from Tata Steel for sinter PSD, served as the baseline for the PSD sensitivity study (Cases 5A and 6A). The variations examined include hopper-side asymmetry (Case 2), reversing the order of pellets and sinter in the weighing bunkers (Case 3), reduced particlewall sliding friction (Case 4), variability in sinter PSD with finer (Case 5A) and coarser (Case 6A) distributions, an alternative lump ore type (Case 7), and the use of non-spherical (clumped) particles for sinter (Case 8). In all cases, only one parameter was varied relative to the reference, enabling the isolated assessment of its effect on segregation.

In the following subsections, the results of the reference case are presented, followed by comparisons with the other cases. To make these comparisons quantitative, the relative difference in RSD between each case and the reference (Case 1) was calculated as:

$$\Delta\text{RSD} = \frac{\text{RSDcase} - \text{RSDref}}{\text{RSD}_{\text{ref}}} \tag{6.4}$$

Table 6.1 Summary of the nine case studies. Case 1 is the reference for Cases 2, 3, 4, 7, and 8, while Case 1A is the reference for the PSD sensitivity analysis of sinter (5A and 6A). The highlighted cells indicate the factors that vary from the corresponding reference case.

Case	Hopper Side	WB Order	Wall Friction	PSD of Sinter	Lump Ore Type	Sinter Shape
Case 1 (Ref)	Left	Normal	WF	Avg	A, B	Spherical
Case 1A	Left	Normal	WF	Avg (updated)	A, B	Spherical
Case 2	Right	Normal	WF	Avg	A, B	Spherical
Case 3	Left	Reversed	WF	Avg	A, B	Spherical
Case 4	Left	Normal	WF –25%	Avg	A, B	Spherical
Case 5A	Left	Normal	WF	Min	A, B	Spherical
Case 6A	Left	Normal	WF	Max	A, B	Spherical
Case 7	Left	Normal	WF	Avg	C	Spherical
Case 8	Left	Normal	WF	Avg	A, B	Non-spherical

ΔRSD expresses how much segregation in a given case increases or decreases relative to the reference. For clarity and a quick overview, Figure 6.7 provides an example of the visualisation method: results for different materials, directions, and locations are colour-coded, with blue indicating lower segregation and red indicating higher segregation compared to the reference case.

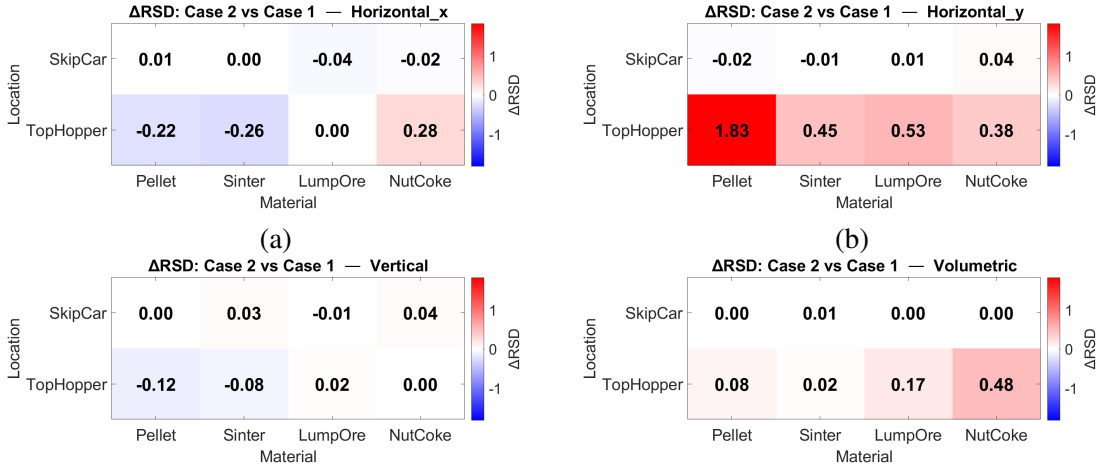

Figure 6.7 Illustration of the relative difference in RSD (ΔRSD) between a given case (e.g., Case 2) and the reference case (Case 1), shown for: a) Horizontal (X), b) Horizontal (Y), c) Vertical (Z), and d) Volumetric directions.

6.3.2 Reference case description (Case 1)

In this section, the segregation behaviour is analysed in detail for the reference case (Case 1). Segregation is evaluated at three key stages of the charging process: within the skip car, within the top hopper, and after discharging from the top hopper.

Before proceeding with the analysis, it is important that the necessity of repeating the simulations be assessed to account for potential variability. To investigate this, the first step of the process, i.e., the discharge of materials from the weighing bunkers into the skip car, was simulated three times. This approach allowed the evaluation of the variability in the segregation measurements across different spatial directions and for each material.

Table 6.2 presents the results of the three simulation repetitions. The last column shows the coefficient of variation (CoV) of the RSD values across the repetitions, expressed as a percentage, and calculated as $\text{CoV}\ (\%) = \frac{\sigma_{\text{RSD}}}{\mu_{\text{RSD}}} \times 100$, where σ_{RSD} and μ_{RSD} are the standard deviation and mean of the RSD values, respectively. CoV reflects the degree of variability in the segregation results due to the stochastic nature of the simulations. As shown in the table, the CoV values are consistently low for all materials and directions, showing very low variability. Therefore, repeating the simulations was deemed unnecessary for the rest of this study.

I. Segregation in the skip car and top hopper. Figure 6.8 presents the RSD values for all four materials (pellets, sinter, lump ore, and nut coke) within the skip car and top hopper, across different spatial directions. Overall, segregation decreases from the skip car to the top

Table 6.2 RSD values from three simulation repetitions (Rep1Rep3) for different materials and directions within the skip car, along with the coefficient of variation (CoV) of the RSD values (expressed in percentage) to quantify variability across repetitions.

Direction	Material	Rep1	Rep2	Rep3	CoV (%)
Vertical	Pellet	0.134	0.129	0.130	1.6
	Sinter	0.244	0.250	0.248	1.0
	LumpOre	1.246	1.220	1.239	0.9
	NutCoke	1.136	1.156	1.144	0.7
Horizontal (X)	Pellet	0.257	0.260	0.257	0.5
	Sinter	0.572	0.576	0.565	1.0
	LumpOre	0.527	0.517	0.495	2.6
	NutCoke	0.661	0.656	0.653	0.6
Horizontal (Y)	Pellet	0.197	0.194	0.202	2.1
	Sinter	0.508	0.505	0.507	0.2
	LumpOre	1.119	1.133	1.140	0.9
	NutCoke	0.895	0.943	0.962	3.2
Volumetric	Pellet	0.513	0.516	0.512	0.3
	Sinter	1.017	1.028	1.018	0.5
	LumpOre	2.115	2.103	2.113	0.2
	NutCoke	2.697	2.810	2.808	1.9

hopper, indicating a degree of remixing during flowing through the receiving funnel. However, an exception is observed for vertical segregation of pellets and sinter, which increases slightly in the top hopper. This may be attributed to the fact that two skip cars are loaded into the top hopper, creating a vertically layered structure where the material from the second skip car is deposited on top of the first. Such sequential filling can increase vertical compositional differences, resulting in higher RSD in the vertical direction.

Pellets and sinter show relatively low RSD values compared to lump ore and nut coke, with sinter showing slightly higher segregation than pellets. For both pellets and sinter, segregation occurs mostly in the horizontal directions, particularly along the x-axis. To investigate this further, the NMR of pellets and sinter in the x-direction within the skip car were examined, as shown in Figure 6.9.

The results clearly show that pellets and sinter are not uniformly distributed in the x-direction of the skip car. For pellets (Figure 6.9(a)), higher concentrations are observed on the left side of the skip car, whereas sinter (Figure 6.9(b)) is more concentrated in the central region. This spatial bias is mainly the result of insufficient mixing of the materials during discharging from the weighing hoppers, as also noted in our preliminary study [231]. In particular, the observed segregation in the x-direction can be linked to the configuration of the weighing hoppers and the presence of the dust cover. The asymmetric positioning and geometry of the weighing bunkers likely promote uneven loading, resulting in the discharge of certain materials into specific areas of the skip car.

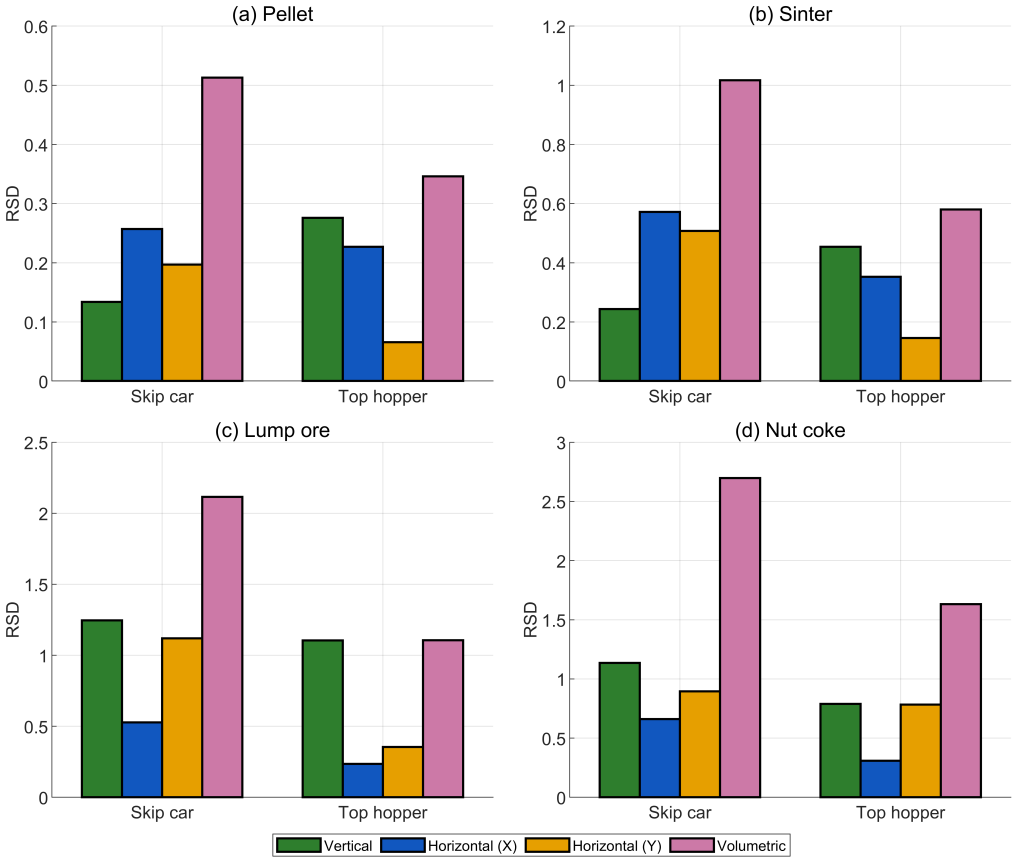

Figure 6.8 RSD values for (a) pellets, (b) sinter, (c) lump ore, and (d) nut coke, measured in different directions within the skip car and the top hopper.

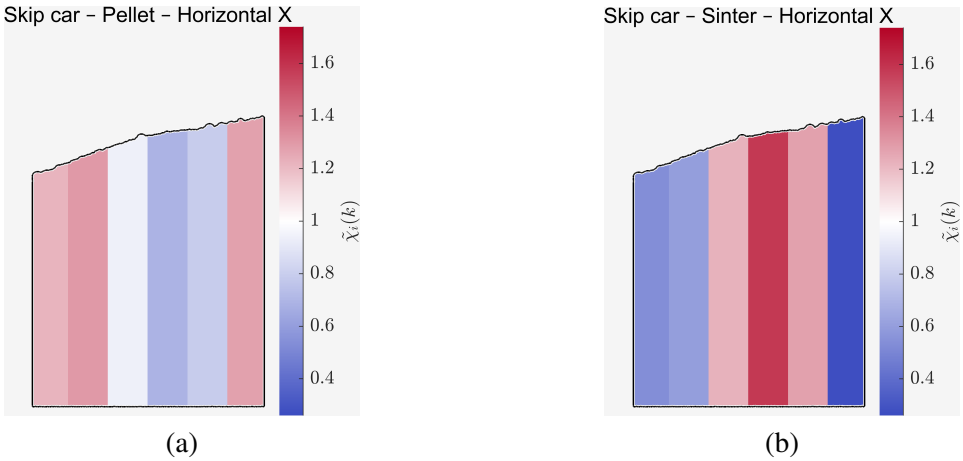

(a) (b)

Figure 6.9 NMR in the x-direction within the skip car for: a) pellets, and b) sinter.

In contrast to pellets and sinter, Figure 6.8 indicates that lump ore and nut coke have substantially higher segregation. This behaviour is mainly due to their relatively smaller total mass, which results in their discharge from the weighing bunker being completed much more quickly than for pellets and sinter. Consequently, they concentrate in specific regions of the skip car, as illustrated in Figure 6.10(a). In addition, nut coke is observed to segregate from lump ore. This separation arises from their density difference, whereby buoyancy-driven segregation causes the heavier lump ore particles to sink deeper into the mixture.

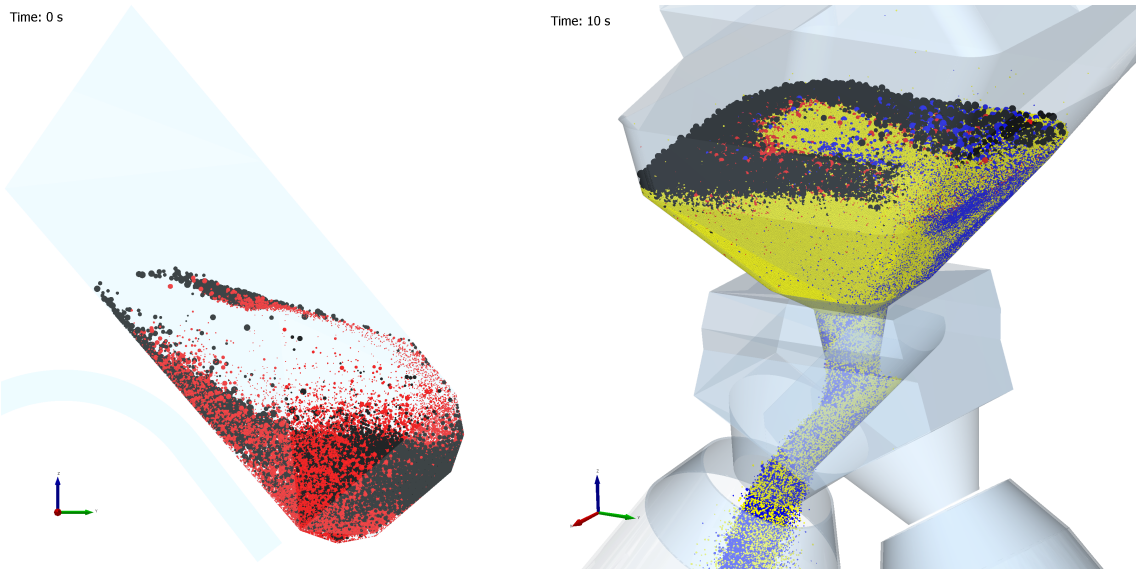

(a) (b)

Figure 6.10 a) Spatial distribution of lump ore (red) and nut coke (black) within the skip car. Pellets and sinter are omitted for clarity. b) Distribution of lump ore and nut coke at the surface of the burden within the receiving funnel.

Since lump ore and nut coke are mostly deposited near the bottom of the skip car (see Figure 6.10(a)), they are discharged last when the skip car tilts, ultimately ending up on the surface of the mixture in the receiving funnel, as illustrated in Figure 6.10(b). This sequence results in a layer of lump ore and nut coke forming at the top of the mixture in the top hopper, which contributes to their sustained high vertical segregation. Figure 6.11 shows the distribution of lump ore and nut coke in the top hopper after the first and second skip car loads.

Another observation from Figure 6.11 is that most of the nut coke tends to move towards the left-hand wall of the hopper during discharge. This behaviour occurs because lump ore,

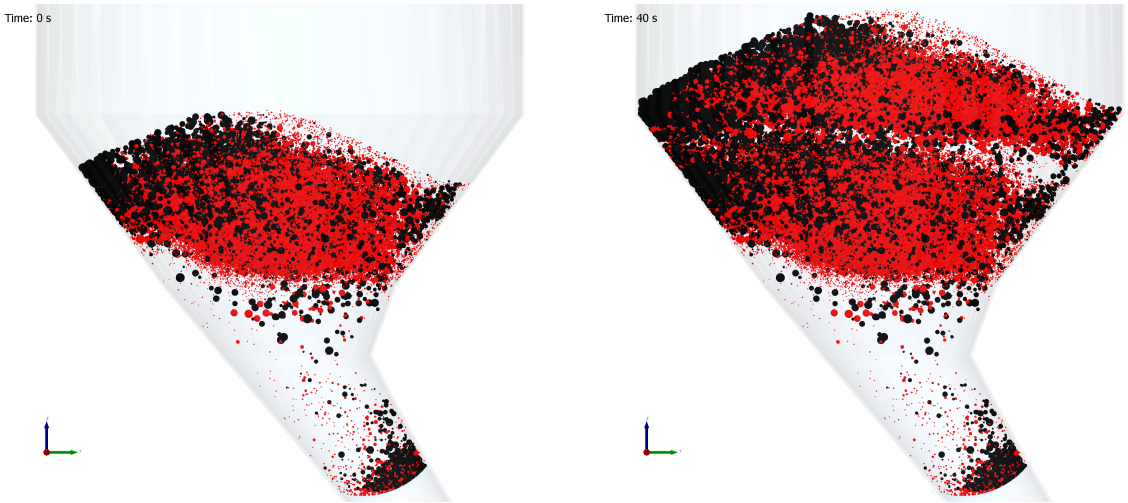

(a) (b)

Figure 6.11 Distribution of lump ore (red) and nut coke (black) within the top hopper after: a) the first skip car load, and b) the second skip car load. Pellets and sinter are omitted for clarity.

with a higher particle density and slightly smaller particle size, tends to deposit and remain closer to the discharge point. Consequently, this promotes greater horizontal segregation in the x-direction of the top hopper for nut coke, as shown in Figure 6.8(d).

It should be noted that the RSD values measured with volumetric bin systems are inherently higher than those calculated for a single direction, as the smaller bin size in the volumetric scheme increases sensitivity to local composition variations. When considering these volumetric RSD values, which capture segregation across all three spatial dimensions, it becomes clear that all materials remain notably segregated, with nut coke exhibiting the highest overall RSD. This indicates that the current charging configuration does not promote effective mixing, even after the material is transferred through the receiving funnel.

II. Segregation after discharging the top hopper. Regarding segregation during the discharge of the top hopper, Figure 6.12 shows the temporal evolution of the NMR for each material (see Eq. 6.3). After an initial discharging period, pellets show a relatively stable discharge profile, whereas sinter and lump ore display moderate fluctuations throughout the process. In contrast, nut coke demonstrates the most pronounced segregation, with its mass ratio rising sharply in the final discharge stage (~5055 s) to more than five times its initial mass ratio within the mixture.

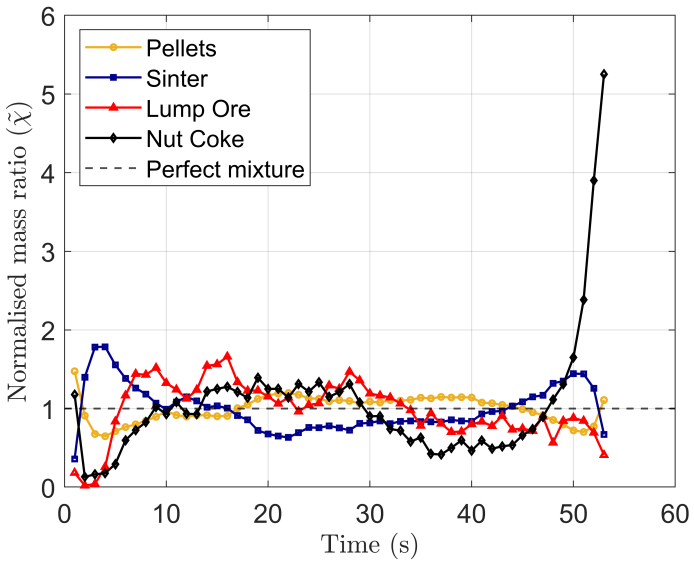

Figure 6.12 NMR of different materials during top hopper discharging. The dashed line represents a perfect mixture.

The whole discharge time can be divided into some regions with different segregation behaviour, as described below.

- **1-9 seconds:** In the initial stage of discharge, all four materials show strong segregation. At t = 1 s, the mixture leaving the hopper consists mainly of pellets and nut coke. Shortly afterwards, the ratio of pellets and nut coke decreases, while sinter and subsequently lump ore become over-represented in the outlet mixture.

  This behaviour can be explained by vertical segregation within the hopper. As shown in Figure 6.13, the NMRs indicate that the bottom layer is predominantly composed of

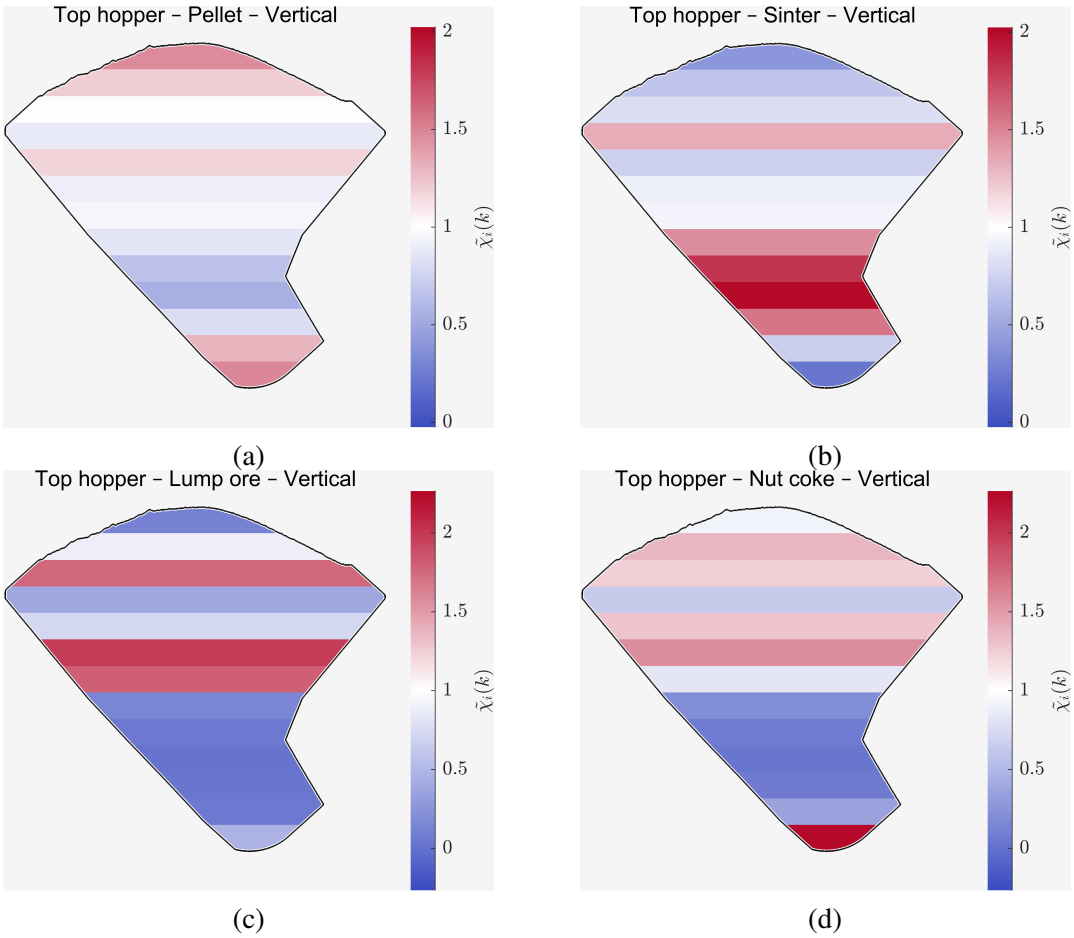

Figure 6.13 NMR in the vertical direction of the top hopper for: a) pellets, b) sinter, c) lump ore, and d) nut coke.

pellets and nut coke. At the beginning of discharge, these materials are released first. With continued discharge, material from the middle section, which is richer in sinter and lump ore, reaches the outlet, resulting in the observed increase in their NMRs.

The discharge pattern can be further explained by the hoppers core flow. Figure 6.14 presents the particle velocity field, showing that particles in the central region move downwards while those near the hopper walls remain nearly stationary. This core flow pattern is beneficial in this context, as the strong segregation present within the hopper is partly mitigated by the vertical mixing induced during the flow.

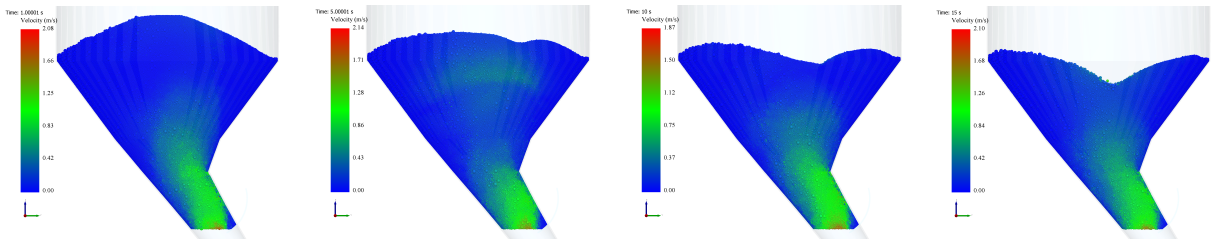

Figure 6.14 Velocity field of the materials during hopper discharge at: a) $t = 1$ s, b) $t = 5$ s, c) $t = 10$ s, and d) $t = 15$ s.

- **9-18 seconds:** At this stage, while pellets, sinter, and nut coke remain relatively well mixed, lump ore becomes over-represented due to the core flow within the hopper. As mentioned earlier, most lump ore particles are concentrated near the hoppers centre, whereas nut coke tends to move towards the hopper walls. Under core flow conditions, the lump ore concentrated in the centre is discharged first, making its NMR higher in the outlet flow.

- **18-30 seconds:** The most noticeable feature in this stage is the low mass ratio of sinter compared to the other materials. This occurs because, under core flow, the upper regions of the hopper, now reaching the outlet, contain a lower proportion of sinter (see Figure 6.13(b)).

- **30-47 seconds:** Compared to the previous stage, the amount of sinter increases, while lump ore decreases at this stage. Pellets show a similar trend and remain relatively well mixed. The main observation in this stage is the under-representation of nut coke. This occurs because nut coke particles mostly accumulate near the hopper walls (see Figure 6.11(b)), where particle motion is limited under core flow conditions. Consequently, these wall-adjacent particles remain in the hopper, while the centrally located material, characterised by a lower nut coke content, is discharged first, resulting in the observed under-representation of nut coke at the outlet.

- **47-53 seconds:** The sharp increase in the nut coke ratio at this stage is clearly observable. As noted earlier, this is because a large proportion of nut coke particles accumulate near the hopper walls (see Figure 6.11(b)) and, under core flow conditions, are discharged last. An increase in the mass ratio of sinter is also noticed. To explain this, the distribution of pellets and sinter near the hopper walls should be examined. Figure 6.15 shows the horizontal mass ratios of these materials within the hopper, indicating that the proportion of sinter near the walls is higher than that of pellets. This difference in the spatial distribution accounts for the observed increase in the sinter mass ratio during this stage.

In summary, the materials discharged from the top hopper show clear segregation, with the strongest segregation occurring during the initial and final stages. Among all materials, pellets display the least degree of segregation. It can be deducted that the observed segregation trends

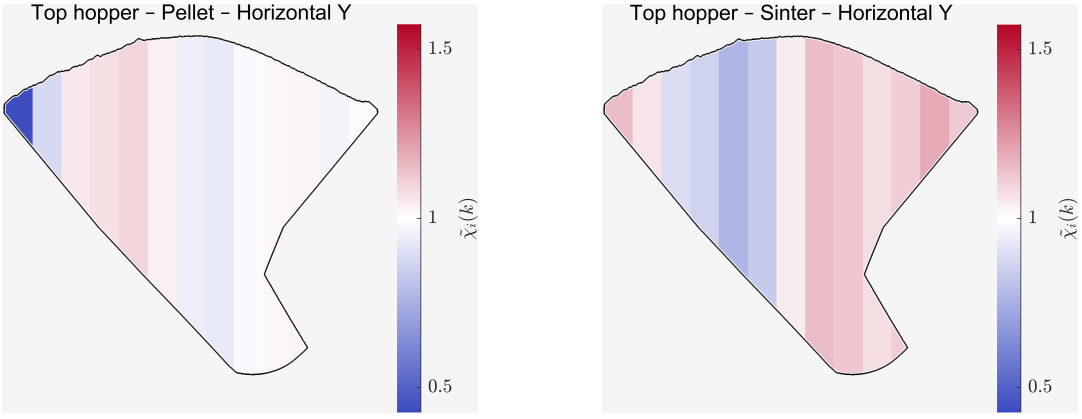

(a) (b)

Figure 6.15 NMRs in the y-direction within the top hopper for: a) pellets, and b) sinter.

in Figure 6.12 are closely related to the vertical segregation established within the hopper (see Figure 6.13). During the intermediate stages, the core flow discharging pattern promotes partial mixing of lump ore and nut coke with pellets and sinter. Nevertheless, this core flow pattern causes the material located near the hopper walls to be discharged last, leading to pronounced segregation of nut coke and sinter towards the end of the discharge.

In the following subsections, each case listed in Table 6.1 is compared with the reference case to evaluate the effect of the varied factor in each case on segregation throughout the charging system.

6.3.3 Effect of hopper side (Case 2 vs. Case 1)

At Tata Steel IJmuiden, the ferrous materials are alternately discharged into the right and left hoppers. Up to this point, segregation has been evaluated for the left hopper. However, due to geometric asymmetry in the y-direction, associated with the configuration of the weighing bunkers and skip car (see Figure 6.2), the segregation for the right hopper needs to be explored as well.

Figure 6.16 presents the ΔRSD (see Eq. 6.4) values for different materials, locations, and directions for the comparison of Case 2 to Case 1. As expected, since Case 2 deviates from Case 1 only after the receiving funnel, there is a negligible difference in the RSD value in the skip car.

Figure 6.16 indicates that, overall, materials are more segregated in the right hopper compared to the left hopper, where segregation in the horizontal y-direction is particularly stronger. To examine this further, Figure 6.17 presents the visual distribution of lump ore and nut coke particles in the left and right hoppers. Qualitatively, lump ore and nut coke appear to be more uniformly distributed in the left hopper; in the right hopper, the left area is noticeably thinned out in lump ore and nut coke.

For a quantitative assessment, the NMRs in the y-direction were compared with the refer-

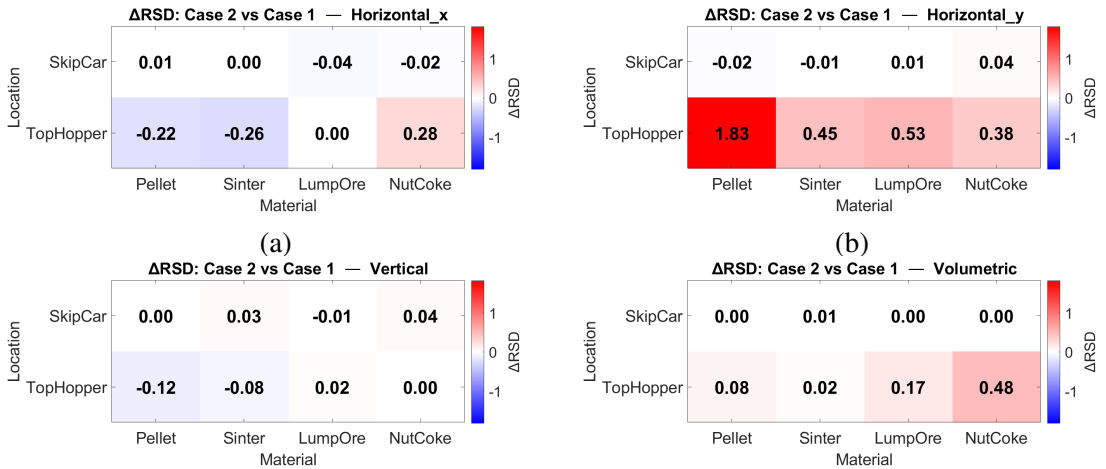

Figure 6.16 Change in RSD for Case 2 vs. Case 1 in a) Horizontal (X), b) Horizontal (Y), c) Vertical (Z), and d) Volumetric directions.

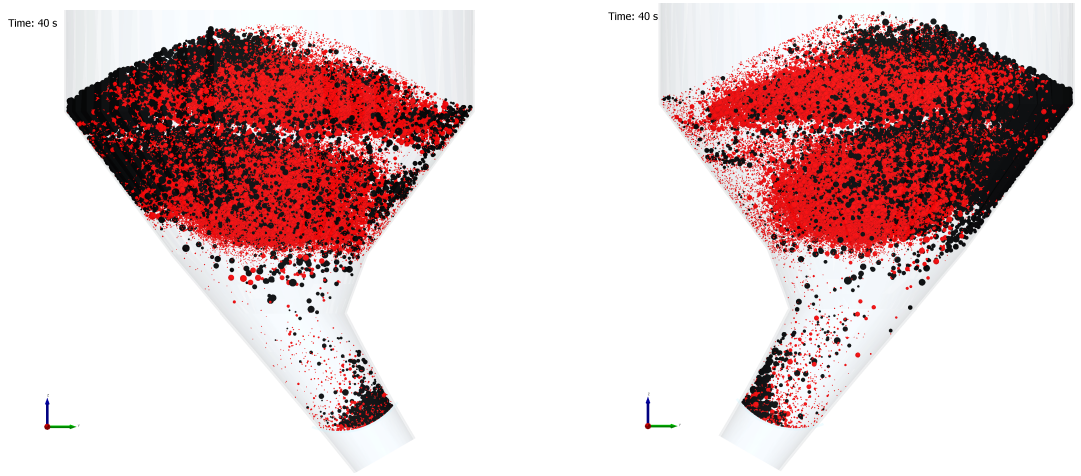

(a) (b)

Figure 6.17 Distribution of lump ore (red) and nut coke (black) within: a) left, and b) right top hoppers. Pellets and sinter are omitted for clarity.

ence case (Case 1) in Figure 6.18. It confirms that pellets and sinter show stronger segregation in the right hopper. In particular, pellets are more concentrated on the left side of the right hopper, whereas in Case 1, they are well mixed in the corresponding region (right side in Case 1, due to mirroring).

To explain the pellet distribution, the average velocity of pellets in the y-direction was analysed immediately after leaving the receiving funnel, as they travel along the chute. This is the location where Case 2 deviates from Case 1. Figure 6.19 presents a visual and quantitative comparison of the y-direction velocity of pellets for Cases 1 and 2, showing that the y-velocity in Case 2 is lower than in Case 1. This reduced y-velocity causes the pellets to be deposited more on the left side of the hopper, as also seen in Figure 6.18(b).

The underlying mechanism can be related to the interaction between the pellet discharge direction and the chute orientation. When pellets are discharged from the skip car into the receiving funnel, they initially have velocity in the negative y-direction. In Case 1, the chute orientation aligns favourably with this velocity, facilitating smooth movement of pellets along the chute. In contrast, in Case 2, the chute orientation is unfavourable, which disrupts the flow. Consequently, this causes the accumulation of particles near the start of the chute, and reduces the flow velocity in the y direction.

When comparing segregation after the top hopper discharge between Case 1 and Case 2, Figure 6.20 shows that the overall trends are generally similar. As discussed in Section 6.3.2, the segregation behaviour after hopper discharge is largely correlated to the vertical segregation established within the top hopper. This is supported by Figure 6.16(c), which indicates only minimal differences in vertical segregation between the two cases. This similarity in the vertical distribution of materials explains the comparable segregation patterns observed in Figure 6.20.

Despite these similarities, certain differences are observed. For most of the discharge period, pellets and sinter have lower segregation in Case 2. However, towards the end of discharge, they become more segregated. This is attributed to differences in their horizontal mass ratio near the hopper walls between the two cases (Figure 6.18). Since the material near the walls is discharged last, these horizontal differences directly influence the late-stage segregation behaviour.

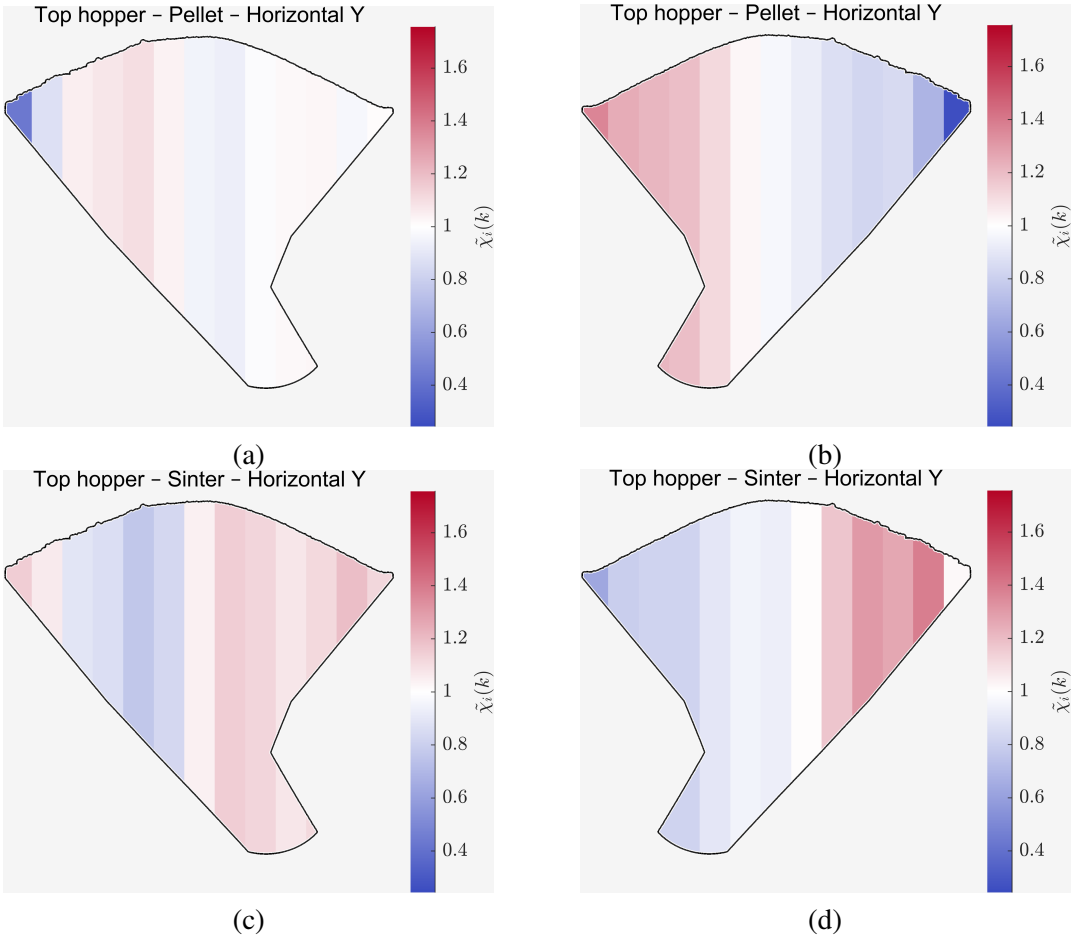

Figure 6.18 NMR in the y-direction within the top hopper for: (a) pellets left hopper, (b) pellets right hopper, (c) sinter left hopper, and (d) sinter right hopper.

Lump ore is also slightly more segregated in Case 2. For nut coke, as noted in Section 6.3.2, particles near the hopper walls are discharged last, causing a sharp increase in their proportion towards the end of discharge. This effect is even more pronounced in Case 2, where a greater quantity of nut coke is deposited near the walls compared to Case 1 (Figure 6.17), which amplifies the late-stage rise in nut coke content.

In summary, although the system appears symmetric after the receiving funnel, the asymmetric charging geometry upstream (i.e., the weighing hoppers and skip car) changes the flow pattern and segregation behaviour. This results in increased segregation in the horizontal (y) direction within the top hopper. During hopper discharge, the overall segregation trends between the two cases are comparable; however, for Case 2, pellets and sinter are generally less segregated, whereas lump ore and nut coke show a slightly higher degree of segregation.

6.3.4 Effect of weighing bunker order (Case 3 vs. Case 1)

Discussions with experts at Tata Steel IJmuiden highlighted that the loading order of the weighing bunkers could be practically modified by discharging pellets into the sinter weighing bunker and, conversely, sinter into the pellets weighing bunker. Based on this insight, an alternative case was developed to evaluate whether this reversed loading order could reduce segregation in

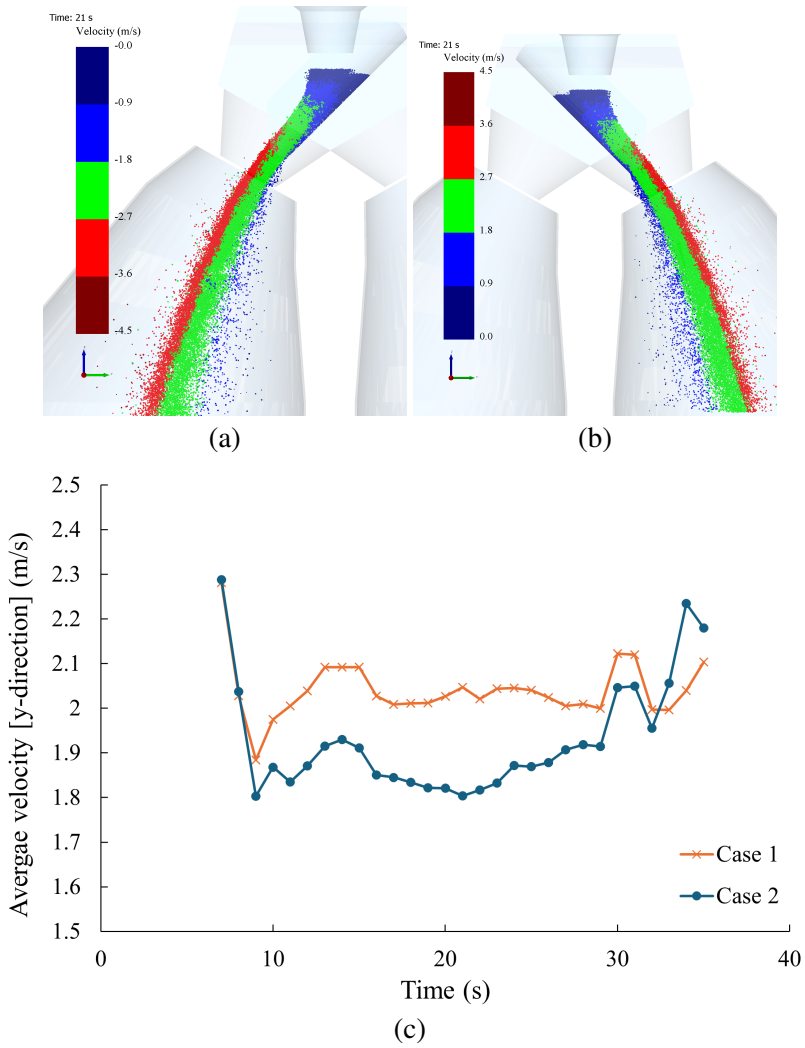

Figure 6.19 Visualisation of the velocity of pellets in the y-direction on the chute for a single time instance in (a) Case 1 and (b) Case 2. (c) Average velocity of pellets in the y-direction on the chute over the entire flow period.

the skip car and, in turn, within the top hopper.

Figure 6.21 shows that reversing the weighing bunker order has varying effects depending on the material. For pellets, segregation increases within the skip car, while in the top hopper the increase is confined to the horizontal direction. For sinter, the impact on segregation is negligible. Lump ore also shows minimal change overall, although horizontal segregation in the x-direction is slightly higher. For nut coke, segregation within the skip car remains largely unchanged, while in the top hopper, horizontal segregation is slightly reduced.

Overall, these results show that reversing the order of the weighing bunkers is not advantageous, as it promotes mixing of pellets and sinter within the skip car and increases pellet segregation. However, nut coke shows less horizontal segregation, with a more uniform distribution in the top hopper, as illustrated in Figure 6.22.

Figure 6.23 shows that the segregation behaviour of the mixture discharged from the hopper differs significantly between Case 3 and Case 1 for pellets and sinter. As discussed earlier, segregation after hopper discharge is largely correlated with the vertical segregation established

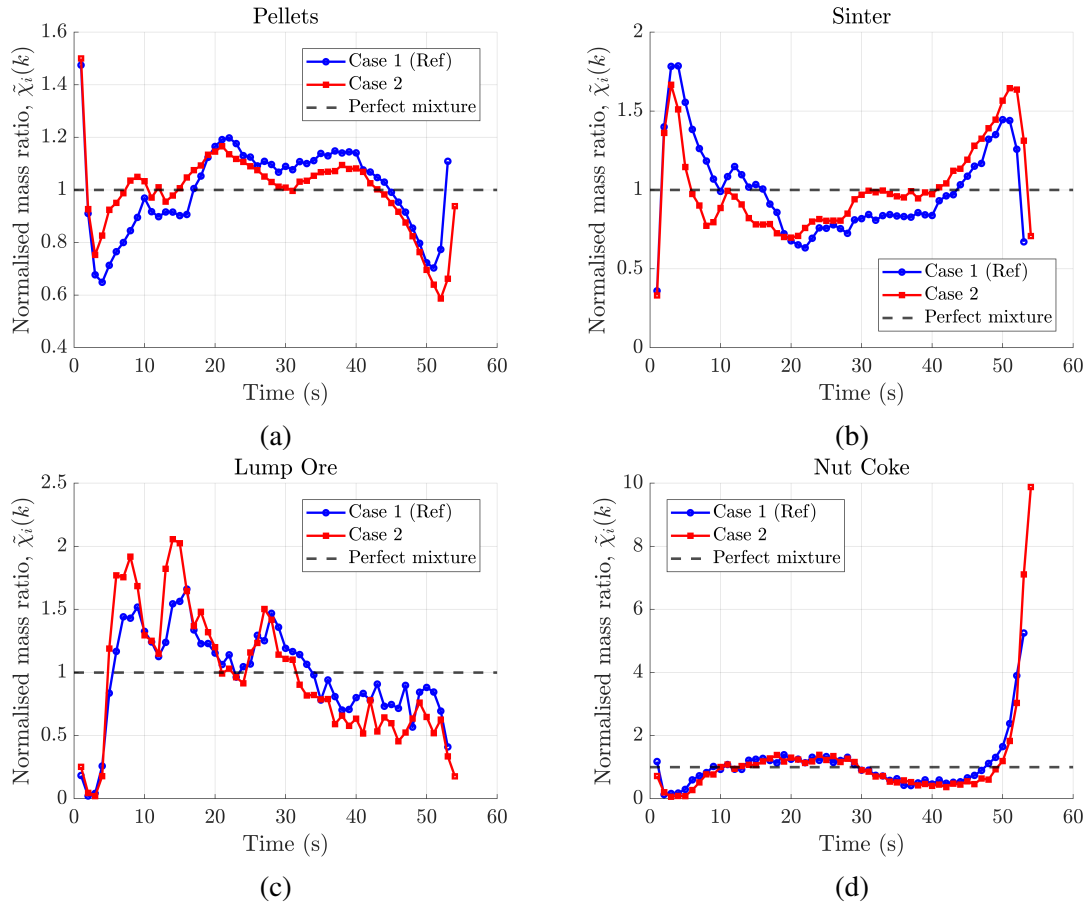

Figure 6.20 Comparison of segregation after hopper discharge between Case 2 and the reference case (Case 1) for: (a) pellets, (b) sinter, (c) lump ore, and (d) nut coke.

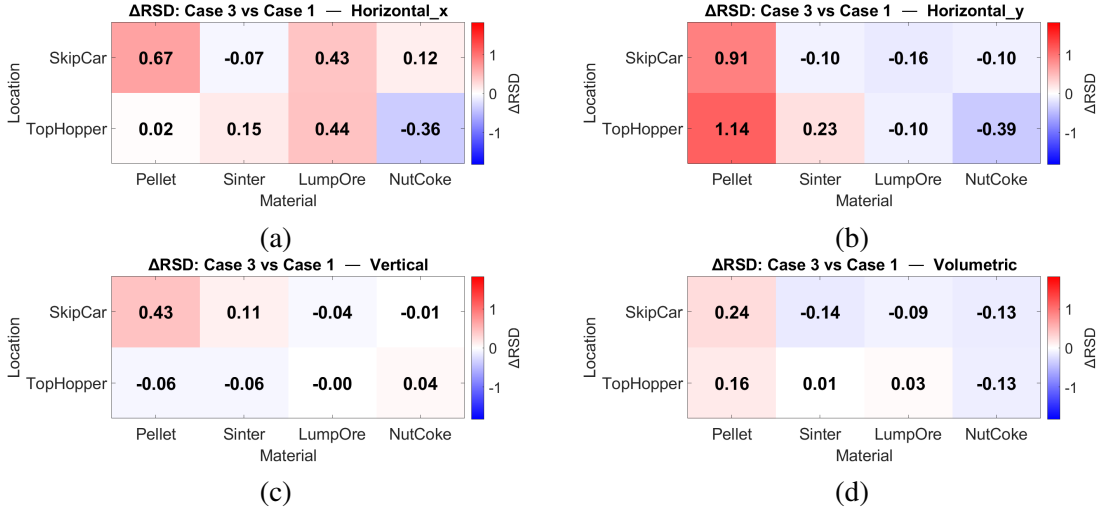

Figure 6.21 Change in RSD for Case 3 vs. Case 1 in a) Horizontal (X), b) Horizontal (Y), c) Vertical (Z), and d) Volumetric directions.

within the hopper. However, Figure 6.21(c) shows that the extent of vertical segregation is not significantly altered in Case 3.

To provide a more complete understanding and gain deeper insight into the vertical distribu-

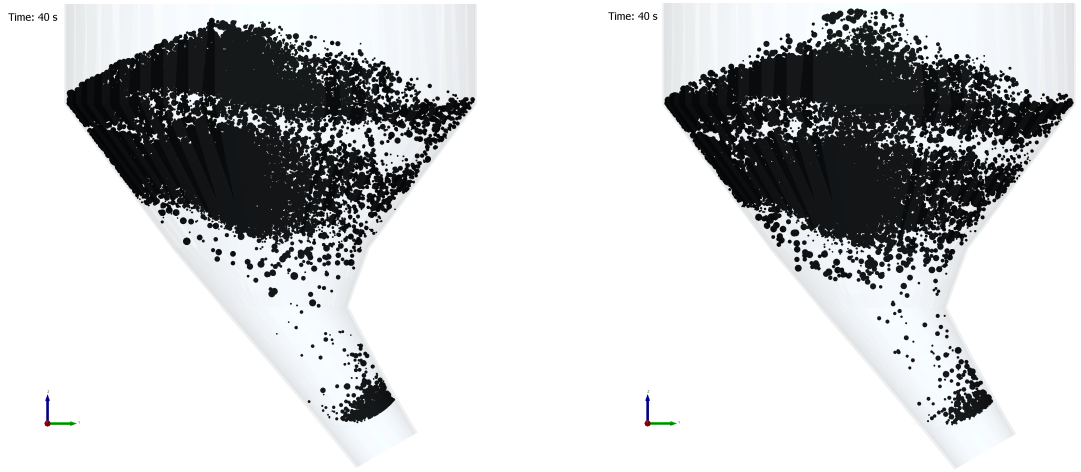

(a) (b)

Figure 6.22 Distribution of nut coke within the top hopper for: a) Case 1, and b) Case 3.

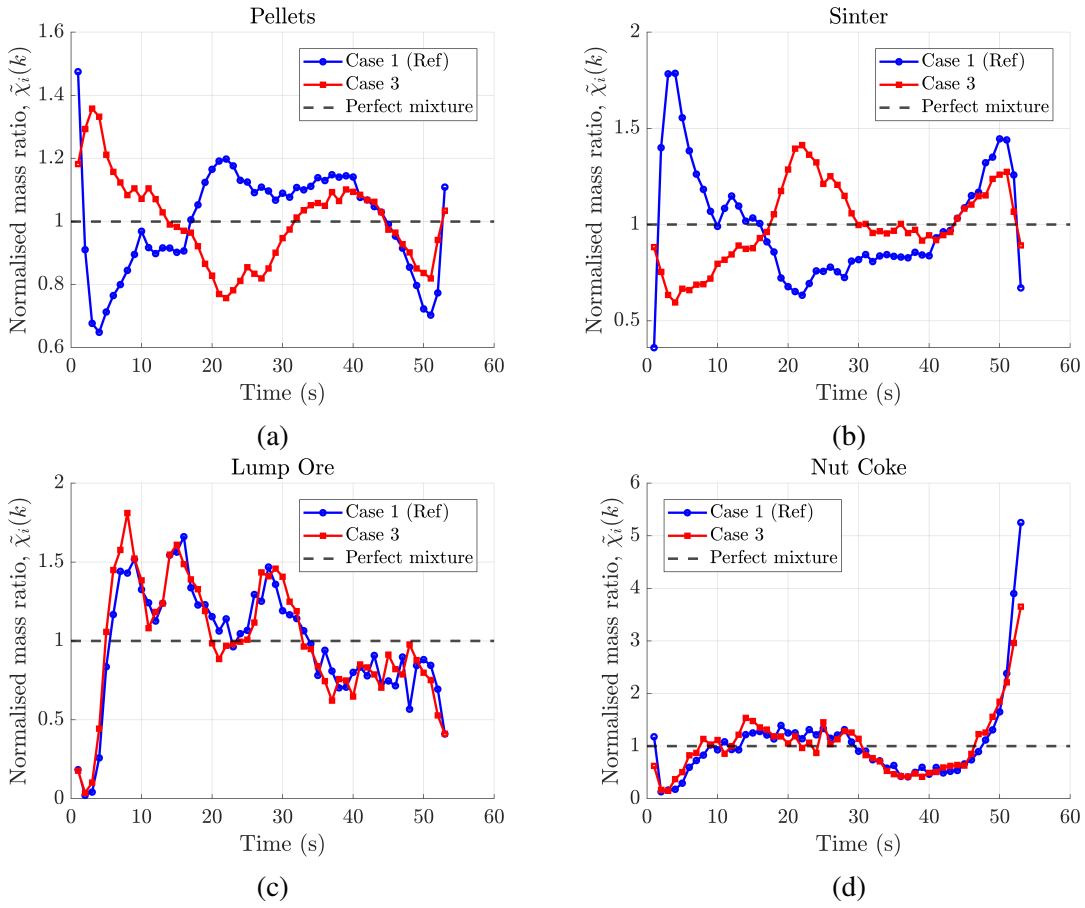

Figure 6.23 Comparison of segregation after hopper discharge between Case 3 and the reference case (Case 1) for: (a) pellets, (b) sinter, (c) lump ore, and (d) nut coke.

tion, the NMRs of pellets and sinter along the hopper height for Case 3 and Case 1 are presented in Figure 6.24. It reveals that, although the vertical RSD values are similar, the distribution patterns differ substantially between the two cases. In Case 3, pellets are concentrated near the bottom of the hopper, while the upper region contains less pellets. This distribution explains the high NMR observed at the start of discharge, followed by a decline (see Figure 6.23(a)). In

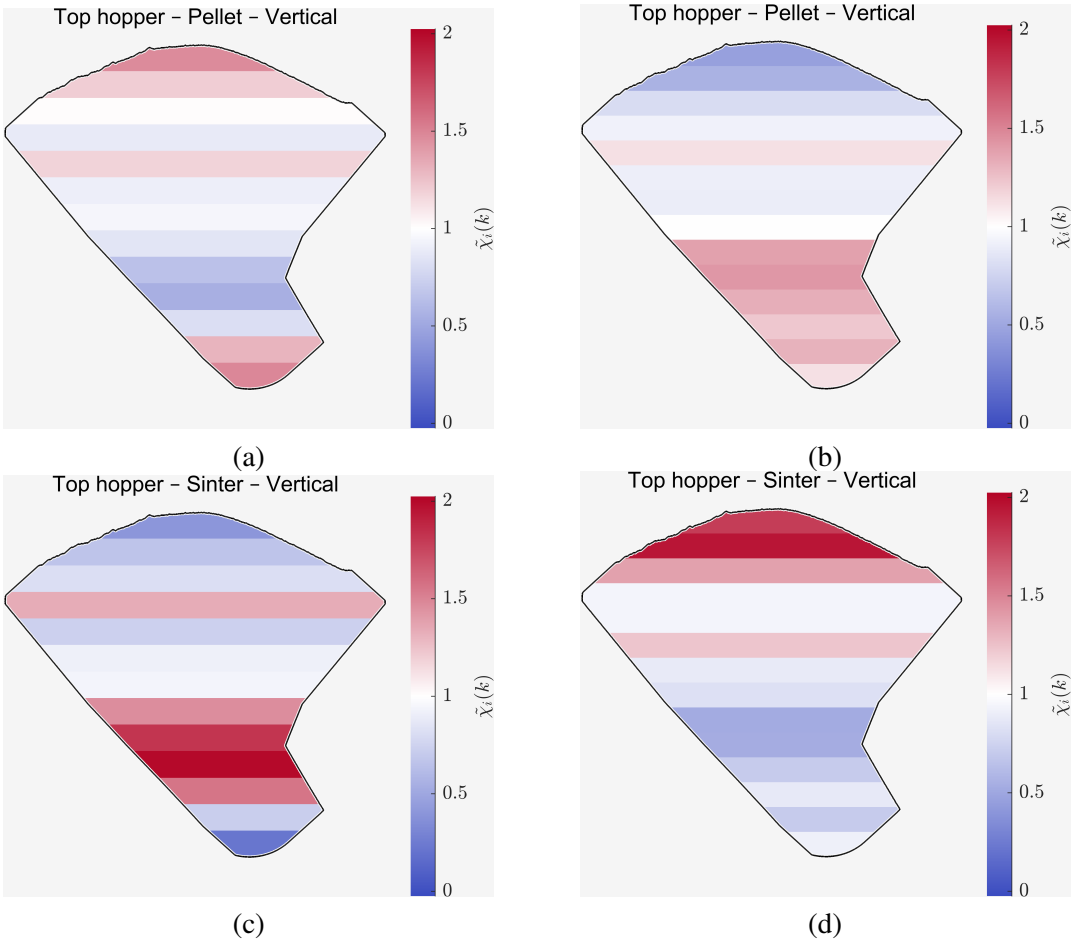

Figure 6.24 NMR in the vertical direction within the top hopper for: (a) pellets Case 1, (b) pellets Case 3, (c) sinter Case 1, and (d) sinter Case 3.

contrast, for sinter, the bottom region has a lower mass ratio, resulting in reduced mass flow at the beginning. As discharge progresses and the top regionricher in sinteris emptied, the mass ratio of sinter increases (Figure 6.23(b)). This change in the discharge pattern could be either beneficial or detrimental, depending on the process requirements and the desired distribution of pellets and sinter on the furnace throat.

For lump ore and nut coke, however, both the trend and the extent of segregation are largely similar between the two cases. The only notable difference is observed for nut coke at the end of discharge, where segregation is reduced. This reduction is linked to the lower horizontal segregation of nut coke within the top hopper (see Figure 6.22).

In summary, reversing the weighing bunkers of pellets and sinter increases segregation within the skip car, particularly for pellets. In the top hopper, it results in higher horizontal segregation of pellets but lower horizontal segregation of nut coke. After hopper discharge, the segregation behaviour of pellets and sinter is significantly affected, which is attributed to their significantly different vertical distributions in the hopper between the two cases. In contrast, lump ore and nut coke show overall similar segregation behaviour after hopper discharge in both cases.

6.3.5 Effect of wall friction (Case 4 vs. Case 1)

At Tata Steel IJmuiden, parts of the internal surfaces of the charging equipment are lined with ceramic tiles to reduce wear, which are generally assumed to be smoother than steel. Although the joints or gaps between tiles may locally hinder flow, as is commonly observed in transfer chutes, the dominant effect is assumed to be a reduction in wall friction. As concluded in Chapter 3, the particlewall coefficient of sliding friction has a significant influence on segregation. To investigate this effect and assess whether the conclusions drawn from small-scale geometry can be translated to the full-scale system, Case 4 was defined and simulated with a 25% reduction in the particlewall sliding friction coefficient for the tiled surfaces, and compared against the reference case (Case 1).

Figure 6.25 shows that the reduction (by 25%) in the particlewall sliding friction coefficient has an insignificant effect on segregation. The only noticeable change is a slight reduction in horizontal segregation in the x-direction within the top hopper. Similarly, Figure 6.26 indicates that the segregation behaviour after hopper discharge remains largely unchanged. The main difference observed is a slightly faster discharge rate, due to the smoother internal surfaces in Case 4. These results suggest that, for the full-scale geometry considered, wall friction is not a dominant factor influencing segregation behaviour.

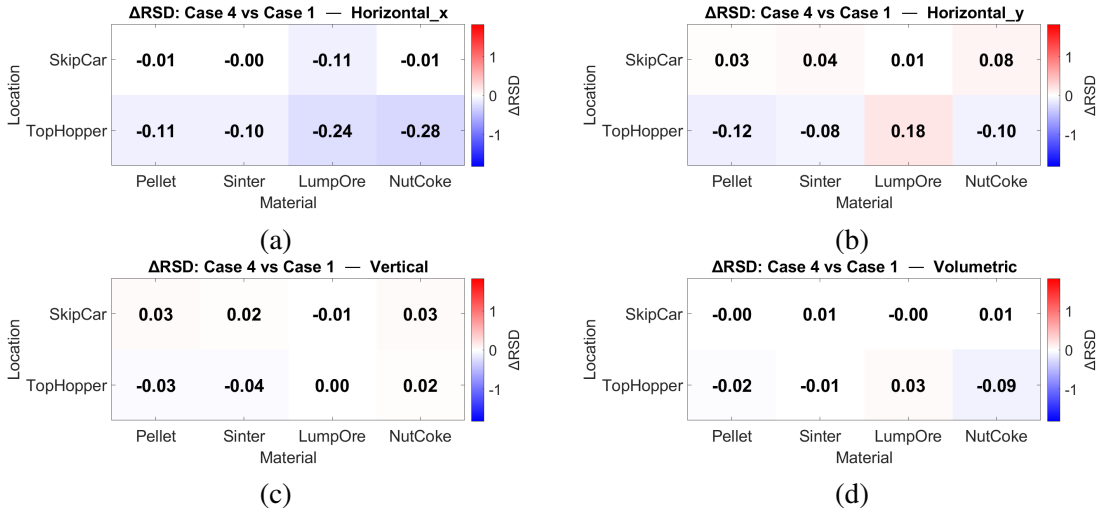

Figure 6.25 Change in RSD for Case 4 vs. Case 1 in a) Horizontal (X), b) Horizontal (Y), c) Vertical (Z), and d) Volumetric directions.

6.3.6 Effect of sinter PSD variability (Cases 5A and 6A vs. Case 1A)

At Tata Steel, the PSD of sinter varies over time. To investigate the effect of these variations on the segregation of the ferrous mixture, three simulation cases were defined and performed: Case 1A, representing the average yearly PSD (reference case); Case 5A, representing the finest monthly PSD; and Case 6A, representing the coarsest monthly PSD, taken as two extremes. The particle size distributions of these variants are illustrated in Figure 6.27, and the exact PSD values are listed in Table E.3 in Appendix E.

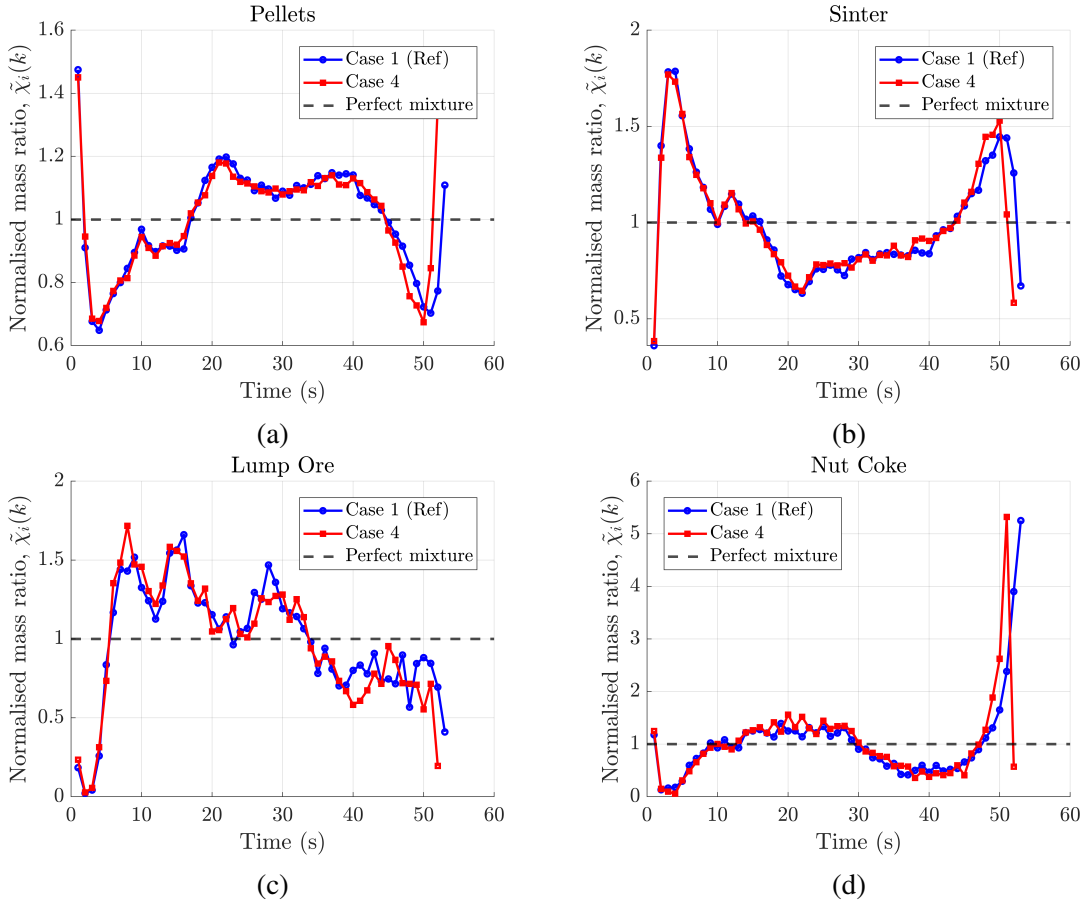

Figure 6.26 Comparison of segregation after hopper discharge between Case 4 and the reference case (Case 1) for: (a) pellets, (b) sinter, (c) lump ore, and (d) nut coke.

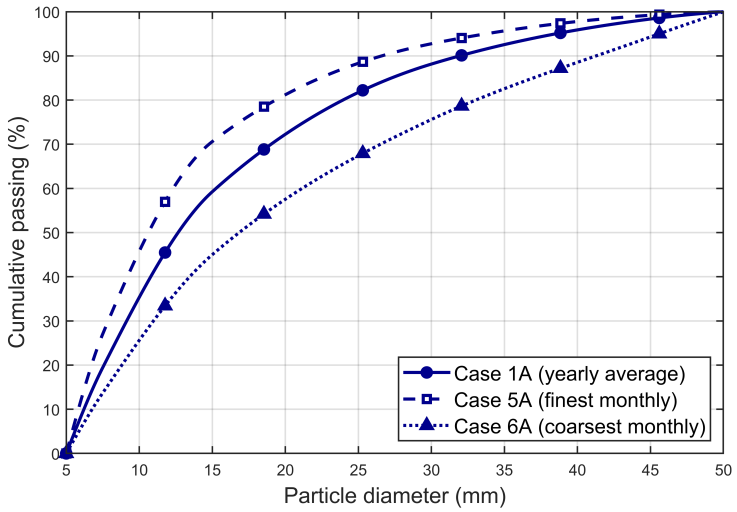

Figure 6.27 Particle size distributions of sinter used in Cases 1A (yearly average), 5A (finest monthly), and 6A (coarsest monthly).

Figure 6.28 and Figure 6.29 show that variations in sinter PSD have no significant overall effect on the extent of segregation; nevertheless, minor differences can be observed. The finer PSD in Case 5A results in slightly higher segregation, which can be attributed to enhanced percolation and reduced interlocking of smaller particles. In contrast, the coarser PSD in Case 6A leads to slightly lower segregation, particularly in the y-direction within the top hopper, as the larger particles exhibit greater stability and reduced tendency to percolate.

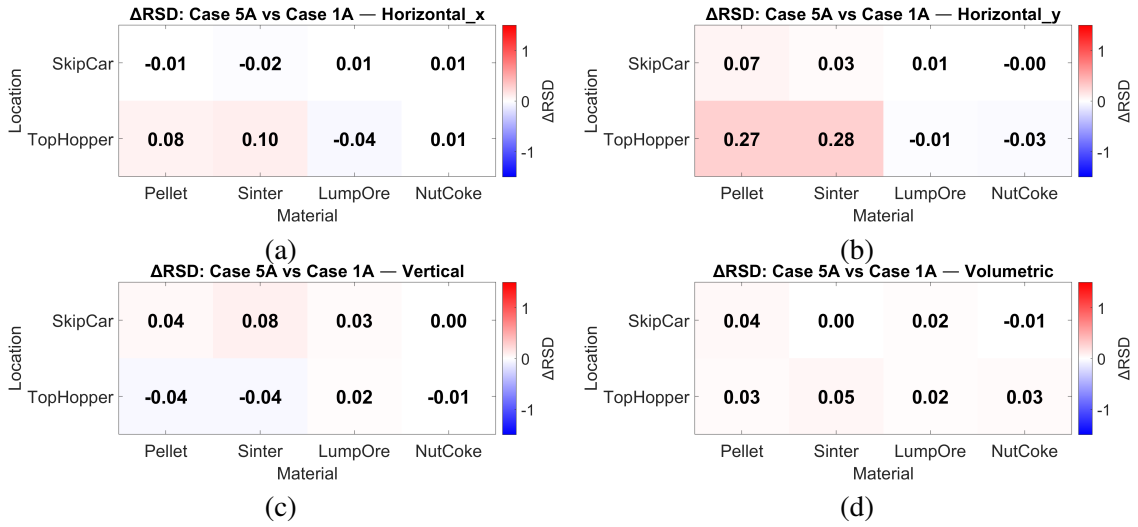

Figure 6.28 Change in RSD for Case 5A vs. Case 1A in a) Horizontal (X), b) Horizontal (Y), c) Vertical (Z), and d) Volumetric directions.

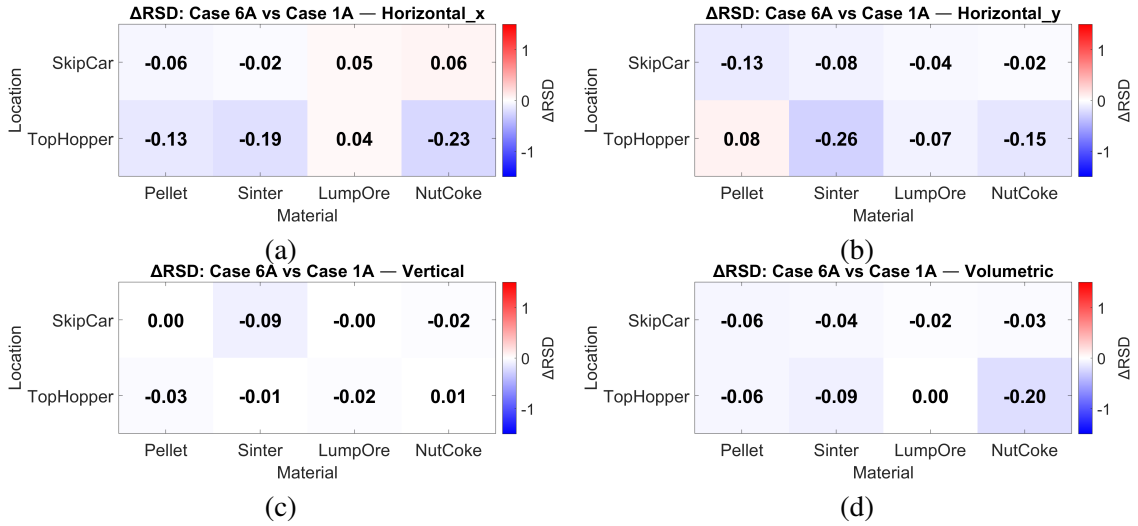

Figure 6.29 Change in RSD for Case 6A vs. Case 1A in a) Horizontal (X), b) Horizontal (Y), c) Vertical (Z), and d) Volumetric directions.

To explain the differences in y-direction segregation of sinter within the top hopper, Figure 6.30 presents the horizontal distribution of sinter for the three cases. For the finer PSD (Case 5A), more sinter accumulates on the right side of the hopper and less on the left. The opposite trend is observed in Case 6A with the coarser PSD. Since the extent of segregation within the skip car is largely the same across all cases (Figure 6.28 and Figure 6.29), these horizontal differences in the top hopper are most likely induced by the chute flow. Larger particles are able

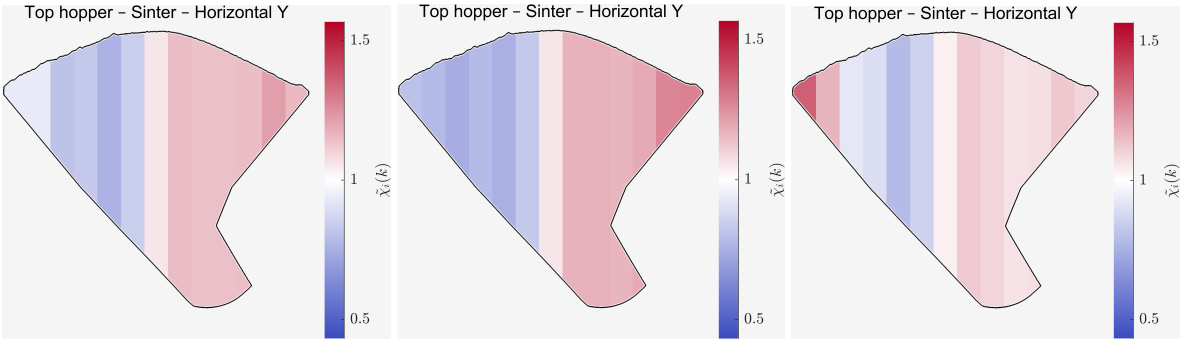

(a) (b) (c)

Figure 6.30 NMR in the horizontal y direction within the top hopper for: a) Case 1A (average PSD), b) Case 5A (fine PSD), and c) Case 6A (coarse PSD).

to maintain higher momentum and therefore travel farther after leaving the chute. As a result, in Case 6A with the coarser PSD, more sinter particles are deposited on the left side of the hopper than in Cases 5A and 1A, as shown in Figure 6.30. This suggests that chute dynamics can amplify relatively small differences in PSD into noticeable variations in horizontal distribution within the hopper.

Figure 6.31 illustrates the segregation of different materials after hopper discharge. The overall segregation behaviour is largely similar across the cases, with the main differences appearing in the final stage of discharge, particularly for pellets and sinter. For sinter, it is observed that the finer the PSD, the lower the segregation towards the end of the discharge. This can be explained by the horizontal segregation in the y-direction within the top hopper, as discussed above. As shown in Figure 6.30(c), in the case of the coarser PSD (Case 6A), more sinter is deposited on the left side of the hopper. As concluded in Section 6.3.2, the material located near the hopper walls is discharged last, which leads to an increase in the sinter content at the outlet in Case 6A. This indicates that finer PSDs may help mitigate late-stage segregation, whereas coarser PSDs tend to exacerbate it.

In summary, variations in the PSD of sinter primarily affect the horizontal distribution of material within the top hopper. A coarser PSD results in particles travelling farther from the chute and accumulating on the left side of the hopper. This, in turn, increases segregation during the final stage of hopper discharge. Nevertheless, PSD variation of sinter had only a minor overall influence on segregation behaviour in the charging system.

6.3.7 Effect of lump ore type (Case 7 vs. Case 1)

At Tata Steel IJmuiden, several types of lump ore (designated as AE) are used. In typical operations, types AC are most common, where types A and B have similar particle size distributions (PSDs), and type C is slightly finer (see Table E.1). To assess whether this difference affects segregation within the charging system, Case 7 was modelled using lump ore type C.

Figure 6.32 shows that changing the lump ore type has a negligible effect on segregation behaviour in both the skip car and the top hopper. Minor variations fall within the expected range of simulation variability. Moreover, segregation after hopper discharge shows negligible differences relative to Case 1 (see Appendix E, Figure E.1).

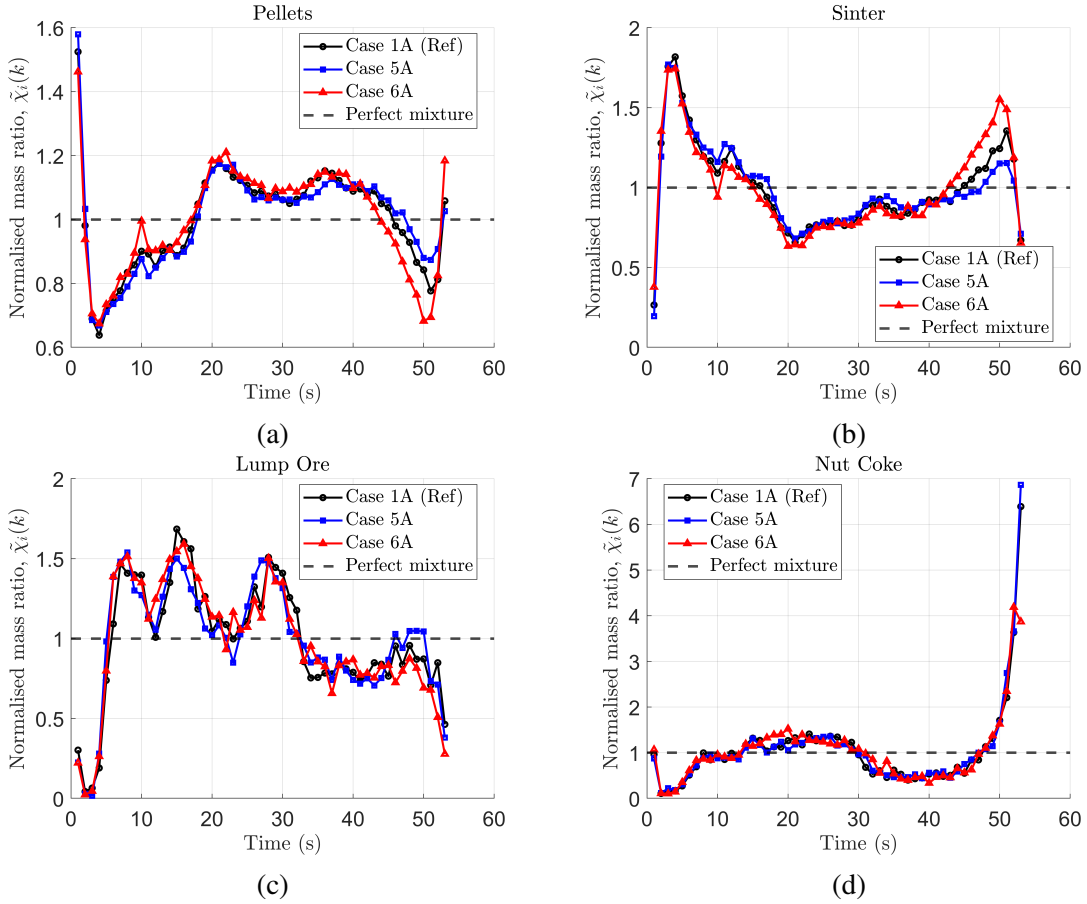

Figure 6.31 Comparison of segregation after hopper discharge between Case 5A, Case 6A, and their reference case (Case 1A) for: (a) pellets, (b) sinter, (c) lump ore, and (d) nut coke.

In this comparison, the only parameter varied between the two ore types was the particle size distribution (PSD). If variations in other properties, such as particle density and friction coefficients, were also considered, the effect might have been more pronounced. Nevertheless, under the current operating conditions, the lump ore type is not a significant factor influencing segregation

6.3.8 Effect of sinter particle shape (Case 8 vs. Case 1)

So far, spherical particles have been used to represent all materials because of their computational efficiency, which is essential for simulating large-scale systems. This simplification is broadly effective, particularly for pellets that are nearly spherical. However, other ferrous materials such as sinter, lump ore, and nut coke exhibit irregular shapes (see Figure 1.4). To evaluate whether accounting for particle shape influences segregation behaviour, sinter, which is the largest fraction among these materials, was selected for more detailed representation. This was achieved using a clumped-sphere approach, as described in Chapter 3 and illustrated in Figure 3.4.

Figure 6.33 shows that the irregular shape of sinter mainly affects the segregation of pellets and sinter, while lump ore and nut coke remain largely unchanged. This is because their total amount is much smaller than that of pellets and sinter, which limits their interaction with sinter

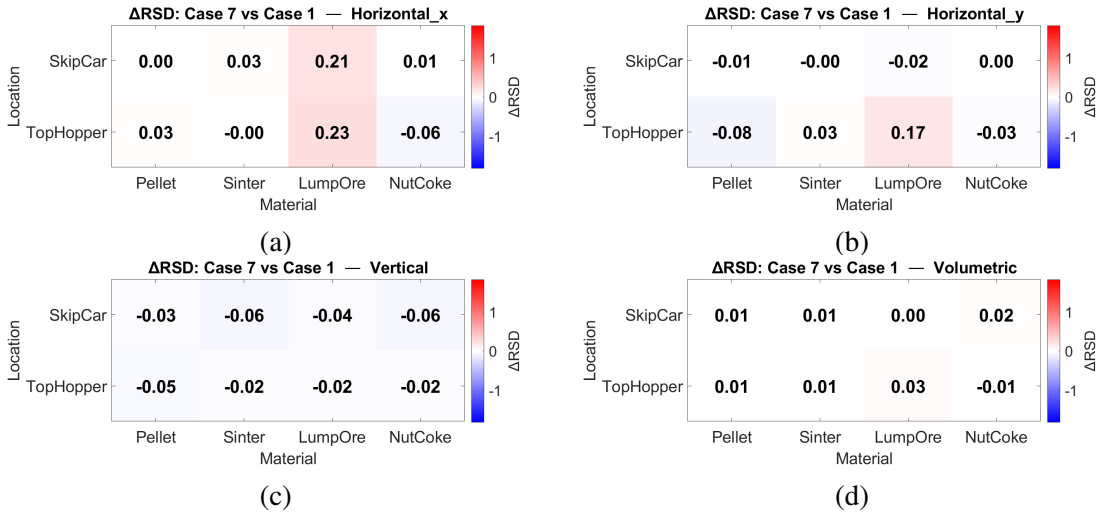

Figure 6.32 Change in RSD for Case 7 vs. Case 1 in a) Horizontal (X), b) Horizontal (Y), c) Vertical (Z), and d) Volumetric directions.

particles during discharge from the weighing bunkers into the skip car. In the skip car, vertical segregation of pellets and sinter is slightly higher in Case 8. A more detailed view is provided in Figure 6.34, which illustrates that non-spherical sinter particles in Case 8 are distributed more extensively near the surface of the skip car. This happens because the non-spherical sinter particles discharge more slowly from the weighing bunker, resulting in a larger proportion of sinter being deposited towards the end of the filling process of the skip car. Consequently, a greater amount of sinter accumulates in the upper region of the skip car. Although this increases the vertical RSD in the skip car in Case 8, it reduces vertical segregation within the top hopper. As shown in Figure 6.35, the bottommost part of the top hopper, which is relatively depleted of sinter in Case 1, is now populated with more sinter in Case 8, leading to a more balanced vertical distribution.

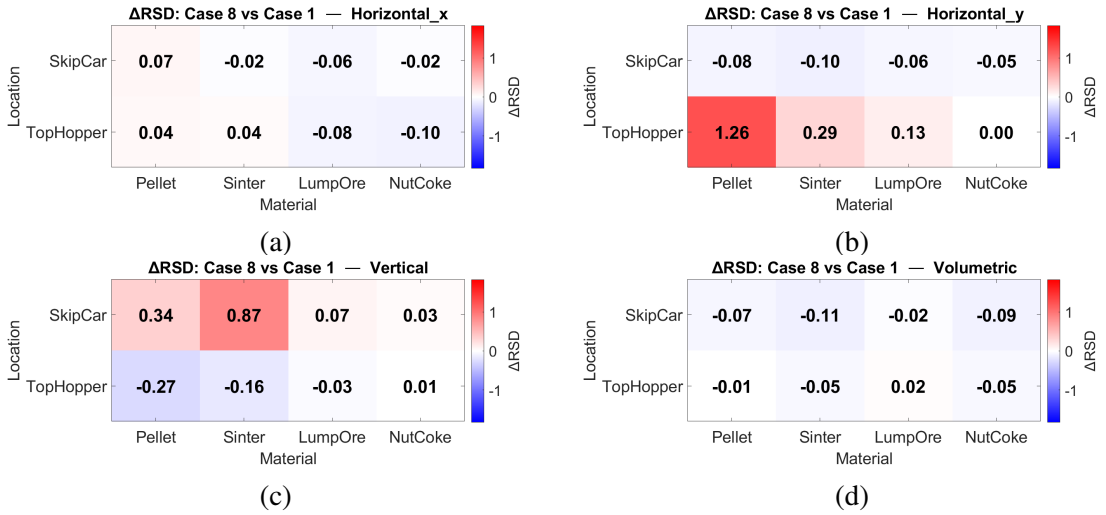

Figure 6.33 Change in RSD for Case 8 vs. Case 1 in a) Horizontal (X), b) Horizontal (Y), c) Vertical (Z), and d) Volumetric directions.

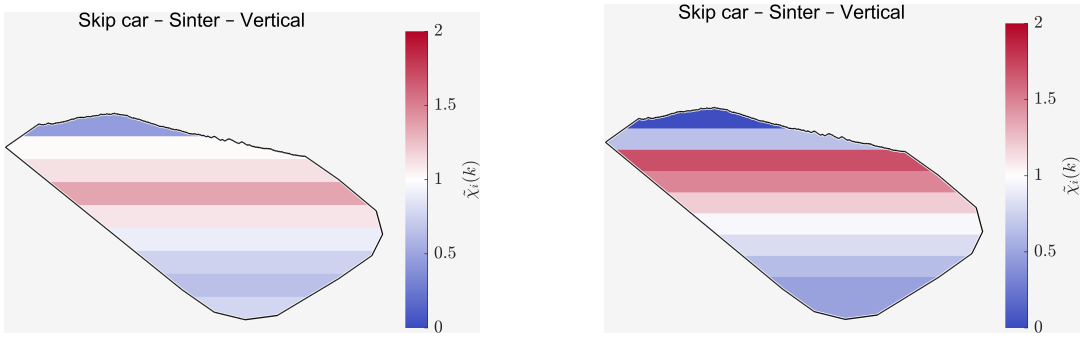

(a) (b)

Figure 6.34 NMR of sinter in the vertical direction within the skip car for: a) Case 1, and b) Case 8.

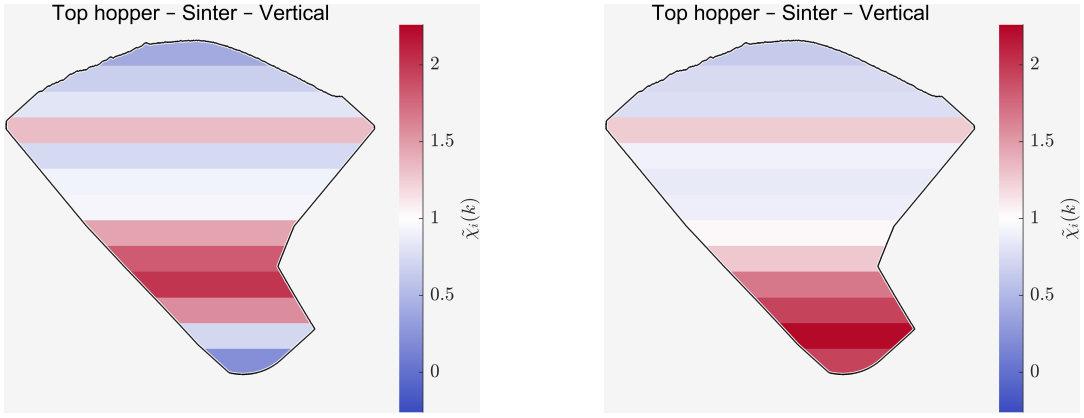

(a) (b)

Figure 6.35 NMR in the vertical direction within the top hopper for: a) Case 1, and b) Case 8.

Figure 6.36 highlights the effects of modelling sinter as non-spherical (clumped) particles. First, the hopper discharge time is prolonged, reflecting a slower flow regime induced by the enhanced interlocking and higher effective resistance of irregularly shaped particles. Second, the segregation behaviour during the mid-discharge period remains largely consistent with Case 1. The main differences are observed during the initial stage of discharge, where the NMR of pellets at the outlet decreases significantly, while that of sinter increases. This observation is explained by the vertical composition at the bottom of the hopper (see Figure 6.35), where in Case 8 a greater proportion of sinter and fewer pellets are present. Beyond this initial stage, the influence of particle shape diminishes, with only minor and inconsistent differences observed thereafter.

In summary, modelling sinter particles as non-spherical shapes affected only the segregation behaviour of pellets and sinter, as lump ore and nut coke are present in much smaller quantities and thus have limited interaction with sinter. The main effect is on the vertical segregation within the skip car and top hopper, which subsequently affects segregation after hopper discharge only during the initial stage. Beyond this, overall segregation trends remain comparable to the spherical-particle case. These findings suggest that while accounting for particle shape improves realism and is relevant for capturing early-stage discharge dynamics, spherical particles remain adequately accurate for representing large-scale segregation behaviour in the charging system.

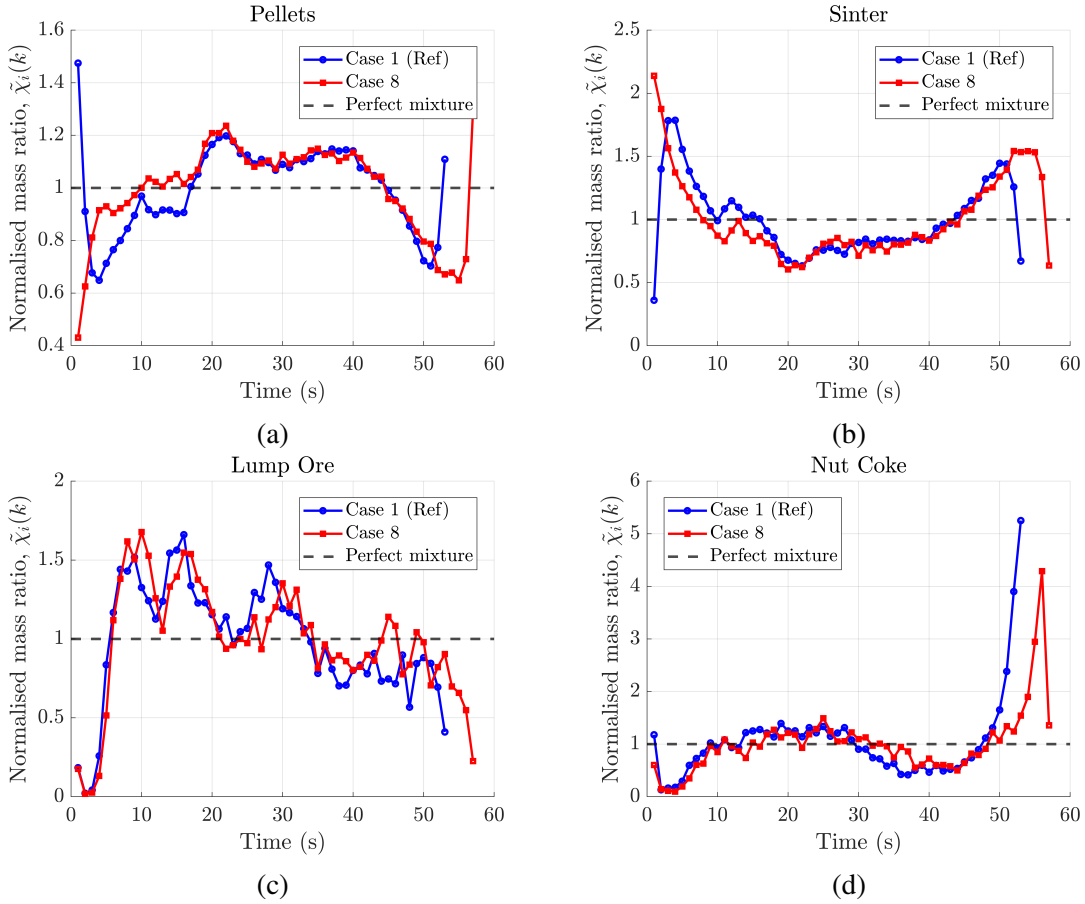

Figure 6.36 Comparison of segregation after hopper discharge between Case 8 and the reference case (Case 1) for: (a) pellets, (b) sinter, (c) lump ore, and (d) nut coke.

6.4 Conclusion

This chapter presented the results of industrial-scale DEM simulations of segregation in the ferrous mixture (pellets, sinter, lump ore, and nut coke) within the blast furnace charging system, from the weighing bunkers through to discharge from the top hopper. A reference case, reflecting the current practice at Tata Steel IJmuiden, was first modelled and analysed in detail to establish the baseline segregation behaviour. Building on this, a series of systematically designed case studies was carried out to investigate the influence of various factors, including material properties, modelling assumptions, and operational parameters, on segregation. The conclusions of this chapter are summarised below:

- Perfect upstream mixing of pellets and sinter in the weighing bunkers virtually eliminates segregation. Under current practice, however, materials are not sufficiently mixed in the skip car and remain largely segregated throughout the charging system.
- Segregation generally decreases from the skip car to the top hopper, due to partial remixing occurring during transfer through the receiving funnel.
- Pellets and sinter exhibit lower segregation levels than lump ore and nut coke, with sinter slightly more segregated than pellets. Specifically, lump ore and nut coke show strong

vertical segregation within the top hopper, where they mostly accumulate near the top surface of the mixture.

- Significant segregation was observed during top hopper discharge, particularly at the beginning and end stages. Among all materials, pellets consistently showed the lowest degree of segregation. The results also indicated that segregation behaviour during discharge was largely correlated to the vertical distribution of the mixture within the hopper.

- The mixture charged into the right hopper showed stronger horizontal (y) segregation than that charged into the left hopper, because of geometric asymmetry and the mirrored orientation of the chute. During hopper discharge, however, the overall segregation patterns remain similar in both cases. The main difference is that pellets and sinter become slightly less segregated, while lump ore and nut coke show a slightly higher degree of segregation.

- Reversing the order of pellets and sinter in the weighing bunkers increases segregation in the skip car, particularly for pellets. In the top hopper, it leads to greater horizontal segregation of pellets while slightly reducing the segregation of nut coke. Moreover, it changes the vertical distribution of pellets and sinter, which in turn significantly influences their segregation behaviour during hopper discharge. By contrast, lump ore and nut coke show segregation patterns that are largely consistent with those of the reference case.

- Varying the PSD of sinter had only a minor effect on segregation in the skip car and top hopper. Finer PSDs (i.e., with smaller D_{50}) led to slightly higher segregation, while coarser PSDs gave slightly lower segregation. During hopper discharge, differences appeared only in the final stage, where the finer PSD (smaller D_{50}) produced less segregation than the coarser PSD.

- Modelling sinter as non-spherical (clumped) particles mainly affected the segregation of pellets and sinter. It altered their vertical distribution in the top hopper, which in turn influenced the initial stage of hopper discharge, where more sinter and fewer pellets were discharged compared to the spherical case. The discharge time also increased, as expected, due to particle interlocking and slower flow velocity. Beyond the initial stage, however, the effect of non-spherical sinter on segregation was negligible, indicating that spherical particles were sufficiently accurate for representing large-scale behaviour.

- Reducing wall friction and changing the lump ore type both had negligible effects on segregation. The only noticeable change was a slightly faster discharge when wall friction was reduced.

Taken together, these findings provide new insights into the factors influencing multi-component segregation in industrial blast furnace charging. They demonstrate that while some factors (e.g., weighing bunker order) can substantially influence segregation patterns, others (e.g., wall friction, lump ore type, or moderate PSD variations) play only a minor role. Importantly, the results highlight the central role of upstream conditions in determining downstream segregation behaviour: promoting homogeneity in the weighing bunkers or early charging stages offers the greatest potential for mitigating segregation throughout the system. These outcomes not only advance the fundamental understanding of segregation in large-scale multi-component flows but

also provide a foundation for developing practical strategies to mitigate segregation in industrial practice. Nevertheless, further work is required to validate the model comprehensively against high-quality data from BF charging systems, in order to ensure accurate and reliable numerical predictions.

Chapter 7

Conclusions and recommendations

7.1 Conclusions

This thesis aimed to develop a systematic, accurate, and computationally efficient approach for modelling the segregation of multi-component mixtures in the blast furnace charging system, from the weighing bunkers to the top hoppers. To achieve this, a robust DEM framework was established and enhanced with surrogate modelling techniques to capture material behaviour and segregation patterns accurately and efficiently. This concluding chapter summarises the key insights gained from the different stages of the research and provides recommendations for future work.

The state-of-the-art review of DEM modelling for segregation of complex multicomponent mixtures highlighted several important gaps. Although most natural and industrial mixtures involve particles differing simultaneously in size, density, and shape, DEM studies addressing such systems remain limited. In addition, systematic calibration is often overlooked, leaving uncertainties about the relative importance of interaction parameters, particle shape, and particle size distribution in reproducing segregation behaviour. The review also showed that segregation is strongly influenced by material properties, system configurations, and operational parameters. Since material properties and system configurations are difficult to alter in practice, operational parameters provide a more practical route for mitigating segregation and were further researched in this work.

Comprehensive DEM sensitivity analysis identified the dominant DEM parameters affecting segregation in a pelletssinter mixture across different stages of blast furnace charging. Segregation after hopper discharge was found to be mainly influenced by particlegeometry interaction parameters, while particleparticle effects were negligible. No significant segregation occurred during the chute flow. In the heap formed after chute flow both particlegeometry and particleparticle interaction parameters play a role, depending on the initial configuration of the mixture within the hopper. The initial configuration was also shown to strongly influence the extent of segregation, highlighting that upstream flow conditions are decisive in shaping segregation patterns downstream.

A machine learning framework was developed to build surrogate models that link DEM interaction parameters to segregation outcomes in multi-component mixtures. Among the tested algorithms, Gaussian Process Regression (GPR) and Ensemble Learning gave the most accurate

results. To improve efficiency and adaptability, transfer learning was introduced so that models trained on previous configurations could be adapted to new cases with only a small amount of extra data. In the case of using TL with GPR (TL-GPR), the RMSE was reduced on average by 50% after retraining with just one additional sample, showing the adaptability of the method. Overall, these developments offer a practical and efficient way to accelerate DEM calibration and to predict segregation behaviour reliably while minimising computational costs.

An efficient and systematic calibration framework for DEM modelling of multi-component mixtures was developed for pelletsinter mixtures commonly used in blast furnace operations. The framework achieved a high-accuracy surrogate model (R^2 of 0.95) for 7 DEM parameters using only 110 data points. This represents a 25%82% reduction in dataset size compared to previous studies [173, 225], while also achieving higher accuracy. This efficiency was achieved by integrating sensitivity analysis, surrogate modelling with adaptive sampling, and optimisation to minimise the number of DEM simulations. It achieved high accuracy with a greatly reduced dataset size, highlighting its computational efficiency. The calibrated parameters were shown to be transferable across different mixture ratios and configurations. Moreover, it was concluded that active calibration of particle density is necessary when dynamic processes are targeted. Finally, sensitivity analysis showed that changes in segregation were mainly caused by DEM stochasticity, indicating that segregation in drawdown tests cannot serve as a reliable calibration target.

Building on the calibrated pelletsinter framework, industrial-scale DEM simulations of the ferrous mixture (pellets, sinter, lump ore, and nut coke) within the blast furnace charging system revealed clear patterns in how upstream and operational factors shape downstream segregation:

- Perfect mixing of pellets and sinter in the weighing bunkers virtually eliminated segregation throughout the system; however, achieving such perfect mixing is difficult in practice, and under current practice, the materials remained largely segregated due to poor mixing. Segregation decreased slightly from the skip car to the top hoppers due to partial remixing. However, strong segregation still persisted, particularly for lump ore and nut coke, which accumulated near the top of the mixture. In contrast, pellets consistently showed the lowest segregation levels.

- The analysis indicated that upstream conditions, such as bunker filling order, strongly affected segregation patterns, while factors such as wall friction, lump ore type, or moderate changes in sinter PSD had only a limited influence. Segregation during hopper discharge was found to depend mainly on the vertical distribution of materials within the top hoppers.

- Although modelling sinter as non-spherical particles altered the early stage of hopper discharge, the overall segregation behaviour was similar to that of spherical particles, suggesting that spheres provide an adequate representation for large-scale studies. Overall, the findings confirmed the importance of upstream conditions and showed that promoting homogeneity at the earliest charging stages is the most effective way to mitigate segregation in industrial blast furnace operation.

Overall, this thesis improves both the tools available for DEM modelling of multi-component mixtures and the practical understanding of how segregation develops during blast furnace

charging. The work shows that it is possible to combine computational efficiency with predictive accuracy, while also pointing to practical ways of reducing segregation in industry.

7.2 Recommendations

Based on the findings of this thesis, as well as wider needs in the field, recommendations are proposed for both future research and industrial practice.

7.2.1 Recommendations for academic research

- Future calibration studies should extend beyond two-component systems to include mixtures composed of several materials, thereby accurately capturing the complexity of real industrial mixtures.
- The current model should be expanded to cover the entire charging cycle, from the stockhouse to the furnace throat, to predict segregation throughout the whole process.
- Future work should examine a broader range of operational parameters that can be adjusted in practice and incorporate them into DEM and data-driven models, as these parameters often provide the most practical means of reducing segregation.
- The influence of size segregation occurring upstream of the weighing bunkers should be examined, as this pre-segregation may significantly affect the mixture composition in the downstream parts.
- Calibrated DEM models should be validated against high-quality datasets from industry. Defining and executing detailed industrial measurement campaigns would greatly strengthen future model validation.
- Developed DEM models, and the proposed framework could be extended to new raw materials for green steel production and may also be transferable to other steelmaking technologies with similar charging conditions, such as Reduction Electric Furnaces (REF) and Electric Arc Furnaces (EAF).
- More advanced data-driven approaches, including surrogate models and reduced-order models, should be developed with operational parameters as inputs to enable fast and reliable prediction of segregation for industrial applications and to support decision-making.
- Future DEM studies should comprehensively address the influence of DEM stochasticity on segregation outcomes by incorporating explicit uncertainty quantification methods. This can be achieved, for example, by performing ensemble simulations with different particle bed initialisations, followed by statistical analysis of segregation metrics to quantify variability and confidence intervals. Such an approach would allow segregation trends to be distinguished from stochastic fluctuations inherent to DEM simulations.

7.2.2 Industrial recommendations

- More investment should be directed towards improving upstream mixing, as even partial mixing at the weighing bunkers can substantially reduce segregation downstream. For instance, discharging different materials onto the same conveyor belt before charging into the weighing bunkers can introduce useful mixing.
- To identify effective strategies for mitigating segregation, more emphasis should be placed on operational parameters, as they are typically easier and more cost-effective to modify than material properties or system design. Future work should therefore systematically assess the sensitivity of segregation to key operational parameters, such as chute angle, rotation speed, and fill level, using targeted parametric studies. In addition, these parameters should be evaluated against practical constraints related to operational flexibility, equipment limitations, and production requirements to identify which adjustments are realistically feasible in industrial settings.
- DEM simulations, supported by surrogate and AI-based modelling, should be integrated into industrial workflows to provide fast predictions at lower computational cost. This would enable the evaluation of alternative operating scenarios, support process optimisation, and eventually improve process control.
- Close collaboration between industry and academia should be encouraged to generate the high-quality datasets needed for validation. In particular, measurements of material flow rates, discharge times, heap profiles of materials at different locations, and local particle compositions (using extensive image analysis techniques) would be valuable to validate the different stages of the DEM simulations and ensure their accurate application in practice.

Overall, these recommendations are intended to guide both future scientific developments in the DEM community and practical steps to mitigate segregation in the blast furnace and similar systems.

Appendix

A Supplementary information for Chapter 2

This chapter presents the supplementary details for Chapter 2. In Table 2.2, the segregation indices used in the literature are summarised. The indices quantify to which degree the tracer particle is homogenously distributed within the mixture. In index no. 1-8, the concentration of tracer particles is determined in each sub-domain, which can be expressed in terms of the number, mass, or volume fraction, as seen in Table A.1.

Table A.1 Equations for calculating the concentration of different types of particles (type-A or type-B) on number, mass, and volume basis. Legend: N = number of particles, m = mass of particles, V = volume of particles.

	Number based	**Mass based**	**Volume based**
Fraction of particle type-A	$(\phi_N)_A = \frac{N_A}{N}$ where $N = N_A + N_B$	$(\phi_m)_A = \frac{m_A}{m}$ where $m = m_A + m_B$	$(\phi_V)_A = \frac{V_A}{V}$ where $V = V_A + V_B$
Fraction of particle type-B	$(\phi_N)_B = \frac{N_B}{N}$	$(\phi_m)_B = \frac{m_B}{m}$	$(\phi_V)_B = \frac{V_B}{V}$
Total (number/ mass/ volume) fraction	$\phi_N = (\phi_N)_A + (\phi_N)_B = 1$	$\phi_m = (\phi_m)_A + (\phi_m)_B = 1$	$\phi_V = (\phi_V)_A + (\phi_V)_B = 1$
Relative fraction of tracer particle in bin i	$y_t^i = \frac{(\phi_N)_t^i}{\phi_N}$	$x_t^i = \frac{(\phi_m)_t^i}{\phi_m}$ where $t = A$ or B	$c_t^i = \frac{(\phi_V)_t^i}{\phi_V}$
Relative fraction of tracer particle in the entire system	$y_t = \frac{(\phi_N)_t}{\phi_N}$	$x_t = \frac{(\phi_m)_t}{\phi_m}$ where $t = A$ or B	$c_t = \frac{(\phi_V)_t}{\phi_V}$

B Supplementary information for Chapter 3

B.1 All DEM parameters used for the sensitivity analysis

Table B.1 A comprehensive overview of DEM parameters used.

DEM Parameter	Pellet	Sinter	Geometry
Particle shape			NA
	10–12.5 (mm): 32.8%	5.6–8 (mm): 14%	
	12.5–16 (mm): 67.2%	8–10 (mm): 22.2%	
Particle size distribution		10–12.5 (mm): 25.9%	NA
		12.5–16 (mm): 21.3%	
		16–20 (mm): 12.2%	
		20–25 (mm): 4.4%	
Shear modulus (G)	1e+8 Pa [147]	1e+8 Pa [147]	2e+11 Pa [150]
Poissons ratio (ν)	0.25 [147]	0.25 [147]	0.3 [150]
Solid density (ρ_s)	1951 (kg/m^3)	1731 (kg/m^3)	7800 (kg/m^3) [150]
Coefficient of static friction (μ_s)			
Coefficient of rolling friction (μ_r)		Variable (see Table 3.2)	
Coefficient of restitution (C_r)			
Time step		7.94e–6 s (20% of Rayleigh time step)	

B.2 The matrix for definitive screening design (DSD)

Table B.2 Definitive screening design matrix.

Run	$\mu_{s,pp}$	$\mu_{r,pp}$	$C_{r,pp}$	$\mu_{s,ss}$	$\mu_{r,ss}$	$C_{r,ss}$	$\mu_{s,ps}$	$\mu_{r,ps}$	$C_{r,ps}$	$\mu_{s,pg}$	$\mu_{r,pg}$	$C_{r,pg}$	$\mu_{s,sg}$	$\mu_{r,sg}$	$C_{r,sg}$
1	0.21	0.05	0.7	0.76	0.08	0.01	0.21	0.38	0.01	0.5	0.35	0.41	0.9	0.2	0.05
2	0.21	0.145	0.7	0.76	0.08	0.35	0.21	0.05	0.01	0.5	0.35	0.2	0.38	0.08	0.5
3	0.7	0.05	0.3	0.76	0.08	0.35	0.76	0.38	0.01	0.31	0.35	0.62	0.9	0.08	0.5
4	0.21	0.05	0.7	0.43	0.38	0.35	0.485	0.38	0.7	0.31	0.35	0.2	0.38	0.08	0.5
5	0.21	0.05	0.3	0.43	0.38	0.01	0.76	0.38	0.355	0.5	0.35	0.2	0.9	0.08	0.05
6	0.7	0.145	0.3	0.43	0.38	0.01	0.76	0.38	0.7	0.31	0.05	0.62	0.9	0.2	0.05
7	0.21	0.24	0.3	0.76	0.38	0.18	0.76	0.38	0.01	0.5	0.05	0.2	0.38	0.2	0.5
8	0.7	0.24	0.7	0.76	0.08	0.35	0.21	0.05	0.355	0.31	0.05	0.62	0.38	0.2	0.5
9	0.21	0.05	0.3	0.43	0.38	0.35	0.21	0.05	0.01	0.5	0.05	0.62	0.9	0.14	0.5
10	0.21	0.24	0.5	0.76	0.38	0.01	0.76	0.05	0.01	0.31	0.35	0.62	0.38	0.08	0.05
11	0.21	0.24	0.7	0.43	0.08	0.01	0.76	0.05	0.7	0.5	0.2	0.62	0.9	0.08	0.5
12	0.21	0.24	0.3	0.43	0.08	0.35	0.21	0.38	0.7	0.405	0.35	0.62	0.38	0.2	0.05
13	0.7	0.24	0.3	0.43	0.38	0.35	0.76	0.05	0.7	0.31	0.05	0.41	0.38	0.08	0.5
14	0.7	0.05	0.7	0.76	0.38	0.01	0.76	0.05	0.01	0.405	0.05	0.2	0.9	0.08	0.5
15	0.21	0.05	0.7	0.76	0.23	0.35	0.76	0.05	0.7	0.31	0.05	0.2	0.9	0.2	0.05
16	0.7	0.05	0.5	0.43	0.08	0.35	0.21	0.38	0.7	0.5	0.05	0.2	0.9	0.2	0.5
17	0.7	0.24	0.3	0.43	0.23	0.01	0.21	0.38	0.01	0.5	0.35	0.62	0.38	0.08	0.5
18	0.21	0.24	0.7	0.43	0.38	0.01	0.21	0.05	0.7	0.5	0.05	0.2	0.38	0.2	0.05
19	0.7	0.05	0.3	0.76	0.38	0.35	0.21	0.38	0.01	0.31	0.2	0.2	0.38	0.2	0.05
20	0.7	0.24	0.3	0.76	0.38	0.35	0.21	0.05	0.7	0.5	0.35	0.2	0.9	0.08	0.05
21	0.455	0.24	0.7	0.76	0.38	0.35	0.76	0.38	0.7	0.5	0.35	0.62	0.9	0.2	0.5
22	0.21	0.24	0.3	0.76	0.08	0.01	0.21	0.38	0.7	0.31	0.05	0.2	0.9	0.08	0.5
23	0.7	0.05	0.7	0.43	0.08	0.18	0.21	0.05	0.7	0.31	0.35	0.62	0.9	0.08	0.05
24	0.7	0.24	0.3	0.76	0.08	0.01	0.485	0.05	0.01	0.5	0.05	0.62	0.9	0.2	0.05
25	0.7	0.05	0.3	0.595	0.08	0.01	0.76	0.05	0.7	0.5	0.35	0.2	0.38	0.2	0.5
26	0.455	0.145	0.5	0.595	0.23	0.18	0.485	0.215	0.355	0.405	0.2	0.41	0.64	0.14	0.275
27	0.7	0.24	0.7	0.43	0.38	0.01	0.21	0.215	0.01	0.31	0.35	0.2	0.9	0.2	0.5
28	0.7	0.05	0.7	0.76	0.38	0.01	0.21	0.38	0.7	0.5	0.05	0.62	0.38	0.08	0.275
29	0.7	0.24	0.7	0.76	0.08	0.01	0.76	0.38	0.7	0.31	0.35	0.2	0.38	0.14	0.05
30	0.455	0.05	0.3	0.43	0.08	0.01	0.21	0.05	0.01	0.31	0.05	0.2	0.38	0.08	0.05
31	0.7	0.24	0.7	0.43	0.08	0.35	0.76	0.38	0.01	0.5	0.05	0.2	0.64	0.08	0.05
32	0.21	0.05	0.3	0.76	0.08	0.35	0.76	0.215	0.7	0.5	0.05	0.62	0.38	0.08	0.05
33	0.7	0.05	0.7	0.43	0.38	0.35	0.76	0.05	0.01	0.5	0.35	0.62	0.38	0.2	0.05
34	0.21	0.24	0.3	0.43	0.08	0.35	0.76	0.05	0.01	0.31	0.35	0.2	0.9	0.2	0.275
35	0.21	0.05	0.7	0.43	0.08	0.01	0.76	0.38	0.01	0.31	0.05	0.62	0.38	0.2	0.5
36	0.21	0.24	0.7	0.595	0.38	0.35	0.21	0.38	0.01	0.31	0.05	0.62	0.9	0.08	0.05
37	0.21	0.05	0.3	0.76	0.38	0.01	0.21	0.05	0.7	0.31	0.35	0.62	0.64	0.2	0.5

C Supplementary information for Chapter 4

Table C.1 Kernel functions of GPR and the relevant equations.

Kernel name	**Kernel function** $(k(x,x'))$
Exponential	$\sigma_f^2 \exp\left(-\frac{r}{\sigma_l}\right)$
Squared exponential	$\sigma_f^2 \exp\left(-\frac{r^2}{2\sigma_l^2}\right)$
Rational quadratic	$\sigma_f^2 \left(1+\frac{r^2}{2\alpha\sigma_l^2}\right)^{-\alpha}$
Matern 5/2	$\sigma_f^2 \left(1+\frac{\sqrt{5}r}{\sigma_l}+\frac{5r^2}{3\sigma_l^2}\right) \exp\left(-\frac{\sqrt{5}r}{\sigma_l}\right)$

$r = \sqrt{(x-x')^{\mathrm{T}}(x-x')}$ is the Euclidean distance between x and x'.
σ_f^2 is the signal variance of the function f.
σ_l is the characteristic length scale.
α is a positive-valued scale-mixture parameter.

Table C.2 Performance comparison of regression models excluding the initial configurations (ICs) as inputs.

Model	**Adjustments**	**RMSE**	R^2	**MAE**	**Training time (sec)**	**Prediction speed (≈observation/sec)**
Linear Regression	-	0.1765	-0.14	0.1486	11.08	1900
	Interactions	0.2044	-0.53	0.1710	7.55	920
	Robust	0.1771	-0.15	0.1487	10.12	1400
	Stepwise	0.1713	-0.07	0.1420	68.30	3000
Regression Tree	Fine	0.2023	-0.50	0.1698	3.83	4900
	Medium	0.1925	-0.36	0.1600	2.96	5800
	Coarse	0.1671	-0.02	0.1397	2.64	6400
	Optimisable (BO)	0.1641	0.01	0.1366	25.23	7400
SVM	Kernel: linear	0.1780	-0.16	0.1443	7.27	3400
	Kernel: quadratic	0.1868	-0.28	0.1553	6.72	5100
	Kernel: cubic	0.1925	-0.36	0.1630	6.24	4900
	Kernel: Fine Gaussian	0.1934	-0.37	0.1638	5.58	6300
	Kernel: Medium Gaussian	0.1916	-0.34	0.1621	4.93	6100
	Kernel: Coarse Gaussian	0.1752	-0.12	0.1419	4.22	6000
	Optimisable (BO)	0.1653	0.00	0.1380	48.24	8100
Ensemble of Trees	Boosted	0.2003	-0.47	0.1661	8.09	1600
	Bagged	0.1853	-0.26	0.1563	7.50	1100
	Optimisable (BO)	**0.1653**	**0.00**	**0.1380**	**247.23**	**1100**
GPR	Kernel = Exponential	0.1653	0.00	0.1380	8.06	2800
	Kernel = Squared Exponential	0.1653	0.00	0.1380	12.35	3900
	Kernel = Rational Quadratic	0.1653	0.00	0.1380	7.32	3800
	Kernel = Matern 5/2	0.1653	0.00	0.1380	8.39	4000
	Optimisable (BO)	**0.1653**	**0.00**	**0.1380**	**89.74**	**8400**
ANN	One layer with [10] neurons	0.2079	-0.58	0.1738	5.92	3500
	One layer with [25] neurons	0.2079	-0.58	0.1738	4.52	3000
	One layer with [100] neurons	0.2079	-0.58	0.1738	8.52	1000
	Two layers with [10,10] neurons	0.2074	-0.57	0.1731	8.05	5400
	Three layers with [10,10,10] neurons	0.2072	-0.57	0.1733	7.50	5200
	Optimisable (BO)	0.1653	0.00	0.1380	152.03	6800

Table C.3 Hyperparameters of Ensemble learning and their search spaces for optimisation by BO given an exploration ratio of 0.5.

Hyperparameter	Search space	Transform function
Ensemble method	{Bagging, LSBoost}	–
Number of learners	[10, 500]	log
Learning rate	[0.001, 1]	log
Minimum leaf size	[1, 74]	log
Maximum number of decision splits	[1, 147]	log
Number of predictors to sample	[1, 18]	–

Table C.4 Hyperparameters of GPR and their search spaces for optimisation by BO given an exploration ratio of 0.5.

Hyperparameter	Search space	Transform function
Sigma	[1.0e-04, 1.6541]	log
Basis function	{Constant, Zero, Linear, Quadratic}	–
Kernel function	{ARD exponential, ARD matern 3/2, ARD matern 5/2, ARD rational quadratic, ARD squared exponential, Exponential, Matern 3/2, Matern 5/2, Rational quadratic, Squared exponential}	–
Kernel scale	[0.002, 2]	log
Standardise data	{True, False}	–

D Supplementary information for Chapter 5

Table D.1 Definitive screening design matrix.

Run	$\mu_{s,pp}$	$\mu_{r,pp}$	$C_{r,pp}$	$\mu_{s,ss}$	$\mu_{r,ss}$	$C_{r,ss}$	$\mu_{s,pg}$	$\mu_{r,pg}$	$C_{r,pg}$	$\mu_{s,sg}$	$\mu_{r,sg}$	$C_{r,sg}$
1	0.613	0.06	0.525	0.525	0.1	0.263	0.285	0.045	0.875	0.475	0.1	0.3
2	0.4905	0.045	0.525	0.525	0.06	0.263	0.285	0.045	0.525	0.285	0.06	0.3
3	0.4905	0.075	0.875	0.875	0.1	0.438	0.475	0.075	0.875	0.475	0.1	0.5
4	0.368	0.045	0.875	0.875	0.08	0.438	0.285	0.045	0.525	0.475	0.1	0.3
5	0.368	0.075	0.875	0.525	0.1	0.263	0.475	0.045	0.525	0.285	0.1	0.3
6	0.613	0.075	0.525	0.875	0.1	0.438	0.475	0.075	0.525	0.475	0.06	0.3
7	0.368	0.045	0.875	0.875	0.06	0.263	0.475	0.075	0.7	0.475	0.1	0.3
8	0.613	0.045	0.875	0.525	0.06	0.3505	0.285	0.075	0.875	0.475	0.06	0.3
9	0.613	0.045	0.7	0.525	0.06	0.438	0.475	0.045	0.525	0.475	0.1	0.5
10	0.368	0.045	0.525	0.875	0.1	0.263	0.285	0.075	0.875	0.38	0.1	0.5
11	0.613	0.075	0.525	0.525	0.08	0.263	0.475	0.075	0.875	0.285	0.06	0.5
12	0.613	0.045	0.525	0.875	0.1	0.438	0.285	0.06	0.525	0.285	0.1	0.3
13	0.613	0.075	0.525	0.875	0.06	0.263	0.475	0.045	0.875	0.475	0.1	0.3
14	0.368	0.075	0.875	0.7	0.1	0.438	0.285	0.045	0.875	0.475	0.06	0.3
15	0.368	0.075	0.525	0.525	0.06	0.438	0.38	0.075	0.875	0.285	0.1	0.3
16	0.613	0.045	0.875	0.525	0.1	0.438	0.475	0.075	0.875	0.285	0.1	0.3
17	0.613	0.045	0.525	0.7	0.06	0.263	0.475	0.075	0.525	0.285	0.1	0.5
18	0.613	0.045	0.525	0.875	0.06	0.438	0.285	0.075	0.875	0.475	0.06	0.5
19	0.368	0.045	0.525	0.525	0.1	0.438	0.475	0.045	0.875	0.475	0.08	0.5
20	0.368	0.045	0.525	0.875	0.06	0.438	0.475	0.045	0.875	0.285	0.06	0.3
21	0.613	0.075	0.875	0.875	0.06	0.438	0.285	0.045	0.875	0.285	0.1	0.5
22	0.368	0.075	0.525	0.525	0.06	0.438	0.285	0.075	0.525	0.475	0.1	0.4
23	0.368	0.045	0.875	0.525	0.06	0.263	0.285	0.045	0.875	0.285	0.1	0.5
24	0.368	0.075	0.7	0.875	0.1	0.263	0.285	0.075	0.875	0.285	0.06	0.3
25	0.613	0.075	0.875	0.525	0.1	0.263	0.285	0.075	0.525	0.475	0.1	0.5
26	0.368	0.045	0.875	0.525	0.1	0.438	0.285	0.075	0.525	0.285	0.06	0.5
27	0.613	0.045	0.875	0.875	0.1	0.263	0.475	0.045	0.875	0.285	0.06	0.4
28	0.613	0.075	0.525	0.525	0.1	0.438	0.285	0.045	0.7	0.285	0.06	0.5
29	0.368	0.075	0.875	0.525	0.06	0.263	0.475	0.06	0.875	0.475	0.06	0.5

Table D.2 Parameters used for Genetic Algorithm.

Parameter	**Value**	**Description**
Population size	1000	Number of individuals in each generation.
Max. number of generations	2000	Maximum number of generations for algorithm to solve.
Crossover probability	0.6	The proportion of the population selected for crossover in each generation.
Mutation probability	0.05	Mutation fraction used to introduce diversity into the population.
Function Tolerance	1e-6	Stopping criterion based on the *minimal* improvement in *fitness function*.

Table D.3 DEM calibration results for 50–50 pellet–sinter mass ratio, presenting the comparison between DEM results and experimental measurements, along with the relative errors for each KPI.

	Angle of repose (°)	**Shear angle** (°)	**Mass flow rate (kg/s)**	**Mass in the lower box (kg)**
Experiments	29.5 ± 0.5	42.5 ± 1.6	10.29 ± 0.35	32.32 ± 0.55
DEM	29.4 ± 0.5	41.9 ± 0.9	10.46 ± 0.11	32.43 ± 0.19
Relative error (%)	-0.38	-1.48	1.67	0.33

Table D.4 DEM calibration results for 50–50 pellet–sinter mass ratio with calibrated particle density, presenting the comparison between DEM results and experimental measurements, along with the relative errors for each KPI.

	Angle of repose (°)	**Shear angle** (°)	**Mass flow rate (kg/s)**	**Mass in the lower box (kg)**
Experiments	29.5 ± 0.5	42.5 ± 1.6	10.29 ± 0.35	32.32 ± 0.55
DEM	29.9 ± 0.6	42.0 ± 1.1	9.68 ± 0.08	32.47 ± 0.06
Relative error (%)	1.56	-1.12	-5.91	0.46

Table D.5 Validation result of the calibrated DEM parameters for 75–25 and 25–75 pellet–sinter mass ratios as well as the reverse layering order, presenting the comparison between DEM results and experimental measurements, along with the relative errors for each KPI.

Case		**Angle of repose** (°)	**Shear angle** (°)	**Mass flow rate** (kg/s)	**Mass in the lower box** (kg)
75–25	Experiments	28.6 ± 0.7	39.0 ± 1.5	10.29 ± 0.10	33.09 ± 0.12
	DEM	28.1 ± 0.5	39.8 ± 1.7	9.55 ± 0.12	33.22 ± 0.16
	Relative error (%)	-1.60	1.99	-7.23	0.39
25–75	Experiments	29.6 ± 0.8	44.8 ± 1.2	10.24 ± 0.45	32.00 ± 0.48
	DEM	31.0 ± 0.3	44.2 ± 0.6	9.84 ± 0.12	32.45 ± 0.08
	Relative error (%)	4.76	-1.23	-3.87	1.39
Reverse	Experiments	29.7 ± 0.5	40.9 ± 1.6	10.39 ± 0.18	32.97 ± 0.20
	DEM	29.0 ± 0.3	41.6 ± 0.7	10.37 ± 0.18	33.42 ± 0.12
	Relative error (%)	-2.52	1.54	-0.17	1.37

E Supplementary information for Chapter 6

Table E.1 Particle-size distributions (PSD, mass %) of all materials.

Pellets		**Sinter**		**Lump ore (A,B)**		**Lump ore (C)**		**Nut coke**	
Size (mm)	%	Size (mm)	%	Size (mm)	%	Size (mm)	%	Size (mm)	%
6.35–9.5	10	5–10	30	5–8	4.56	5–8	3.71	10–16	5
9.5–11.2	40	10–20	40	8–10	4.88	8–10	3.67	16–30	45
11.2–12.5	40	20–40	20	10–16	16.46	10–16	23.88	30–45	45
12.5–15	10	40–50	10	16–20	11.58	16–20	16.85	45–50	5
–	–	–	–	20–25	16.14	20–25	20.56	–	–
–	–	–	–	25–31.5	21.32	25–31.5	21.71	–	–
–	–	–	–	31.5–40	19.09	31.5–40	8.88	–	–
–	–	–	–	40–50	5.97	40–50	0.74	–	–

Table E.2 DEM parameters used in the simulations.

Parameter		**Pellets**	**Sinter**	**Lump ore**	**Nut coke**	**Geometry**
Solid density (kg/m^3)		3350	3208	4231	1118	7800
Youngs modulus (Pa)		1.0×10^8	1.0×10^8	1.0×10^8	1.0×10^8	1.0×10^{11}
Poissons ratio		0.25	0.25	0.21	0.22	0.30
Static friction coefficient [μ_s]						
	Pellets	0.73	0.815	0.665	0.80	0.90
	Sinter		0.90	0.75	0.885	0.83
	Lump ore			0.60	0.735	0.69
	Nut coke				0.87	0.41
Rolling friction coefficient [μ_r]						
	Pellets	0.12	0.16	0.095	0.135	0.16
	Sinter		0.20	0.135	0.175	0.20
	Lump ore			0.07	0.11	0.09
	Nut coke				0.15	0.09
Restitution coefficient [C_r]						
	Pellets	0.76	0.555	0.585	0.555	0.70
	Sinter		0.35	0.38	0.35	0.40
	Lump ore			0.41	0.38	0.43
	Nut coke				0.35	0.20
Time step (s)		2.909×10^{-5} (30% of Rayleigh time step)				

Table E.3 Different PSDs of sinter used in Cases 1A, 5A, and 6A.

Size (mm)	Sinter (updated)	Sinter (fine)	Sinter (coarse)
5–10	38.9	54.1	27.4
10–20	40.7	33.0	35.2
20–40	17.1	11.3	26.0
40–50	3.3	1.6	11.4

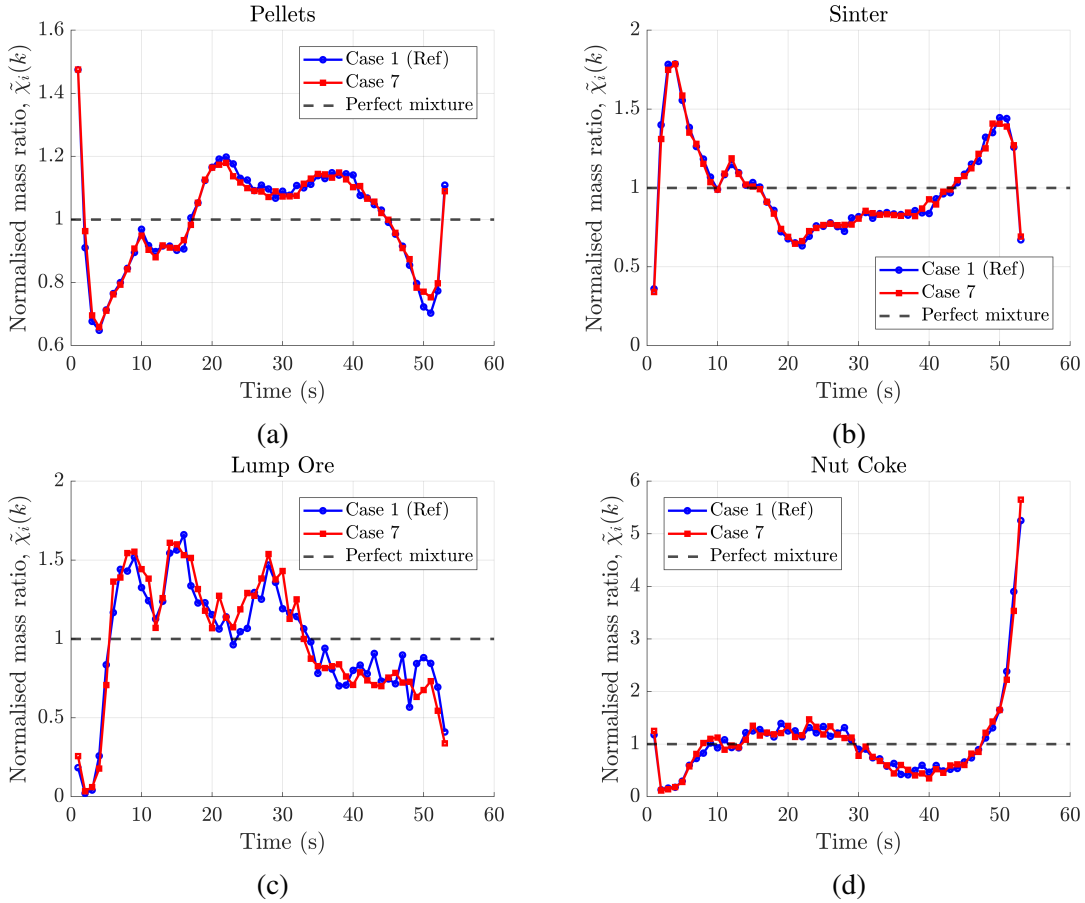

Figure E.1 Comparison of segregation after hopper discharge between Case 7 and the reference case (Case 1) for: (a) pellets, (b) sinter, (c) lump ore, and (d) nut coke.

Bibliography

[1] Patrick Richard, Mario Nicodemi, Renaud Delannay, Philippe Ribière, and Daniel Bideau. Slow relaxation and compaction of granular systems. Nature Materials, 4:121–128, 2005.

[2] Martin Rhodes. Introduction to Particle Technology, SECOND EDITION. John Wiley & Sons, 2008.

[3] P Tang and V M Puri. Methods for minimizing segregation: a review. Particulate Science and Technology, 22:321–337, 2004.

[4] J. M. Ottino and D. V. Khakhar. Mixing and segregation of granular materials. Annual Review of Fluid Mechanics, 32:55–91, 2000.

[5] JC Williams and MJ Rhodes. Mixing and segregation in powders. Principles of powder technology, pages 71–90, 1990.

[6] Rénard Chaigneau, Oscar Lingiardi, Ron Molenaar, Rob van Opbergen, Yongzhi Sha, and Jim Warren. Modern blast furnace ironmaking: an introduction (2020). SAGE Publications Limited, 2020.

[7] Ian Cameron, Mitren Sukhram, Kyle Lefebvre, and William Davenport. Blast furnace ironmaking: Analysis, control, and optimization. Elsevier, 2019.

[8] Krzysztof M Graczyk and Maciej Matyka. Predicting porosity, permeability, and tortuosity of porous media from images by deep learning. Scientific reports, 10(1):21488, 2020.

[9] Yaowei Yu and Henrik Saxén. Experimental and DEM study of segregation of ternary size particles in a blast furnace top bunker model. Chemical Engineering Science, 65:5237–5250, 9 2010.

[10] Tathagata Bhattacharya and J. J. McCarthy. Chute flow as a means of segregation characterization. Powder Technology, 256:126–139, 4 2014.

[11] R. N. Roeplal. Mixtures in Motion: High-Velocity DEM Modeling of Blast Furnace Charging. PhD dissertation, Delft University of Technology, 2025.

[12] Raïsa Roeplal, Yusong Pang, Allert Adema, Jan van der Stel, and Dingena Schott. Modelling of phenomena affecting blast furnace burden permeability using the discrete element method (DEM)–A review. Powder Technology, 415:118161, 2023.

[13] Ken Kamrin, Kimberly M Hill, Daniel I Goldman, and Jose E Andrade. Advances in modeling dense granular media. Annual Review of Fluid Mechanics, 56(1):215–240, 2024.

[14] Peter A Cundall and Otto D L Strack. A discrete numerical model for granular assemblies. geotechnique, 29:47–65, 1979.

[15] Yaowei Yu and Henrik Saxén. Segregation behavior of particles in a top hopper of a blast furnace. Powder Technology, 262:233–241, 2014.

[16] Hiroshi Mio, Yoichi Narita, Kaoru Nakano, and Seiji Nomura. Validation of the burden distribution of the 1/3-scale of a blast furnace simulated by the discrete element method. Processes, 8:6, 2020.

[17] Wenxuan Xu, Shusen Cheng, Qun Niu, Wei Hu, and Jiawen Bang. The DEM study of segregation phenomena of burden distribution during the charging process of blast furnace with two parallel hoppers. Ironmaking & Steelmaking, 47:337–343, 2020.

[18] C. X. Li, K. J. Dong, S. D. Liu, G. R. Chandratilleke, Z. Y. Zhou, and Y. S. Shen. DEM study of particle segregation in the throat region of a blast furnace. Powder Technology, 407:117660, 2022.

[19] Reza Alizadeh, Janet K Allen, and Farrokh Mistree. Managing computational complexity using surrogate models: a critical review. Research in Engineering Design, 31(3):275–298, 2020.

[20] Jiayuan Zhang, Ziguo Hu, Wei Ge, Yongjie Zhang, Tinghua Li, and Jinghai Li. Application of the discrete approach to the simulation of size segregation in granular chute flow. Industrial and Engineering Chemistry Research, 43:5521–5528, 2004.

[21] Sunil R de Silva, Are Dyrøy, and Gisle G Enstad. Segregation mechanisms and their quantification using segregation testers. In IUTAM Symposium on Segregation in Granular Flows: Proceedings of the IUTAM Symposium held in Cape May, NJ, USA June 5–10, 1999, pages 11–29. Springer, 2000.

[22] John Mark Nicholas Timm Gray. Particle segregation in dense granular flows. https://doi.org/10.1146/annurev-fluid-122316-045201, 50:407–433, 1 2018.

[23] Shawn P. Duffy and Virendra M. Puri. Primary segregation shear cell for size-segregation analysis of binary mixtures. KONA Powder and Particle Journal, 20:196–207, 2002.

[24] Kunio Shinohara and Shinichi Miyata. Mechanism of density segregation of particles in filling vessels. Industrial & Engineering Chemistry Process Design and Development, 23(3):423–428, 1984.

[25] Nitin Jain, Julio M. Ottino, and Richard M. Lueptow. Regimes of segregation and mixing in combined size and density granular systems: An experimental study. Granular Matter, 7:69–81, 2005.

[26] Maryam Asachi, Ehsan Nourafkan, and Ali Hassanpour. A review of current techniques for the evaluation of powder mixing. Advanced Powder Technology, 29:1525–1549, 2018.

[27] Alexander Lewis Bowler, Serafim Bakalis, and Nicholas James Watson. A review of in-line and on-line measurement techniques to monitor industrial mixing processes. Chemical Engineering Research and Design, 153:463–495, 2020.

[28] Stefan Luding. Introduction to discrete element methods: Basic of contact force models and how to perform the micro-macro transition to continuum theory. European Journal of Environmental and Civil Engineering, 12:785–826, 2008.

[29] H. P. Zhu, Z. Y. Zhou, R. Y. Yang, and A. B. Yu. Discrete particle simulation of particulate systems: Theoretical developments. Chemical Engineering Science, 62:3378–3396, 2007.

[30] Michele Marigo and Edmund Hugh Stitt. Discrete element method (DEM) for industrial applications: Comments on calibration and validation for the modelling of cylindrical pellets. KONA Powder and Particle Journal, pages 236–252, 2015.

[31] Thomas Roessler and André Katterfeld. Scaling of the angle of repose test and its influence on the calibration of DEM parameters using upscaled particles. Powder Technology, 330:58–66, 2018.

[32] Mikio Sakai. How should the discrete element method be applied in industrial systems?: A review. KONA Powder and Particle Journal, 2016:169–178, 2016.

[33] Behzad Soltanbeigi, Alexander Podlozhnyuk, Stefanos-Aldo Papanicolopulos, Christoph Kloss, Stefan Pirker, and Jin Y Ooi. DEM study of mechanical characteristics of multi-spherical and superquadric particles at micro and macro scales. Powder Technology, 329:288–303, 2018.

[34] Wenjing Yang, Zongyan Zhou, David Pinson, and Aibing Yu. Periodic boundary conditions for discrete element method simulation of particle flow in cylindrical vessels. Industrial and Engineering Chemistry Research, 53:8245–8256, 2014.

[35] W J Yang, Z Y Zhou, and A B Yu. Discrete particle simulation of solid flow in a three-dimensional blast furnace sector model. Chemical Engineering Journal, 278:339–352, 2015.

[36] C. J. Coetzee. Particle upscaling: Calibration and validation of the discrete element method. Powder Technology, 344:487–503, 2019.

[37] Stef Lommen, Mohammadjavad Mohajeri, Gabriel Lodewijks, and Dingena Schott. DEM particle upscaling for large-scale bulk handling equipment and material interaction. Powder Technology, 352:273–282, 2019.

[38] Paul W. Cleary and Mark L. Sawley. DEM modelling of industrial granular flows: 3d case studies and the effect of particle shape on hopper discharge. Applied Mathematical Modelling, 26:89–111, 2002.

[39] Stef Lommen, Dingena Schott, and Gabriel Lodewijks. DEM speedup: Stiffness effects on behavior of bulk material. Particuology, 12:107–112, 2014.

[40] Anurag Tripathi and D V Khakhar. Density difference-driven segregation in a dense granular flow. Journal of Fluid Mechanics, 717:643–669, 2013.

[41] Anurag Tripathi and D V Khakhar. Rheology of binary granular mixtures in the dense flow regime. Physics of Fluids, 23:113302, 2011.

[42] William R Ketterhagen, Jennifer S Curtis, Carl R Wassgren, and Bruno C Hancock. Modeling granular segregation in flow from quasi-three-dimensional, wedge-shaped hoppers. Powder Technology, 179:126–143, 2008.

[43] G. G. Pereira and P. W. Cleary. De-mixing of binary particle mixtures during unloading of a v-blender. Chemical Engineering Science, 94:93–107, 2013.

[44] Saleema Panda and Danielle S Tan. Effect of external factors on segregation of different granular mixtures. Advanced Powder Technology, 31(2):571–594, 2020.

[45] Xingjian Huang, Qijun Zheng, Dedao Liu, Aibing Yu, and Wenyi Yan. A design method of hopper shape optimization with improved mass flow pattern and reduced particle segregation. Chemical Engineering Science, 253:117579, 2022.

[46] Wenxuan Xu, Shusen Cheng, Qun Niu, Wei Hu, and Jiawen Bang. Investigation on the uneven distribution of different types of ores in the hopper and stock surface during the charging process of blast furnace based on discrete element method. Metallurgical Research & Technology, 116(3):314, 2019.

[47] Tristan Vuilloz, David Cantor, and Carlos Ovalle. DEM modeling of segregation and stratification in pouring heaps of bidispersed mixtures of rounded particles. EPJ Web of Conferences, 249:03049, 2021.

[48] Y. Zhao, Y. Luo, W. Wang, S. Liu, and Z. Zhan. Effect of base roughness on flow behaviour and size segregation in dry granular flows. Geotechnique Letters, 12:1–7, 2022.

[49] He Tao, Wenqi Zhong, Baosheng Jin, and Bing Ren. DEM simulation of non-spherical granular segregation in hopper. In AIP Conference Proceedings, volume 1547, pages 720–726. American Institute of Physics, 2013.

[50] Sushil S Shirsath, Johan T Padding, J. A.M. Kuipers, and Herman J.H. Clercx. Simulation study of the effect of wall roughness on the dynamics of granular flows in rotating semicylindrical chutes. AIChE Journal, 61:2117–2135, 2015.

[51] Jian Xu, Zhaowen Hu, Yang Xu, Dongdong Wang, Liangying Wen, and Chenguang Bai. Transient local segregation grids of binary size particles discharged from a wedge-shaped hopper. Powder Technology, 308:273–289, 2017.

[52] T F Zhang, J Q Gan, D Pinson, and Z Y Zhou. Size-induced segregation of granular materials during filling a conical hopper. Powder Technology, 340:331–343, 2018.

[53] Bhargav Mantravadi and Danielle S Tan. Effect of bend angle on granular size segregation in the chute flow under periodic flow inversion. Powder Technology, 360:177–192, 2020.

[54] Jianliang Zhang, Jiayong Qiu, Hongwei Guo, Shan Ren, Hui Sun, Guangwei Wang, and Zhengkai Gao. Simulation of particle flow in a bell-less type charging system of a blast furnace using the discrete element method. Particuology, 16:167–177, 10 2014.

[55] Ya Zhao, Shiliang Yang, Liangqi Zhang, and Jia Wei Chew. DEM study on the discharge characteristics of lognormal particle size distributions from a conical hopper. AIChE Journal, 64:1174–1190, 4 2018.

[56] Ya Zhao and Jia Wei Chew. Effect of lognormal particle size distributions of non-spherical particles on hopper discharge characteristics. Chemical Engineering Research and Design, 163:230–240, 2020.

[57] Raj Kumar, Srikanth R Gopireddy, Arun K Jana, and Chetan M Patel. Study of the discharge behavior of rosin-rammler particle-size distributions from hopper by discrete element method: A systematic analysis of mass flow rate, segregation and velocity profiles. Powder Technology, 360:818–834, 2020.

[58] William R Ketterhagen, Jennifer S Curtis, Carl R Wassgren, and Bruno C Hancock. Predicting the flow mode from hoppers using the discrete element method. Powder Technology, 195:1–10, 2009.

[59] William R. Ketterhagen and Bruno C. Hancock. Optimizing the design of eccentric feed hoppers for tablet presses using DEM. Computers and Chemical Engineering, 34:1072–1081, 2010.

[60] Mingyin Kou, Jian Xu, Heng Zhou, Bingjie Wen, Kai Gu, Shun Yao, and Shengli Wu. Effects of bottom base shapes on burden profiles and burden size distributions in the upper part of a corex shaft furnace based on DEM. Advanced Powder Technology, 29:1014–1024, 2018.

[61] Mingyin Kou, Shengli Wu, Geoff Wang, Baojun Zhao, and Qingwu Cai. Numerical simulation of burden and gas distributions inside corex shaft furnace. Steel Research International, 86:686–694, 2015.

[62] A. Cliff, L. A. Fullard, E. C.P. Breard, J. Dufek, and C. E. Davies. Granular size segregation in silos with and without inserts. Proceedings of the Royal Society A: Mathematical, Physical and Engineering Sciences, 477, 2021.

[63] Yaowei Yu and Henrik Saxén. Particle flow and behavior at bell-less charging of the blast furnace. Steel Research International, 84:1018–1033, 10 2013.

[64] Haotian Liao, Yanbing Zong, Kejiang Li, Yushan Bu, Zhisheng Bi, Chunhe Jiang, Zhengjian Liu, and Jianliang Zhang. Influence of lump ore ratio and shapes on the particle flow behavior inside the direct reduction shaft furnace by discrete element modeling model. steel research international, 94(1):2200531, 2023.

[65] Maryam Asachi, Mohammadreza Alizadeh Behjani, Ehsan Nourafkan, and Ali Hassanpour. Tailoring particle shape for enhancing the homogeneity of powder mixtures: Experimental study and DEM modelling. Particuology, 54:58–68, 2021.

[66] Xu Tian, Heng Zhou, Jian Huang, Shengli Wu, Guangwei Wang, and Mingyin Kou. DEM study on discharge behavior of ternary cylindrical activated coke particles. Powder Technology, 409:117785, 2022.

[67] Y Yu, J Zhang, J Zhang, and H Saxén. DEM and experimental studies on pellet segregation in stockpile build-up. Ironmaking and Steelmaking, 45:264–271, 2018.

[68] Yang Xu, Jian Xu, Chengfeng Sun, Kaihui Ma, Cheng Shan, Liangying Wen, Shengfu Zhang, and Chenguang Bai. Quantitative comparison of binary particle mass and size segregation between serial and parallel type hoppers of blast furnace bell-less top charging system. Powder technology, 328:245–255, 2018.

[69] Sandip Mandal and D. V. Khakhar. Dense granular flow of mixtures of spheres and dumbbells down a rough inclined plane: Segregation and rheology. Physics of Fluids, 31:23304, 2019.

[70] Ya Zhao and Jia Wei Chew. Discrete element method study on hopper discharge behaviors of binary mixtures of nonspherical particles. AIChE Journal, 66(8):e16254, 2020.

[71] T F Zhang, J Q Gan, A B Yu, D Pinson, and Z Y Zhou. Size segregation of granular materials during paul-wurth hopper charging and discharging process. Powder Technology, 378:497–509, 2021.

[72] Yaowei Yu and Henrik Saxén. Flow of pellet and coke particles in and from a fixed chute. Industrial and Engineering Chemistry Research, 51:7383–7397, 5 2012.

[73] Mingyin Kou, Shengli Wu, Kaiping Du, Wei Shen, Jing Sun, and Zhekai Zhang. DEM simulation of burden distribution in the upper part of corex shaft furnace. ISIJ International, 53:1002–1009, 2013.

[74] Shengli Wu, Mingyin Kou, Jian Xu, Xinying Guo, Kaiping Du, Wei Shen, and Jing Sun. DEM simulation of particle size segregation behavior during charging into and discharging from a paul-wurth type hopper. Chemical Engineering Science, 99:314–323, 8 2013.

[75] Yang You, Qin Fu Hou, Zhi Guo Luo, Hai Feng Li, Heng Zhou, Ren Chen, and Zong Shu Zou. Three-dimensional DEM study of coal distribution in the melter gasifier of corex. Steel Research International, 87:1543–1551, 2016.

[76] Wenxuan Xu, Shusen Cheng, and Changrong Li. Experimental study of the segregation of burden distribution during the charging process of bell-less top blast furnace with two parallel hoppers. In Journal of Physics: Conference Series, volume 2044, page 012129. IOP Publishing, 2021.

[77] Mingyin Kou, Jian Xu, Shengli Wu, Heng Zhou, Kai Gu, Shun Yao, and Bingjie Wen. Effect of cross-section shape of rotating chute on particle movement and distribution at the throat of a bell-less top blast furnace. Particuology, 44:194–206, 2019.

[78] Deside Kudzai Chibwe, Geoffrey Michael Evans, Elham Doroodchi, Brian Joseph Monaghan, David John Pinson, and Sheng Jason Chew. Charge material distribution behaviour in blast furnace charging system. Powder Technology, 366:22–35, 2020.

[79] Zhibin Hong, Heng Zhou, Jianlong Wu, Longling Zhan, Yibo Fan, Zongwang Zhang, Shengli Wu, Haifa Xu, Li Pang Wang, and Mingyin Kou. Effects of operational parameters on particle movement and distribution at the top of a bell-less blast furnace based on discrete element method. Steel Research International, 92:2000262, 2021.

[80] Zhongliang Zhang, Yongqi Liu, Bin Zheng, Peng Sun, and Ruiyang Li. Local percolation of a binary particle mixture in a rectangular hopper with inclined bottom during discharging. ACS omega, 5(33):20773–20783, 2020.

[81] Edouard Izard, Maxime Moreau, and Pascal Ravier. Discrete element method simulation of segregation pattern in a sinter cooler charging chute system. Particuology, 59:34–42, 2021.

[82] Mohammadreza Alizadeh, Ali Hassanpour, Mehrdad Pasha, Mojtaba Ghadiri, and Andrew Bayly. The effect of particle shape on predicted segregation in binary powder mixtures. Powder Technology, 319:313–322, 2017.

[83] Kang Min Kim, Jong Ho Bae, Jong In Park, and Jeong Whan Han. Segregation charging behavior of ultra-fine iron ore briquette in sinter feed bed: DEM analysis. Metals and Materials International, 26:1218–1225, 2020.

[84] Peiyong Qiu and Thomas Pabst. Waste rock segregation during disposal: Calibration and upscaling of discrete element simulations. Powder Technology, 412:117981, 2022.

[85] Miao Wang, Lun xun Liang, Shao heng Guan, Gang Ma, Zhi qiang Lai, Xin qiang Niu, Si fan Zhang, Wen xiang Tian, and Wei Zhou. Experimental and numerical investigation of the collapse of binary mixture of particles with different densities. Powder Technology, 415:118167, 2023.

[86] Santosh K. Barik, V. N. Lad, I. Sreedhar, and Chetan M. Patel. Investigation of mass discharge rate, velocity, and segregation behaviour of microcrystalline cellulose powder from a copley flow tester. Powder Technology, 417:118234, 2023.

[87] Hiroshi Mio, Satoshi Komatsuki, Masatoshi Akashi, Atsuko Shimosaka, Yoshiyuki Shirakawa, Jusuke Hidaka, Masatomo Kadowaki, Shinroku Matsuzaki, and Kazuya Kunitomo. Validation of particle size segregation of sintered ore during flowing through laboratory-scale chute by discrete element method. ISIJ International, 48:1696–1703, 2008.

[88] Hiroshi Mio, Satoshi Komatsuki, Masatoshi Akashi, Atsuko Shimosaka, Yoshiyuki Shirakawa, Jusuke Hidaka, Masatomo Kadowaki, Shinroku Matsuzaki, and Kazuya Kunitomo. Effect of chute angle on charging behavior of sintered ore particles at bell-less type charging system of blast furnace by discrete element method. ISIJ International, 49:479–486, 4 2009.

[89] Hiroshi Mio, Satoshi Komatsuki, Masatoshi Akashi, Atsuko Shimosaka, Yoshiyuki Shirakawa, Jusuke Hidaka, Masatomo Kadowaki, Hirokazu Yokoyama, Shinroku Matsuzaki, and Kazuya Kunitomo. Analysis of traveling behavior of nut coke particles in bell-type charging process of blast furnace by using discrete element method. ISIJ International, 50:1000–1009, 7 2010.

[90] Hiroshi Mio, Masatomo Kadowaki, Shinroku Matsuzaki, and Kazuya Kunitomo. Development of particle flow simulator in charging process of blast furnace by discrete element method. In Minerals Engineering, volume 33, pages 27–33, 6 2012.

[91] Masanori Nakano, Tsukasa Abe, Junya Kano, and Kazuya Kunitomo. DEM analysis on size segregation in feed bed of sintering machine. ISIJ International, 52:1559–1564, 2012.

[92] Chengzhi Li, Tom Honeyands, Damien O'Dea, and Roberto Moreno-Atanasio. The angle of repose and size segregation of iron ore granules: DEM analysis and experimental investigation. Powder Technology, 320:257–272, 2017.

[93] Chengzhi Li, Tom Honeyands, Damien O'Dea, and Roberto Moreno-Atanasio. DEM study on size segregation and voidage distribution in green bed formed on iron ore sinter strand. Powder Technology, 356:778–789, 2019.

[94] Atsuko Shimosaka, Yoshiyuki Shirakawa, and Jusuke Hidaka. Effects of particle shape and size distribution on size segregation of particles. Journal of Chemical Engineering of Japan, 46:187–195, 2013.

[95] M. Combarros, H. J. Feise, H. Zetzener, and A. Kwade. Segregation of particulate solids: Experiments and DEM simulations. Particuology, 12:25–32, 2014.

[96] M. Combarros Garcia, H. J. Feise, S. Strege, and A. Kwade. Segregation in heaps and silos: Comparison between experiment, simulation and continuum model. Powder Technology, 293:26–36, 2016.

[97] Koki Terui, Yusuke Kashihara, Toshiyuki Hirosawa, and Taihei Nouchi. Optimization of coke mixed charging based on discrete element method. ISIJ International, 57:1804–1810, 2017.

[98] Pooja Bhalode and Marianthi Ierapetritou. Discrete element modeling for continuous powder feeding operation: Calibration and system analysis. International Journal of Pharmaceutics, 585, 2020.

[99] Migyung Cho, Prashanta Dutta, and Jaesool Shim. A non-sampling mixing index for multicomponent mixtures. Powder Technology, 319:434–444, 2017.

[100] Xin Jin, Ganga Rohana Chandratilleke, Shuai Wang, and Yansong Shen. DEM investigation of mixing indices in a ribbon mixer. Particuology, 60:37–47, 2022.

[101] Anthony Rosato and Christopher Windows-Yule. Segregation in Vibrated Granular Systems. Academic Press, 2020.

[102] Thomas Roessler, Christian Richter, André Katterfeld, and Frank Will. Development of a standard calibration procedure for the DEM parameters of cohesionless bulk materials part i: Solving the problem of ambiguous parameter combinations. Powder Technology, 343:803–812, 2019.

[103] William R Ketterhagen, Jennifer S Curtis, Carl R Wassgren, Angela Kong, Padma J Narayan, and Bruno C Hancock. Granular segregation in discharging cylindrical hoppers: A discrete element and experimental study. Chemical Engineering Science, 62:6423–6439, 2007.

[104] C. J. Coetzee. Review: Calibration of the discrete element method. Powder Technology, 310:104–142, 2017.

[105] Xuewen Wang, Haozhou Ma, Bo Li, Tiejun Li, Rui Xia, and Qingbao Bao. Review on the research of contact parameters calibration of particle system. Journal of Mechanical Science and Technology, 36:1363–1378, 2022.

[106] C. M. Wensrich and A. Katterfeld. Rolling friction as a technique for modelling particle shape in DEM. Powder Technology, 217:409–417, 2012.

[107] C. J. Coetzee. Calibration of the discrete element method and the effect of particle shape. Powder Technology, 297:50–70, 2016.

[108] Huy Q. Do, Alejandro M. Aragón, and Dingena L. Schott. A calibration framework for discrete element model parameters using genetic algorithms. Advanced Powder Technology, 29:1393–1403, 2018.

[109] Bilal El Kassem, Nizar Salloum, Thomas Brinz, Yousef Heider, and Bernd Markert. A semi-automated DEM parameter calibration technique of powders based on different bulk responses extracted from auger dosing experiments. KONA Powder and Particle Journal, 38:235–250, 2021.

[110] M. Javad Mohajeri, Huy Q. Do, and Dingena L. Schott. DEM calibration of cohesive material in the ring shear test by applying a genetic algorithm framework. Advanced Powder Technology, 31:1838–1850, 2020.

[111] C. González-Montellano, J. M. Fuentes, E. Ayuga-Téllez, and F. Ayuga. Determination of the mechanical properties of maize grains and olives required for use in DEM simulations. Journal of Food Engineering, 111:553–562, 2012.

[112] Wenxuan Xu, Shusen Cheng, Qun Niu, Wei Hu, and Jiawen Bang. Investigation on the uneven distribution of different types of ores in the hopper and stock surface during the charging process of blast furnace based on discrete element method. Metallurgical Research and Technology, 116, 2019.

[113] Song Gao, Julio M. Ottino, Paul B. Umbanhowar, and Richard M. Lueptow. Modeling granular segregation for overlapping species distributions. Chemical Engineering Science, 231, 2021.

[114] N. Standish. Studies of size segregation in filling and emptying a hopper. Powder Technology, 45:43–56, 11 1985.

[115] G Lu, J R Third, and C R Müller. Discrete element models for non-spherical particle systems: From theoretical developments to applications. Chemical Engineering Science, 127:425–465, 2015.

[116] James C Williams. The segregation of particulate materials. a review. Powder Technology, 15:245–251, 1976.

[117] TF Zhang, JQ Gan, AB Yu, D Pinson, and ZY Zhou. Segregation of granular binary mixtures with large particle size ratios during hopper discharging process. Powder Technology, 361:435–445, 2020.

[118] Zhengkai Gao, Jian Liu, and Tai Gao. Advanced inside-furnace monitoring techniques implemented on the new large blast furnace of shagang. In AISTech - Iron and Steel Technology Conference Proceedings, pages 565–571, 2010.

[119] N Standish and A Kilic. Comparison of stop-start and continuous sampling methods of studying segregation of materials discharging from a hopper. Chemical Engineering Science, 40:2152–2153, 1985.

[120] Can Wang, An Deng, and Abbas Taheri. Digital image processing on segregation of rubber sand mixture. International Journal of Geomechanics, 18:04018138, 2018.

[121] Yoshimasa Kajiwara, Yoichi Aminaga, Takanobu Inada, Tsutomu Tanaka, and Ken ichi Sato. Size segregation of sinter in the top bunker of a bell-less type blast furnace. Tetsu-To-Hagane/Journal of the Iron and Steel Institute of Japan, 74:978–984, 1988.

[122] An Ni Huang and Hsiu Po Kuo. Developments in the tools for the investigation of mixing in particulate systems - a review. Advanced Powder Technology, 25:163–173, 2014.

[123] Fernando J. Muzzio, Priscilla Robinson, Carolyn Wightman, and Dean Brone. Sampling practices in powder blending. International Journal of Pharmaceutics, 155:153–178, 1997.

[124] Humair Nadeem and Theodore J. Heindel. Review of noninvasive methods to characterize granular mixing. Powder Technology, 332:331–350, 2018.

[125] Pooja Shenoy, Fredrik Innings, Kristel Tammel, John Fitzpatrick, and Lilia Ahrné. Evaluation of a digital colour imaging system for assessing the mixture quality of spice powder mixes by comparison with a salt conductivity method. Powder Technology, 286:48–54, 2015.

[126] Ralf Stannarius. Magnetic resonance imaging of granular materials. The Review of scientific instruments, 88:051806, 2017.

[127] Mohsen Asadi, Klaus Thoeni, and Ahmad Mahboubi. An experimental and numerical study on the compressive behavior of sand-rubber particle mixtures. Computers and Geotechnics, 104:185–195, 2018.

[128] J Bridgwater. Mixing and segregation mechanisms in particle flow. In Granular matter: An interdisciplinary approach, pages 161–193. Springer, 1994.

[129] P Artega and U Tüzün. Flow of binary mixtures of equal-density granules in hoppers-size segregation, flowing density and discharge rates. Chemical Engineering Science, 45:205–223, 1990.

[130] J. Bridgwater, M. H. Cooke, and A. M. Scott. Inter-particle percolation: Equipment development and mean percolation velocities. Trans Inst Chem Eng, 56:157–167, 1978.

[131] P. Tang and V. M. Puri. An innovative device for quantification of percolation and sieving segregation patterns - single component and multiple size fractions. Particulate Science and Technology, 23:335–350, 2005.

[132] James W Vallance and Stuart B Savage. Particle segregation in granular flows down chutes. In IUTAM Symposium on Segregation in Granular Flows: Proceedings of the IUTAM Symposium held in Cape May, NJ, USA June 5–10, 1999, pages 31–51. Springer, 2000.

[133] J. A. Drahun and J. Bridgwater. The mechanisms of free surface segregation. Powder Technology, 36:39–53, 1983.

[134] D. V. Khakhar, J. J. McCarthy, and J. M. Ottino. Mixing and segregation of granular materials in chute flows. Chaos, 9:594–610, 1999.

[135] Philippe Seil, Jaione Ortega Gómez, Stefan Pirker, and Christoph Kloss. Numerical and experimental studies on segregation patterns in granular flow from two hoppers. In ECCOMAS 2012 - European Congress on Computational Methods in Applied Sciences and Engineering, e-Book Full Papers, pages 5389–5402, 2012.

[136] Shishir Shekhar, G. G. Pereira, K. P. Hapgood, D. A.V. Morton, and P. W. Cleary. Simulation study on the influence of particle properties on radial and axial segregation in a freeman rheometer. Chemical Engineering Science, 265:118210, 2023.

[137] Fuhai Yu, Yun Zhang, Yang Zheng, Mengzhi Han, Guojie Chen, and Zhihao Yao. Comparison of different effective diameter calculating methods for sphero-cylinders by geometrically exact DEM simulations. Powder Technology, 360:1092–1101, 2020.

[138] A. W. Jenike. Quantitative design of mass-flow bins. Powder Technology, 1:237–244, 1967.

[139] Khashayar Saleh, Shahab Golshan, and Reza Zarghami. A review on gravity flow of free-flowing granular solids in silos basics and practical aspects. Chemical Engineering Science, 192:1011–1035, 2018.

[140] Dietmar Schulze. Powders and bulk solids. Springer, 2021.

[141] Deliang Shi, Adetola A Abatan, Watson L Vargas, and J J McCarthy. Eliminating segregation in free-surface flows of particles. Physical Review Letters, 99:148001, 2007.

[142] Wei Zhou, Zhiqiang Lai, Gang Ma, Lifu Yang, and Yuan Chen. Effect of base roughness on size segregation in dry granular flows. Granular Matter, 18:1–14, 2016.

[143] Lu Jing, Fiona C.Y. Kwok, and Andy Y.F. Leung. Discrete element modelling of grain size segregation in bi-disperse granular flows down chute. In Proceedings of the 4th International Conference on Particle-Based Methods - Fundamentals and Applications, PARTICLES 2015, pages 474–484. CIMNE, 2015.

[144] Dizhe Zhang, Zongyan Zhou, and David Pinson. DEM simulation of particle stratification and segregation in stockpile formation. In EPJ Web of Conferences, volume 140, page 15018. EDP Sciences, 2017.

[145] Jun Ai, Jian-Fei Chen, J Michael Rotter, and Jin Y Ooi. Assessment of rolling resistance models in discrete element simulations. Powder Technology, 206:269–282, 2011.

[146] Aman Tripathi, Vimod Kumar, Arpit Agarwal, Anurag Tripathi, Saprativ Basu, Arijit Chakrabarty, and Samik Nag. Quantitative DEM simulation of pellet and sinter particles using rolling friction estimated from image analysis. Powder Technology, 380:288–302, 2021.

[147] Arijit Chakrabarty, Rituparna Biswas, Saprativ Basu, and Samik Nag. Characterisation of binary mixtures of pellets and sinter for dem simulations. Advanced Powder Technology, 33(1):103358, 2022.

[148] Delft High Performance Computing Centre (DHPC). DelftBlue Supercomputer (Phase 2). https://www.tudelft.nl/dhpc/ark:/44463/DelftBluePhase2, 2024.

[149] Ahmed Hadi, Yusong Pang, and Dingena L Schott. Calibration of DEM parameters for multi-component segregation. In ICBMH2023: 14th International Conference on Bulk Materials Storage, Handling and Transportation: 14th International Conference on Bulk Materials Storage, Handling and Transportation, pages 221–233. The Institution of Engineers, Australia Wollongong, NSW, 2023.

[150] Han Wei, Hao Nie, Ying Li, Henrik Saxén, Zhijun He, and Yaowei Yu. Measurement and simulation validation of DEM parameters of pellet, sinter and coke particles. Powder Technology, 364:593–603, 2020.

[151] Claudia Hildebrandt, Srikanth R. Gopireddy, Regina ScherlieSS, and Nora A. Urbanetz. Assessment of material and process attributes' influence on tablet quality using a qbd and DEM combined approach. Powder Technology, 345:390–404, 2019.

[152] Siu Hua Chang, Tjoon Tow Teng, and Norli Ismail. Screening of factors influencing cu(ii) extraction by soybean oil-based organic solvents using fractional factorial design. Journal of Environmental Management, 92:2580–2585, 2011.

[153] Jeroen Emmerink, Ahmed Hadi, Jovana Jovanova, Chris Cleven, and Dingena L. Schott. Parametric analysis of a double shaft, batch-type paddle mixer using the discrete element method (DEM). Processes, 11, 2023.

[154] Rui Xia, Bo Li, Xuewen Wang, Tiejun Li, and Zhaojian Yang. Measurement and calibration of the discrete element parameters of wet bulk coal. Measurement: Journal of the International Measurement Confederation, 142:84–95, 2019.

[155] Rohit Dilip Nalawade, Krishna Pratap Singh, Ajay Kumar Roul, and Abhishek Patel. Parametric study and calibration of hysteretic spring and linear cohesion contact models for cohesive soils using definitive screening design. Computational Particle Mechanics, 10:707–728, 2023.

[156] Yunpeng Yan, Rudy Helmons, Craig Wheeler, and Dingena Schott. Optimization of a convex pattern surface for sliding wear reduction based on a definitive screening design and discrete element method. Powder Technology, 394:1094–1110, 2021.

[157] Bradley Jones and Christopher J. Nachtsheim. A class of three-level designs for definitive screening in the presence of second-order effects. Journal of Quality Technology, 43:1–15, 2011.

[158] Bradley Jones and Christopher J. Nachtsheim. Effective design-based model selection for definitive screening designs. Technometrics, 59:319–329, 2017.

[159] Tamoghna Mitra. Modeling of Burden Distribution in the Blast Furnace. PhD dissertation, Åbo Akademi University, 2016.

[160] Yuanxiang Lu, Zeyi Jiang, Xinru Zhang, Jingsong Wang, and Xinxin Zhang. Vertical section observation of the solid flow in a blast furnace with a cutting method. Metals, 9, 2019.

[161] Saprativ Basu, Arijit Chakrabarty, Samik Nag, Pradeep Chaudhary, Surajit Sinha, Thrilok Jain, Mohan S. Nainegali, Victor A. Rodriguez, and Luís Marcelo Tavares. Modeling and simulation of mechanical degradation of iron ore sinter in a complex transfer chute system using the discrete element model and a particle breakage model. Powder Technology, 417, 2023.

[162] Gabriel K.P. Barrios, Rodrigo M. de Carvalho, Arno Kwade, and Luís Marcelo Tavares. Contact parameter estimation for DEM simulation of iron ore pellet handling. Powder Technology, 248:84–93, 2013.

[163] Giovanni Di Leo and Francesco Sardanelli. Statistical significance: p value, 0.05 threshold, and applications to radiomicsreasons for a conservative approach. European Radiology Experimental, 4, 2020.

[164] Leslie M. Moore and David S. Moore. The basic practice of statistics. Technometrics, 38:404, 1996.

[165] GDR MiDi http://www. lmgc. univ-montp2. fr/MIDI/gdrmidi@ polytech. univ-mrs. fr. On dense granular flows. The European Physical Journal E, 14(4):341–365, 2004.

[166] Yoël Forterre and Olivier Pouliquen. Flows of dense granular media. Annu. Rev. Fluid Mech., 40(1):1–24, 2008.

[167] Jacob Cohen. Statistical power analysis for the behavioral sciences. Academic press, 2013.

[168] Shlomo S. Sawilowsky. New effect size rules of thumb. Journal of Modern Applied Statistical Methods, 8:597–599, 2009.

[169] Ahmed Hadi, Raïsa Roeplal, Yusong Pang, and Dingena L Schott. DEM modelling of segregation in granular materials: a review. KONA Powder and Particle Journal, 41:78–107, 2024.

[170] Seung Jae Lee, Youssef M.A. Hashash, and Erfan G. Nezami. Simulation of triaxial compression tests with polyhedral discrete elements. Computers and Geotechnics, 43:92–100, 2012.

[171] Hai Huang and Erol Tutumluer. Discrete element modeling for fouled railroad ballast. Construction and Building Materials, 25:3306–3312, 2011.

[172] Martin Obermayr, Klaus Dressler, Christos Vrettos, and Peter Eberhard. Prediction of draft forces in cohesionless soil with the discrete element method. In Journal of Terramechanics, volume 48, pages 347–358, 2011.

[173] Joaquín Irazábal, Fernando Salazar, and David J Vicente. A methodology for calibrating parameters in discrete element models based on machine learning surrogates. Computational Particle Mechanics, 10:1031–1047, 2023.

[174] Christian Richter, Thomas RöSSler, Günter Kunze, Andre Katterfeld, and Frank Will. Development of a standard calibration procedure for the DEM parameters of cohesionless bulk materials part ii: Efficient optimization-based calibration. Powder Technology, 360:967–976, 2020.

[175] Jeoungseok Yoon. Application of experimental design and optimization to pfc model calibration in uniaxial compression simulation. International Journal of Rock Mechanics and Mining Sciences, 44:871–889, 2007.

[176] Georg Hess, Christian Richter, André Katterfeld, et al. Simulation of the dynamic interaction between bulk material and heavy equipment: Calibration and validation. In ICBMH–12th International Conference on Bulk Materials Storage, Handling and Transportation, Proceedings, pages 427–436, 2016.

[177] Marc P. Fransen, Matthijs Langelaar, and Dingena L. Schott. Application of DEM-based metamodels in bulk handling equipment design: Methodology and DEM case study. Powder Technology, 393:205–218, 2021.

[178] Francisco Chinesta, Elias Cueto, and Benjamin Klusemann. Empowering materials processing and performance from data and AI. Materials, 14(16):4409, 2021.

[179] Michael Rackl and Kevin J. Hanley. A methodical calibration procedure for discrete element models. Powder Technology, 307:73–83, 2017.

[180] Johannes Grobbel, Stefan Brendelberger, Matthias Henninger, Christian Sattler, and Robert Pitz-Paal. Calibration of parameters for DEM simulations of solar particle receivers by bulk experiments and surrogate functions. Powder Technology, 364:831–844, 2020.

[181] Jan De Pue, Gemmina Di Emidio, R. Daniel Verastegui Flores, Adam Bezuijen, and Wim M. Cornelis. Calibration of DEM material parameters to simulate stress-strain behaviour of unsaturated soils during uniaxial compression. Soil and Tillage Research, 194, 2019.

[182] Marc Patrick Fransen, Matthijs Langelaar, and Dingena L. Schott. Including stochastics in metamodel-based DEM model calibration. Powder Technology, 406, 2022.

[183] Fabian Westbrink, Alexander Elbel, Andreas Schwung, and Steven X. Ding. Optimization of DEM parameters using multi-objective reinforcement learning. Powder Technology, 379:602–616, 2021.

[184] Hongyang Cheng, Takayuki Shuku, Klaus Thoeni, Pamela Tempone, Stefan Luding, and Vanessa Magnanimo. An iterative bayesian filtering framework for fast and automated calibration of DEM models. Computer Methods in Applied Mechanics and Engineering, 350:268–294, 2019.

[185] Philipp Hartmann, Hongyang Cheng, and Klaus Thoeni. Performance study of iterative bayesian filtering to develop an efficient calibration framework for DEM. Computers and Geotechnics, 141, 2022.

[186] Bilal El-Kassem, Nizar Salloum, Thomas Brinz, Yousef Heider, and Bernd Markert. A multivariate regression parametric study on DEM input parameters of free-flowing and cohesive powders with experimental data-based validation. Computational Particle Mechanics, 8:87–111, 2021.

[187] L. Benvenuti, C. Kloss, and S. Pirker. Identification of DEM simulation parameters by artificial neural networks and bulk experiments. Powder Technology, 291:456–465, 2016.

[188] Haili Zhou, Zhanqi Hu, Jigang Chen, Xuan Lv, and Nan Xie. Calibration of DEM models for irregular particles based on experimental design method and bulk experiments. Powder Technology, 332:210–223, 2018.

[189] Fangping Ye, Craig Wheeler, Bin Chen, Jiquan Hu, Kaikai Chen, and Wei Chen. Calibration and verification of DEM parameters for dynamic particle flow conditions using a backpropagation neural network. Advanced Powder Technology, 30:292–301, 2019.

[190] Wenbo Zheng and Dwayne D Tannant. Grain breakage criteria for discrete element models of sand crushing under one-dimensional compression. Computers and Geotechnics, 95:231–239, 2018.

[191] John T. Hancock and Taghi M. Khoshgoftaar. Survey on categorical data for neural networks. Journal of Big Data, 7, 2020.

[192] Ahmed Hadi, Morteza Moradi, Yusong Pang, and Dingena Schott. Adaptive ai-based surrogate modelling via transfer learning for DEM simulation of multi-component segregation. Scientific Reports, 14:27003, 2024.

[193] Leo Breiman. Bagging predictors. Machine Learning, 24:123–140, 1996.

[194] Leo Breiman. Random forests. Machine Learning, 45:5–32, 2001.

[195] Carl Edward Rasmussen. Gaussian processes in machine learning, pages 63–71. Springer, 2003.

[196] Zhijun Wu, You Wu, Lei Weng, Mengyi Li, Zhiyang Wang, and Zhaofei Chu. Machine learning approach to predicting the macro-mechanical properties of rock from the meso-mechanical parameters. Computers and Geotechnics, 166:105933, 2024.

[197] Sylvain Arlot and Alain Celisse. A survey of cross-validation procedures for model selection. Statistics Surveys, 4:40–79, 2010.

[198] Jasper Snoek, Hugo Larochelle, and Ryan P. Adams. Practical bayesian optimization of machine learning algorithms. In Advances in Neural Information Processing Systems, volume 4, pages 2951–2959, 2012.

[199] Karl Weiss, Taghi M Khoshgoftaar, and DingDing Wang. A survey of transfer learning. Journal of Big data, 3(1):9, 2016.

[200] Sinno Jialin Pan and Qiang Yang. A survey on transfer learning. IEEE Transactions on Knowledge and Data Engineering, 22:1345–1359, 2010.

[201] Mohammadreza Iman, Hamid Reza Arabnia, and Khaled Rasheed. A review of deep transfer learning and recent advancements. Technologies, 11, 2023.

[202] K. Gnana Sheela and S. N. Deepa. Review on methods to fix number of hidden neurons in neural networks. Mathematical Problems in Engineering, 2013, 2013.

[203] Christian Wellmann and Peter Wriggers. A two-scale model of granular materials. Computer Methods in Applied Mechanics and Engineering, 205:46–58, 2012.

[204] Chao Yuan and Bruno Chareyre. A pore-scale method for hydromechanical coupling in deformable granular media. Computer Methods in Applied Mechanics and Engineering, 318:1066–1079, 2017.

[205] Songkai Ren, Pei Zhang, Yifeng Zhao, Xiaoqing Tian, and S A Galindo-Torres. A coupled metaball discrete element material point method for fluidparticle interactions with free surface flows and irregular shape particles. Computer Methods in Applied Mechanics and Engineering, 417:116440, 2023.

[206] Sadegh Nadimi, Ali Ghanbarzadeh, Anne Neville, and Mojtaba Ghadiri. Effect of particle roughness on the bulk deformation using coupled boundary element and discrete element methods. Computational Particle Mechanics, pages 1–11, 2019.

[207] F Mostafaei, C Davies, M Wong, R Turki, P Liu, A Sarkar, P Doshi, J G Khinast, and D Jajcevic. Analysis of powder behaviour in bin blending processes at different scales using DEM. Advanced Powder Technology, 34:104166, 2023.

[208] Yangyu Hu and Ye Lu. A novel framework for calibrating DEM parameters: A case study of sand and soil-rock mixture. Computers and Geotechnics, 174:106619, 2024.

[209] Rutger van Sleeuwen, Stefan Pantaleev, and Mohammadreza Ebrahimi. Efficient DEM modeling of solid flavor particle mixing in a rotary drum. Powder Technology, 437:119559, 2024.

[210] Ahmed Hadi, Hao Shi, Yusong Pang, and Dingena Schott. Identification of dominant DEM parameters for multi-component segregation during heap formation, hopper discharge and chute flow. Powder Technology, 444:119985, 2024.

[211] Jacob G Wasserfall, Corné J Coetzee, and Chris J Meyer. A submerged draw down test calibration method for fully-coupled CFD-DEM modelling. Frontiers in Chemical Engineering, 6:1376974, 2024.

[212] Cristina Ramírez-Aragón, Fernando Alba-Elías, Ana González-Marcos, and Joaquín Ordieres-Meré. Segregation in the tank of a rotary tablet press machine using experimental and discrete element methods. Powder Technology, 328:452–469, 2018.

[213] Bangxing Jian and Xi Gao. Investigation of spherical and non-spherical binary particles flow characteristics in a discharge hopper. Advanced Powder Technology, 34:104011, 2023.

[214] Hamzah M. Beakawi Al-Hashemi and Omar S. Baghabra Al-Amoudi. A review on the angle of repose of granular materials. Powder Technology, 330:397–417, 2018.

[215] Ahmed Hadi, Yusong Pang, and Dingena Schott. Experimental data on pellet-sinter mixtures in draw down tests. 4TU.ResearchData, 2025.

[216] Neil A Weiss, Paul T Holmes, and Michael Hardy. A course in probability. Pearson Addison Wesley Boston, MA, USA:, 2006.

[217] Jason L Loeppky, Jerome Sacks, and William J Welch. Choosing the sample size of a computer experiment: A practical guide. Technometrics, 51:366–376, 2009.

[218] Haitao Liu, Yew-Soon Ong, and Jianfei Cai. A survey of adaptive sampling for global metamodeling in support of simulation-based complex engineering design. Structural and Multidisciplinary Optimization, 57:393–416, 2018.

[219] Donald R Jones, Matthias Schonlau, and William J Welch. Efficient global optimization of expensive black-box functions. Journal of Global optimization, 13:455–492, 1998.

[220] Jan N Fuhg, Amélie Fau, and Udo Nackenhorst. State-of-the-art and comparative review of adaptive sampling methods for kriging. Archives of Computational Methods in Engineering, 28:2689–2747, 2021.

[221] David E Golberg. Genetic algorithms in search, optimization, and machine learning. Addison-Wesley, 1989:36, 1989.

[222] Hans-Georg Beyer and Bernhard Sendhoff. Robust optimizationa comprehensive survey. Computer methods in applied mechanics and engineering, 196:3190–3218, 2007.

[223] Behzad Majidi, Kamran Azari, Houshang Alamdari, Mario Fafard, and Donald Ziegler. Simulation of vibrated bulk density of anode-grade coke particles using discrete element method. Powder technology, 261:154–160, 2014.

[224] Andre Katterfeld, Corne Coetzee, Timothy Donohue, Johannes Fottner, Andrew Grima, Alvaro Ramirez Gomez, Dusan Ilic, Rimantas Kaianauskas, Jan Necas, and Dingena Schott. Calibration of DEM parameters for cohesionless bulk materials under rapid flow conditions and low consolidation. White Paper, 2019.

[225] Chen Xu, Xiaoli Liu, Enzhi Wang, and Sijing Wang. Calibration of the microparameters of rock specimens by using various machine learning algorithms. International Journal of Geomechanics, 21:04021060, 2021.

[226] Jiansheng Chen, Haibin Zuo, Qingguo Xue, and Jingsong Wang. A review of burden distribution models of blast furnace. Powder Technology, 398, 2022.

[227] Xiaohui Zhang, Nan Wang, Zongyan Zhou, Zeyao Ning, and Min Chen. Effect of combined ferrous burden composition and ore-coke interaction on blast furnace burden distribution. Powder Technology, 449:120416, 2025.

[228] Meng Li, Yaowei Yu, and Henrik Saxén. Numerical study on the behaviour and distribution of sinter during charging of a blast furnace with bell-less top. Minerals Engineering, 228:109365, 2025.

[229] Liang He, Xin Jiang, Haiwei An, Haiyan Zheng, Qiangjian Gao, and Fengman Shen. Effects of pellet ratio on the burden movement and distribution characteristics in the bf throat. Powder Technology, 432, 2024.

[230] Ahmed Hadi, Yusong Pang, and Dingena Schott. Systematic DEM calibration of two-component mixtures using ai-accelerated surrogate models. Powder Technology, page 121190, 2025.

[231] A Hadi, Y Pang, A Adema, J van der Stel, and D Schott. Insights into the segregation in the blast furnace charging system: from the stockhouse to top hoppers. La Metallurgia Italiana, page 16, 2024.

Glossary

List of abbreviations

The following abbreviations are used in this thesis:

AI	Artificial Intelligence
ANOVA	Analysis of Variance
ANN	Artificial Neural Network
ARD	Automatic Relevance Determination (kernel)
BF	Blast Furnace
BO	Bayesian Optimisation
CFD-DEM	Computational Fluid DynamicsDiscrete Element Method (coupled)
CoV	Coefficient of Variation
CV	Cross-Validation
DEM	Discrete Element Method
DoE	Design of Experiments
DSD	Definitive Screening Design
EDEM	DEM software by Altair
EI	Expected Improvement
GA	Genetic Algorithm
GP	Gaussian Process
GPR	Gaussian Process Regression
HM	HertzMindlin (contact model)
HPC	High-Performance Computing
IC	Initial Configuration
KPI	Key Performance Indicator
LIGGGHTS	LAMMPS Improved for General Granular and Granular Heat Transfer Simulations
LOOCV	Leave-One-Out Cross-Validation
LSD	Linear SpringDashpot (contact model)
MAE	Mean Absolute Error
ML	Machine Learning
NMR	Normalised Mass Ratio
NCV	Nested Cross-Validation
PFC3D	Particle Flow Code 3D (Itasca)
PSD	Particle Size Distribution

PTV	Particle Tracking Velocimetry
PW	Paul Wurth (bell-less charging system)
R2	Coefficient of Determination (R-squared)
RMSE	Root-Mean-Square Error
RSD	Relative Standard Deviation
SI	Segregation Index
SM	Surrogate Model
SVM	Support Vector Machine
TL	Transfer Learning
TL-GPR	Transfer Learning based on Gaussian Process Regression
TL-SM	Transfer Learning-based Surrogate Model
WB	Weighing Bunker
WF	Wall Friction

List of symbols and notations

Below follows a list of the most frequently used symbols and notations in this thesis. Units are given where applicable.

DEM / materials

d_p	Particle diameter (m)
D_{50}	Median particle diameter (mm)
E	Youngs modulus (Pa)
G	Shear modulus (Pa)
ρ_s	Solid (particle) density (kg /m^3)
ν	Poissons ratio ()
μ_s	Coefficient of sliding friction ()
μ_r	Coefficient of rolling friction ()
C_r	Coefficient of restitution ()

Segregation metrics

χ_p	Instantaneous mass ratio of pellets ()
χ_0	Initial pellet mass ratio ()
$\chi_{\max}$	Maximum pellet mass ratio ()
SI	Segregation index ()
NMR_i	Normalised mass ratio of component i ()
φ_N	Number fraction ()
φ_m	Mass fraction ()
φ_V	Volume fraction ()
y_t^i	Relative number fraction of tracer t in bin i ()
x_t^i	Relative mass fraction of tracer t in bin i ()
c_t^i	Relative volume fraction of tracer t in bin i ()
$y_t,\ x_t,\ c_t$	System-wide relative fractions of tracer t ()

$t_{\min},\ t_{\max}$	Start / end times of sampling window (s)
$\hat{t}$	Normalised time $\hat{t} = (t - t_{\min})/(t_{\max} - t_{\min})$ ()

Gaussian Process Regression (GPR)

$f(x)$	Latent function ()
$\mu(x)$	GP mean function ()
$k(x,x')$	Covariance kernel ()
$\mathbf{K}$	Gram (covariance) matrix $[k(x_i,x_j)]$ ()
$\hat{k}(x)$	Covariance vector $[k(x_1,x),\ldots,k(x_n,x)]^T$ ()
x	Test input location ()
I_n	$n \times n$ identity matrix ()
μ	Predictive mean at x ()
σ^2	Predictive variance at x ()
$\alpha,\ \alpha_i$	Weights in kernel expansion ()
$r = \sqrt{(x-x')^T(x-x')}$	Euclidean distance between inputs
σ_f^2	Signal (output) variance ()
σ_l	Characteristic length scale ()
α	Rationalquadratic mixture parameter ()

Ensemble / Transfer Learning

B	Number of learners in ensemble ()
$f_0(x)$	Initial ensemble prediction ()
$f_m(x)$	Ensemble prediction after m iterations ()
$h_m(x)$	Weak learner at iteration m ()
η_m	Learning rate at iteration m ()
$r_i^{(m)}$	Residual for sample i at iteration m ()
$D_s,\ D_t$	Source and target datasets ()
$w_0,\ \theta_0$	Initial parameters / hyperparameters ()
$w_s,\ \theta_s$	Source-trained parameters / hyperparameters ()
w_t	Parameters after target update ()
N_t	Number of target samples used ()

Model evaluation metrics

RMSE	Root-mean-square error ()
R^2	Coefficient of determination ()
MAE	Mean absolute error ()
T_{train}	Training time (s)
ν_{pred}	Prediction speed (obs. s^{-1})

Subscripts and superscripts

pp, pw	Particleparticle / particlewall contact
i	Sample, bin or material index (context-dependent)
avg	Average

Summary

Segregation, or de-mixing, is a significant challenge in the handling and processing of granular materials. It can lead to several problems, including inconsistent product quality, poor flowability, and process inefficiencies. In blast furnace steelmaking, segregation of the ferrous mixture (consisting of pellets, sinter, lump ore, and nut coke) causes uneven distribution of mixture components at the furnace throat. This reduces permeability and disrupts the gasburden interaction, which is critical for stable and efficient operation. Therefore, understanding segregation is essential. The Discrete Element Method (DEM) offers a powerful way to investigate segregation, particularly in the blast furnace, where direct measurements and experiments are difficult due to the harsh operating environment.

This thesis developed a systematic, accurate, and computationally efficient approach based on DEM to model the flow behaviour of multi-component mixtures, and to apply the developed model to the blast furnace charging system, from the weighing bunkers to the top hopper.

The work began with a review of existing DEM studies on segregation, which showed that although real mixtures usually contain particles differing simultaneously in size, density and shape, most DEM research is still focused on simpler binary systems. It also revealed that systematic calibration is often missing, which leaves uncertainty about the role of interaction parameters, particle shape, and size distribution. These gaps underlined the need for improved calibration frameworks and more efficient modelling strategies.

Next, a comprehensive sensitivity analysis was conducted for pelletsinter mixtures. This identified which DEM parameters most strongly influenced segregation at different charging stages and confirmed that, across the charging system, upstream conditions largely determine the segregation observed downstream. Building on these insights, a machine learning-based surrogate modelling framework was developed to improve computational efficiency and enable fast prediction of segregation outcomes. To make the framework more versatile, transfer learning was integrated so that models trained on previous configurations could be adapted to new configurations with only a small amount of additional data.

Together, these developments formed the basis for a systematic calibration framework for multi-component mixtures that combined sensitivity analysis, surrogate modelling with adaptive sampling, and optimisation. The calibration framework achieved high accuracy with far fewer DEM simulations, and the resulting parameters could be applied across different mixture ratios and configurations. It also showed that particle density needs to be calibrated when dynamic processes are considered, and that segregation in draw-down tests cannot be used for calibration because of the dominant effect of DEM stochasticity.

The calibrated DEM model was then applied at the industrial scale to study segregation of

the ferrous mixture in the blast furnace charging system, from the weighing bunkers to hopper discharge. Perfect mixing of pellets and sinter at the weighing bunkers was found to almost eliminate segregation, whereas under current practice, the materials remained largely segregated. Segregation decreased slightly during transfer from the skip car to the top hopper due to partial remixing. Nevertheless, strong segregation persisted, particularly for lump ore and nut coke, which accumulated near the top of the mixture in the hopper. Pellets, by contrast, consistently showed the lowest segregation levels throughout the charging system. Case studies further confirmed that upstream conditions, such as the order of filling the bunkers, had a strong effect on segregation. However, factors such as wall friction, lump ore type, or moderate changes in sinter size distribution were found to have only a limited influence.

Overall, this thesis advances both the modelling tools available for studying segregation in multi-component mixtures and the understanding of how segregation develops in the blast furnace charging system. Scientifically, it shows that DEM can be combined with surrogate modelling and systematic calibration to deliver accuracy while greatly improving efficiency. From an industrial perspective, it demonstrates that promoting upstream mixing is the most effective strategy for reducing segregation and that operational parameters offer a more practical approach for mitigating segregation than material properties or system design. The contributions of this thesis provide a basis for future developments in DEM modelling and support ongoing efforts to make steelmaking processes more efficient and sustainable.

Samenvatting

Segregatie, ofwel ontmenging van deeltjes, vormt een belangrijke uitdaging bij de overslag en verwerking van granulaire materialen. Het kan tot verschillende problemen leiden, waaronder inconsistente productkwaliteit, verslechte stroombaarheid en procesinefficiënties. Segregatie van de ijzerhoudende mengselstroom (bestaande uit pellets, sinter, lump ore en kleine kooks) die optreedt tijdens hoogovenbelading leidt tot een ongelijke verdeling van mengseldeeltjes in de hoogoven. Dit vermindert de permeabiliteit en verstoort de interactie tussen gas en deeltjes, die cruciaal is voor een stabiele en efficiënte operatie. Inzicht in segregatie is daarom essentieel. De Discrete Element Method (DEM) biedt een krachtig middel om segregatie te onderzoeken, met name in de hoogoven, waar directe metingen en experimenten moeilijk uitvoerbaar zijn vanwege de zware bedrijfsomstandigheden.

Dit proefschrift had tot doel een systematische, nauwkeurige en rekentechnisch efficiënte DEM-gebaseerde aanpak te ontwikkelen om het stroomgedrag van multicomponentmengsels te modelleren, en het ontwikkelde model toe te passen op het hoogovenlaadsysteem, van de weegbunkers tot aan de topbunker.

Het werk begon met een overzicht van bestaande DEM-studies over segregatie, waaruit bleek dat echte mengsels doorgaans bestaan uit deeltjes die tegelijk verschillen in grootte, dichtheid en vorm, terwijl veel DEM-onderzoek nog steeds is gericht op eenvoudigere binaire systemen. Ook kwam naar voren dat systematische kalibratie vaak ontbreekt, waardoor onduidelijkheid blijft bestaan over de rol van interactieparameters, deeltjesvorm en grootteverdeling. Deze tekortkomingen onderstreepten de behoefte aan verbeterde kalibratiekaders en efficiëntere modelleringsstrategieën.

Vervolgens is een uitgebreide gevoeligheidsanalyse uitgevoerd voor pellet-sinter-mengsels. Daarmee is vastgesteld welke DEM-parameters de segregatie het sterkst beïnvloeden in verschillende laadstadia, en werd bevestigd dat in het gehele laadsysteem de initiële (upstream) condities grotendeels bepalend zijn voor de mate van segregatie verderop in het proces. Op basis van deze inzichten is een machine-learning-gebaseerd surrogaatmodel ontwikkeld om de rekenkosten te verlagen en snelle voorspellingen van segregatieresultaten mogelijk te maken. Om het raamwerk veelzijdiger te maken, is transfer learning geïntegreerd, zodat modellen die op eerdere configuraties zijn getraind kunnen worden aangepast aan nieuwe configuraties met slechts een kleine hoeveelheid aanvullende data.

Gezamenlijk vormden deze ontwikkelingen de basis voor een systematisch kalibratiekader voor multicomponentmengsels, dat gevoeligheidsanalyse, surrogaatmodellering met adaptieve sampling en optimalisatie combineert. Het kalibratiekader bereikte hoge nauwkeurigheid met aanzienlijk minder DEM-simulaties, en de resulterende parameters bleken toepasbaar over verschillende mengverhoudingen en configuraties. Ook werd aangetoond dat de deeltjesdichtheid

moet worden gekalibreerd wanneer dynamische processen worden beschouwd, en dat segregatie in draw-down testen ongeschikt is voor kalibratie vanwege het dominante effect van DEM-stochastiek. Het gekalibreerde DEM-model werd vervolgens op industriële schaal toegepast om segregatie van de ijzerhoudende mengstroom in het hoogovenlaadsysteem te bestuderen, van de weegbunkers tot en met de lozing uit de topbunker. Perfecte menging van pellets en sinter in de weegbunkers bleek segregatie vrijwel te elimineren, terwijl onder de huidige praktijk de materialen grotendeels gesegregeerd bleven. Tijdens de overdracht van de skipwagen naar de topbunker nam de segregatie licht af door gedeeltelijke hermenging. Niettemin hield sterke segregatie aan, vooral voor lump ore en kleine kooks, die zich bovenin het mengsel in de topbunker ophoopten. Pellets vertoonden daarentegen consequent de laagste segregatieniveaus in het gehele laadsysteem. Casestudies bevestigden bovendien dat upstream condities, zoals de volgorde waarin de bunkers worden gevuld, een sterke invloed hebben op segregatie. Factoren zoals wandwrijving, het type lump ore of gematigde veranderingen in de sintergrootteverdeling bleken echter slechts een beperkte invloed te hebben.

Al met al draagt dit proefschrift bij aan zowel de beschikbare modelleringshulpmiddelen voor het bestuderen van segregatie in multicomponentmengsels als aan het begrip van hoe segregatie zich ontwikkelt in het hoogovenlaadsysteem. Wetenschappelijk toont het aan dat DEM kan worden gecombineerd met surrogaatmodellering en systematische kalibratie om hoge nauwkeurigheid te leveren met een sterk verbeterde efficiëntie. Vanuit industrieel perspectief toont het aan dat het bevorderen van initiële menging de meest effectieve strategie is om segregatie te verminderen, en dat operationele parameters een praktischer aangrijpingspunt bieden dan materiaaleigenschappen of systeemontwerp. De bijdragen van dit proefschrift vormen een basis voor toekomstige ontwikkelingen in DEM-modellering en ondersteunen lopende inspanningen om staalproductieprocessen efficiënter en duurzamer te maken.

Acknowledgements

My PhD journey began in a way I did not expect. I initially planned to pursue my doctoral studies in Australia, but the border closures during the COVID-19 pandemic made that impossible. I then shifted my focus and eventually came across this position at TU Delft. Looking back, I am deeply grateful for how things unfolded, and I learned that letting go of carefully made plans can sometimes lead to something even better. Doing a PhD here, and living far from my home country, helped me grow both personally and professionally, and made me realise how deeply I value my family and my roots. Along this journey, I was fortunate to be surrounded by many people whose support made this experience possible, meaningful, and enjoyable.

First and foremost, I would like to express my sincere gratitude to **Prof.dr.ir. Dingena Schott** and **Dr.ir. Yusong Pang** for their guidance and support throughout my PhD. **Yusong**, I especially appreciated your attention to detail while always keeping an eye on the bigger picture. **Dingena**, you are a genuinely kind and caring person, a great supervisor, and a true leader. Very early in my PhD, I understood why people kept telling me how lucky I was to have you as my supervisor. I learned a lot from you, not only scientifically, but also from the way you work with people. Thank you for always being considerate, for trusting me, and for giving me the freedom to explore side projects alongside my PhD. I am also very grateful for the many opportunities you gave me to attend conferences and engage with the wider research community. All of this made the PhD journey both richer and more enjoyable.

I would like to thank Tata Steel Netherlands and M2i for funding this project and for making this research possible. I am grateful to **Jan van der Stel**, **Allert Adema**, and **Niels van den Burg** from Tata Steel for their support throughout the project and their valuable insights that contributed to Chapter 6 of this thesis. I would especially like to thank **Allert Adema** for his support in securing funding that allowed the continuation of this research beyond the PhD, and **Jan van der Stel** for encouraging me to attend the ECIC conference in Italy, which was a valuable experience. I would also like to thank **Viktoria Savran** from M2i for her kind support and involvement in the project.

Dr Sadegh Nadimi and **Dr Vasileios Angelidakis**, I have known you since 2020, even before the start of my PhD, when we began a small project on master curve implementation. This collaboration was later resumed in 2024 and ultimately completed during my research visit to Newcastle University. I would like to thank the COST ON-DEM Action for supporting this visit, and both of you for your continued support throughout the work. I am especially grateful to **Dr Sadegh Nadimi** for kindly hosting me at Newcastle University and for his support during my PhD interview.

I would like to thank all my colleagues at the Department of MTT for making the day-to-day life of a PhD far more enjoyable than it could have been. A big thank you to **Javad**, **Raïsa**, **Hao**,

Marcel, **Ana**, **Adrien**, **Marc**, **Jesper**, **Yunpeng**, **Aaron**, **Wenhua**, **Saeed**, **Mikhail**, **Nandini**, **Xiaohuan**, and **Pan**. Being surrounded by such a diverse, supportive, and thoughtful group of people made the difficult moments more manageable. I am also grateful to my current officemates, **Nandini** and **Marcel**, and my former officemates, **Xiaohuan** and **Pan**, for creating an office environment that was both productive and pleasant. **Javad**, thank you for acting as a mentor during the early stages of my PhD, especially at times when I felt lost or unsure about the direction I was taking. Your guidance helped me a lot. **Marcel**, I truly enjoyed the many scientific and non-scientific discussions we shared in the office, as well as the time we spent together at conferences in Australia and Japan. **Hao**, I want to thank you in particular for your contribution to Chapter 3 of this thesis, where your input and deep technical knowledge strengthened the quality of the work. **Raïsa**, I was very lucky to have you working next to me on a closely related topic. It made a huge difference not to feel like I was working on an island. Thank you for sharing ideas, for listening to my complaints about the challenges of DEM and experiments, and for sharing your own. Talking things through together somehow made them easier to handle and, at times, even a bit funny. **Jesper**, I really enjoyed our Coffee? Tea! Tea is also fine! moments and the philosophical conversations we shared over those breaks. **Adrien**, you are a genuinely kind and caring person. I feel very lucky that our time as colleagues grew into a meaningful friendship. Your presence made a real difference in the department for me, and it was clearly felt when you were no longer around.

I would like to express my gratitude to the members of the defence committee for accepting the invitation to take part in my PhD defence and for taking the time to read my thesis. I would like to especially thank **Prof.dr. Henrik Saxén** and **Prof.dr.ir. Ruud van Ommen** for the careful reading of the manuscript and for the constructive feedback, which helped strengthen the quality of this thesis.

To my friends in Iran (**Soleyman**, **Behnam**, **Hamid**, **Ali**, **Mohammad**, **Alireza Teimouri**, **Alireza Khalili**, and **Milad**) and in the Netherlands (**Morteza**, **Hesam**, **Soroush**, **Saman**, **Amirhossein**, **Mohammad Javad**, **Hani**, **Azadeh**, **Rasoul**, **Negar**, **Neda**, **Parastou**, **Sana**, **Eszter**, **Farhad**, and **Mozhgan**): having you around, whether close by or at a distance, made this PhD period much easier to go through. Your support, conversations, and simple presence helped in many direct and indirect ways, especially during the more challenging moments, including times when there were tensions back home in Iran. You helped me stay grounded and made this journey more manageable and more enjoyable than it would have been otherwise. **Soleyman**, you were always the one who checked in to ask how I was doing and reminded me to travel back to Iran. Those messages meant more to me than you might think, and made me feel remembered, even from far away. Also, thanks for designing such a nice cover for this thesis. **Morteza**, it was a genuinely nice coincidence to meet you on my first flight to the Netherlands, which later grew into a real and meaningful friendship, and eventually into a research collaboration that contributed to Chapter 4 of this thesis. It was great to have you as someone who always motivated me to aim higher and do better. **Hesam**, **Soroush**, and **Saman**, I feel very lucky to have had such a close friendship circle with you. I will always remember our lunch-break conversations, which ranged from light and casual to surprisingly deep, as well as the two trips we had, both of which remain very special and memorable to me.

برای سپاسگزاری از خانواده، واژه‌ها همواره ناتوان و کم‌جان‌اند؛ با این حال می‌نویسم تا گواهی باشد بر قدردانی عمیق و همیشگی من از حضوری که معنا و استواری زندگی‌ام از آن ریشه گرفته است. **حنان، قاسم و فاطمه، زهرا و ماهر، مریم**، و نوه‌های شیرین خانواده؛ بودن شما، چه در نزدیکی و چه در فاصله‌های دور، همواره مایه دلگرمی، امید و آرامش من بوده و هست. از **خانواده همسر عزیزم** که در میانه مسیر دکتری به دایره عزیزانم افزوده شدند و با مهر و همراهی صمیمانه‌شان، بار این مسیر را برای من سبک‌تر و دلگرم‌کننده‌تر کردند، سپاسگزارم. خواهر عزیزم **رویا**، در کنار محبت بی‌دریغ و مادرانه‌ات، حضورت در کنار پدر و مادرمان و مراقبت دلسوزانه‌ات از آنان، منبعی پایدار از اطمینان و آرامش خاطر برای من، در تمام دوران دکتری و پس از آن بوده است؛ نعمتی که هر روز به خاطرش سپاسگزارم. **زینب** و **مصطفی** عزیز، سپاسگزار میزبانی گرم و به‌یادماندنی شما در سال ۲۰۲۳ هستم؛ خاطراتی که در سفر استرالیا برای ما ساختید و در سفرهای اخیرتان به اروپا، با همان سخاوت و صمیمیت، ادامه دادید. از **پدرم** سپاسگزارم؛ که معنای تعهد و مسئولیت‌پذیری را به من آموخت و با رفتار و کردار خود نشان داد چگونه می‌توان، با وجود فراز و نشیب‌های بزرگ و کوچک، همواره ستون استوار خانواده باقی ماند. و از **مادر** عزیزتر از جانم؛ که با مدیریت خردمندانه زندگی و مهربانی بی‌پایانش، همیشه کانون خانواده را گرم و پابرجا نگاه داشت. از تو مهربانی، سخت‌کوشی و تاب‌آوری در برابر دشواری‌ها را آموختم؛ درس‌هایی که همواره با من خواهند ماند.

To my **Parvin**: I feel very lucky to have met you at the very beginning of my PhD and to have shared this entire journey with you. Your patience during long days and busy periods, your encouragement when I doubted myself, and your steady emotional support meant more to me than I can easily express. You stood by me generously, even while facing your own PhD challenges, which I deeply admire. You also supported me in countless practical ways, from conferences to my research visit to Newcastle, and by taking care of daily life when my attention was often elsewhere. Your love gave me calm and stability, and helped me fall into a routine that brought structure to my days. Through the way you handled everything, with strength and resilience, you showed me in a very real way how powerful a woman can be. I am deeply grateful and proud to share this journey, and my life, with you.

I would like to close with a short poem by **Hafez**, which reflects the personal and spiritual journey I have experienced in recent years:

سال‌ها دل طلبِ جامِ جم از ما می‌کرد وآنچه خود داشت ز بیگانه تمنّا می‌کرد

گوهری کز صدفِ کون و مکان بیرون است طلب از گمشدگانِ لبِ دریا می‌کرد

مشکلِ خویش بَرِ پیرِ مُغان بُردم دوش کاو به تأییدِ نظر حلِّ معمّا می‌کرد

دیدمش خُرَّم و خندان قدحِ باده به دست واندر آن آینه صد گونه تماشا می‌کرد

گفتم این جامِ جهان‌بین به تو کِی داد حکیم؟ گفت آن روز که این گنبدِ مینا می‌کرد

بی‌دلی در همه احوال خدا با او بود او نمی‌دیدش و از دور خدایا می‌کرد

Ahmed Hadi
Delft, February 2026

About the author

Ahmed Hadi was born on 15 April 1992 in Isfahan, Iran. He obtained his Bachelors degree in Civil Engineering from Isfahan University of Technology in 2015, followed by a Masters degree in Civil Engineering with a specialisation in Geotechnical Engineering at the University of Tehran, which he completed in 2018. During his masters studies, he investigated the mechanical behaviour of granular soils under complex loading conditions using the Discrete Element Method (DEM), which sparked his interest in the numerical modelling of granular materials.

In 2021, he joined the GranChaM Lab at Delft University of Technology as a PhD researcher under the supervision of Prof.dr.ir. Dingena Schott and Dr.ir. Yusong Pang. His doctoral research focused on understanding and predicting the flow, mixing, and segregation behaviour of iron ore mixtures within blast furnace charging systems using DEM. A central theme of the project was industrial applicability, with particular emphasis on model calibration, validation, and scalability. This work also fostered a strong interest in the use of surrogate modelling and machine learning techniques to accelerate simulation workflows and enable data-driven decision-making in industrial settings. This thesis presents the outcomes of that research, from laboratory experiments and advanced numerical modelling to plant-scale simulations carried out in collaboration with Tata Steel Netherlands.

During his PhD, Ahmed also undertook a short research visit to Newcastle University, where he worked with Dr Sadegh Nadimi and Dr Vasileios Angelidakis on the implementation of a variable inter-particle friction model. This work contributed to the development of more physically representative contact models for heterogeneous granular systems and complemented his broader doctoral research on modelling complex industrial granular flows.

His current research interests focus on the application of surrogate modelling and machine learning techniques to accelerate high-fidelity numerical simulations and support decision-making in industrial problems.

Publications

Journal articles related to this thesis

1. **Ahmed Hadi**, Raïsa Roeplal, Yusong Pang, and Dingena Schott. DEM modelling of segregation in granular materials: a review. KONA Powder and Particle Journal, 41:78107, 2024.

2. **Ahmed Hadi**, Hao Shi, Yusong Pang, and Dingena Schott. Identification of dominant DEM parameters for multi-component segregation during heap formation, hopper discharge and chute flow. Powder Technology, 444:119985, 2024.

3. **Ahmed Hadi**, Morteza Moradi, Yusong Pang, and Dingena Schott. Adaptive AI-based surrogate modelling via transfer learning for DEM simulation of multicomponent segregation. Scientific Reports, 14:27003, 2024.

4. **Ahmed Hadi**, Yusong Pang, and Dingena Schott. Systematic DEM calibration of two-component mixtures using AI-accelerated surrogate models. Powder Technology, page 121190, 2025.

5. **Ahmed Hadi**, Yusong Pang, Allert Adema, Jan van der Stel, and Dingena Schott. Industrial-scale DEM Modelling of Segregation in the Blast Furnace Charging System. Powder Technology, 471:122116, (2026).

Other journal articles

1. Jeroen Emmerink, **Ahmed Hadi**, Jovana Jovanova, Chris Cleven, and Dingena Schott. Parametric analysis of a double shaft, batch-type paddle mixer using the discrete element method (DEM). Processes, 11, 2023.

2. **Ahmed Hadi**, Vasileios Angelidakis, Dingena Schott, and Sadegh Nadimi. Effect of variable inter-particle friction on complex granular flows. Powder Technology (under review)

Conference papers

1. **Ahmed Hadi**, Yusong Pang, and Dingena Schott. Calibration of DEM parameters for multi-component segregation. In ICBMH2023: 14th International Conference on Bulk Materials Storage, Handling and Transportation, pages 221233. The Institution of Engineers, Australia, Wollongong, NSW, 2023.

2. **Ahmed Hadi**, Yusong Pang, Allert Adema, Jan van der Stel, and Dingena Schott. Insights into the segregation in the blast furnace charging system: from the stockhouse to top hoppers. La Metallurgia Italiana, page 16, 2024.

TRAIL Thesis Series

The following list contains the most recent dissertations in the TRAIL Thesis Series. For a complete overview of more than 400 titles, see the TRAIL website: www.rsTRAIL.nl.

The TRAIL Thesis Series is a series of the Netherlands TRAIL Research School on transport, infrastructure and logistics.

Hadi, A.H., *DEM Modelling of Multi-Component Segregation in the Blast Furnace Charging System*, February 2026, TRAIL Thesis Series, The Netherlands

Farhani, M., *Demand Management Strategies for Operations of Shared Mobility Services*, February 2026, TRAIL Thesis Series, The Netherlands

Yao, X., *Driving Heterogeneity in Traffic Flow Theory: An action-based framework for identification, modelling, and simulation*, January 2026, TRAIL Thesis Series, The Netherlands

Versluis, N.D., *Optimising Railway Traffic Management under Radio-Based Distance-to-Go Signalling*, January 2026, TRAIL Thesis Series, The Netherlands

Jiao, Y., *Proactive Collision Risk Quantification in Multi-directional Traffic Interactions*, January 2026, TRAIL Thesis Series, The Netherlands

Asadi, M., *Accessibility and Road Safety: Integration of road safety in accessibility evaluation*, November 2025, TRAIL Thesis Series, The Netherlands

Akse, R., *Understanding and untangling the uncertainty knot: How to catalyse decision-making in mobility innovations*, November 2025, TRAIL Thesis Series, The Netherlands

Führer, K., *Participatory Decision-making under Deep Uncertainty: Modelling mobility transitions*, November 2025, TRAIL Thesis Series, The Netherlands

Picco, A., *Monitoring and Feedback in Driving*, T2025/17, October 2025, TRAIL Thesis Series, The Netherlands

Cebeci, M.S., *Behaviour of Prosumers in Last-mile Logistics: The case of crowdshipping*, T2025/16, September 2025, TRAIL Thesis Series, The Netherlands

Kuijpers, A., *Enabling Inter-Organizational Collaboration Through Platforms: The role of*

trust, T2025/15, September 2025, TRAIL Thesis Series, The Netherlands

Song, R., *Human-MASS Interaction in Decision-Making for Safety and Efficiency in Mixed Waterborne Transport Systems*, T2025/14, June 2025, TRAIL Thesis Series, The Netherlands

Destyanto, A.R., *A Method for Evaluating Port Resilience in an Archipelago*, T2025/13, June 2025, TRAIL Thesis Series, The Netherlands

Karademir, C., *Synchronized Two-echelon Routing Problems: Exact and approximate methods for multimodal city logistics*, T2025/12, May 2025, TRAIL Thesis Series, The Netherlands

Vial, A., *Eyes in Motion: A new traffic sensing paradigm for pedestrians and cyclists*, T2025/11, May 2025, TRAIL Thesis Series, The Netherlands

Chen, Q., *Towards Mechanical Intelligence in Soft Robotics: Model-based design of mechanically intelligent structures*, T2025/10, April 2025, TRAIL Thesis Series, The Netherlands

Eftekhar, Z., *Exploring the Spatial and Temporal Patterns in Travel Demand: A data-driven approach*, T2025/9, June 2025, TRAIL Thesis Series, The Netherlands

Reddy, N., *Human Driving Behavior when Interacting with Automated Vehicles and the Implications on Traffic Efficiency*, T2025/8, May 2025, TRAIL Thesis Series, The Netherlands

Durand, A., *Lost in Digitalisation? Navigating public transport in the digital era*, T2025/7, May 2025, TRAIL Thesis Series, The Netherlands

Dong, Y., *Safe, Efficient, and Socially Compliant Automated Driving in Mixed Traffic: Sensing, Anomaly Detection, Planning and Control*, T2025/6, May 2025, TRAIL Thesis Series, The Netherlands

Droffelaar, I.S. van, *Simulation-optimization for Fugitive Interception*, T2025/5, May 2025, TRAIL Thesis Series, The Netherlands

Fan, Q., *Fleet Management Optimisation for Ride-hailing Services: from mixed traffic to fully automated environments*, T2025/4, April 2025, TRAIL Thesis Series, The Netherlands

Hagen, L. van der, *Machine Learning for Time Slot Management in Grocery Delivery*, T2025/3, March 2025, TRAIL Thesis Series, The Netherlands

Schilt, I.M. van, *Reconstructing Illicit Supply Chains with Sparse Data: a simulation approach*, T2025/2, January 2025, TRAIL Thesis Series, The Netherlands

Ruijter, A.J.F. de, *Two-Sided Dynamics in Ridesourcing Markets*, T2025/1, January 2025, TRAIL Thesis Series, The Netherlands

Fang, P., *Development of an Effective Modelling Method for the Local Mechanical Analysis of*

Submarine Power Cables, T2024/17, December 2024, TRAIL Thesis Series, The Netherlands

Zattoni Scroccaro, P., *Inverse Optimization Theory and Applications to Routing Problems*, T2024/16, October 2024, TRAIL Thesis Series, The Netherlands

Kapousizis, G., *Smart Connected Bicycles: User acceptance and experience, willingness to pay and road safety implications*, T2024/15, November 2024, TRAIL Thesis Series, The Netherlands

Summary

Granular segregation is a significant challenge in blast furnace (BF) operation. This thesis presents an accurate and computationally efficient approach based on the discrete element method (DEM) to study this phenomenon. Machine learning-based surrogate modelling is first employed for efficient model calibration, after which the calibrated DEM model is applied at the industrial scale to analyse segregation in BF and provide practical strategies to mitigate it.

About the author

Ahmed Hadi has conducted his PhD research in Machines & Materials Interactions (MMI) at Delft University of Technology, in the Netherlands. Prior to this, he obtained a Master's degree in Geotechnical Engineering from the University of Tehran, in Iran.

TRAIL Research School ISBN 978-90-5584-380-0